TECHNOLOGY CHANGE FOR STRATOSPHERIC OZONE MEASUREMENT

A thesis submitted to the University of Manchester for the degree of Doctor of Philosophy in the Faculty of Science and Engineering

YEAR OF SUBMISSION

2022

Eric Gonzalez Peralta

School of Natural Sciences

Total number of words: 40722

Table of Contents

Table of Contents **2**

Table of Figures **5**

List of Tables **16**

Abstract **17**

Declaration **19**

Copyright Statement **19**

Acknowledgements **20**

Chapter 1. Introduction **21**

1.1. Stratospheric ozone 21

1.2. Solar radiation 22

1.2.1. Interaction of UV radiation with stratospheric ozone 23

1.2.2. Interaction of UV radiation with living species 27

1.3. Ozone depletion and Chlorofluorocarbons (CFCs) 27

1.3.1. Contributions of polar stratospheric clouds (PSCs) and Polar vortex to Polar ozone depletion 30

1.4. Montreal Protocol 32

1.5. Stratospheric ozone monitoring 36

1.6. Importance of ground measurements of total ozone column 38

1.7. Ground-based spectrometers 41

1.7.1. Dobson spectrometer 42

1.7.2. Brewer spectrometer 43

1.8. Aims and objectives of the research 45

1.9. Outline of the thesis 45

Chapter 2. Atmospheric attenuation and the DOAS technique for deriving total ozone column **47**

2.1. Beer-Lambert law 47

2.2. Optical depth 49

2.3. Sun Position 49

2.3.1. Declination angle of the Sun 50

2.3.2. Local solar time and hour angle 51

2.3.3. Solar zenith angle 52

2.4. Relative optical air mass 52

2.5. Ozone absorption cross-section 55

2.6. Differential optical absorption spectroscopy (DOAS) technique 58

2.7. Rayleigh-scattering and Mie-scattering calculations 59
2.7.1. Inelastic collisions: Raman scattering 60
2.7.2. Elastic collisions: Rayleigh and Mie scattering 60
2.7.3. Rayleigh scattering 61
2.7.4. Mie scattering 65
2.8. Beer-Lambert Law for total ozone column 66
Chapter 3. Acousto-optic tunable filter (AOTF) 69
3.1. Differences between the proposed spectrometer and current spectrometers 69
3.1.1. Prisms and diffraction Gratings 69
3.1.2. Photodiode arrays and Photomultiplier Tubes (PMTs) 70
3.2. Acousto-optic tunable filter (AOTF) 72
3.2.1. Birefringence 73
3.2.2. Quartz as a birefringent crystal 75
3.2.3. Acousto-optic effect 76
3.2.4. Collinear and Non-collinear configuration 77
Chapter 4. The AOTF spectrometer 80
4.1. Optical design 81
4.1.1. Quartz crystal and transductor of AOTF 81
4.1.2. Band-pass filter 83
4.1.3. Glan-Tylor polarizers 85
4.1.4. Plano-convex lens 86
4.2. Electronics 87
4.2.1. RF controller 87
4.2.2. Thermo-electric controller of AOTF 88
4.2.3. Analogue to digital converter (ADC) 89
4.2.4. Avalanche photodiode (APD) 89
4.3. Locking amplifier 91
4.4. User interface 94
Chapter 5. Optimization of the initial design 97
5.1. The transfer function of the AOTF spectrometer 97
5.2. Alignment of polarizers 99
5.3. Importance of lock-in amplifier 100
5.4. The optimum number of integrations 101
Chapter 6. Laboratory characterization and calibration 103
6.1. Initial wavelength alignment 104
6.2. Measurement of spectral lines 109
6.2.1. Mercury lamp 109

6.2.2. Cadmium lamp 109
6.2.3. Zinc Lamp 110
6.2.4. Measurement of Helium-Cadmium (HeCd) laser 111
6.3. Full width half maximum 113
6.4. 50W and 200W Halogen lamp 115
6.5. Temperature stability test using a temperature chamber 116
6.6. Broadband sources and fine-scale modulation 121
6.7. White LED (6500K) 121
6.8. UV LED (365 nm) 122
6.9. Undesired second wavelength reaching the detector. 122
6.10. Summary 123
Chapter 7. Direct solar measurements 125
7.1. Direct solar measurements at Kipp and Zonen facilities in Delft, The Netherlands 125
7.2. Direct measurements at The University of Manchester, UK 128
7.3. Measurements of Total ozone column at The University of Manchester, UK 132
7.3.1. Instrument intercomparison-calibration with Brewer #172 132
7.3.2. TOC measurements on 18th September 2020 137
7.3.3. TOC measurements on 25th September 2020 139
7.3.4. Simple two-wavelength DOAS technique to retrieve TOC 142
7.4. Discussion of results 148
Chapter 8. Conclusions and further work 151
8.1. Conclusions 151
8.2. Further work 153
8.2.1. Characterization and calibration improvements 153
8.2.2. Replacing the detector 153
8.2.3. Addition of a mounting case and mechanical improvements 154
8.2.4. New RF controller and customized electronics 155
8.2.5. User interface improvements 155
8.2.6. Additional side-to-side comparisons with calibrated spectrometers 155
8.2.7. Adding a second AOTF to the spectrometer 156
References 157

Table of Figures

Figure 1.1 Peak ozone concentration occurs between 30 km and 35 km of altitude (https://ozonewatch.gsfc.nasa.gov/facts/SH.html). 22

Figure 1.2 Comparison of the solar irradiance in the outer atmosphere, the electromagnetic radiation of a black body at 5900 K, and the solar irradiance at ground level for clear-sky conditions (Ortenberg, 2013). 23

Figure 1.3. The satellite spectrometer GOME FM obtained the ozone absorption cross-section at 293K (Burrows et al., 1999). It illustrates the spectral bands used by the DOAS technique to get the total column of ozone. 24

Figure 1.4. Absorption cross-section of SO2 molecules at 295 K (Rufus et al., 2003). 24

Figure 1.5 Comparison between the solar radiation in the outer atmosphere (red area) and the solar radiation measured at ground level (blue area). The bottom chart compares the UV radiation spectrum before and after passing through the atmospheric ozone (note the log scale on the y-axis). Less than 1% of the radiation at wavelengths less than 300 nm is transmitted due to a strong ozone absorption at shorter wavelengths (Aucamp et al., 2020). 25

Figure 1.6 Chapman cycle of ozone formation and destruction (Vázquez and Hanslmeier, 2006). 26

Figure 1.7. It shows the maximum ozone hole and the minimum total ozone column in 1985, respectively. They are based on the data from the satellite measurements performed by the Total Ozone Mapping Spectrometer (TOMS). Images were taken from the ozone hole watch on the NASA website (NASA, 2020). 28

Figure 1.8 The interaction of halogen gases (such as CFCs) with atmospheric compounds and ultraviolet radiation results in reservoir forms of chlorine and ozone-depleting substances at stratospheric altitudes. The image is taken from https://esrl.noaa.gov/csd/assessments/ozone/2006/chapters/Q8.pdf 29

Figure 1.9 Cycle 1 describes the stratospheric regeneration of a Cl or ClO molecule when interacting with a molecule of ozone and oxygen, depleting a large number of ozone molecules in the process. Cycles 2 and 3 describe the photochemical interactions where Cl and Br are generated from ClO, BrO, and BrC (WMO, 2010a). 30

Figure 1.10 Generation process of reservoir chlorine gases in the stratosphere. The image is taken from Owen and Richard (1991). 30

Figure 1.11 Average of Arctic and Antarctic winter temperatures (WMO, 2010a). 31

Figure 1.12 Pie charts compare Antarctic stratospheric compounds before chemical reactions happen on PSCs and after photolysis reactions start (Jacobson, 2005). 31

Figure 1.13 Comparison between atmospheric models with and without implementing the Montreal protocol and satellite measurements WMO (2018). 34

Figure 1.14 Annual mixing ratios from 2009 to 2019 in China according to Yi et al. (2021). 35
Figure 1.15 Global emissions of ozone-depleting substances generated in China from 2009 to 2019 (Yi et al., 2021). 35
Figure 1.16 Dobson-spectrophotometer diagram. The image is taken from Dobson's manual (R. & J. Beck LTD). 36
Figure 1.17 Brewer spectrophotometer model MKIII (double monochromator). 37
Figure 1.18 Comparison of southern ozone depletion during the austral spring (September). The first two images are based on satellite measurements from the Total Ozone Mapping Spectrometer (TOMS), while the last two use satellite measurements from the Ozone Monitoring Instrument (OMI). These mages were taken from the ozone hole watch on the NASA website (NASA, 2020). 38
Figure 1.19 Trend of the total column ozone over Antarctica from 1979 to 2013 from satellite observations of TOMS and MERRA. The red line is dated from 1980, the black line is the mean value from 1979 to 2013, while the remaining data in the grey scale is the statistical representation from 1979 to 2013 according to the scale on the right-hand side (NASA, 2020). 39
Figure 1.20 Trend of ozone hole area over Antarctica from 1979 to 2013 from satellite observations of TOMS and MERRA. The red line is dated from 1980, the black line is the mean value from 1979 to 2013, while the remaining data in the grey scale is the statistical representation from 1979 to 2013 according to the scale on the right-hand side (NASA, 2020). 40
Figure 1.21 It summarizes the evolution of total ozone columns for different Representative Concentration Pathways (RCP). Mean observations of total ozone column (TOC) (solid black) compared with predictions of TOC by Chemistry-Climate Models (CCM). Red line REF-C2 (19 models performed a total of 33 realizations), blue line SEN-C2-RCP45 (7 models, 9 realizations), and orange line SEN-C2-RCP85 (8 models, 10 realizations). The shaded regions show one standard deviation variability compared with respect to the lines of the same colour (WMO, 2018). 41
Figure 1.22 General diagram of a Dobson's monochromator. The upper schematic displays the diagram of Dobson's monochromator from a vertical perspective (Image taken from: http://www.o3soft.eu). And the Bottom schematic illustrates its horizontal diagram, where M, P and L are the mirrors, prisms and lenses, respectively (Komhyr, 1980). 42
Figure 1.23 Internal design of a Brewer single monochromator (Josefsson, 1986). 43
Figure 1.24 Brewer spectrophotometer model MKIII (double monochromator) mounted on a solar tracker. 43
Figure 1.25 Central wavelengths and FWHM obtained from Brewer wavelength measurements (red marks) using a tunable laser with steps of 0.04 nm. (Redondas et al., 2018). 44
Figure 2.1 Sample analysed by the Beer-Lambert law. The image was taken from (https://pharmaxchange.info/2012/04/ultraviolet-visible-uv-vis-spectroscopy-%E2%80%93-derivation-of-beer-lambert-law/) 48
Figure 2.2 Annual variation of the solar declination angle (Kalogirou, 2014) 50

Figure 2.3 Seasonal values of the solar declination angle for the northern hemisphere. Image is taken from http://www.reuk.co.uk/wordpress/solar/solar-declination/ 50

Figure 2.4 Displays the correction in minutes made by the equation of time (EOT). Image is taken from http://www.reuk.co.uk/wordpress/solar/solar-declination/ 52

Figure 2.5 Image of the Earth's atmosphere at the 75ºN polar latitude. It displays the solar incident beam at the outer atmosphere (point A illustrates the sun's actual position) and its refraction through the atmospheric path. The apparent solar zenith angle θ would point to the sun's position if there were no atmospheric refraction at all. Image taken from (Tomasi and Petkov, 2014) 53

Figure 2.6 Average vertical profiles of H_2O, O_3, NO_3, and O_2 molecular densities ($mol \cdot cm^{-3}$) from 50 m to 120 km at Ny-Alessund, Norway (~79°N). There is an H2O molecular density comparison between radiosounding measurements at Ny-Alessund, Norway (~79°N) during June and July from 2000 to 2003 (solid blue curve) and the measurements by Mario Zucchelli (~75°N) during December and January of the 1987-1998 multiyear period (Blue dashed curve). O3 molecular density values from ozonesonde measurements performed at Ny-Alesund (~79°N) and Neumayer (~70°S) are described by a solid red line and red dashed line respectively during local summer months from 1978 to 1994. NO2 molecular density near 75°N (solid green curve) and 75°S latitudes (green dashed curve) were obtained by the Odin-OSIRIS satellite instrument over summertime from 2002 to 2005. Finally, the O2 was estimated from the vertical profile ratio p(z)/T(z) at Ny-Alessund (solid brown curve) and ~75°N (brown dashed line) (Tomasi and Petkov, 2014). 54

Figure 2.7 O_3 absorption cross-section values in the ultraviolet, visible and near-infrared (NIR) spectrum at 223 K from 213 nm to 1100 nm obtained by Serdyuchenko et al. (2014) and Gorshelev et al. (2014). 56

Figure 2.8 Ozone cross-section measurements at eleven different temperatures from 193 K to 293 K with a step of 10 K. Dashed lines represent the wavelengths used by Brewer spectrometers to estimate the total ozone column and the total SO_2 column (306.3 nm, 310.1 nm, 313.5 nm, 316.8 nm and 320.1 nm) (Source: personal collection). 56

Figure 2.9 Comparison of absorption cross-section values of ozone (blue line) and SO_2 (orange line) in cm^2 per molecule used in the Brewer algorithm to estimate the total ozone column. O_3 cross-section at -45° C was obtained using Eq. (2.21) by Serdyuchenko et al. (2014) and Gorshelev et al. (2014), while SO_2 values were obtained from the SCIAMACHY satellite spectrometer. Where the black lines indicated the Brewer wavelengths $\lambda 1$=306.3 nm, $\lambda 2$=310.1 nm, $\lambda 3$=313.5 nm, $\lambda 4$=316.8 nm and $\lambda 5$=320.1 nm (Source: personal collection). The only differences with the graph from León-Luis et al. (2018) are the Brewer wavelngths $\lambda 1$=306.4 nm and $\lambda 5$=320.1 nm. 57

Figure 2.10 Visible scattering of solar radiation by atmospheric particles. Image is taken from: http://hyperphysics.phy-astr.gsu.edu 59

Figure 2.11 Displays the changes of energy of a photon during the Raman scattering process. (image taken from https://www.nanophoton.net/raman/raman-spectroscopy.html) 60

Figure 2.12 Schematic of scattered patterns from particles with different dimensions and the same incident beam (Mölders, 2014). 61

Figure 2.13 Scattering regimes of different atmospheric compounds (https://www.e-education.psu.edu/meteo300/node/785). 61

Figure 3.1 Block diagram of the spectrometer used in this work. 69

The monochromator is considered the core of any spectrophotometer. It disperses the incident beam and focuses light at the desired wavelength into the detector. Prisms and diffraction gratings are the traditional diffractive elements in traditional spectrometry (see Figure 3.2). Most monochromators possess the same internal structure: entrance and exit slits, a prism or diffraction grating, fore-optics and focusing lenses. 69

Figure 3.3 Visual representation of a prism and a diffraction grating dispersing a beam of light. 70

Figure 3.4 Brewer monochromator diagram compared with its exposed parts (taken by the INTA, Spain during intercomparison 2015). 70

Figure 3.5 Schematic of a typical photomultiplier tube (Hamamatsu Photonics, 2006). 71

The PDA is a photodetector made from semiconductor materials capable of simultaneously measuring a wide spectral range of wavelengths from a broadband source. They are commonly used in spectrometry due to their versatility in measuring a broad spectrum at once (see Figure 3.6). 71

Figure 3.7 Diagram of a photodiode array working in conjunction with a diffraction grating. 71

Figure 3.8 Comparison between an isotropic and an anisotropic crystal (calcite), left and right side, respectively. The image is taken from https://www.slideserve.com/vernados/birefringence 73

Figure 3.9 Response of a birefringent crystal to three different angles between the input beam and the optical axis: (a) arbitrary, (b) perpendicular, and (c) parallel. The image is taken from https://www.olympus-lifescience.com/ja/microscope-resource/primer/java/polarizedlight/crystalwavefronts/. 74

Figure 3.10 Approximate transmittance of four quartz crystals classified by their methods of manufacture. #1 is fused quartz (direct fusion of quartz crystal). #2 is the Heracus process (flame fusing of powdered quartz crystal). #3 is synthetic (vapour-phase hydrolysis of an organosilicon compound). #4 is water-free synthetic. (Elson et al., 1979) 75

Figure 3.11 Refractive indexes of the ordinary and extraordinary in a quartz crystal along different wavelengths. The image is taken from https://www.rp-photonics.com/birefringence.html 76

Figure 3.12 Comparison between Raman-Nath (left-diagram) and Bragg regime (right-diagram). Images are taken from https://isomet.com/App-Manual_pdf/AOTF-Notes.pdf and https://slidetodoc.com/acoustooptic-modulators-left-acoustooptic-tunable-filters-right-acoustooptic/. 77

Figure 3.13 Non-collinear AOTF configuration with unpolarized incident light (Katrašnik et al., 2010). 78

Figure 3.14 Collinear configuration of the AOTF suggested by the manufacturer. 78
Figure 4.1 Initial design of the prototype using a water-cooling system for the AOTF. 80
Figure 4.2 Final prototype using the replaced AOTF with thermoelectrical cooling. 81
Figure 4.3 The image displays a 3D model of the AOTF spectrometer. 81
Figure 4.4 Display the 5 mm x 5 mm optical aperture of the AOTF. 82
Figure 4.5 Piezoelectric transducer of the AOTF used in this project. 83
Figure 4.6 Spectral response of the FGUV11 filtered manufactured by Thorlabs. 84
Figure 4.7 Spectral response comparison of the filter UVC7, manufactured by Inrad Optics, at different widths. 84
Figure 4.8 Spectral response of the bandpass filter used in this project (UG11 with a thickness of 2mm). 85
Figure 4.9 The diagram on the left shows the internal parts of a Glan-Taylor polarizer. The right graph displays the typical acceptable field of view values for α-BBO Glan-Taylor polarizers. Where FOV1 is the field of view for ordinary rays escaping the window, and FOV2 is the field of view for extraordinary rays passing through the polarizer (THORLABS, 2017). 85
Figure 4.10 Typical spectral response of Glan-Tylor polarizers (THORLABS, 2017). 86
Figure 4.11 Plano-convex lens configured to focus a collimated beam. 86
Figure 4.12 Reflectance graph of the AR coating deposited on UV fused silica with a spectral range from 245 nm to 400 nm (THORLABS, 2017). 87
Figure 4.13 Waterproof case contains the TE controller of the AOTF, environmental sensors, and an Arduino as a modulation signal generator. 87
Figure 4.14 Picture of the RF controller used in this project (300 mm wide, 150 mm high, 280 mm deep). 88
Figure 4.15 Silicon APDs with different photosensitive areas (Hamamatsu, 2004). 89
Figure 4.16 Spectral response of different Si APDs, at 25º C and a multiplication factor M of 50 (Hamamatsu, 2004). 90
Figure 4.17 Functional block diagram of an APD detector, including the photodetection and the avalanche multiplication stage, as well as the electrical amplification process (Kobayashi and Mikawa, 2002). 90
Figure 4.18 Spectral response of an APD at a typical temperature of 25º C, where M is the gain factor of the APDs (THORLABS, 2017). 91
Figure 4.19 Common example of a phase-sensitive detection system using a chopper wheel (PerkinElmer Instruments, 2000). 92
Figure 4.20 Block diagram of a lock-in amplifier algorithm. 94
Figure 4.21 User interface provided by the AOTF manufacturer in 2016. 94
Figure 4.22 Customised User interface of the AOTF spectrometer. 96
Figure 5.1. This is the measurement made by the AOTF of a spectral line at 324.97 nm using a HeCd laser as a light source. It compares the transfer function of the AOTF with a sinc^2 function at the same wavelength. FWHM=0.226 nm. 98

Figure 5.2 This is the measurement made by the AOTF of a spectral line at 441.92 nm using a HeCd laser as a light source. It compares the transfer function of the AOTF with a $sinc^2$ function at the same wavelength. FWHM=0.48 nm. 98

Figure 5.3 Block diagram of the optical system used to test the lock-in and the extinction coefficient of polarizers. 99

Figure 5.4 Extinction coefficient of polarizers from 0 up to 360 degrees with a step of 0.05 degrees. The detector output was normalized to 1 to compare measurements when the polarizers are parallel and orthogonal to each other without saturating the detector. 100

Figure 5.5 Zoom of the extinction coefficient near 90 degrees. 100

Figure 5.6 Spectral line measurements at 296.67 nm with 100 integrations using the lock-in amplifier algorithm (purple) and without (blue). 101

Figure 5.7 Single spectral measurements of a Hg lamp source (100W) (one single integration). 101

Figure 5.8 Measurement of spectral lines from a Hg lamp source (100W), integrating the signal 100 times and using a higher resolution near its spectral lines. 101

Figure 6.1 Solid-state spectrometer performing measurements of a 50W halogen lamp at Kipp and Zonen Facilities. 104

Figure 6.2 Relationship between the radio frequency applied to the AOTF and the filtered wavelength (AOTF manual). 104

Figure 6.3 Internal diagram of the calibration lamp ORIEL model 6025. 105

Figure 6.4 Setup during the Hg pencil lamp measurements. 105

Figure 6.5 Spectral response of the mercury lamp, taken from the user manual (ORIEL model 6025). They were recorded using the manufacturer's spectrograph and an unspecified diode array detector. 106

Figure 6.6 Typical performance of the mercury lamp when it is operated continuously using a new alkaline battery. Note that it is possible to achieve longer operating times if the lamp is used intermittently. 106

Figure 6.7 Blue graph represents the digitalized graph from the manual, and the red graph displays the polynomial fitting applied to the measurements. 107

Figure 6.8 Spectral measurement of the mercury pencil lamp at the University of Manchester, integrating 100 times each measurement. 108

Figure 6.9 FWHM of the mercury lines at 435.8 nm and 253 nm, respectively. Notice that all the spectral measurements were integrated ten times and normalized to 1. Improvements in the polynomial fitting function are necessary to achieve better wavelength calibration. 108

Figure 6.10 Comparison between main spectral lines of a standard Hg lamp and the measured spectral lines of a Hg lamp by the proposed spectrometer (integrated 50 times) (https://www2.keck.hawaii.edu/inst/lris/arc_calibrations.html). 109

Figure 6.11. Comparison between spectral lines of a standard Cd lamp and the measured spectral lines of a Cd lamp by the prototype AOTF spectrometer (integrated 50 times) (https://www2.keck.hawaii.edu/inst/lris/arc_calibrations.html). 110

Figure 6.12. Comparison between Spectral lines of a standard Zn lamp and spectral lines of a Zn lamp measured by the proposed spectrometer (integrated 100 times) (https://www2.keck.hawaii.edu/inst/lris/arc_calibrations.html). 111

Figure 6.13 Arrangement of optics to perform measurements of the Cd laser. 112

Figure 6.14 Spectral measurements of the HeCd laser at 325 nm using the AOTF spectrometer. 112

Figure 6.15 Spectral measurements of the HeCd laser at 442 nm using the AOTF spectrometer. 112

Figure 6.16 Spectral line of Cd laser at 325 nm with an FWHM of 0.6 nm measured by the Brewer spectrophotometer (plot provided by K&Z). 113

Figure 6.17 Measurements of Hg lamp and Cd lamps performed by the Brewer spectrophotometer #223 (courtesy of Kipp and Zonen). 113

Figure 6.18 Displays the Hg spectral line at 296.728 nm measured by Brewer #223, having an FWHM of 0.6 nm (plot provided by K&Z). 114

Figure 6.19 Displays the Hg spectral line at 334.138 nm measured by Brewer #223, having an FWHM of 0.56 nm (plot provided by K&Z). 114

Figure 6.20 Spectral power distribution of a 200W halogen lamp (SLS201L from Thorlabs) compared with a black body. 115

Figure 6.21 Setup of the mounting used to measure Schreder UV stability kit 116

Figure 6.22 Setup of the temperature chamber test, where the RF generator was the only device inside the temperature chamber. 116

Figure 6.23 Plot of Hg spectral lines measured during the temperature chamber test. These variations are the result of temperature changes in the RF generator. 117

Figure 6.24 Measurements of mercury spectral lines during temperature chamber tests. These variations are the result of temperature changes in the RF generator. 118

Figure 6.25 Setup used during the temperature stability test. The whole optics of the AOTF spectrometer are placed inside the temperature chamber. 119

Figure 6.26 Illustration of measurements performed during the temperature stability test for each spectral line. Each colour line represents one measurement at the indicated temperature, starting at 47.3º C (red) and finishing at -10º C (blue). The Amplitude was normalized based on the measurements at 47.3º C. 120

Figure 6.27 The spectrum of the white-LED manufacturer is shown on the left, and the spectrum measured using the AOTF is shown on the right. 122

Figure 6.28 The spectrum of UV-LED provided by the manufacturer (Thorlabs) is shown on the left, and the measurements of the proposed solid-state spectrometer are shown on the right. The measurements were integrated ten times and normalized to 1. 122

Figure 6.29 Linear representation of Hg spectral measurements. 123

Figure 7.1 Setup used during direct solar radiation measurements at Delft June 2018. 125

Figure 7.2. Normalized measurement comparison between the AOTF spectrometer (blue) and the Brewer #223 (pink) without UG11 on 26th June 2018. The wavelength step of Brewer and the

AOTF spectrometer is 0.05 nm from 290 nm to 363 nm (CZ scan). The AOTF had to integrate about 18 times to match the speed of the Brewer of ~0.5 seconds per wavelength. 126

Figure 7.3 Normalized measurement comparison between the AOTF spectrometer (blue) and the Brewer #223 (pink) using UG11 filter on 27th June 2018 (integration value=10). The wavelength step of Brewer is 0.05 nm (CZ scan), and the AOTF spectrometer is 0.1 nm from 290 nm to 340 nm. 127

Figure 7.4. It displays a clear sky measurement comparison between the AOTF spectrometer with an integration value of 20 times (blue) and the Brewer #223 (pink) on 29th June 2018 across the entire wavelength range of the Brewer (CZ scan from 290 nm to 363 nm with a step of 0.05 nm). 127

Figure 7.5. Zoom of the figure Figure 7.4 to cover the wavelength range used for TOC measurements from 305 nm to 321 nm on 29th June 2018 at 15:26 UTC. It displays normalized comparison measurements between the AOTF spectrometer (blue) and the Brewer #223 (pink), as well as the residual between the two datasets. The red lines show the wavelengths used for TOC estimations from Brewer's manual (306.3 nm, 310 nm, 313.5 nm, 316.8 nm and 320 nm). The amplitude of both datasets was normalized..... 128

Figure 7.6 Picture of the AOTF mounted on a solar tracker while performing direct solar measurements (Manchester, UK). 129

Figure 7.7 The AOTF is mounted on a solar tracker and pointing at the zenith sky (Manchester, UK). Note that the silver pole that appears to be protruding from the top of the tracker is another instrument mounted further back on the platform. 129

Figure 7.8 Spectral comparison of direct solar measurements on 25th September 2020 at 15:14 UTC, SZA equals 67.76° from 300 nm to 320 nm. The blue line represents the AOTF scan measurements (0.05 nm resolution), the pink graph displays the measurements of Brewer 172 (0.5 nm resolution), and the light blue line indicates the residual between the two datasets. The red lines show the wavelengths used for TOC estimations from Brewer's manual (306.3 nm, 310 nm, 313.5 nm, 316.8 nm and 320 nm). Note that after the return of the AOTF, the detailed wavelength calibration from Delft could not be assumed to remain. It was checked for the returned system, but only with a number of Hg lines. These indicated that the wavelength calibration was still viable and matched Figure 6.7. 130

Figure 7.9 Solar zenith angles and direct ozone measurements on 17th September 2020. The left graph compares the total number of measurements performed by the Brewer (Blue) and the AOTF (red) at different times during the day with their respective SZA. The diagram on the right displays the Brewer ozone measurements with a standard deviation below 2.5 (blue dots). .. 132

Figure 7.10 Displays AOTF measurements on 17th September 2020 of single and double ratios used for ozone (R2, R3, R4 and R6) and SO_2 estimations (R1 and R5). The plot shows the single ratios: R1 in light green, R2 in red, R3 in blue, and R4 in light blue; and the double ratios: R5 in green and R6 in purple..... 134

Figure 7.11 Displays measurements on 17th September 2020 of single and double ratios used for ozone (R2, R3, R4 and R6) obtained by Brewer #172. R2, R3, R4 and R6 are represented by

a green, purple, light blue and dark blue line, respectively. Negative SZA represents values obtained before noon. 134

Figure 7.12 The equation y= 0.0013858669x - 0.00558188025 represents the linear fitting (red line) used for the calibration of the AOTF instrument (differential absorption coefficient for ozone=0.0013858669 and ETC for ozone=0.00558188025). Blue dots stand for direct solar measurements of the AOTF. 135

Figure 7.13 Output of the AOTF spectrometer during a solar scan on 17th September 2020 at 13:18 UTC (blue line). The red lines display the wavelengths that the spectrometer uses for ozone measurements (306.3 nm, 310.05 nm, 313.48 nm, 316.74 nm and 320.05 nm). 136

Figure 7.14 Estimated TOC values on 17th September 2020 based on the linear fitting displayed in Figure 7.12. Blue symbols plot the Brewer data in its daily routine monitoring mode, while pink plots represent data associated with the AOTF. 137

Figure 7.15 Solar zenith angles and direct ozone measurements on 18th September 2020. The left graph compares the total number of measurements performed by the Brewer (Blue) and the AOTF (red) at different times during the day with their respective SZA. The diagram on the right displays the Brewer ozone measurements with a standard deviation below 2.5 (blue dots). .. 137

Figure 7.16 Displays AOTF measurements on 18th September 2020 of single and double ratios used for ozone (R2, R3, R4 and R6) and SO_2 estimations (R1 and R5). The panel as described in Figure 7.10. 138

Figure 7.17 Estimated TOC values on 18th September 2020 based on the linear fitting displayed in Figure 7.12. Blue symbols plot the Brewer data in its daily routine monitoring mode, while pink plots represent data associated with the AOTF. 139

Figure 7.18 Solar zenith angles and direct ozone measurements on 25th September 2020. Panels are as described in Figure 7.15. 140

Figure 7.19. It compares the R6 ratios obtained on 25th September and the fitting R6 slant obtained on 17th September by the AOTF spectrometer (see Figure 7.12). 140

Figure 7.20 Displays AOTF measurements on 25th September 2020 of single and double ratios used for ozone (R2, R3, R4 and R6) and SO_2 estimations (R1 and R5). Panel as described in Figure 7.10. 141

Figure 7.21 Estimated TOC values on 25th September 2020 based on the linear fitting displayed in Figure 7.12. Blue symbols plot the Brewer data in its daily routine monitoring mode, while pink plots represent data associated with the AOTF. 141

Figure 7.22 Displays AOTF measurements on 17th September 2020 of single ratios used for TOC estimations. The analysed ratios are obtained from measurements at the four wavelengths used by the Brewer algorithm to retrieve TOC (F2 → 306.3 nm, F3 → 310 nm, F4 → 313.5 nm, F5 → 316.8 nm and F6 → 320 nm), and compared with the SZA. The plot shows single ratios R4=F6-F5 in light green, F6-F4 in red, F6-F3 in blue, R3=F5-F4 in light blue, R2=F5-F3 in green, and F4-F3 in purple marks. 142

Figure 7.23 Displays AOTF measurements on 25th September 2020 of single ratios used for TOC estimations. Panel as described in Figure 7.22. 143

Figure 7.24 Calibration transferred to the AOTF on 17th September 2020, considering the TOC values from the Brewer 172 and the single ratio F6-F5 (320 nm and 316.8 nm) obtained by the presented spectrometer. The left figure shows the single ratios (blue dots) and the fitting equation (red line), with the differential absorption coefficient for ozone equals 0.000079987775, and the ETC for ozone equals 0.202313273. The right figure displays the estimated TOC values based on the linear fitting shown on the left chart, see Eq. (7.9). Blue symbols plot the Brewer data in its daily routine monitoring mode, while pink plots represent data associated with the AOTF measurements. 143

Figure 7.25 TOC Measurements obtained on 25th September 2020 using the single ratios F6-F5 and the calibration shown in Figure 7.24. The left figure compares the fitting calibration (red line) on 17th September 2020 with the single measured ratios (blue dots). The right figure displays the estimated TOC values found from Eq. (7.9), where blue symbols represent Brewer data in its daily routine monitoring mode, and pink plots represent data associated with the AOTF measurements. 144

Figure 7.26 Calibration transferred to the AOTF on 17th September 2020, considering the TOC values from the Brewer 172 and the single ratio F6-F4 (320 nm and 313.5 nm) obtained by the presented spectrometer. Panels as described in Figure 7.24. The differential absorption coefficient for ozone equals 0.00050226608, and the ETC for ozone equals 0.435349404.... 144

Figure 7.27 Measurements obtained on 25th September 2020 using the single ratio F6-F4 and the calibration shown in Figure 7.26. Panels as described in Figure 7.25. 145

Figure 7.28 Calibration transferred to the AOTF on 17th September 2020, considering the TOC values from the Brewer 172 and the single ratio F6-F3 (320 nm and 310 nm) obtained by the presented spectrometer. Panels as described in Figure 7.24. The differential absorption coefficient for ozone equals 0.0006459861, and the ETC for ozone equals 1.30661416..... 145

Figure 7.29 Measurements obtained on 25th September 2020 using the single ratio F6-F3 and the calibration shown in Figure 7.28. Panels as described in Figure 7.25. 145

Figure 7.30 Calibration transferred to the AOTF on 17th September 2020, considering the TOC values from the Brewer 172 and the single ratio F5-F4 (316.8 nm and 313.5 nm) obtained by the presented spectrometer. Panels as described in Figure 7.24. The differential absorption coefficient for ozone equals 0.00042642659, and the ETC for ozone equals 0.233452818.... 146

Figure 7.31 Measurements obtained on 25th September 2020 using the single ratio F5-F4 and the calibration shown in Figure 7.30. Panels as described in Figure 7.25. 146

Figure 7.32 Calibration transferred to the AOTF on 17th September 2020, considering the TOC values from the Brewer 172 and the single ratio F5-F3 (316.8 nm and 310 nm) obtained by the presented spectrometer. Panels as described in Figure 7.24. The differential absorption coefficient for ozone equals 0.00057320005, and the ETC for ozone equals 1.10286999..... 147

Figure 7.33 Measurements obtained on 25th September 2020 using the single ratio F5-F3 and the calibration shown in Figure 7.32. Panels as described in Figure 7.25. 147

Figure 7.34 Calibration transferred to the AOTF on 17th September 2020, considering the TOC values from the Brewer 172 and the single ratio F4-F3 (313.5 nm and 310 nm) obtained by the

presented spectrometer. Panels as described in Figure 7.24. The differential absorption coefficient for ozone equals 0.00013436294, and the ETC for ozone equals 0.875095412.... 147

Figure 7.35 Measurements obtained on 25th September 2020 using the single ratio F4-F3 and the calibration shown in Figure 7.34. Panels as described in Figure 7.25. 148

List of Tables

Table 1.1 Mixing ratios and atmospheric lifetimes of some CFCs, HCFCs and other chlorine compounds (Jacobson, 2005). 33

Table 1.2 Brewer spectrometer specifications obtained from the operator manual of Brewer MKIII 44

Table 2.1 King correction factor Fk, depolarization factor ρn and γ values for wavelengths within the range of the Brewer spectrometer from 280 nm to 370 nm for standard dry air. It is taken from (Bucholtz, 1995). 62

Table 2.2 'A' coefficient values are used in Eq. (2.35) to determine the Rayleigh Optical Depth at 0 km altitude with different atmospheric models (Bucholtz, 1995). 64

Table 2.3 Rayleigh optical depth values obtained by Bucholtz (1995) from Eq. (2.37). 65

Table 3.1 AOTF Devices operated in space (Korablev et al., 2018) 72

Table 3.2 Properties of some crystals used in AOTFs. 75

Table 6.1. FWHM comparison as a function of wavelength between the AOTF spectrometer and Brewer #223. 114

Table 7.1 Minimum and maximum values of SZA during measurements with the presented spectrometer 131

Abstract

Technology change for stratospheric ozone measurement.

Eric Gonzalez Peralta

A thesis submitted to the University of Manchester for the degree of Doctor of Philosophy in the Faculty of Science and Engineering

Ground-based measurements of total column ozone use differential optical absorption spectrometry (DOAS) techniques to determine the ozone concentration in the path between the sun and the observation point. While there are several retrieval techniques, the underlying method is to measure and compare wavelengths of solar radiation strongly and weakly absorbed by ozone and thus determine the amount of ozone along the pathlength.

Traditional spectrometers used for this purpose possess a monochromator with diffraction gratings or prisms as dispersive elements. The necessity of removing stray light from the measurements often requires a double monochromator for the highest quality measurements. Such monochromators need the rotation or other movement of internal mechanical parts to filter the desired wavelength. For example, it could require using a slit-mask, or the rotation of the diffraction grating(s), to align the output beam of almost monochromatic radiation onto the detector. The need to, for example, rotate the grating(s) to direct each wavelength onto a detector sequentially makes measurements with such systems slow. For example, a Brewer spectrometer, the current standard for total ozone column measurements, performs a wavelength measurement after five sets of 20 cycles of the slit mask, with each cycle taking 0.28 seconds, and completing an ozone observation in around three minutes.

The work described in this thesis demonstrates the performance of a solid-state monochromator (Acousto Optic Tunable Filter) filtering wavelengths in the ultraviolet spectrum from 280 nm to 440 nm. Its FWHM varies from 0.2 nm in the shorter wavelengths up to 0.4 nm in the longer wavelengths. The AOTF technology is based on the acousto-optic effect of birefringent materials, whose wavelength selection is controlled by an electrical signal of a radiofrequency generator.

The distinct advantage of the AOTF spectrometer is the absence of moving parts. In this thesis, single wavelength measurements were achieved in 0.14 seconds based on two integration samples, completing wavelength scans from 300 nm to 325 nm with 0.05 nm steps in 70 seconds. The maximum selecting speed reached by an AOTF is equal to the time required for the RF signal

generation, plus the time the acoustic wave requires to pass through the crystal. This time is usually tens of nanoseconds. However, it is necessary to consider serial communication between te RF generator and the PC, the acquisition time and digital data processing to assess a scan duration fully. Nonetheless, this is considerably faster than a scanning instrument based on traditional monochromators.

The laboratory characterisation of the instrument shows that in its current configuration, it has a wavelength range from 300 nm to 370 nm, with a slit function varying from 0.2 nm for the shortest wavelength to 0.4 nm for the longest wavelengths. The system was also shown to be temperature sensitive. It was always known that the AOTF crystal had to be temperature stabilised to avoid damage. Still, the temperature sensitivity of the current RF controller must be overcome or stabilised for outdoor operation to avoid applying temperature corrections to the acquired data.

Limited outdoor evaluation of the AOTF instrument was possible, but the preliminary results were promising while indicating areas for improvement. The high-resolution spectral shape of the solar spectrum was well reproduced. Brief attempts to measure total column ozone compared with co-located Brewer measurements had limited success. The best results were achieved using single ratio wavelength measurements, with the most successful wavelength pair tested at 316.8 nm and 313.5 nm, giving results within ±15 DU of Brewer data for the same time. Applying the double ratio Brewer technique to ozone retrieval did not improve matters, leading to an agreement of ±30 DU at best. However, the results were not consistent from day to day, with calibration of one day not applying at a later time. This may have been mechanical instability in the alignment of the laboratory prototype taken outside and placed on a sun tracker or something more fundamental in the instrument or processing techniques.

The research described in this thesis has revealed the promising potential of the AOTF technology when applied in atmospheric spectrometry. However, there are still some areas of improvement due to current technology limitations and time to continue the research. For example, the proposed instrument uses the Brewer spectrometer methodology to retrieve the total column of ozone, but different techniques to retrieve ozone could be tested in future to improve its performance.

Declaration

No portion of the work referred to in the thesis has been submitted in support of an application for another degree or qualification of this or any other university or other institute of learning.

Copyright Statement

Acknowledgements

First and foremost, I would like to express my deepest gratitude to my supervisors, Prof. Ann Webb and Dr John Rimmer, for their patience and invaluable advice and their unconditional and continuous support during the difficult times throughout my PhD. Their kindness and willingness to share their ample experience allowed me to grow personally, academically, professionally, and personally. They were beyond the established duties of a supervisor, bringing joy to my research.

I would also like to thank Dr Andrew Smedley and Dr Richard Kift, who are part of the same research group and were actively involved in each stage of this project. Their advice, feedback, and mentorship were extremely useful in my research, directly impacting my studies.

In addition, I would also like to thank the entire team of Research and development of Kipp & Zonen, especially Keith Wilson and Pavel Babal, for their assistance in conducting numerous tests and for making productive and pleasant my trips to their facilities in Delft, the Netherlands.

I thankfully acknowledge CONACyT (Mexican National Council for Science and Technology), Kipp & Zonen and the University of Manchester for their financial support. I also appreciate the World Meteorological Organization for its financial support during conferences, workshops and calibration campaigns.

Finally, I would like to express my gratitude to my wife, family and friends for their encouragement and invaluable emotional support. This accomplishment would not have been possible without them.

Chapter 1.Introduction

This chapter presents the importance of stratospheric ozone for most living species on the Earth's surface and the significance of its worldwide monitoring. The ozone concentration in the atmosphere is linked to the attenuation of most of the high-energy solar radiation reaching Earth's surface. Regrettably, human activities released a considerable amount of ozone-depleting substances into the atmosphere, causing extensive damage to stratospheric ozone before the so-called Antarctic ozone hole was discovered in 1985 (Farman et al., 1985), due to consistent ground-based measurements of total column ozone by the British Antarctic Survey. Fortunately, the Montreal protocol was created afterwards to impose global binding obligations and timetables to phase out ozone-depleting substances.

Stratospheric ozone has been continuously monitored worldwide to supervise its recovery. Today satellite measurements provide a global view of stratospheric ozone, but ground-based data is still vital for maintaining the really long-term records and for satellite validation. This thesis describes the development of a new instrument for ground-based monitoring of total column ozone, centred on the acousto-optic tunable filter, which has many potential advantages over existing ozone spectrometers and could contribute to future worldwide monitoring of column ozone. The work begins with background detail on ozone in the atmosphere and the detailed aims and objectives of the research.

1.1. Stratospheric ozone

Ozone (O_3) is a highly reactive molecule formed by three oxygen atoms with average concentration values from 1.2 parts per million volume (ppmv) to 8 ppmv of the total atmospheric volume in mid-latitudes (Tummon et al., 2015). It has a non-homogeneous distribution across different altitudes and latitudes, with about 90% of total ozone found in the stratosphere between 10 km and 50 km altitude (see Figure 1.1). The remaining molecules are mainly located in the troposphere, where ground-level O_3 is considered an air pollutant with harmful effects on humans and vegetation. On the other hand, stratospheric ozone acts as a protective layer against high-energy ultraviolet radiation from the Sun that threatens life on Earth.

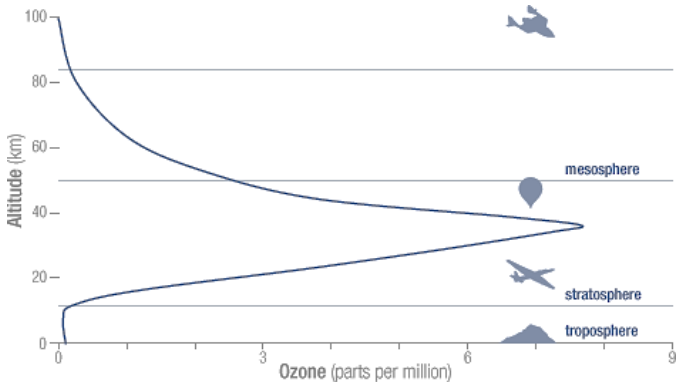

Figure 1.1 Peak ozone concentration occurs between 30 km and 35 km of altitude (https://ozonewatch.gsfc.nasa.gov/facts/SH.html).

The Dobson Unit (DU), in honour of Gordon Miller Bourne Dobson (inventor of the Dobson spectrophotometer), is the standard unit to measure the total column of ozone. The Dobson unit is the number of ozone molecules required to create an ozone layer 0.01 millimetres thick at standard temperature and pressure. If all the stratospheric ozone were compressed and uniformly distributed worldwide at standard temperature and pressure of 0 Celsius (273.15 Kelvin) and one atmosphere (101.325 kPa), the global average thickness of stratospheric ozone would be around 3 mm or 300 DU.

1.2. Solar radiation

Solar radiation provides the heat, light and energy required for living organisms as it is responsible for most physical and biological cycles on Earth. Direct sunlight reaches the Earth's surface at different angles depending on the latitude, season and hour of the day. Then, solar radiation becomes more scattered and diffused the longer it travels through the atmosphere. Thus, only a portion of the solar radiation makes it to the Earth's surface, while the rest is absorbed or reflected by the atmosphere.

Extra-terrestrial solar radiation is the electromagnetic energy emitted by the sun that reaches the outer atmosphere. Satellite observations of the incident solar radiation that is normal to the Earth's surface show that the total energy per unit of time emitted by the Sun is comparable to the energy produced by a black body when it is at the same temperature as the surface of the Sun (average temperature of 5900 K). Therefore, the deviations observed between the solar radiation measured at ground level and the energy of a black body at 5900 K are a consequence of the interaction between the incident solar radiation and the elements within the Earth's atmosphere (Figure 1.2).

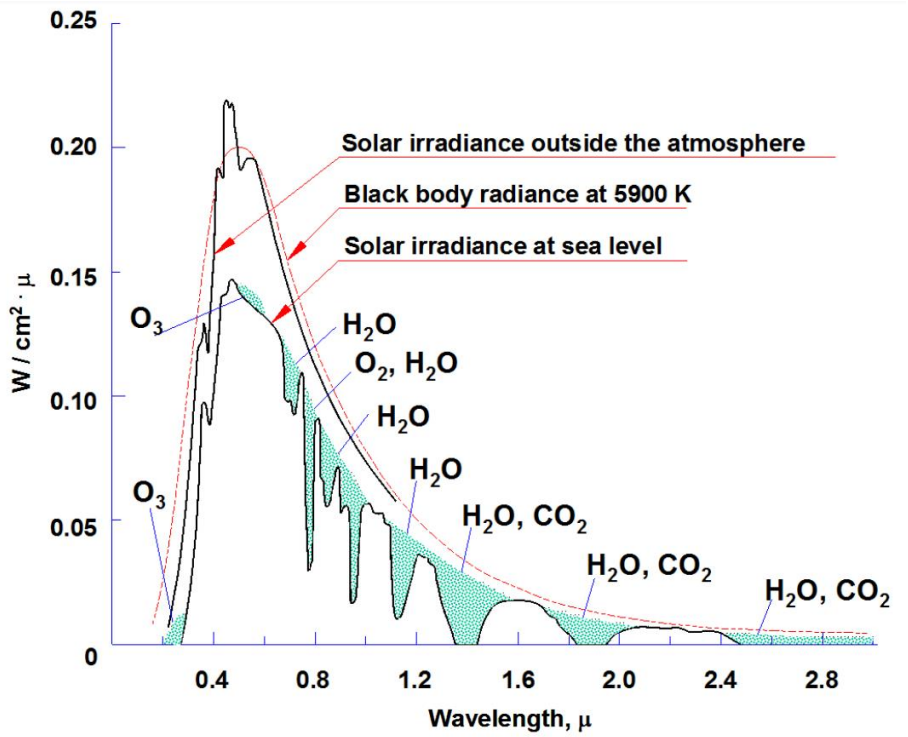

Figure 1.2 Comparison of the solar irradiance in the outer atmosphere, the electromagnetic radiation of a black body at 5900 K, and the solar irradiance at ground level for clear-sky conditions (Ortenberg, 2013).

About 97% of solar radiation is distributed in the wavelength range between 290 nm and 3000 nm, which includes: UV (ultraviolet) radiation, visible radiation to the human eye (visible light), and infrared radiation (WMO, 2010b). However, during its path to reach the Earth's surface, part of the extra-terrestrial solar radiation is reflected, scattered or absorbed by aerosol particles, cloud droplets, cloud crystals, air molecules, such as oxygen (O_2), nitrogen (N_2), water vapour (H_2O), and trace gases such: ozone, sulphur dioxide (SO_2), carbon dioxide (CO_2) and nitrous oxides (NO_x). It is observed from Figure 1.2 that ozone molecules produce a significant attenuation in the ultraviolet spectrum.

1.2.1. Interaction of UV radiation with stratospheric ozone

Each molecule and aerosol in the atmosphere attenuates, scatters, or absorbs the solar radiation, attenuating the solar irradiance at specific wavelengths before it reaches the surface of the Earth. It is because the absorption cross-section of each atmospheric compound possesses a particular spectral fingerprint. Cornu (1881) suggested that ground-based solar radiation measurements were attenuated in the ultraviolet region by the molecules in the atmosphere. Then, Hartley (1881) proved that such attenuation was because of stratospheric ozone. Figure 1.3 illustrates the spectral absorption of ozone when it interacts with solar radiation, mostly attenuating the ultraviolet region.

Satellite observations directly measure the total solar irradiance of the incident solar radiation that is normal to the Earth's surface per unit of time and area. This value fluctuates with solar activity, such as the solar cycles.

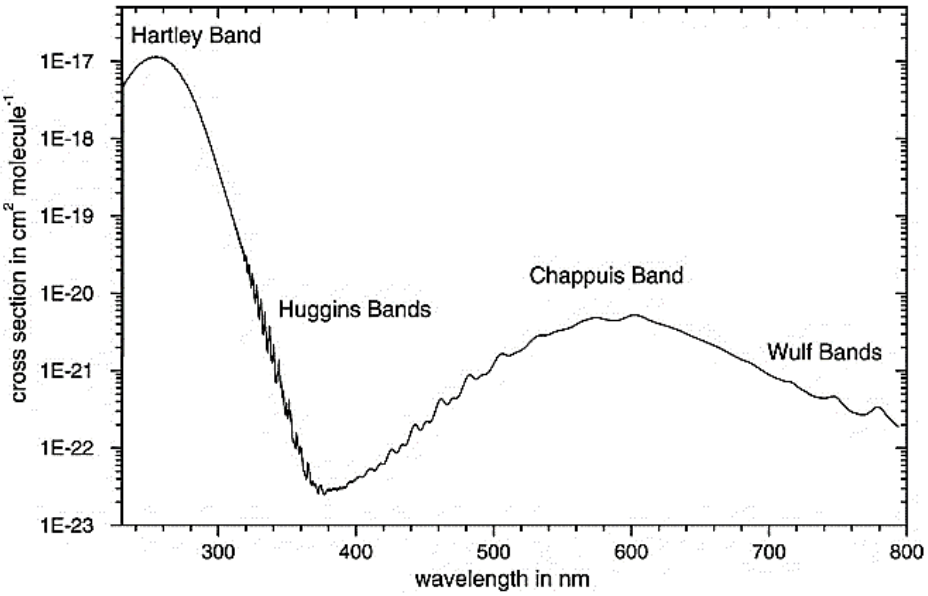

Figure 1.3. The satellite spectrometer GOME FM obtained the ozone absorption cross-section at 293K (Burrows et al., 1999). It illustrates the spectral bands used by the DOAS technique to get the total column of ozone.

Additionally, there is a minor but noticeable attenuation of UV radiation produced by sulphur dioxide (SO2) molecules in the atmosphere. Figure 1.4 displays the spectral absorption of such molecules from 220 to 320 nm.

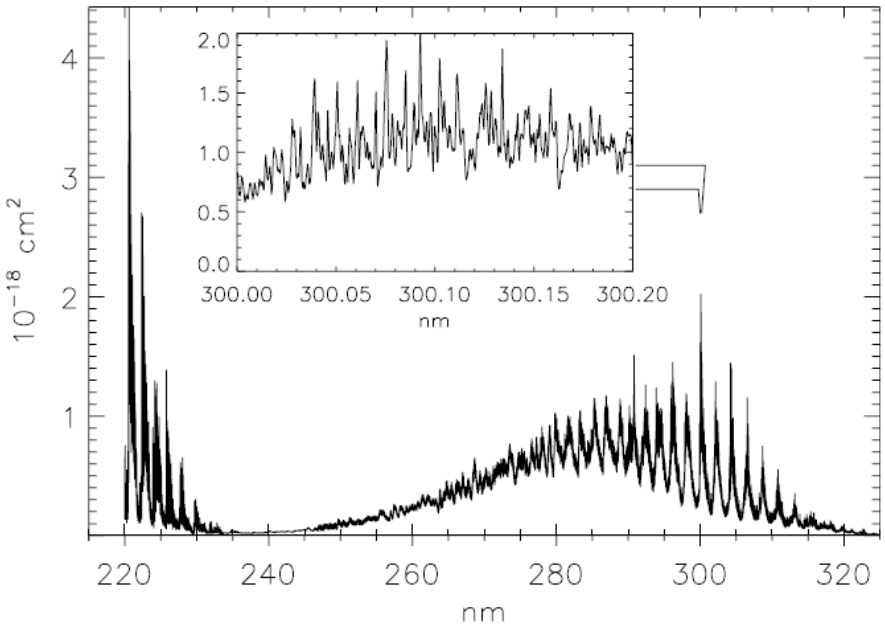

Figure 1.4. Absorption cross-section of SO2 molecules at 295 K (Rufus et al., 2003).

By relying on the spectral fingerprint of a particular compound and performing solar-radiation measurements at specific wavelengths, where there are different attenuation rates, it is possible

to estimate the total atmospheric column of the substance. This method, known as Differential Optical Absorption Spectroscopy (DOAS), is discussed further in section 0. Note that the most accurate results are obtained by measuring the direct solar beam and not scattered light, requiring the region around the sun to be cloud-free.

The ultraviolet radiation is divided into three wavebands according to the BS ISO 21348:2007 standard (Ace, 2007): UV-A from 315 nm to 400 nm, UV-B from 280 nm to 315 nm and UV-C from 100 nm to 280 nm. The stratospheric ozone, often called the ozone layer, absorbs almost all UV-C wavelengths, which is the waveband with the highest energy and most harmful radiation. Likewise, this trace gas considerably attenuates solar radiation in the UV-B range (~90% absorption), whose overexposure could damage living species at a molecular level. On the other hand, UV-A radiation is only partially attenuated (~50%) and reaches the surface of the Earth (see Figure 1.5).

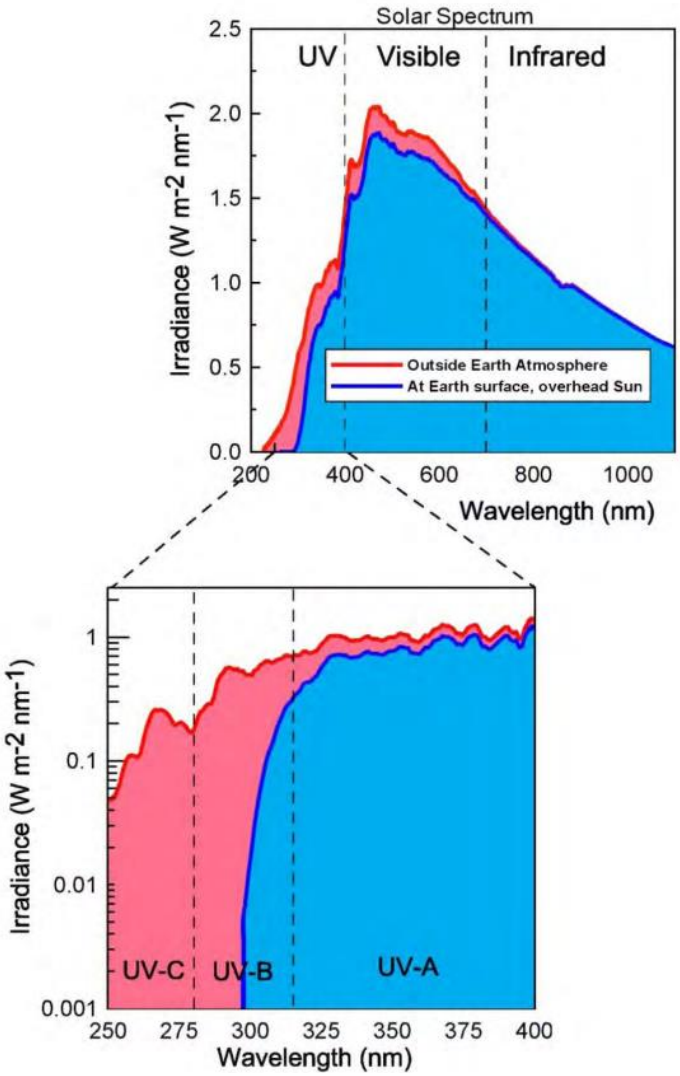

Figure 1.5 Comparison between the solar radiation in the outer atmosphere (red area) and the solar radiation measured at ground level (blue area). The bottom chart compares the UV radiation spectrum before and after passing through the atmospheric ozone (note the log scale on the y-axis). Less than 1% of the radiation at wavelengths less than 300 nm is transmitted due to a strong ozone absorption at shorter wavelengths (Aucamp et al., 2020).

Stratospheric ozone is destroyed and generated in a natural cycle of photochemical reactions called the Chapman cycle (Chapman, 1930) due to the interaction between high-energy solar radiation with oxygen and ozone (see Figure 1.6). When a high-energy photon (λ <200 nm) interacts with oxygen, it is dissociated into two highly reactive oxygen atoms Eq. (1.1). If one of those free oxygen atoms joins an O_2 molecule, an ozone molecule is produced during the exothermic reaction Eq. (1.2), having a peak ozone generation at ~185 nm. On the other hand, if one of those free atoms interacts with an ozone molecule, ozone will be naturally dissociated into two oxygen molecules Eq. (1.4). Moreover, when a high-energy photon (~200 nm< λ < ~315 nm) interacts with an O_3 molecule, it dissociates into an O_2 molecule and a free oxygen atom Eq. (1.3). This generation-destruction cycle of ozone is repeated as long as there is solar radiation, having a peak ozone destruction at ~254 nm. Note that the excess kinetic energy generated during some reactions is dispersed into the stratosphere, playing an essential role in the temperature structure of the atmosphere.

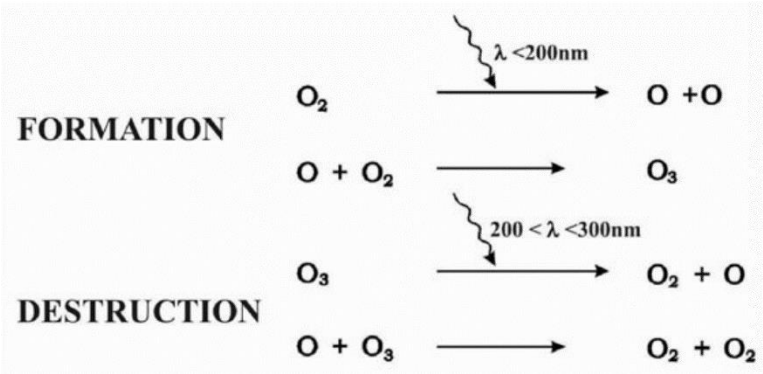

Figure 1.6 Chapman cycle of ozone formation and destruction (Vázquez and Hanslmeier, 2006).

$$O_2 + hv \longrightarrow O^{\blacksquare} + O^{\blacksquare} \quad (1.1)$$

$$O^{\blacksquare} + O_2 + M \longrightarrow O_3 + M \quad (1.2)$$

(M is considered an inert particle)

$$O^{\blacksquare} + O_3 \longrightarrow 2O_2 \quad (1.3)$$

$$O_3 + hv \longrightarrow O^{\blacksquare} + O_2 \quad (1.4)$$

Due to more intense UV radiation at small zenith angles, a higher amount of stratospheric ozone is generated near the Tropics. However, a natural atmospheric circulation pattern called Brewer-Dobson circulation transports stratospheric air rich in ozone from the Tropics to the polar regions (Miyazaki et al., 2005), producing higher stratospheric ozone concentration at high altitudes than in the tropics, mainly in the winter-spring season. Because of the reasonably constant solar radiation during the year in the tropics, stratospheric ozone concentrations tend to present small seasonal fluctuations compared to the significant seasonal variations at higher latitudes. Generally, stratospheric ozone concentrations worldwide vary from about 230 DU to 500 DU depending on the season and the location of the measurements.

Though O_3 is mainly located in the stratosphere, ozone molecules can also be produced at lower altitudes (troposphere) by the interaction of much reduced solar UV radiation with oxides of nitrogen (NO_X) in the presence of organic or manufactured volatile organic compounds (VOCs). Ozone at tropospheric altitudes is considered a pollutant that affects air quality, threatening human and animal health and having agricultural impacts. Some consequences of exposure to high concentrations of ozone may be pulmonary irritations and the worsening of respiratory diseases such as pneumonia, asthma, and rhinitis, which significantly impact the elderly and children (Ebi and McGregor, 2008, Lippmann, 1991). Additionally, tropospheric O_3 affects the photosynthesis of wild and cultivated plants, producing yield losses in staple crops such as soybean, maize, and wheat (Avnery et al., 2011, Rai and Agrawal, 2012, Pinto et al., 2010).

1.2.2. Interaction of UV radiation with living species

Because every location on Earth receives sunlight for at least part of the year, all living organisms are affected by the ultraviolet radiation (UVR) that reaches the Earth's surface. Non-prolonged UV-B exposure is a natural source of vitamin D for humans, whose benefits include maintaining healthy muscular and skeletal systems and likely immune system effects (Calvo et al., 2005, Juzeniene and Moan, 2012). However, overexposure to high-energy UV radiation can produce damage at a molecular level, generating single or double-strand breaks in the DNA that might result in losing genetic material, cancerous or precancerous cells, malfunction or death of cells. Some consequences of overexposure to UV radiation on humans include the risk of skin cancer, sunburns, and eye damage (Morison, 1989, Ravanat et al., 2001, Matsumura and Ananthaswamy, 2004).

Living organisms have adapted to deal with moderate UVR. For example, humans around the tropics evolved with protective melanin pigmentation in the upper layers of the skin, losing this characteristic as they moved to higher latitudes. Nowadays, glasses, hats, clothing and artificial sunscreens are used worldwide to avoid UVR overexposure. Additionally, some plants and animals synthesize their protective pigments, and other animals have evolved to cover themselves with hair or feathers.

As a consequence of stratospheric ozone depletion, higher UV irradiance reaches not only the polar regions but also surrounding and populated areas in South America, Australia, and to a lesser degree North America and northern Europe (Solomon, 2008).

1.3. Ozone depletion and Chlorofluorocarbons (CFCs)

Stratospheric ozone records from NASA since the late 1970s have shown a pronounced seasonal depletion of ozone around the South Pole, covering almost the entire Antarctic continent. This remarkable southern depletion, called the ozone hole, was identified in 1985 by

ground measurements performed by British Antarctic Survey staff at Halley Research Station and validated by satellite measurements (Farman et al., 1985). Figure 1.7 illustrates the maximum ozone hole and the minimum total column amount of ozone recorded in October 1985. Since then, the monitoring of global ozone depletion and recovery has received international prominence.

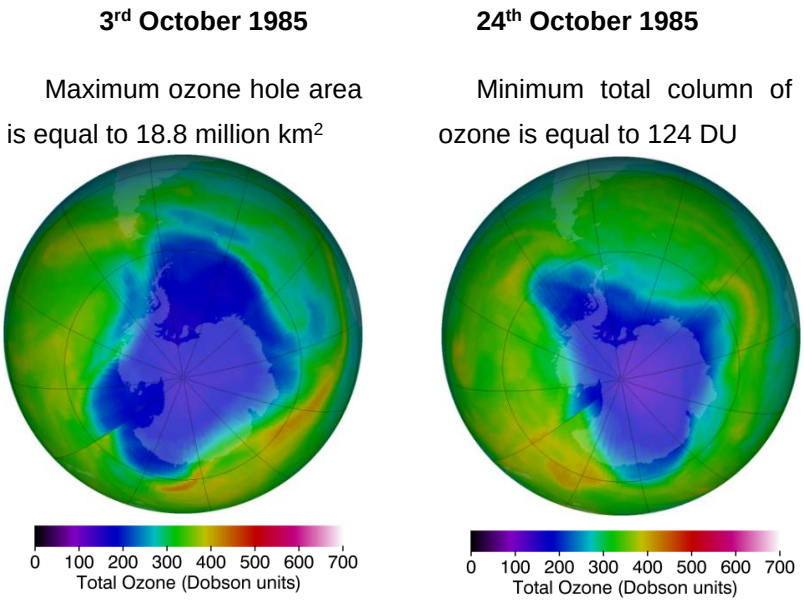

Figure 1.7. It shows the maximum ozone hole and the minimum total ozone column in 1985, respectively. They are based on the data from the satellite measurements performed by the Total Ozone Mapping Spectrometer (TOMS). Images were taken from the ozone hole watch on the NASA website (NASA, 2020).

Chlorofluorocarbons (CFCs) are the most critical stratospheric contributors to inorganic chlorine compounds (Cl, ClO, HCl, $ClONO_2$, $2Cl_2O_2$, HOCl, OClO, BrCl and $2Cl_2$). They have been a critical factor in the catalytic destruction of stratospheric ozone (Farman et al., 1985, Molina and Rowland, 1974). These artificial compounds, first discovered in the late 1920s, became widely used in the late 1970s due to their low toxicity, non-carcinogenicity, and no-reactiveness in the lower atmosphere. Thus, they were produced in massive quantities, mainly used as refrigerants, propellants in sprays, and the manufacturing of several plastic materials. The low ultraviolet radiation in the troposphere does not break CFCs down because of the low energy of the available UV photons, allowing them to reach the stratosphere. Once there, higher energy radiation breaks them down into compounds such as $ClONO_2$ and HCl, which are reservoir forms of unreactive chlorine and the source of the reactive compound chlorine monoxide (ClO) (see Figure 1.8). Once a ClO molecule is released in the stratosphere, the catalytic cycle reactions of chlorine start, destroying a significant amount of ozone molecules before it becomes an unreactive compound.

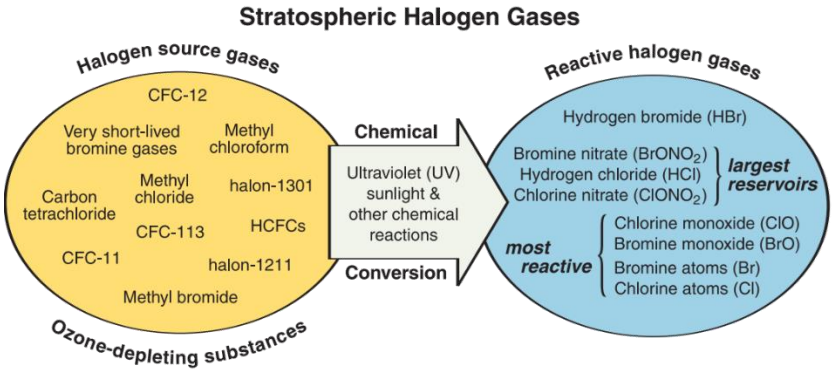

Figure 1.8 The interaction of halogen gases (such as CFCs) with atmospheric compounds and ultraviolet radiation results in reservoir forms of chlorine and ozone-depleting substances at stratospheric altitudes. The image is taken from https://esrl.noaa.gov/csd/assessments/ozone/2006/chapters/Q8.pdf

Natural processes such as the evaporation of oceans and volcanic eruptions also produce reactive halogens that may release chlorine atoms into the stratosphere. However, they are dissolved mainly by rainwater, ice and snow in the lower atmosphere. On the other hand, the long lifetime of the human-made compounds (CFCs and HCFCs) are not broken down chemically in the troposphere, allowing them to reach the stratosphere in three to six years (Jones et al., 2010).

The catalytic cycle reactions of chlorine, described in Figure 1.9, allow the massive depletion of stratospheric ozone. One molecule of these halogen substances destroys ozone at a higher rate than the stratospheric ozone generated by the Chapman cycle (see Figure 1.6). Such depleting substances regenerate after each cycle destroying ozone molecules countless times.

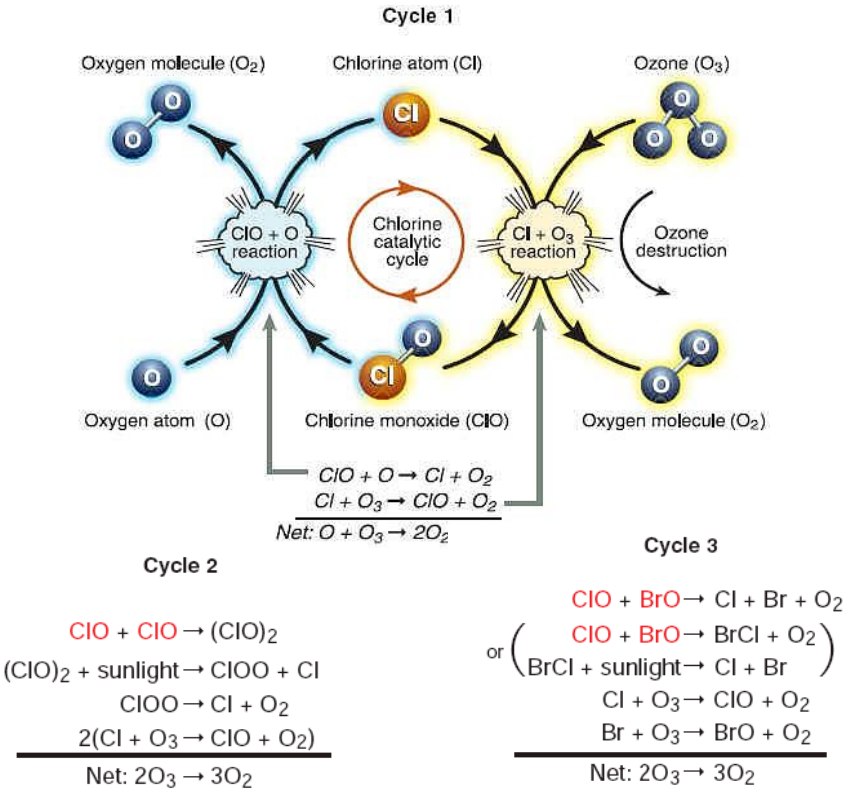

Figure 1.9 Cycle 1 describes the stratospheric regeneration of a Cl or ClO molecule when interacting with a molecule of ozone and oxygen, depleting a large number of ozone molecules in the process. Cycles 2 and 3 describe the photochemical interactions where Cl and Br are generated from ClO, BrO, and BrC (WMO, 2010a).

Stratospheric gases such as nitrogen dioxide (NO_2) and methane (CH_4) react with ClO and chlorine atoms, generating inert chemical reservoirs of chlorine nitrate ($ClONO_2$) and hydrochloric acid (HCl). Those new compounds remain unreactive in ultraviolet radiation, and finally, the cycle of stratospheric ozone depletion due to chlorine is stopped (see Figure 1.10).

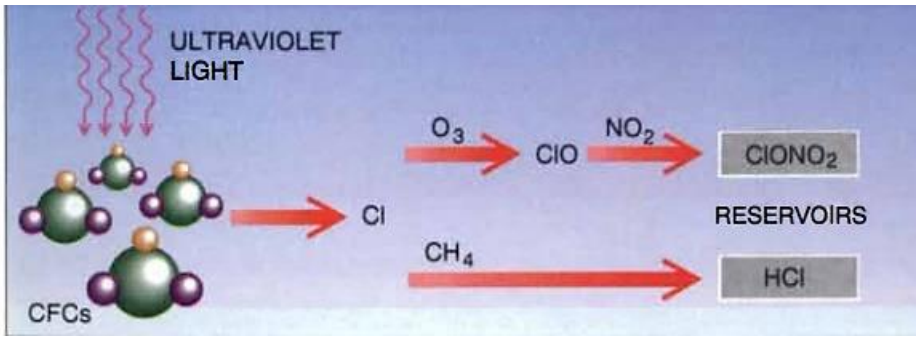

Figure 1.10 Generation process of reservoir chlorine gases in the stratosphere. The image is taken from Owen and Richard (1991).

1.3.1. Contributions of polar stratospheric clouds (PSCs) and Polar vortex to Polar ozone depletion

After the discovery of the Antarctic ozone hole (Farman et al., 1985), researchers found a relationship between the stratospheric ozone depletion and the presence of polar stratospheric clouds (PSCs) (Salawitch et al., 1988, Poole et al., 1989). Although there is a general absence of clouds in the stratosphere due to the dryness at high altitudes, the extreme conditions of winter cooling in the polar regions enable the formation of different PSCs. PSCs are categorized according to their composition into type I and type II, made of water, nitric acid and sulfuric acid and entirely of water-ice, respectively.

Due to their distinctive luminescent effect, PSCs type II, mainly formed from water-ice crystals, are called nacreous or mother-of-pearl clouds. They produce a pearly-white appearance visible to the naked eye due to their unique light scattering. PSCs type II occurs mainly during polar winter over Antarctica when condensed water vapour from the upper troposphere cools to stratospheric temperatures below –83° Celsius (see Figure 1.11). An initial hypothesis about the composition of all PSCs suggested that water-ice was the only component. However, later measurements from the Stratospheric Aerosol Measurement (SAM) II satellite instrument (McCormick et al., 1982) showed different stratospheric clouds at warmer temperatures.

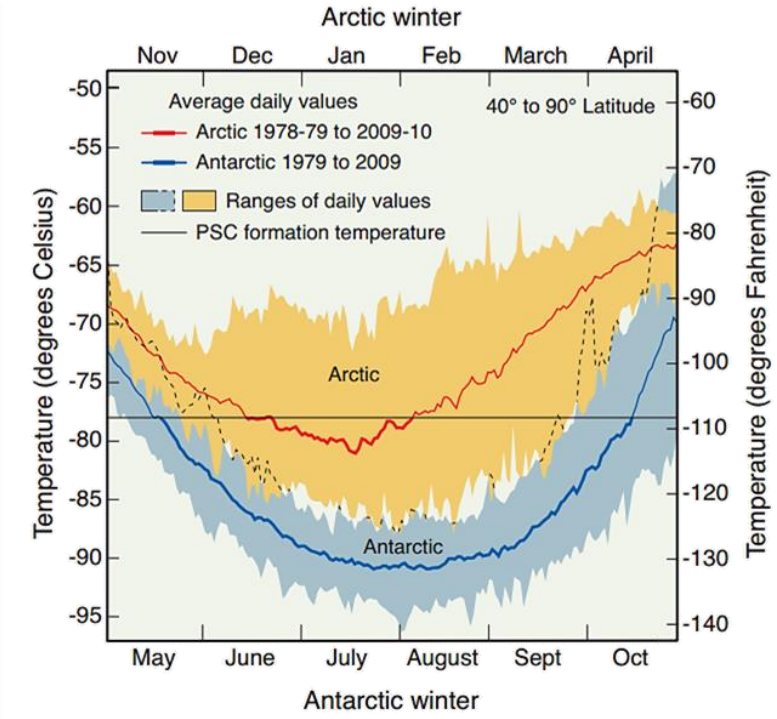

Figure 1.11 Average of Arctic and Antarctic winter temperatures (WMO, 2010a).

Some researchers, such as Owen and Richard (1991), found that some of those clouds are not made entirely of water-ice but consist of hydrated droplets of nitric acid (HNO_3) and sulphuric acid (H_2SO_4) that become solid due to temperatures below –78° Celsius (Hofmann et al., 1989). Although these PSCs are primarily generated over Antarctica, they also are rarely found over the Arctic for a shorter time. PSCs type I are critical components of the dramatic stratospheric ozone depletion over Antarctica. Their surface provides the ideal conditions to transform unreactive reservoirs of chlorine radicals Cl-O-NO_2 and HCl into molecular chlorine Cl_2 (see Figure 1.12). Equation (1.5) describes this reaction on a third body molecule M.

$$ClONO_2 + HCL \xrightarrow{M} HNO_3 + Cl_2 \tag{1.5}$$

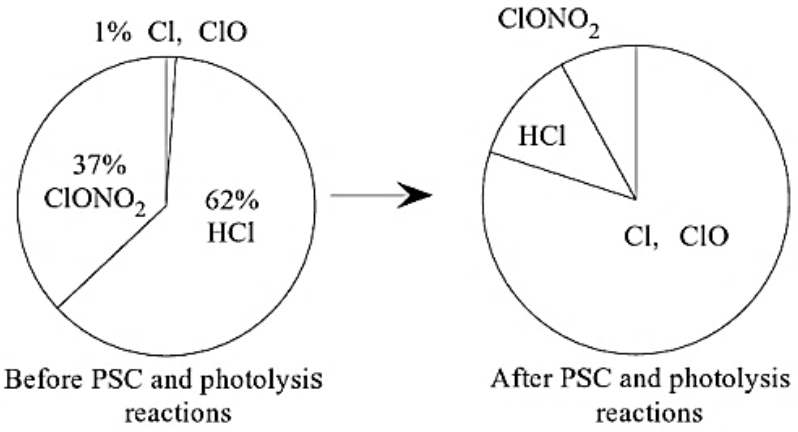

Figure 1.12 Pie charts compare Antarctic stratospheric compounds before chemical reactions happen on PSCs and after photolysis reactions start (Jacobson, 2005).

Another critical contribution to Antarctic ozone depletion is the polar vortex formed in winter. This vortex isolates stratospheric air with jet streams that regularly exceed 250 km/hr, far more potent and more prominent than its counterpart in the northern hemisphere. It prevents mixing with warmer air from lower latitudes and contributes to cooling the stratosphere to temperatures below –78° Celsius, allowing the formation of PSCs. Furthermore, once the vortex encircles the stratospheric polar regions, it prevents chlorine molecules from dispersing and mixing with stratospheric air rich in ozone coming from different latitudes.

Then, nothing further happens due to the absolute darkness of winter, and the reservoir of stratospheric reactive chlorine continues increasing. Consequently, once Austral spring arrives and solar radiation reaches the stratosphere (between September and October), the molecular chlorine is dissociated into atomic Cl. Then, the catalytic cycle of ozone depletion illustrated in Figure 1.9 occurs. Although the polar vortex and PSC are present in both hemispheres during winter, Arctic ozone depletion is less severe than in the Antarctic. The atmospheric conditions generated by the land-sea distribution in the Arctic produce a weaker polar vortex with a shorter lifespan when compared with its counterpart in the northern hemisphere (Schoeberl and Hartmann, 1991).

The polar vortex starts vanishing, and the PSC particles start the melting process once the atmospheric temperature increases due to solar radiation and photochemical reactions. Then, those particles fall to a lower atmosphere level under gravity. And finally, this seasonal ozone depletion ends when the stratospheric ozone is redistributed and mixed by dynamic transport.

1.4. Montreal Protocol

International concern about ozone depletion increased after discovering the ozone hole by Farman et al. (1985) and the recognition of Molina and Rowland (1974) describing the catalytic cycle of stratospheric ozone depletion by chlorofluoromethanes. Global efforts were then conducted by researchers, world leaders and politicians to control the production of ozone-depleting substances. As a result, in 1987, 46 countries initially signed a treatment called ‘The Montreal Protocol on Substances that Deplete the Ozone Layer’ (commonly called The Montreal Protocol) to regulate CFCs heavily (UNEP, 2012). Nowadays, around 200 countries have signed the international treaty, imposing binding obligations and timetables on developed and developing countries to phase out ozone-depleting substances. Although some globally agreed exceptions are considered essential to human health and laboratory procedures, all the established CFCs and HCFCs were phased out in 2010 (UNEP, 2012). However, ozone destruction has not stopped because CFCs and HCFCs can remain in the atmosphere for several decades due to their large average atmospheric lifetime (see Table 1.1). For this reason, the global regulations have been updated and progressively strengthened to phase out the production of CFCs substitutes such as HCFCs and hydrofluorocarbons (HFCs), aiming to mitigate further stratospheric ozone depletion.

Table 1.1 Mixing ratios and atmospheric lifetimes of some CFCs, HCFCs and other chlorine compounds (Jacobson, 2005).

Chemical formula	Trade name	Chemical name	Tropospheric mixing ratio (pptv*)	Estimated overall atmospheric lifetime (yrs)
Chlorofluorocarbons (CFCs)				
$CFCl_3$	CFC-11	Trichlorofluorocarbonmethane	270	45
CF_2Cl_2	CFC-12	Dichlorodifluorocarbonmethane	550	100
$CFCl_2CF_2Cl$	CFC-113	Trichlorotrifluoroethane	70	85
CF_2ClCF_2Cl	CFC-114	Dichlorotetrafluoroethane	15	220
CF_2ClCF_3	CFC-115	Chloropentafluoroethane	5	550
Hydrochloroflourcarbons (HCFCs)				
CF_2ClH	HCFC-22	Chlorodifluoromethane	130	11.8
CH_3CFCl_2	HCFC-141b	Dichloro-1-fluoroethane	6	9.2
CH_3CF_2Cl	HCFC-142b	2-Difluoromethane	8	18.5
Other chlorocarbons				
CCl_4		Carbon tetrachloride	100	35
CH_3CCl_3		Methyl chloroform	90	4.8
CH_3Cl		Methyl chloride	610	1.3
Other chlorinated compounds				
HCl		Hydrochloric acid	1-1000	<1

*pptv means ‘parts-per-trillion by volume.’

According to Khalil et al. (1999), chlorine trace gases with an atmospheric lifetime longer than two years tend to be artificial compounds such as CFCs and HCFCs. Those synthetic compounds remain in the troposphere until they are slowly transported to the lower stratosphere, where ultraviolet radiation breaks them down into ClO or chlorine atoms. Notice that only a portion of the total HCFC emissions reaches the stratosphere because they are easier to break down in the troposphere by atmospheric chemistry than the CFCs. Finally, stratospheric air streams move most chlorine compounds to the North and South Poles, where the polar vortex and PSCs set up the perfect conditions for significant stratospheric ozone depletion.

The Montreal Protocol is updated frequently based on scientific reviews provided by the WMO. Each scientific assessment of ozone depletion report provides recent discoveries based on long-term records of data. For example, it was acknowledged that the Montreal Protocol's regulation of depleting ozone substances avoided increments of several centimetres on the sea level due to the thermal expansion of the oceans, which would have been occasioned by additional global warming produced by such chemicals (WMO, 2018). The list of banned substances by the Montreal Protocol and its deadlines are updated according to discoveries. Such is the case of HFCs, which are not depleting ozone substances, but it was discovered that they increase climate warming (WMO, 2014).

The Montreal Protocol plays a crucial role in reverting humankind's effects on the Earth's atmosphere and diminishing as much as possible future regrets. One example of the achieved results is shown in Figure 1.13, where there is a comparison between two atmospheric models of stratospheric ozone with and without the Montreal Protocol. Those models show the areas in the North hemisphere that would have been affected by higher solar radiation due to the newly formed ozone hole in the Artic zone. Fortunately, the tight regulations of ozone-depleting substances prevented this terrible scenario from happening.

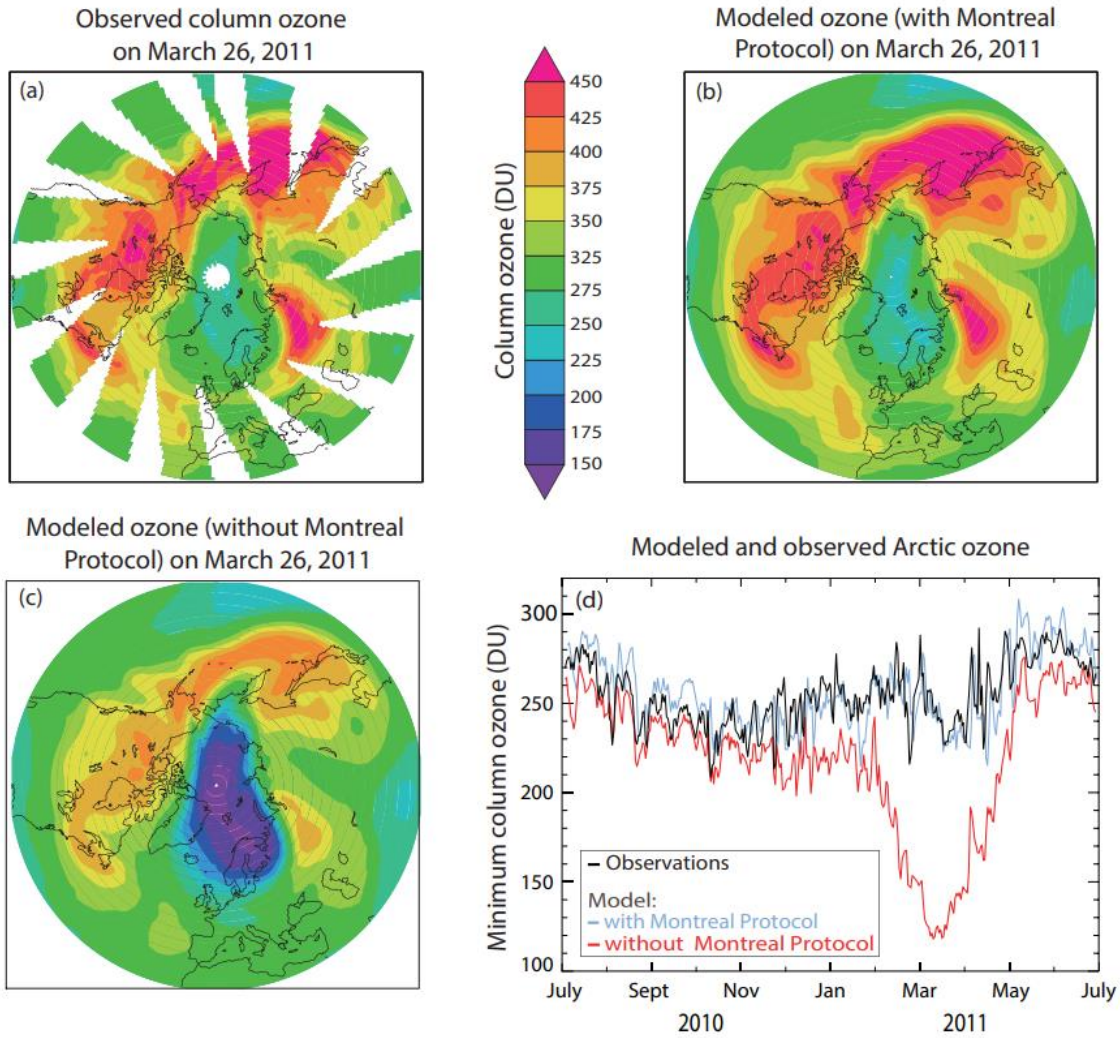

Figure 1.13 Comparison between atmospheric models with and without implementing the Montreal protocol and satellite measurements WMO (2018).

Despite global efforts to eradicate ozone-depleting substances, China is still one of the main contributors to halocarbon emissions, along with India and the United States. Yi et al. (2021) presented the trends of atmospheric concentrations and emissions of major halocarbons (CFC-11, CFC-12, HCFC-22, HCFC-141b, HCFC-142b and HCFC-134a) from 2009 to 2019 in five cities in China: Beijing, Hangzhou, Guangzhou, Lanzhou and Chengdu. Although there is a declining trend for CFC-11, CFC-12, HCFC-141b and HCFC-142b, the atmospheric concentrations of HCFC-22 and HFC-134a increased (see Figure 1.14). China emissions of

HCFC-141b and HCFC-142b contributed to the 17.8% and 48% of the global emissions (see Figure 1.15). Therefore, eliminating HCFCs in China will produce a beneficial global impact.

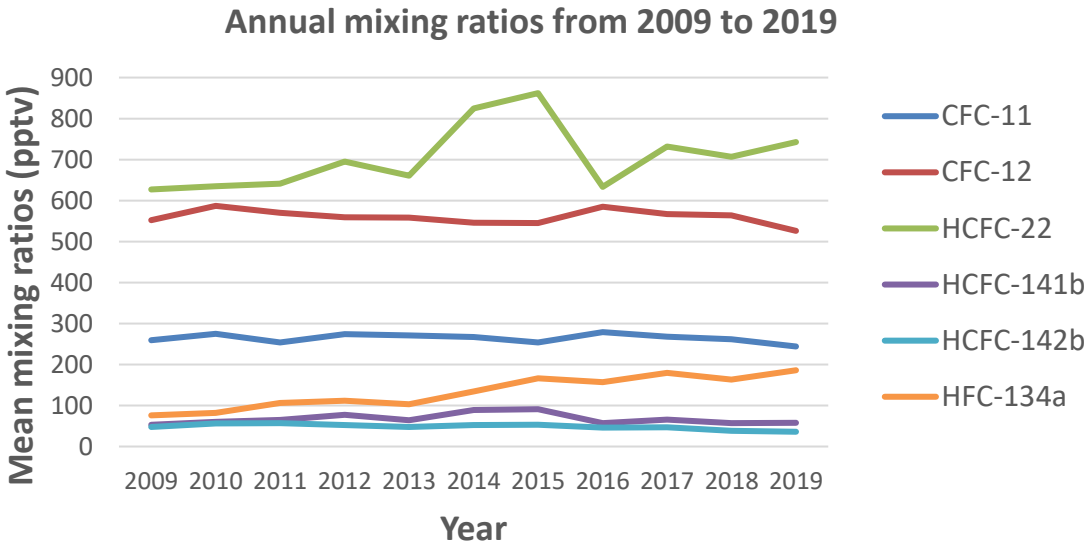

Figure 1.14 Annual mixing ratios from 2009 to 2019 in China according to Yi et al. (2021).

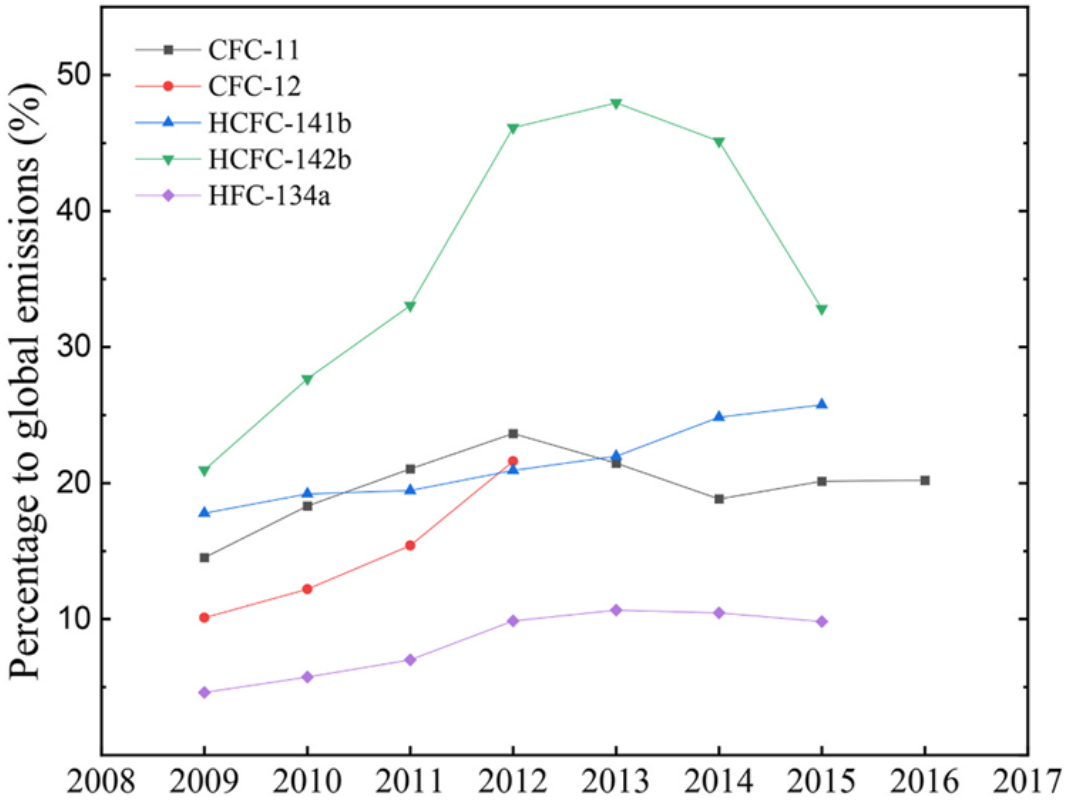

Figure 1.15 Global emissions of ozone-depleting substances generated in China from 2009 to 2019 (Yi et al., 2021).

1.5. Stratospheric ozone monitoring

The first instrument able to perform a total column of ozone measurement was the spectrograph produced by Fabry and Buisson (1921). They achieved a series of measurements for 14 days from 21st May 1920 to 23rd June 1920 in Marseilles, France, having irregular daily variations at different hours. They obtained a rough estimate of the total column of ozone going from 275 to 335 Dobson units, which is relatively close to what would be expected today. Then, Harrison and Dobson (1925) designed a homemade Fèry spectrograph, a more portable instrument than its predecessor. And in the late 1920s, the Dobson spectrophotometer was developed. It was a robust instrument designed to be manually operated on a routine basis without a scientific background (see Figure 1.16). Finally, this instrument was gradually improved according to the availability of new technologies such as photomultiplier tubes and transistors, but it remains manually operated, and it is not weatherproof.

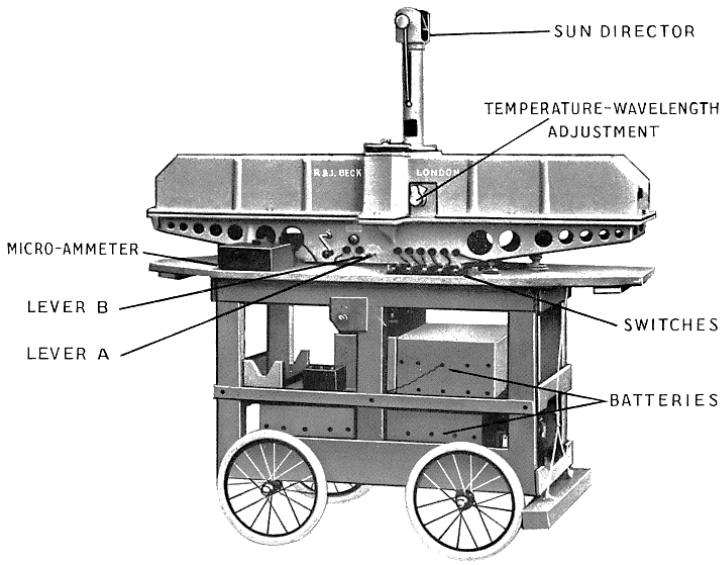

Figure 1.16 Dobson-spectrophotometer diagram. The image is taken from Dobson's manual (R. & J. Beck LTD).

Fortunately, the need to monitor stratospheric ozone was recognized, and the International Ozone Commission was created in 1948. By the time the International Geophysical Year (IGY) took place in July 1957, ozone monitoring stations were increased worldwide. During the IGY, the first stratospheric ozone measurement at the Halley research station, which is part of the British Antarctic Survey (BAS), was performed. Furthermore, a global network of Dobson spectrophotometers started a continuous ozone monitoring programme that continues today. According to WMO (2015), about 60 Dobson spectrophotometers were still performing measurements in 2012.

Although there were ozone measurements before the IGY, their quality is considered poor compared to those obtained from 1957–1958 due to improved observation techniques (Brönnimann et al., 2003b, Brönnimann et al., 2003a). To maintain a uniform data record, the World Meteorological Organization (WMO) chose the Dobson spectrophotometer #083 as the

ground-based reference for stratospheric ozone in 1980 (Komhyr et al., 1989). Such instrument is still operational and performs direct or indirect calibrations of other spectrophotometers under the guidance of NOAA/ESRL Global Monitoring Division, Boulder, Colorado (USA), and in the framework of the Global Atmospheric Watch programme created by the WMO.

Despite the success of the Dobson spectrophotometer as a ground-based instrument, technological advances in electronics and photonics allowed the development of the Brewer spectrophotometer in 1973. This instrument is a computer-controlled instrument that can be operated remotely or programmed to follow a specific routine (see Figure 1.17). In addition, improvements in the temperature dependence allow the Brewer spectrophotometer to function outdoors and unattended unless on-site maintenance or mechanical corrections are needed (Kerr et al., 1981).

Figure 1.17 Brewer spectrophotometer model MKIII (double monochromator).

The first satellite measurement of ozone was in 1979 by the Total Ozone Mapping Spectrometer (TOMS), launched on board the satellite Nimbus-7 (NASA, 1996). Although the satellite was operational until 1993, more TOMS instruments were mounted in satellites such as Meteor 3, ADEOS and Earth Probe, which was still active until 2006. Then, several satellite-spectrophotometers have continued the long-term record of ozone retrieval, such as the Global Ozone Monitoring Experiment (GOME), launched in 1995 and operated until 2011; the Scanning Imaging Absorption Spectrometer for Atmospheric Cartography (SCIAMACHY), operational until 2012; and the Ozone Monitoring Instrument (OMI), which is still active.

The global ozone coverage made by satellites from the National Aeronautics and Space Administration (NASA) and the European Space Agency (ESA) is continuously validated by ground-based spectrophotometers of the WMO Global Atmosphere Watch (GAW) ozone network. Similarly, satellite and ground-based reference spectrophotometers are used to check and validate spectrometers worldwide. However, before the ozone hole was detected in 1985, it was thought that retrieval errors and uncertainties in the systems were responsible for the inconsistencies between satellite and Dobson measurements at the South Pole. Indeed, data analysis from NASA did not trigger low stratospheric ozone flags until it reached a threshold of

180 DU, expecting typical values between 300 and 400 DU (Christie, 2001). Thus, the ozone hole went unnoticed until the British Antarctic Survey staff at the Halley Research Bay Station proved its existence (Farman et al., 1985). Figure 1.18 displays some images of the southern ozone depletion obtained by NASA since 1979 during the austral spring.

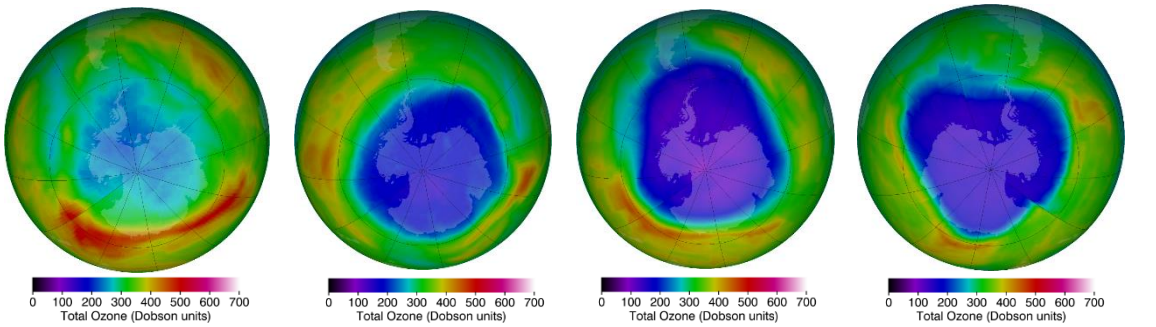

Figure 1.18 Comparison of southern ozone depletion during the austral spring (September). The first two images are based on satellite measurements from the Total Ozone Mapping Spectrometer (TOMS), while the last two use satellite measurements from the Ozone Monitoring Instrument (OMI). These mages were taken from the ozone hole watch on the NASA website (NASA, 2020).

The importance of long-term ozone measurements rests on maintaining accurate data about ozone recovering and monitoring changes in the atmospheric chemistry to assess the effectiveness of the Montreal Protocol and opportunely apply additional regulations. Although the production of ozone-depleting substances has been considerably reduced, the severe ozone depletion in Antarctica will continue for more decades because ozone-depleting substances such as CFCs and HCFCs are long-lived compounds (see Table 1.1) (Jacobson, 2005).

1.6. Importance of ground measurements of total ozone column

Identifying flaws and retrieval errors in satellite systems in charge of monitoring the Earth's atmosphere is a challenge. Thus, the existence of ground reference instruments allows the validation of satellite measurements by comparing and overlapping their observations. As a result, retrieving errors and uncertainties on satellite or ground-based spectrometers and applying the proper corrections is possible. In addition, by incrementing the number of remote sensing spectrometers and supporting in-situ measurements like ozone sondes around the world, scientists will be able to discover or confirm rare events occurring in the atmosphere and improve existing atmospheric models to predict the behaviour of the Earth's atmosphere more accurately.

The World Meteorological Organization (WMO) is responsible for observing the Earth's atmosphere composition. Its long-term data records of stratospheric ozone allow the design of mathematical models to estimate its depletion and recovery rates and assess the impact on climate and living organisms due to variations in the UV radiation that reaches the Earth's surface.

Thus, the continuation of long-term monitoring of stratospheric ozone is essential as feedback to estimate its future recovery and understand its impact on climate change.

The general goal of the Montreal Protocol is to achieve stratospheric ozone values measured in 1980 (before discovering the ozone hole). Figure 1.19 and Figure 1.20 show the trend from 1979 to 2013 of the total ozone column and the ozone hole area over Antarctica, respectively, with reference measurements from 1980. The satellite measurements data is from the Total Ozone Mapping Spectrometer (TOMS) mounted on Nimbus-7 (1978-1994), Meteor-3 (1991-1994), and TOMS-Earth Probe (1996-2006) and the long-term model-based analysis from Modern Era Retrospective-Analysis for Research Applications (MERRA, from 1979 to 2016) (NASA, 2020). Unfortunately, there is still a long way to go to revert to the 1980 ozone levels.

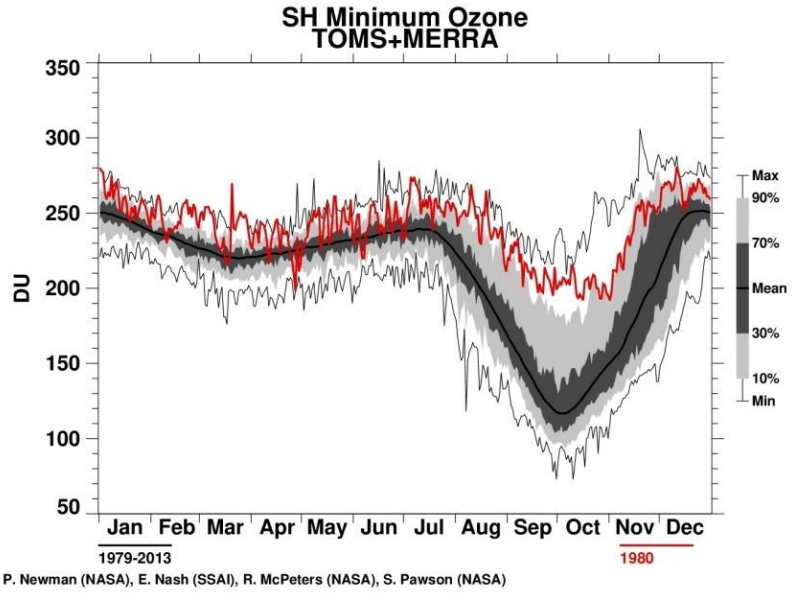

Figure 1.19 Trend of the total column ozone over Antarctica from 1979 to 2013 from satellite observations of TOMS and MERRA. The red line is dated from 1980, the black line is the mean value from 1979 to 2013, while the remaining data in the grey scale is the statistical representation from 1979 to 2013 according to the scale on the right-hand side (NASA, 2020).

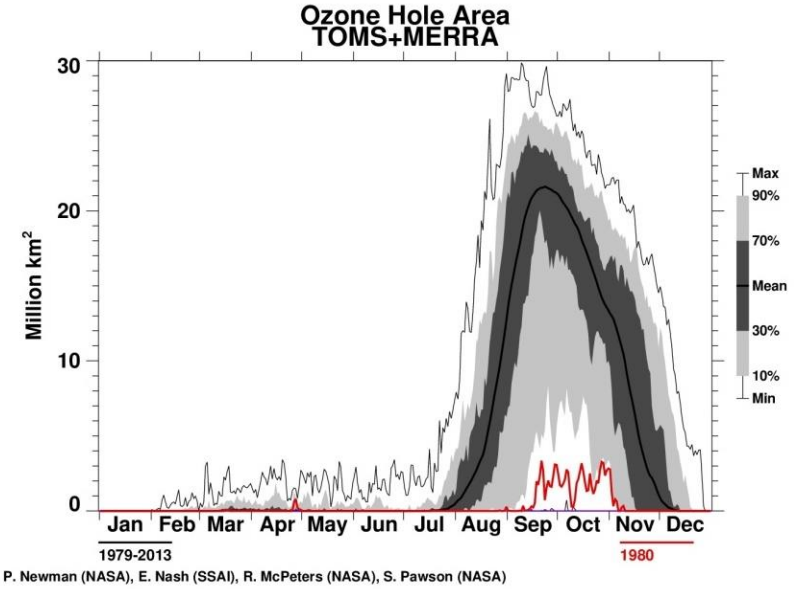

Figure 1.20 Trend of ozone hole area over Antarctica from 1979 to 2013 from satellite observations of TOMS and MERRA. The red line is dated from 1980, the black line is the mean value from 1979 to 2013, while the remaining data in the grey scale is the statistical representation from 1979 to 2013 according to the scale on the right-hand side (NASA, 2020).

Despite the decay of atmospheric ozone-depleting substances because of the Montreal Protocol, such as chlorine and bromine compounds, it is challenging to assess the ozone recovery because of complex atmospheric dynamics. Other variables, such as solar irradiance variability, seasonal atmospheric phenomena such as the polar vortexes, increased aerosol loading, temperature changes, and greenhouse gas concentrations, affect directly or indirectly the total ozone column.

Though there is an apparent stratospheric ozone recovery in the Antarctic, current models predict that the ozone hole will still be a seasonal phenomenon until mid-century (WMO, 2018), see Figure 1.21. Although most scenarios predict a total ozone column recovery in the following decades, it is necessary to continue recording ozone and other trace gas measurements to verify its recovery and validate models and simulations of its recovery.

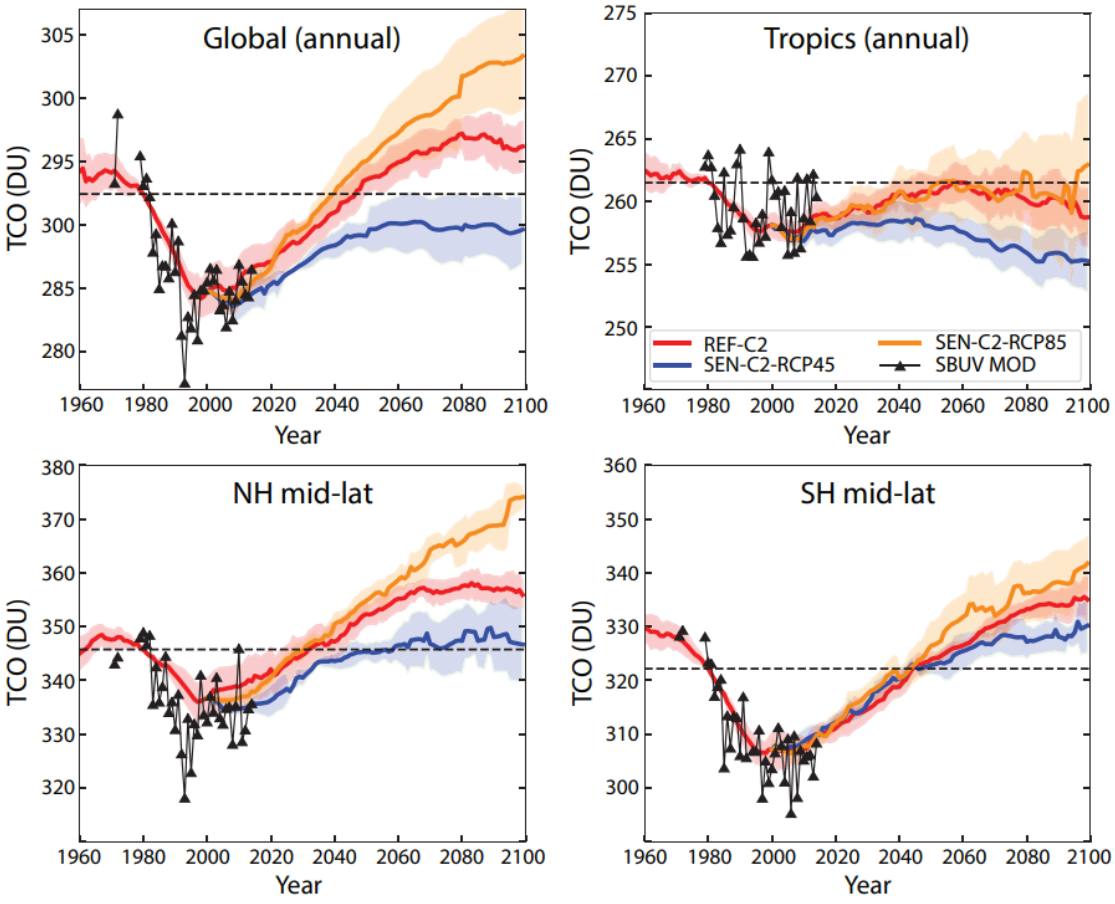

Figure 1.21 It summarizes the evolution of total ozone columns for different Representative Concentration Pathways (RCP). Mean observations of total ozone column (TOC) (solid black) compared with predictions of TOC by Chemistry-Climate Models (CCM). Red line REF-C2 (19 models performed a total of 33 realizations), blue line SEN-C2-RCP45 (7 models, 9 realizations), and orange line SEN-C2-RCP85 (8 models, 10 realizations). The shaded regions show one standard deviation variability compared with respect to the lines of the same colour (WMO, 2018).

1.7. Ground-based spectrometers

Nowadays, WMO only recognizes Brewer and Dobson spectrometers as worldwide references for ground-based remote sensing of the total ozone column. This chapter briefly describes the current spectrometers measuring TOC and other experimental instruments still in the developing stage.

After recognising the Antarctic ozone hole in 1985, the Montreal Protocol was implemented in 1987 to regulate and phase out ozone-depleting substances. Therefore, long-term records from well-maintained and calibrated instruments are used to evaluate the stratospheric ozone recovery and apply further regulations if required. The World Meteorological Organization (WMO) considers Dobson and Brewer spectrophotometers as the only ground references used to validate satellite measurements of the total ozone column (TOC). Although Dobson and single-

monochromator versions of the Brewer are still operating around the world, MKII (286.5 nm-363 nm), MKIV (286.5 nm-363 nm and 430 nm-450 nm for NO_2) and MKV (550 nm-620 nm for O_3); the Brewer spectrometer MKIII (double monochromator) is the only one commercially available.

1.7.1. Dobson spectrometer

In the late 1920s, Dobson designed a state-of-the-art spectrophotometer able to estimate the total ozone column on-site. It possesses a double monochromator based on two aligned prisms and a photomultiplier tube as a detector. Since a double monochromator rejects more stray light than a single one, the Dobson spectrometer can achieve accuracy within 1% (Dobson, 1968).

Compared to modern devices, the disadvantages of the Dobson spectrometer are the need for an operator with a minimum scientific background to perform direct solar measurements, its high-temperature dependence, and its need to be protected from rain and snow.

Figure 1.22 illustrates the internal design of the monochromator inside the Dobson spectrophotometer.

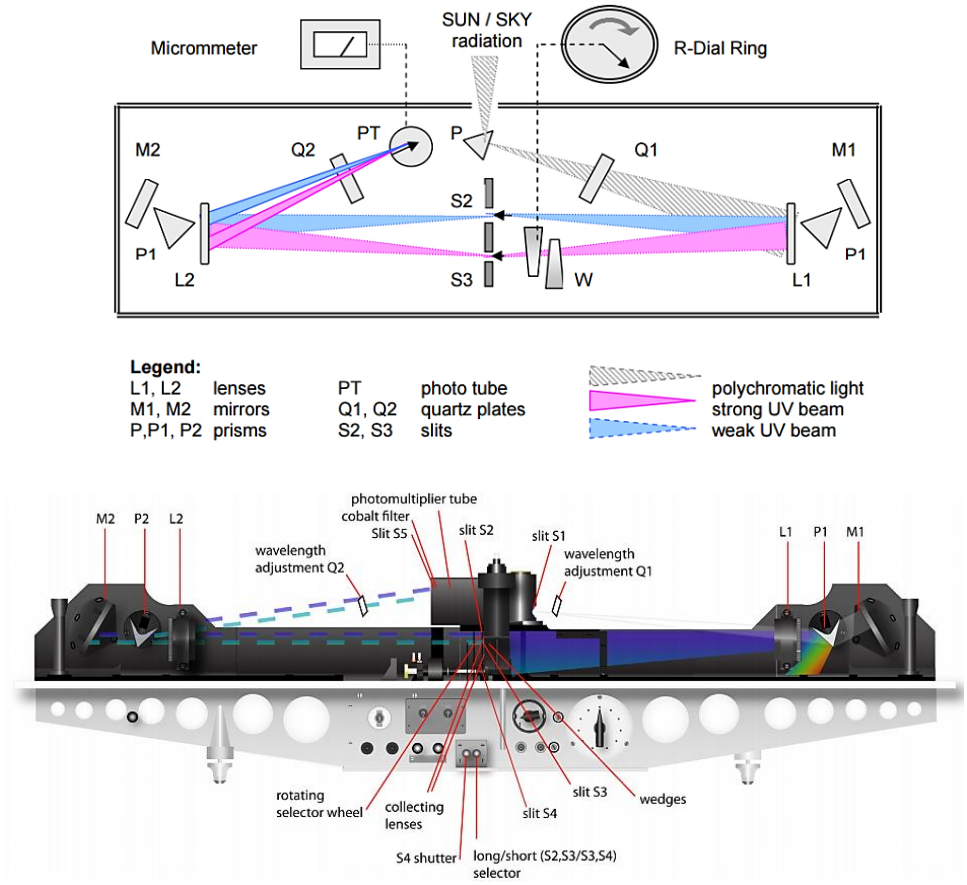

Figure 1.22 General diagram of a Dobson's monochromator. The upper schematic displays the diagram of Dobson's monochromator from a vertical perspective (Image taken from: http://www.o3soft.eu). And the Bottom schematic illustrates its horizontal diagram, where M, P and L are the mirrors, prisms and lenses, respectively (Komhyr, 1980).

1.7.2. Brewer spectrometer

The Brewer spectrometer is an automated outdoor spectrophotometer remotely controlled by a computer. It was designed to operate in extreme cold at Polar Regions (-20ºC) and tropical temperatures (+50ºC). An internal heater keeps the temperature above +10ºC or +20ºC, depending on its customized configuration. In addition, a self-compressing system compensates for the expansion and contraction of internal elements to minimize variations in measurements. However, changes in the internal temperature will still produce uncertainties due to electronic, optical and mechanical parts such as gears and micrometres, but more importantly, due to the temperature dependence of the photomultiplier tube (PMT). Thus, customized corrections and adjustments are made to minimize those uncertainties within acceptable levels: about 1% for TOC measurements and less than ~6.5% for UV irradiance measurements higher than 305 nm using a well-maintained and calibrated instrument (Kerr et al., 1981) (Fountoulakis et al., 2017).

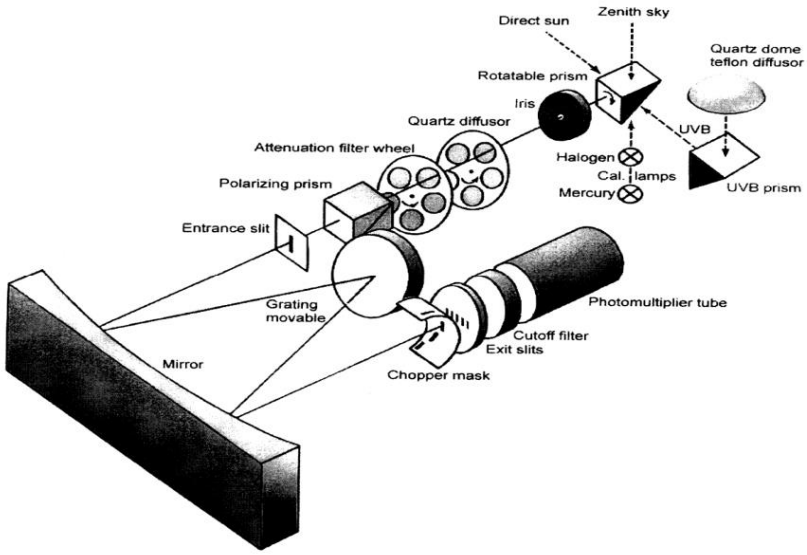

Figure 1.23 Internal design of a Brewer single monochromator (Josefsson, 1986).

Figure 1.24 Brewer spectrophotometer model MKIII (double monochromator) mounted on a solar tracker.

Table 1.2 illustrate the general specification of a double monochromator Brewer spectrometer MKIII.

Table 1.2 Brewer spectrometer specifications obtained from the operator manual of Brewer MKIII

The spectral output of the slit mask	306.3 nm, 310.1 nm, 313.5 nm, 316.8 nm, 320.1 nm (Ozone measurements) 303.2 nm (Hg spectral calibration)
Resolution	302.15 nm
Stability	±0.01 nm (over full temperature range)
Precision	0.006 ± 0.002 nm
Measurement range	286.5 nm to 363.0 nm
Exit-slit mask cycling	0.12 sec/slit, 1.6 sec for full cycle
O3 Measurement accuracy	±1% (for direct-sun total ozone)
Operating temperature range inside the spectrometer	0°C to +50°C (without any temperature stabilizer)
Physical dimensions (external weatherproof container)	Size: 70 x 46 x 34 cm Weight: 34 kg

The slit functions used during direct solar measurements are illustrated in Figure 1.25. It is worth noticing that the full width half maximum (FWHM) is constant with insignificant variations in contrast with the wavelength-dependent FWHM of the AOTF (see Chapter 6).

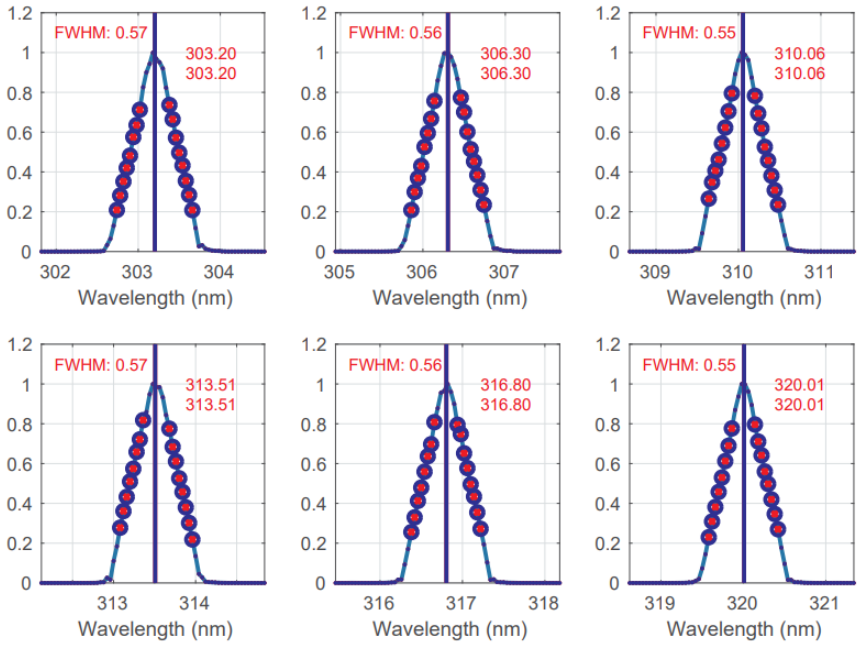

Figure 1.25 Central wavelengths and FWHM obtained from Brewer wavelength measurements (red marks) using a tunable laser with steps of 0.04 nm. (Redondas et al., 2018).

1.8. Aims and objectives of the research

Stratospheric ozone has been monitored on a continuous and long-term basis worldwide under the supervision of the Global Atmospheric Watch (GAW), a program of the World Meteorological Organization (WMO) in charge of performing reliable observations of the atmosphere's chemical composition. Such long-term monitoring of stratospheric ozone has been performed by satellites and Dobson and Brewer spectrophotometers (see Chapter 1). However, there is still a need to develop instruments based on new technologies to perform equivalent, reliable total ozone column measurements on a regular basis or for short-term projects.

Nowadays, the Dobson spectrophotometer is no longer manufactured. The double monochromator spectrophotometer Brewer MKIII is the only commercially available instrument dedicated to performing worldwide total ozone column measurements. Thus, this research aims to build a previously designed new spectrophotometer based on solid-state technology, showing proof-of-principle of its ability to perform reliable stratospheric ozone measurements to the same standards as Dobson and Brewer spectrophotometers.

This aim is achieved if the resulting instrument can meet the following design objectives. The proposed instrument filters the input beam from direct solar radiation, providing the detector with a (virtually) monochromatic signal in the UV spectrum. It gathers a spectrum, or specified wavelengths for ozone retrieval, in seconds rather than minutes, reducing the impact of changing cloud conditions t has no moving parts and requires no high voltage power supply: this removes some of the practical drawbacks and sources of wear and tear with the Brewer.

The final system should be weatherproof and either insensitive to temperature and humidity or carefully characterised and the operating conditions recorded so that processing can correct for the environment.

The entire system, including the signal processing, results in stable and reliable measurements of the total ozone column at the level achieved by a well-maintained double monochromator Brewer.

The selected key technology at the core of this new instrument design is the Acousto-optic tunable filter (AOTF).

1.9. Outline of the thesis

The structure of the thesis is summarized below.

Chapter 1 has described the interaction between solar radiation and ozone molecules, its importance, the unfortunate reduction of stratospheric ozone due to ozone-depleting substances in the atmosphere, the developed countermeasures, its monitoring and the reason why the proposed spectrometer was designed and developed. Chapter 2 details the background

knowledge needed to understand the calculations of ozone retrieval and explains the interaction of photons in the ultraviolet spectrum with particles in the atmosphere.

Chapter 3 explains the technology used in the proposed spectrometer to diffract the light and how it differs from current instruments, while Chapter 4 describes the complete instrument design. Chapter 5 presents some considerations and optimizations to the spectrometer design during construction. The calibration and characterization of the developed spectrometer are described in Chapter 6. Direct solar scans and total ozone column measurements performed by the AOTF spectrometer are presented in Chapter 7, as well as the side-to-side comparisons with Brewer spectrometers.

Finally, Chapter 8 presents the conclusions and describes further work that needs to be done to obtain better results and improve the spectrometer design. This last chapter also contains ideas to continue the research on this topic.

Chapter 2. Atmospheric attenuation and the DOAS technique for deriving total ozone column

In general, spectroscopy studies the interaction between photons and the particles in a sample based on its spectral absorbance and the scattering generated by the elastic and inelastic collisions (see section 2.7). It allows the identification of the sample's chemical composition by measuring the amount of attenuated or transmitted radiation. The sample size and its state (solid, liquid or gas) vary depending on the application, allowing in-situ and remote measurements. Consequently, spectroscopy is widely used in electronics, chemistry, biology, geology, astronomy and atmospheric sciences due to its versatility. Here it is used to determine the total ozone column (TOC) by estimating the relative attenuation of ultraviolet wavelengths through the depth of the atmosphere, understanding that the majority of ozone resides in the stratosphere and considering the known interactions of such wavelengths with all other atmospheric compounds. This chapter explains all the attenuation processes that are relevant to solar radiation in the atmosphere.

2.1. Beer-Lambert law

The Beer-Lambert law states that the transmittance (T) of a sample is correlated to the relation between the optical path length and its molecular concentration. It defines the interaction between the initial collimated electromagnetic intensity I_0 and the transmitted intensity (I) once it has passed through the sample.

The absorption cross-section (σ) is the property of any particle or chemical compound that describes the ability to block or absorb electromagnetic radiation across the spectrum. Its unique spectral pattern indicates the effective area of the particle absorbing or scattering the incident radiation at a specific wavelength (cm^2 per molecule). Figure 2.1 shows a small part of a sample in a homogeneously distributed medium, where dx and its density are small enough to avoid absorber elements shadowing each other.

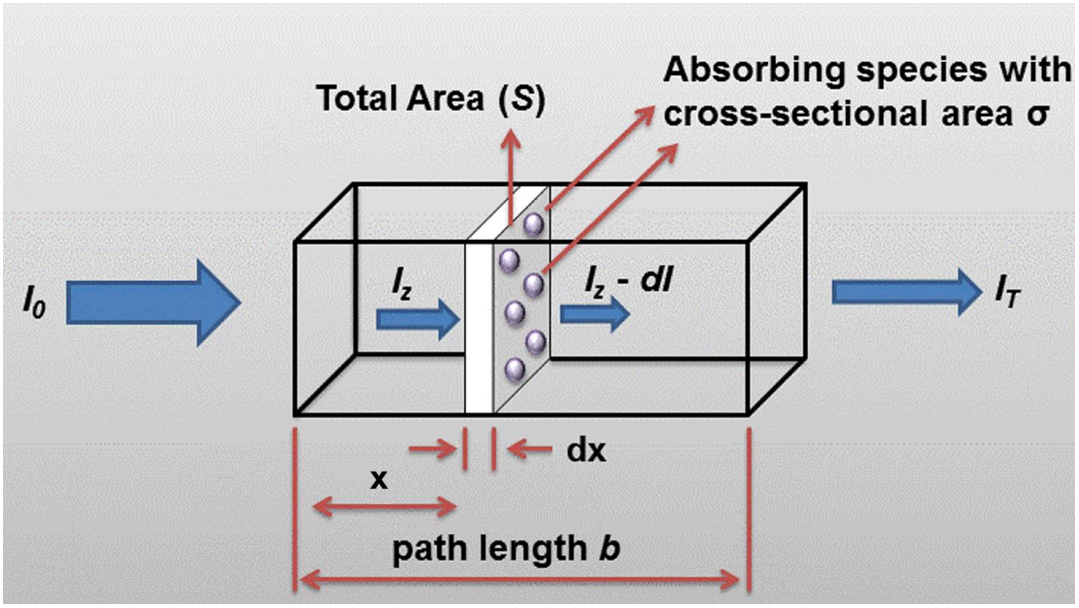

Figure 2.1 Sample analysed by the Beer-Lambert law. The image was taken from (https://pharmaxchange.info/2012/04/ultraviolet-visible-uv-vis-spectroscopy-%E2%80%93-derivation-of-beer-lambert-law/)

The fraction of light that is not transmitted by the sample $\left(\frac{dI_x}{I_x}\right)$ is proportional to the effective area where light interacts with the molecules $(\sigma NSdx)$ divided by the total cross-section area of the sample, see Eq. (2.1).

$$-\frac{dI_x}{I} = \frac{\sigma NSdx}{S} \tag{2.1}$$

Where:

$-dIx =$ Change in intensity across x (the variation is always negative).
$I =$ Intensity of the incident light.
$\sigma =$ Absorption cross-section or extinction coefficient.
$N =$ Molecular number density in 1cm^3.
$S =$ Total cross-section area of the sample to be analysed.
$dx =$ Thickness.

Reducing the expression and integrating both sides:

$$\int_{I_0}^{I} \frac{dI_x}{I} = -\int_0^L \sigma N dx \tag{2.2}$$

$$In\left(\frac{I}{I_0}\right) = -\sigma NL \tag{2.3}$$

Where $L =$ Path length.

Solving for I

$$I = I_0 e^{-\sigma NL} \tag{2.4}$$

The expression σN, which is wavelength dependent, is known as the total extinction coefficient, the total extinction cross-section or the volume extinction coefficient $\beta(\lambda)$. It includes the absorption coefficient $\beta_a(\lambda)$ and the scattering coefficient $\beta_s(\lambda)$, measuring the total spectral scattering and the total spectral absorption of a sample of 1cm^3 volume.

$$\beta(\lambda) = \sigma(\lambda)N \tag{2.5}$$

$$\beta(\lambda) = \beta_a(\lambda) + \beta_s(\lambda) \tag{2.6}$$

To analyse a sample that contains a mixture of different compounds, $\beta_a(\lambda)$ is considered the sum of all the absorption extinction coefficients. Thus, each one can be analysed separately.

$$\beta_a(\lambda) = \sum_{i=1}^{M} \sigma_i N_i \tag{2.7}$$

Where M is the number of compounds taken into account in the sample.

A complete Beer-Lambert equation is obtained by substituting Eq. (2.6) and Eq. (2.7) in Eq. (2.4). It estimates the amount of transmitted light after a portion of the initial radiation was absorbed or scattered by a homogeneously distributed sample.

$$I(\lambda) = I_0(\lambda) e^{-L\sum_i \sigma_i(\lambda)N_i - L\beta_s(\lambda)} \tag{2.8}$$

2.2. Optical depth

The optical depth or optical thickness, τ(λ), is a monochromatic atmospheric variable used in spectroscopy. It integrates the total volume of total extinction cross-section coefficient β(λ,z) along the vertical optical path from a given altitude z_0 to the outer atmosphere. The following equation estimates the optical depth:

$$\tau(\lambda, z_0) = \int_{z_0}^{\infty} \beta(\lambda, z)\, dz \tag{2.9}$$

Equation (2.10) expresses the Beer-Lambert law regarding optical depth and the relative optical air mass m, also known as air mass factor (AMF).

$$I(\lambda) = I_0(\lambda) e^{-m\tau(\lambda)} \tag{2.10}$$

2.3. Sun Position

The solar radiation measured at ground level possesses direct and diffuse components due to the scattering by air molecules and aerosols in the atmosphere. The solar beam's semi-angle divergence is minimal (around 0.25°) (Fontani et al., 2013) because of the large distance between the Earth and the Sun (approximately 150 million kilometres on average). Thus, the direct solar

beam that reaches the Earth's surface is considered a collimated beam when the solar disk is clear of clouds, and the atmospheric scattering is negligible.

Accurate measurements of the total ozone column are mainly obtained by direct measurements of the collimated solar beam during clear-sky conditions. The reduced atmospheric aerosol minimizes the diffuse component within the instrument's field of view, which is generally large enough for the whole solar collimated beam plus some tolerances to pass through to compensate for irregularities of the solar tracker. Most spectrometers are designed with a field of view larger than the angular size of the solar disc (~0.53 degrees) to compensate for inaccuracies of the solar tracker. Besides the reliability of ground-based spectrometers, reliable direct solar measurements also depend on the accuracy of the solar tracker, which may carry the complete spectrometer or just the input optics. Its correct auto-positioning, smooth transition, and alignment to the solar disk centre play an essential role in atmospheric measurements.

2.3.1. Declination angle of the Sun

The declination of the Sun (δ) is the angle between the equatorial plane and the imaginary line connecting the centre of the Sun with the centre of the Earth. It varies seasonally due to the tilt of the Earth (23.45°), affecting the number of daylight hours at different locations depending on its latitude (see Figure 2.2). The declination angle reaches maximum and minimum values in the Northern hemisphere during June and December, respectively (see Figure 2.3).

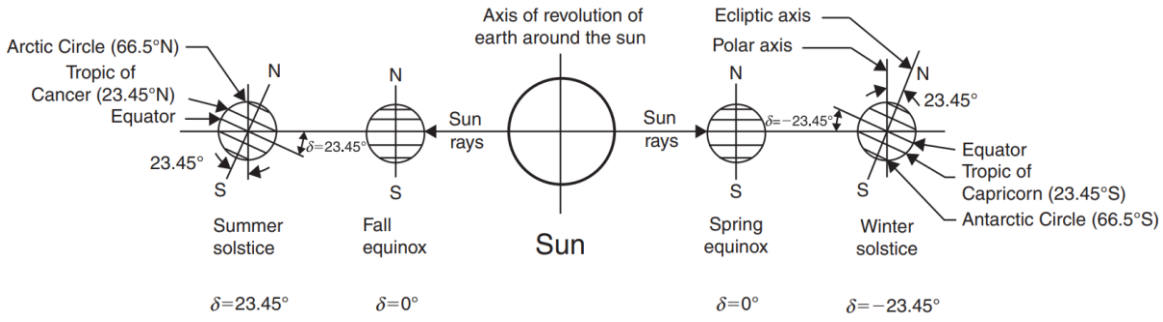

Figure 2.2 Annual variation of the solar declination angle (Kalogirou, 2014)

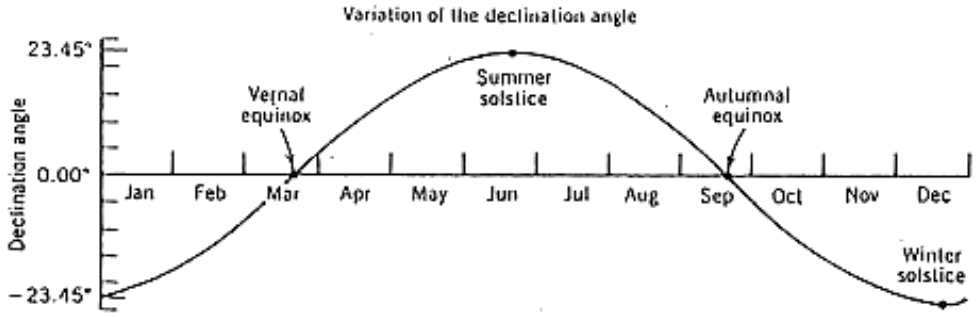

Figure 2.3 Seasonal values of the solar declination angle for the northern hemisphere. Image is taken from http://www.reuk.co.uk/wordpress/solar/solar-declination/

Scharmer and Greif (2000) provided an approximation of the declination angle of the Sun in Eq. (2.11). It considers the elliptical movement of the Earth around the Sun and provides mean daily values over the solar cycle of four years.

$$\delta = arcsin\left\{0.3978 \cdot sin\left[\frac{360N}{365.25} - 80.2° + 1.92° \cdot sin\left(\frac{360N}{365.25} - 2.8°\right)\right]\right\} \quad (2.11)$$

Where N is the day number or ordinal date.

2.3.2. Local solar time and hour angle

Local solar time (LST) is defined as the time according to the position of the Sun in the sky relative to one specific location on the ground. It has slight and periodic irregularities mainly due to the Earth's obliquity and the elliptical movement of the Earth around the Sun. The local solar time in Eq. (2.12) is in 24-hour format and is based on the UTC instead of the local clock time to avoid daylight-saving correction.

$$LST = UTC + \frac{1}{60}[4 \times (Longitude\ of\ the\ location\ ) + EOT] \quad (2.12)$$

Where:

LST = Local solar time in hours.
UTC = Universal Time Coordinated in 24-hour format.
Longitude of the location (degrees west).
EOT = Equation of time adjustments in minutes; see Eq. (2.13)

Equation (2.12) considers that the Earth takes four minutes to travel one degree in longitude and the daily variations in the length of each year throughout the whole year (Masters, 2013). The equation of time (EOT) applies these daily corrections caused by the combined effects of the Earth's axial tilt and orbital speed changes through the year due to the Earth's elliptical orbit. The EOT in Eq. (2.13) is estimated in hours, graphed in Figure 2.4.

$$EOT = \frac{1}{60}(9.87 \sin 2B - 7.53 \cos B - 1.5 \sin B) \quad (2.13)$$

Where:

$$B = \frac{360(N - 81)}{364}\ [degrees] \quad (2.14)$$

Where N is the day number or ordinal date.

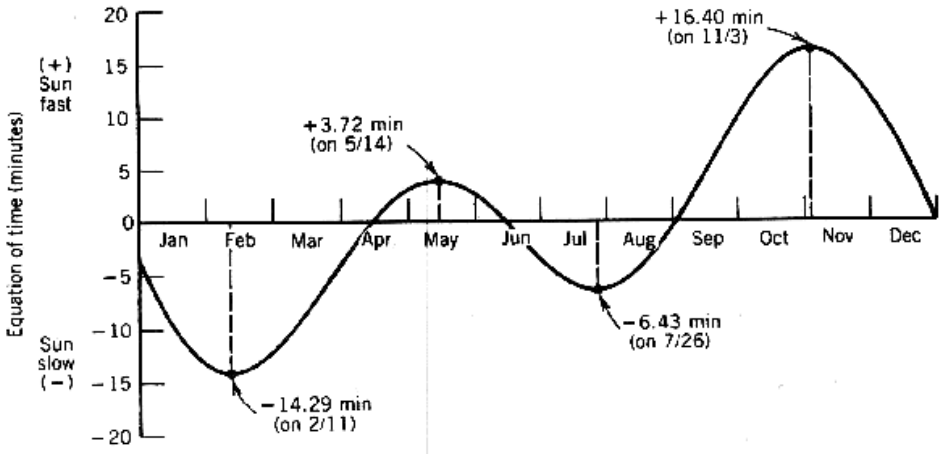

Figure 2.4 Displays the correction in minutes made by the equation of time (EOT). Image is taken from http://www.reuk.co.uk/wordpress/solar/solar-declination/

Equation (2.15) estimates the solar hour angle (ω) by converting the LST to degrees. The sign convention establishes that ω is negative before solar noon and positive otherwise.

$$\omega = 15°(LST - 12hrs) \tag{2.15}$$

2.3.3. Solar zenith angle

The solar zenith angle (θ) is defined as the angle between the local zenith and the line of sight to the solar disc centre. Equation (2.16) describes the relationship between the solar zenith angle, the declination angle, the hour angle and the local latitude of the observer.

$$cos(\theta) = sin\,\varphi\,sin\,\delta + cos\,\varphi\,cos\,\delta\,cos\,\omega \tag{2.16}$$

Where:

θ is the solar zenith angle.
φ is the local latitude angle of the observer.
δ is the declination angle of the Sun.
ω is the hour angle in the local solar time.

2.4. Relative optical air mass

The relative optical air mass is defined as the ratio between the optical path length of incident solar photons at different zenith solar angles and the length of the optical atmospheric path in the zenith direction. Equation (2.17) approximates the relative optical air mass as a function of the apparent solar zenith angle, considering the atmosphere's diffraction index equals 1. It is only valid if the sun is not low on the horizon, showing acceptable discrepancies smaller than 1% for zenith angles lower than 60º (Tomasi and Petkov, 2014).

$$m = \frac{1}{cos\,\theta} \tag{2.17}$$

However, relative optical air mass values under clear-sky conditions are influenced by temperature, pressure, the curvature of the Earth, and the vertical profile of atmospheric compounds (see Figure 2.5). Thus, a more accurate value is obtained by analysing the atmosphere with Snell's law as a collection of thin layers with a diffractive index as a function of the altitude $n(z)$, see Eq. (2.18) (Thomason et al., 1983).

$$m_\lambda(\theta) = \left[\frac{1}{\tau_\lambda}\right] \int_{z_0}^{\infty} \frac{\sigma_\lambda(z)dz}{\left[1 - \frac{n_0}{n(z)}\left(\frac{z_0\, sin(\theta_0)}{z}\right)^2\right]^{1/2}} \tag{2.18}$$

Where:

$m_\lambda(\theta)$= Relative optical air mass as a function of θ at a specific wavelength.
τ_λ= Optical depth at a given wavelength.
θ_0= Apparent solar zenith angle.
z= Altitude.
$n(z)$= Refractive index of the atmosphere at altitude z.
n_0= Refractive index at the Earth's surface.

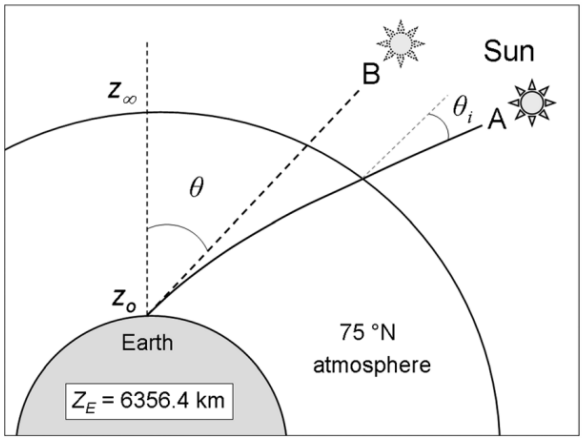

Figure 2.5 Image of the Earth's atmosphere at the 75ºN polar latitude. It displays the solar incident beam at the outer atmosphere (point A illustrates the sun's actual position) and its refraction through the atmospheric path. The apparent solar zenith angle θ would point to the sun's position if there were no atmospheric refraction at all. Image taken from (Tomasi and Petkov, 2014)

Equation (2.19) from Bernhard et al. (2005) simplifies Eq. (2.18) by neglecting the wavelength dependence of m_λ in the spectral operational range of the Dobson and Brewer spectrometer, and considering a thin attenuation layer at a height h above the instrument.

$$m(\theta) = \frac{n_h(R+h)}{[{n_h}^2(R+h)^2 - {n_0}^2(R+r)^2 \cdot sin^2(\theta_0)]^{1/2}} \tag{2.19}$$

Where:

n_h = The refractive index at height h.
R= Radius of the Earth (6370 km).
r= Altitude of the spectrophotometer.
h= Height above the sea level where radiation attenuation occurs.

It is essential to mention that several assumptions about the atmosphere are made to get relative air mass calculations. For example, Eq. (2.20) produces a practical approximation of the relative optical depth (Bernhard et al., 2005) if the diffraction index of the air at sea level n_0 and the diffraction index of the air where the attenuation occurs is equal to unity $(n_0 = n_h = 1)$. This approximation is used by Dobson and Brewer spectrometers to get the relative optical depth related to ozone, sulphur dioxide and Rayleigh scattering (Savastiouk and McElroy, 2005, Staehelin et al., 2003, Tomasi and Petkov, 2014).

$$m(\theta) = \frac{R + h}{\sqrt{(R + h)^2 - (R + r)^2 \sin^2 \theta}} \tag{2.20}$$

Note that the formula considers the radius of the Earth as a fixed value $R = 6370km$ instead of the actual radius of the Earth at the location of the measurement. Thus, significant errors might be noticeable only at high altitudes and high air mass values. Additionally, the Brewer algorithm to retrieve the total ozone column considers that the maximum absorption of solar radiation in the ultraviolet spectrum due to ozone occurs approximately at an altitude of $h = 22\ km$, a value that was adopted by the Brewer community as a constant in its calculations (Savastiouk and McElroy, 2005). Figure 2.6 displays the average vertical profile of ozone and other atmospheric compounds.

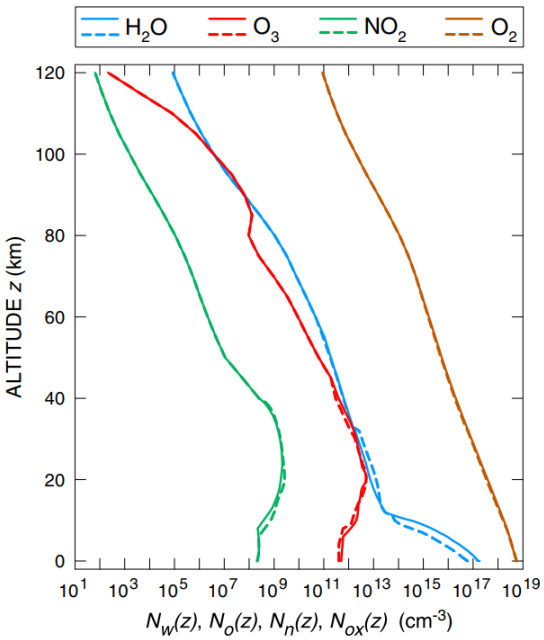

Figure 2.6 Average vertical profiles of H_2O, O_3, NO_3, and O_2 molecular densities (mol·cm^{-3}) from 50 m to 120 km at Ny-Alessund, Norway (~79°N). There is an H2O molecular density comparison between radiosounding measurements at Ny-Alessund, Norway (~79°N) during June and July from 2000 to 2003 (solid blue curve) and the measurements by Mario Zucchelli (~75°N) during December and January of the 1987-1998 multiyear period (Blue dashed curve). O3 molecular density values from ozonesonde measurements performed at Ny-Alesund (~79°N) and Neumayer (~70°S) are described by a solid red line and red dashed line respectively during local summer months from 1978 to 1994. NO2 molecular density near 75°N (solid green curve) and 75°S latitudes (green dashed curve) were obtained by the Odin-OSIRIS satellite instrument over summertime from 2002 to 2005. Finally, the O2 was estimated from the vertical profile ratio p(z)/T(z) at Ny-Alessund (solid brown curve) and ~75°N (brown dashed line) (Tomasi and Petkov, 2014).

The total column of SO_2 is mainly detected by satellite spectrometers, such as the Michelson Interferometer for Passive Atmospheric Sounding on Envisat (MIPAS), the Atmospheric Chemistry Experiment Fourier transform spectrometer (ACE-FTS), in addition to ground spectrometers such as Brewer spectrometers. The atmospheric SO_2 is commonly measured in Dobson Units (DU) and part per trillion by volume mixing ratios. At standard temperature and pressure of 0 Celsius (273.15 Kelvin) and one atmosphere (101.325 kPa), the global average thickness of stratospheric SO_2 would be around 0.01 mm or 1 DU, and it would possess a mass of 0.0285 grams per square meter.

The primary sources of sulphur dioxide (SO_2) are burning fossil fuels and volcanic emissions. Generally, maximum SO_2 concentrations are close to their source, with a lifetime of hours to a few days in the troposphere, mostly because it is soluble in water droplets, and it reacts rapidly with OH to create sulphate aerosol particles that can be transformed into sulphuric acid if combined with water. Therefore, SO_2 can remain in the stratosphere for several days because of its dryness and the small concentration of OH particles (Eisinger and Burrows, 1998). However, violent volcanic eruptions can produce large amounts of sulphate aerosols that can remain for nearly one month in the atmosphere (Zhu et al., 2020).

2.5. Ozone absorption cross-section

The absorption cross-section estimates the interaction of particles with incident photons at a particular wavelength. Each chemical compound attenuates, scatters or absorbs the light in a unique and distinctive spectral pattern. Therefore, knowing the absorption cross-section is essential in spectrometry to identify the concentration of a particular chemical compound in a mixed sample. In atmospheric sciences, the whole atmosphere is the sample to be analysed, and the collimated beam source commonly is solar radiation.

Estimating the total ozone column from the ground to the outer atmosphere is done by performing spectral measurements at specific wavelengths with different attenuation rates. Ground-based instruments such as Dobson and Brewer spectrometers get estimations of the total ozone column (TOC) by measuring the direct solar radiation at wavelengths where peaks and valleys of the ozone cross-section stand out from other trace gases.

The ozone molecule (O_3) absorbs solar radiation over a wide spectral range, mostly from 200 nm to 1100 nm. The highest absorption occurs in the ultraviolet radiation within the Hartley band, around 250 nm. Other strong lines of the O_3 absorption cross-section are found at Huggins, where most of the current spectrometers operate. Lidars, on the other hand, perform spectral measurements in the near-infrared (Wulf band). Figure 2.7 displays the O_3 absorption cross-section values in the UV, visible and near-infrared (NIR) spectrum at 223 K from 220 nm to 1100 nm. Such measurements were performed by Serdyuchenko et al. (2014) and Gorshelev et al. (2014).

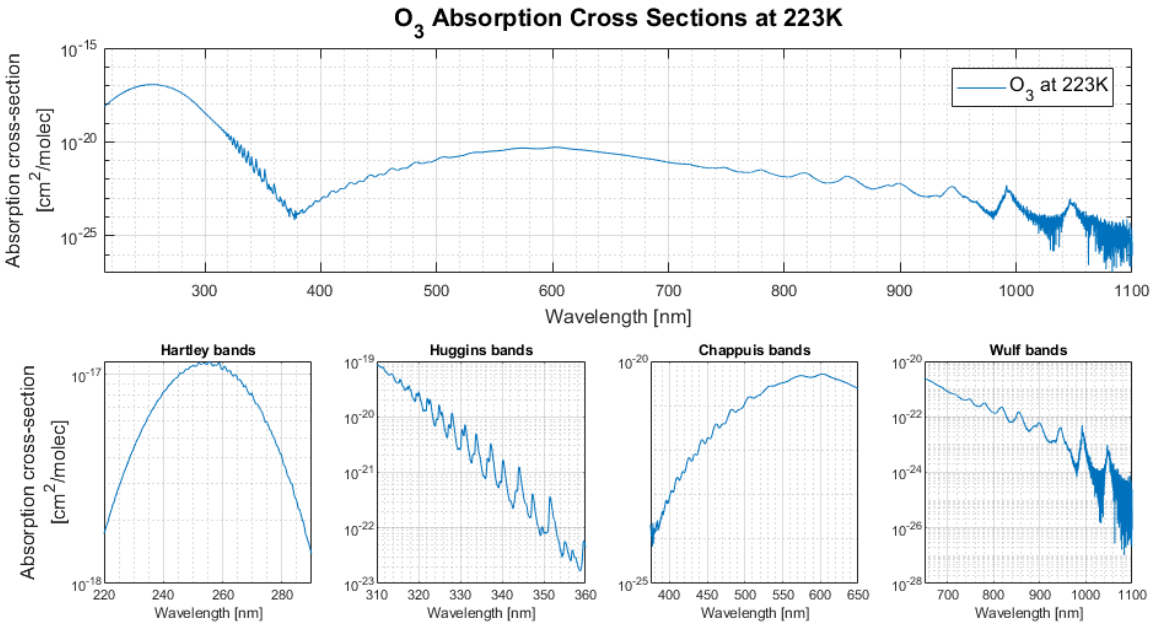

Figure 2.7 O_3 absorption cross-section values in the ultraviolet, visible and near-infrared (NIR) spectrum at 223 K from 213 nm to 1100 nm obtained by Serdyuchenko et al. (2014) and Gorshelev et al. (2014).

Figure 2.8 displays the ozone cross-section at eleven temperatures from 193 K to 293 K obtained by Serdyuchenko et al. (2014) and Gorshelev et al. (2014). The five wavelengths used by the Brewer spectrometer are represented by dashed lines at 306.3 nm, 310.1 nm, 313.5 nm, 316.8 nm and 320.1 nm.

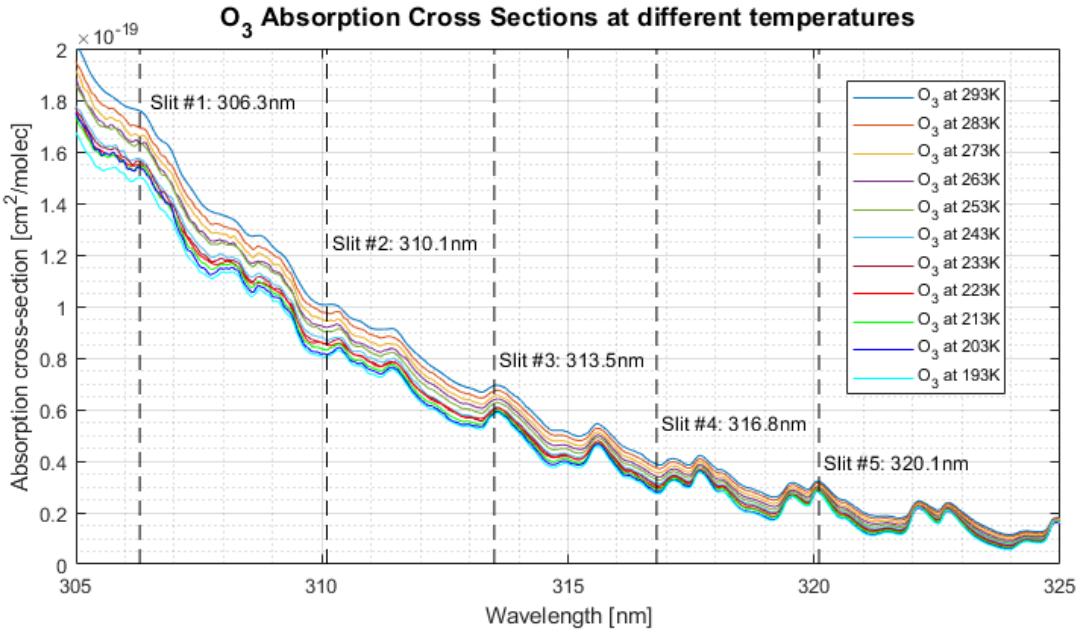

Figure 2.8 Ozone cross-section measurements at eleven different temperatures from 193 K to 293 K with a step of 10 K. Dashed lines represent the wavelengths used by Brewer spectrometers to estimate the total ozone column and the total SO_2 column (306.3 nm, 310.1 nm, 313.5 nm, 316.8 nm and 320.1 nm) (Source: personal collection).

Brewer spectrometers use ozone cross-section values at -45°C (228.15 K) because that is the mean temperature at 22 km, where the absorption by ozone is higher. Serdyuchenko et al. (2014)

and Gorshelev et al. (2014) provide a quadratic fit expression to estimate the absorption cross-section at a given temperature and wavelength from 300 nm to 370 nm, see Eq. (2.21). The ozone cross-section values obtained by such equation have been recently authorized to be used by Brewer spectrometers in the total ozone column retrieval algorithm. Note that the fitting coefficients of the quadratic polynomial in Eq. (2.21): a0, a1, and a2 were obtained from the website: http://www.iup.uni-bremen.de/gruppen/molspec/databases/referencespectra/o3spectra2011/index.html.

$$\sigma(T,\lambda) = 10^{-20} a0(\lambda) \times [1 + a1(\lambda)T + a2(\lambda)T^2] \quad (2.21)$$

Where

T = Temperature in degree Celsius
σ= Ozone cross-section in cm^2/molecule.
$a0, a1, a2$= Fitting coefficients of the quadratic polynomial given by Serdyuchenko et al. (2014) and Gorshelev et al. (2014).

Figure 2.9 displays the O_3 and SO_2 absorption-cross section values used by Brewer spectrometers to estimate the total ozone column.

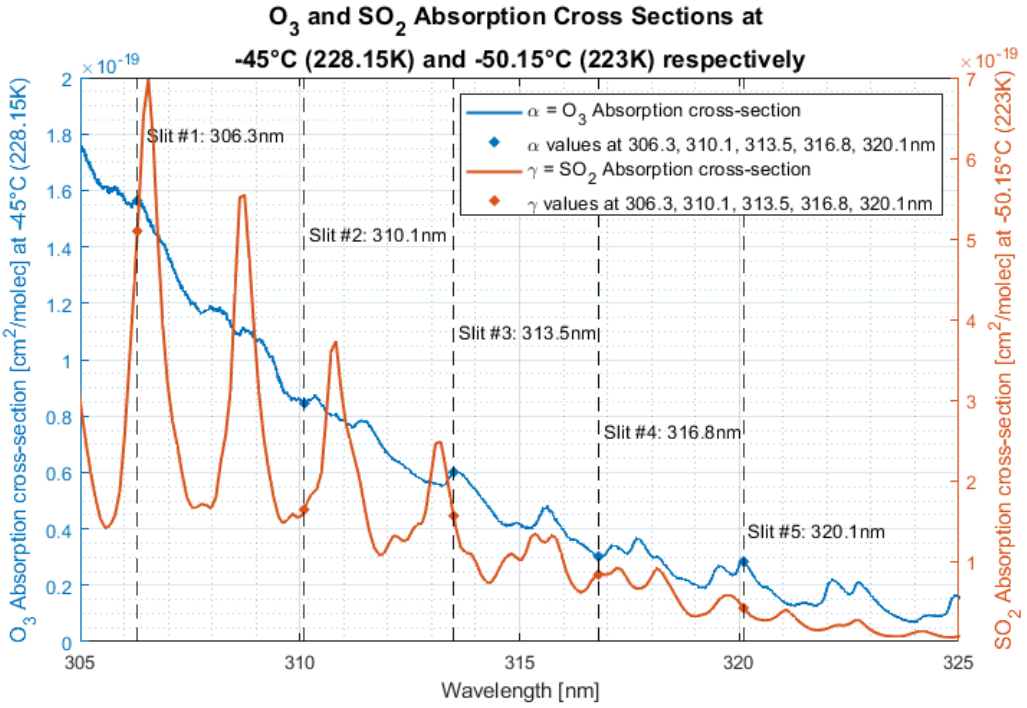

Figure 2.9 Comparison of absorption cross-section values of ozone (blue line) and SO_2 (orange line) in cm^2 per molecule used in the Brewer algorithm to estimate the total ozone column. O_3 cross-section at -45° C was obtained using Eq. (2.21) by Serdyuchenko et al. (2014) and Gorshelev et al. (2014), while SO_2 values were obtained from the SCIAMACHY satellite spectrometer. Where the black lines indicated the Brewer wavelengths λ_1=306.3 nm, λ_2=310.1 nm, λ_3=313.5 nm, λ_4=316.8 nm and λ_5=320.1 nm (Source: personal collection). The only differences with the graph from León-Luis et al. (2018) are the Brewer wavelngths λ_1=306.4 nm and λ_5=320.1 nm.

The ozone absorption cross-section values used by the Brewer spectrometer are: $\sigma(306.3\,nm)$=1.5631x10^{-19}, $\sigma(310.1\,nm)$=8.4512x10^{-20}, $\sigma(313.5\,nm)$=6.0092x10^{-20}, $\sigma(316.8\,nm)$=3.0175x10^{-20}, and $\sigma(320.1\,nm)$=2.8453x10^{-20} cm^2 per molecule. Finally, these

values need to be convoluted by the slit function of the spectrometer see Eq. (2.22), where $S_i(\lambda)$ is the instrument slit function and α_i is the ozone absorption.

$$\alpha_i(\lambda) = \frac{\int \sigma(\lambda) S_i(\lambda) d\lambda}{\int S_i(\lambda)} \quad (2.22)$$

2.6. Differential optical absorption spectroscopy (DOAS) technique

Differential optical absorption spectroscopy is a highly effective technique widely used in remote sensing to measure atmospheric trace gases. Depending on the application, DOAS analyses and applies Beer-Lamber's law to the spectral absorption of atmospheric compounds in the UV, visible or near IR. Although it is mainly based on direct or zenith-sky measurements of solar radiation, other light sources such as the moon, stars, and lasers are also used.

A critical achievement in atmospheric spectroscopy was achieved in 1881 when Cornu (1881) found that atmospheric compounds attenuate the solar irradiance measured at the Earth's surface. In the same decade, Hautefeuille and Chappuis (1880), Hartley (1881), and Huggins (1890) achieved important discoveries regarding stratospheric ozone absorption, marking the beginning of stratospheric ozone monitoring (see Figure 1.3).

The classical DOAS approach is widely used in light measurements. It is based on Beer-Lambert's Law, and it can be applied to estimate the total amount of any atmospheric compound by comparing the extra-terrestrial solar radiation with the attenuated spectrum reaching the spectrometer and using the known absorption cross-section of the targeted chemical compound. This approach is used in the Brewer spectrometer to estimate the total column of ozone. The only requirement is that the absorption values of the targeted chemical compound $\sigma'(\lambda)$ change rapidly with wavelength compared with the smooth slope of the combined absorption values of all the other atmospheric elements $\sigma_b(\lambda)$.

Substituting $\sigma'(\lambda)$ and $\sigma_b(\lambda)$ into the Beer-Lambert law Eq. (2.8):

$$\boldsymbol{I(\lambda) = I_0(\lambda) \cdot e^{-L\sigma'(\lambda)X} \cdot e^{-L\sum_i \sigma_{b_i}(\lambda) N_i - L\beta_s}} \quad (2.23)$$

Equation (2.23) describes the absorption of the trace gas in the first exponential function. In contrast, the second exponential function represents the absorption of all the other atmospheric components plus Rayleigh and Mie scattering. Where X represents the total column amount of the trace gas of interest in the atmosphere and β_s represents the scattering extinction coefficient.

The effectiveness of DOAS is why it is widely used by ground-based spectrometers and spectrometers mounted in satellites and aeroplanes. Additionally, it allows identifying more than one trace gas simultaneously, as long as there are enough measurements at different wavelengths.

Multi-axis differential optical absorption spectroscopy (MAX-DOAS)

The traditional DOAS technique is most sensitive to stratospheric absorbers. On the other hand, the MAX-DOAS technique combines scattered sunlight from multiple viewing directions to achieve a higher sensitivity to absorbers in the lowest few kilometres of the troposphere. Therefore, it is possible to achieve a higher sensitivity because of the detection of much weaker absorption features of the desired chemical compound. It also enables the simultaneous measurement of several absorbers eliminating the influence of Mie scattering in the calculations (Hönninger et al., 2004).

2.7. Rayleigh-scattering and Mie-scattering calculations

Light scattering is a physical process in which photons are forced to change their original trajectory after colliding with existing particles while travelling through a medium. This phenomenon occurs within the atmosphere when the trajectory of a single photon from solar radiation changes its direction after colliding with atmospheric compounds such as air molecules, water droplets, ice particles, and aerosol particles in general. If there is a change in energy between the scattered and the incident photon, it is an inelastic collision. Otherwise, it is an elastic collision with a particular scattering pattern (Figure 2.10), which would depend on the size, shape and composition of the particle, as well as the wavelength of the incident photon. Elastic collisions produce the main types of atmospheric scattering (Rayleigh and Mie scattering), described in the following paragraphs.

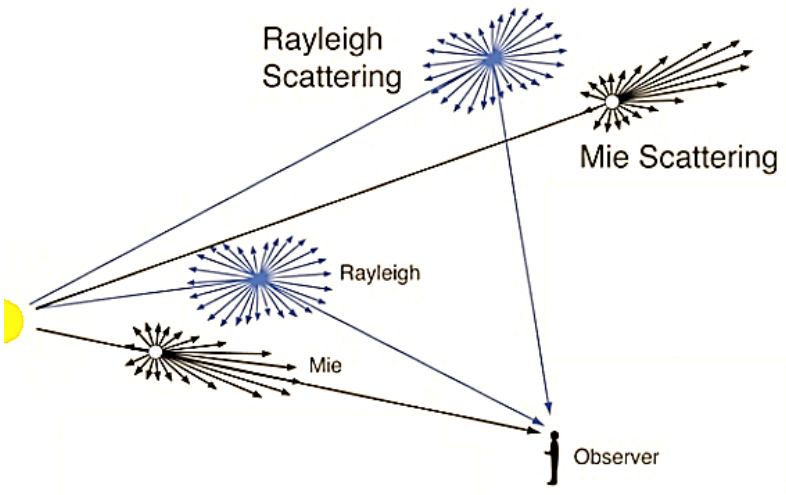

Figure 2.10 Visible scattering of solar radiation by atmospheric particles. Image is taken from: http://hyperphysics.phy-astr.gsu.edu

2.7.1. Inelastic collisions: Raman scattering

Raman scattering is an inelastic scattering process involving an energy exchange between the incident photon and the particle. Thus, the wavelength of the scattered photon will be higher or lower than the wavelength of the incident one (see Figure 2.11). This phenomenon is wavelength dependent and only occurs if the diameter of the particle is significantly larger than the wavelength of the incident photon. It is commonly used in infrared spectroscopy, but its effects are almost negligible in ultraviolet measurements.

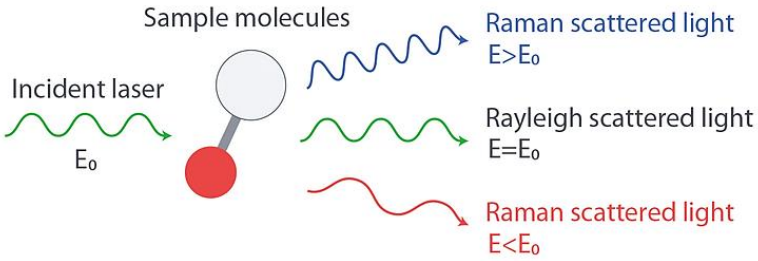

Figure 2.11 Displays the changes of energy of a photon during the Raman scattering process. (image taken from https://www.nanophoton.net/raman/raman-spectroscopy.html)

2.7.2. Elastic collisions: Rayleigh and Mie scattering

Rayleigh and Mie scatterings are elastic collisions without energy transfer between the photon and the particle. The mathematical analysis is simplified, assuming that the photon-scattering is independent of other particles instead of analysing it as the dispersion of electromagnetic waves due to a collection of particles (Mölders, 2014). The pattern of the scattered radiation depends on the ratio between the size of the particle and the wavelength of the incident light (X). Such a ratio is given by the Eq. (2.24), where the particle is considered a sphere of radius r.

$$X = \frac{particle\ circumference}{wavelength\ of\ incident\ radiation} = \frac{2\pi r}{\lambda} \tag{2.24}$$

Depending on the value of X, there are three atmospheric scattering patterns caused by elastic collisions in the solar spectral range (see Figure 2.12), which are described mathematically by:

- Rayleigh scattering for $X \leq 0.1$.
- Mie-theory scattering for $0.1 < X < 50$ (there is no clear upper limit).
- Geometric optics approximation for $X \geq 50$ (there is no clear limit).

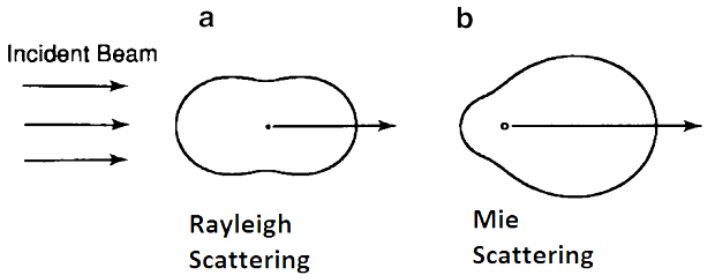

Figure 2.12 Schematic of scattered patterns from particles with different dimensions and the same incident beam (Mölders, 2014).

Figure 2.13 displays the different scattering regimes depending on the ratio between the wavelength of the incident solar radiation and the size of atmospheric compounds.

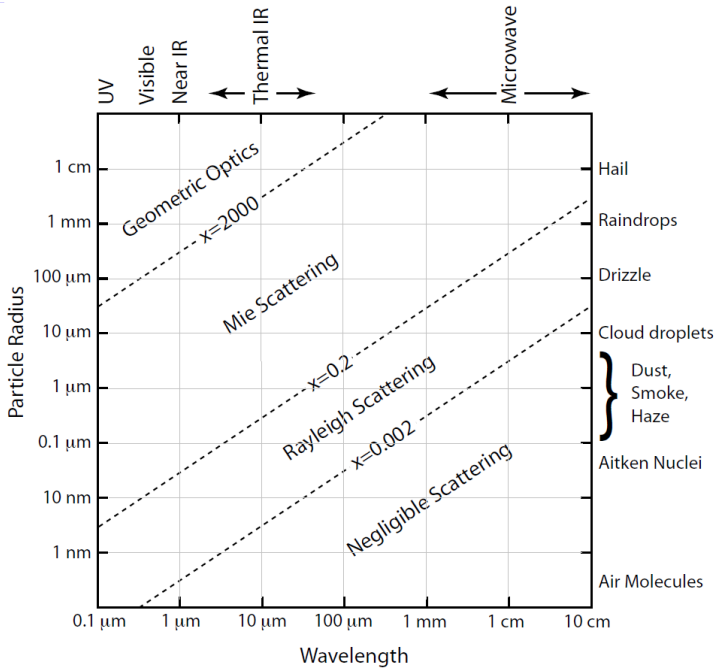

Figure 2.13 Scattering regimes of different atmospheric compounds (https://www.e-education.psu.edu/meteo300/node/785).

2.7.3. Rayleigh scattering

The interaction between light or any other electromagnetic radiation and molecules much smaller than the incident wavelength will produce elastic collisions without energy loss. The produced elastic scattering is called Rayleigh-scattering in honour of Lord Rayleigh. Most of this scattering occurs in the atmosphere when short wavelengths from solar radiation interact with air particles mainly concentrated in the troposphere, providing the visual perception of a blue sky under clear atmospheric conditions. Thus, most of the scattering occurs at the centre of mass of the atmosphere with a wavelength dependence of λ^{-4} around 5 km over sea level (Savastiouk and McElroy, 2005).

Equation (2.25) solves the Rayleigh scattering cross-section in square meters per air molecule (Bucholtz, 1995, Boucher, 2015, Tomasi et al., 1998). It indicates the effective molecular area that scatters a specific wavelength of unpolarised (natural) incident radiation. Note that the mathematical analysis considers stationary particles.

$$\alpha(\lambda) = \frac{24\pi^3(n^2+1)^2}{\lambda^4 N^2(n^2+2)^2}\left(\frac{6+3\rho_n}{6-7\rho_n}\right) \quad (2.25)$$

Where

$\alpha(\lambda)$ is the total Rayleigh scattering cross-section $(cm^2 molecule^{-1})$.
λ is the wavelength of the incident photon (in centimetres)
n is the refractive index of the particle at λ.
N is the molecular number density of air (~2.547x10^{19} molecules per cm^3).
ρ_n is depolarization factor (the dispersion of light due to air molecules is not uniform).
$\left(\frac{6+3\rho_n}{6-7\rho_n}\right)$ is considered the King correction factor for the anisotropy of air molecules.

Although the value of the refractive index n is commonly considered as 1.003, Eq. (2.26) estimates a more accurate value of n as a function of wavelength for standard air at standard air pressure P=101.325 kPa and standard air temperature 288.15 K (Bucholtz, 1995). Note that λ is measured in micrometres within the range of 230 nm to 1.69 μm.

$$(n-1)\times 10^8 = \frac{5791817}{238.0185-\lambda^{-2}} + \frac{167909}{57.362-\lambda^{-2}} \quad (2.26)$$

The molecular number density N ($\cong 2.547\times 10^{19}\ molecules\ cm^{-3}$) is calculated from Avogadro's number ($6.02214076\times 10^{23} molecules\ mol^{-1}$) (Analytical Methods Committee, 2019) and the molar volume of an ideal gas at standard temperature and pressure ($22.413962\ L\ mol^{-1}$ at 273.15 K and 101.325 kPa) (NIST, 1994), and then scaled to 288.15 K.

$$N(molecules\ cm^{-3}) = \frac{6.02214076\times 10^{23} molecules\ mol^{-1}}{22.413962\ L\ mol^{-1}}\left(\frac{373.15K}{288.15K}\right)\times\frac{1\ L}{1000 cm^3} \quad (2.27)$$

The polarization factor ρ_n accounts for the anisotropic scattering caused by fluctuations in the molecular orientation of air particles, which are considered small ellipsoids instead of perfect spheres. The polarization factor is influenced by the gas mixture and not by temperature and pressure. At the same time, the molecular number density and the refractive index depend on temperature and pressure and not on the gas mixture. Table 2.1 lists the values of ρ_n as a function of wavelength within the range of the brewer spectrometer from 280 to 370 nm (Bucholtz, 1995).

Table 2.1 King correction factor F_k, depolarization factor ρ_n and γ values for wavelengths within the range of the Brewer spectrometer from 280 nm to 370 nm for standard dry air. It is taken from (Bucholtz, 1995).

Wavelength (nm)	$\boldsymbol{F_k}$	$\boldsymbol{\rho_n}$	$\boldsymbol{\gamma}$
280	1.057	3.289×10^{-2}	1.672×10^{-2}
290	1.056	3.233×10^{-2}	1.643×10^{-2}

300	1.055	3.178×10^{-2}	1.614×10^{-2}
310	1.055	3.178×10^{-2}	1.614×10^{-2}
320	1.054	3.122×10^{-2}	1.586×10^{-2}
330	1.053	3.066×10^{-2}	1.557×10^{-2}
340	1.053	3.066×10^{-2}	1.557×10^{-2}
350	1.052	3.010×10^{-2}	1.528×10^{-2}
360	1.052	3.010×10^{-2}	1.528×10^{-2}
370	1.052	3.010×10^{-2}	1.528×10^{-2}

The King correction factor F_k for the anisotropy of air molecules is defined by Eq. (2.28). Table 2.1 provides some F_k values for standard dry air for wavelengths within the Brewer spectrometer spectrum.

$$F_k = \left(\frac{6 + 3\rho_n}{6 - 7\rho_n}\right) \tag{2.28}$$

There are several calculations to estimate the Rayleigh cross-section (Nicolet, 1984, Fröhlich and Shaw, 1980, Penndorf, 1957, Bucholtz, 1995, Tomasi et al., 2005, Bodhaine et al., 1999). However, Eq. (2.29) use the least-squares fit of the Rayleigh cross-section given by Bucholtz (1995), Eq. (2.29), to estimate the Rayleigh cross-sections (Savastiouk and McElroy, 2005).

$$\sigma(\lambda) = A\lambda^{-\left(B + C\lambda + \frac{D}{\lambda}\right)} \tag{2.29}$$

Where λ is the wavelength in micrometres (μm), $A = 3.01577 \times 10^{-28}$, $B = 3.55212$, $C = 1.35579$, and $D = 0.11563$ for the wavelength range from 0.2 to 0.5 μm for standard air at 101.325 k Pa and 288.15 K. Note that the coefficients were selected for wavelengths below 500 nm under cloudless atmospheric conditions.

Substituting the coefficients A, B, C and D into Eq. (2.29):

$$\sigma(\lambda) = 3.01577 \times 10^{-28} \times \lambda^{-\left(3.55212 + 1.35579\lambda + \frac{0.11563}{\lambda}\right)} \tag{2.30}$$

The total Rayleigh volume-scattering coefficient $\beta_s(\lambda)$ is estimated by substituting Eq. (2.30) and the molecular number density for standard air 1013.25 mBars and 288.15 K into Eq. (2.5). Additionally, Eq. (2.31) is multiplied by the factor $10^5\, cm/km$ to get kilometre units for future processing. Note that Bucholtz (1995) specifies the molecular number density as 2.54743×10^{19} $molecules\ cm^{-3}$.

$$\beta_s(\lambda) = N_s(3.01577 \times 10^{-28}) \cdot \lambda^{-\left(3.55212 + 1.35579\lambda + \frac{0.11563}{\lambda}\right)} \cdot \left(10^5 \frac{cm}{km}\right) \tag{2.31}$$

Thus, the simplified equation of the total Rayleigh extinction coefficient for wavelengths within the range of 200 nm to 500 nm is:

$$\beta_s(\lambda) = 7.68246\text{x}10^{-4}\lambda^{-\left(3.55212+1.35579\lambda+\frac{0.11563}{\lambda}\right)} \quad (2.32)$$

In order to obtain the Rayleigh optical depth τ at altitude z_0, Eq. (2.33) integrates the total Rayleigh extinction coefficient (also called Rayleigh volume scattering coefficient) from z_0 to the top of the atmosphere with air pressure and air temperature varying as a function of altitude z.

$$\tau(\lambda,z_0) = \int_{z_0}^{\infty} \beta(\lambda,z)\frac{P(z)}{P_s}\frac{T_s}{T(z)}dz \quad (2.33)$$

T_s and P_s represent the reference temperature and pressure for standard air at 288.15 K and 1013.25 mBars.

Boucher (2015) provides a simple approximation of the Rayleigh optical depth for the whole atmosphere in Eq. (2.34). Note that the wavelength is given in micrometres.

$$\tau(\lambda) \cong 0.01\lambda^{-4} \quad (2.34)$$

Bucholtz (1995) estimated the Rayleigh optical depth for atmospheric temperature and pressure profiles from the 1962 U.S Standard Atmosphere, see Eq. (2.35), by integrating Eq. (2.33) from 0 to 100 km of altitudes with 1 km increments using the trapezoidal rule. Then, a least-squares fitting is applied to obtain an expression of the form of Eq. (2.29). The values of the B, C, and D coefficients remain the same, and A varies depending on the selected atmospheric model (see Table 1.1).

$$\tau(\lambda) = A \cdot \lambda^{-\left(3.55212+1.35579\lambda+\frac{0.11563}{\lambda}\right)} \quad (2.35)$$

Table 2.2 'A' coefficient values are used in Eq. (2.35) to determine the Rayleigh Optical Depth at 0 km altitude with different atmospheric models (Bucholtz, 1995).

Model	**A coefficient**		$\mathbf{P(z_0 = 0)}$ **(mbars)**	$\mathbf{T(z_0 = 0)}$ **(K)**
	200 nm – 500 nm	**λ>500 nm**		
Tropical	6.52965×10^{-3}	8.68094×10^{-3}	1013	300
Mid-latitude Summer	6.51949×10^{-3}	8.66735×10^{-3}	1013	294
Mid-latitude Winter	6.53602×10^{-3}	8.68941×10^{-3}	1018	272.2
Subarctic Summer	6.48153×10^{-3}	8.61695×10^{-3}	1010	287
Subarctic Winter	6.49997×10^{-3}	8.64145×10^{-3}	1013	257.1
1962 U.S. Standard	6.50362×10^{-3}	8.64627×10^{-3}	1013	288.1

The Rayleigh optical depth approximation is expressed in Eq. (2.36) (Savastiouk and McElroy, 2005):

$$\tau(\lambda) = 0.008659 \cdot \lambda^{-\left(3.6772+0.389\lambda+\frac{0.09426}{\lambda}\right)} \quad (2.36)$$

Finally, Eq. (2.36) needs to be corrected by the atmospheric pressure at the site where the spectrometer is located (P) because τ escalates with the molecular number density N (Kipp & Zonen, 2014, Bucholtz, 1995).

$$\tau(\lambda) = \frac{P}{P_s} 0.008659 \cdot \lambda^{-\left(3.6772+0.389\lambda+\frac{0.09426}{\lambda}\right)} \quad (2.37)$$

Where λ is in micrometres, P_s is the standard air pressure of 1013.25 mbars used to calculate N.

Table 2.3 displays the Rayleigh optical depth values from Bucholtz (1995) for the five Brewer wavelengths (306.3 nm, 310.1 nm, 313.5 nm316.8 nm and 320.1 nm) valid for sea level with 1013.25 mbar pressure. Values obtained from Eq. (2.37).

Table 2.3 Rayleigh optical depth values obtained by Bucholtz (1995) from Eq. (2.37).

Rayleigh optical depth at				
306.3 nm	**310.1 nm**	**313.5 nm**	**316.8 nm**	**320.1 nm**
1.11267	1.05493	1.00648	0.962136	0.920262

2.7.4. Mie scattering

It is a phenomenon produced by the elastic collision of photons and particles, where the diameter of the particle is similar to the wavelength of the incident electromagnetic radiation. A larger forward lobe characterizes its scattering pattern (Figure 2.12). Mie theory is a complete analytical solution to Maxwell's equation to express the electromagnetic scattering due to spherical particles. These approximations can be calculated by an infinite series of mathematical expressions as long as the particle is considered a homogeneous and isotropic sphere (Wriedt, 2012). Water droplets in clouds, for example, produce multiple scattering within this category. They uniformly scatter a range of wavelengths in the visible spectrum, making clouds with neutral colouration from white to dark grey when the sun is not below the horizon. However, the complexity of Mie-scattering approximations resides in considering the particles as non-spherical to represent better atmospheric aerosols such as pollen, ash, dust, or ice particles.

Geometric optics approximation is part of the Mie theory used to analyse radiation scattering by larger particles (Yu et al., 2009, Liou and Hansen, 1971). The accuracy of this approximation increases as the size of the particle approaches infinity.

It is essential to mention that Mie scattering does not play an important role for most spectrometers performing ozone retrieving measurements when performing direct solar measurements during clear sky conditions.

2.8. Beer-Lambert Law for total ozone column

Savastiouk and McElroy (2005) use Eq. (2.38) to estimate the total column of ozone based on Eq. (2.23).

$$In[I(\lambda)] = In[I_0(\lambda)] - \mu X^{O_3}\alpha(\lambda) - \mu' X^{SO2}\gamma(\lambda) - m_R\beta(\lambda) - m_a C\lambda^{-1} \quad (2.38)$$

Where:

$I_0(\lambda)$ =Total irradiance measured at the outer atmosphere.
$\mu =$ Relative optical air mass corresponding to O_3absorption (stratospheric airmass factor).
X^{O_3}= Total column of ozone.
$\alpha(\lambda) =$ Ozone extinction coefficient.
$\mu' =$ Relative optical air mass corresponding to SO_2 absorption (stratospheric air-mass factor).
$X^{SO_2} =$ Total column of sulfur dioxide (SO_2).
$\gamma(\lambda) = SO_2$ extinction coefficient
$m_R =$ Relative optical air mass corresponding to Rayleigh scattering
$\beta(\lambda) =$ Rayleigh scattering extinction coefficient at 1013.25 hPa.
$m_a =$ Tropospheric air mass factor.
$C\lambda^{-1}$= Aerosol extinction coefficient.

One method to obtain the extraterrestrial constant for every wavelength is the Langley plot technique, which assumes a stable atmosphere at the time of the measurements. This method is usually performed at high altitudes, where the effect of slight variations in the aerosol optical depth (AOD) can be ignored by the zero-airmass extrapolation technique. Since the Rayleigh scattering can be considered as a linear function of the airmass when ozone values remain constant, this method consists of linearly regressing Eq. (2.38) vs airmass values and then extrapolate the values when the airmass is zero. This calibration is generally performed over several days to reduce the effects of daytime ozone variability. The second method to obtain ETC values is often called the calibration transfer method. It uses the total ozone column measurements from the calibrated spectrometer during clear sky conditions to remove the effect of AOD. Then, the side-to-side comparisons over one or two days provide a large range of airmass values to perform the extrapolation technique (Gröbner et al., 2017).

Then, the constant S will replace the sum of the known constant values of Eq. (2.38).

$$S = In[I_0(\lambda)] - In[I(\lambda)] - m_R\beta(\lambda) \quad (2.39)$$

Substituting Eq. (2.39) into Eq. (2.38) and measuring at five different wavelengths

$$\mu X^{O_3}\begin{bmatrix}\alpha_1\\ \alpha_2\\ \alpha_3\\ \alpha_4\\ \alpha_5\end{bmatrix}+\mu' X^{SO2}\begin{bmatrix}\gamma_1\\ \gamma_2\\ \gamma_3\\ \gamma_4\\ \gamma_5\end{bmatrix}+m_a C\begin{bmatrix}{\lambda_1}^{-1}\\ {\lambda_2}^{-1}\\ {\lambda_3}^{-1}\\ {\lambda_4}^{-1}\\ {\lambda_5}^{-1}\end{bmatrix}=\begin{bmatrix}S_1\\ S_2\\ S_3\\ S_4\\ S_5\end{bmatrix} \tag{2.40}$$

Equation (2.40) is then multiplied by the row vector $[k_1^{O3} \quad k_2^{O3} \quad k_3^{O3} \quad k_4^{O3} \quad k_5^{O3}]$

$$\mu X^{O_3}\sum_{i=1}^{5}k_i^{O3}\alpha_i+\mu' X^{SO2}\sum_{i=1}^{5}k_i^{O3}\gamma_i+m_a C\sum_{i=1}^{5}k_i^{O3}{\lambda_i}^{-1}=\sum_{i=1}^{5}k_i^{O3}S_i \tag{2.41}$$

$$\mu X^{O_3}\begin{bmatrix}\alpha_1\\ \alpha_2\\ \alpha_3\\ \alpha_4\\ \alpha_5\end{bmatrix}+\mu' X^{SO2}\begin{bmatrix}\gamma_1\\ \gamma_2\\ \gamma_3\\ \gamma_4\\ \gamma_5\end{bmatrix}+m_a C\begin{bmatrix}{\lambda_1}^{-1}\\ {\lambda_2}^{-1}\\ {\lambda_3}^{-1}\\ {\lambda_4}^{-1}\\ {\lambda_5}^{-1}\end{bmatrix}=\begin{bmatrix}S_1\\ S_2\\ S_3\\ S_4\\ S_5\end{bmatrix} \tag{2.42}$$

Where k_i are the weighting coefficients that help in the linear fitting process of the DOAS technique, as long as the next conditions are valid:

$$\begin{cases}\sum_{i=1}^{5}k_i^{O3}\gamma_i=0\\ \sum_{i=1}^{5}k_i^{O3}{\lambda_i}^{-1}=0\\ \sum_{i=1}^{5}k_i^{O3}=0\end{cases} \tag{2.43}$$

Substituting Eq. (2.43) into Eq. (2.41) and solving for X^{O_3}

$$\boldsymbol{X^{O_3}=\frac{\sum_{i=1}^{5}k_i^{O3}S_i}{\mu\sum_{i=1}^{5}k_i^{O3}\alpha_i}} \tag{2.44}$$

Equation (2.44) is used to estimate the total amount of stratospheric ozone once Brewer spectrometers measured solar irradiance at 306.3 nm, 310.1 nm, 313.5 nm, 316.8 nm and 320.1 nm. Although the weight coefficients are generally fixed values: $k_1^{O3}=0$ (to discard SO_2 influence at 306.3 nm), $k_2^{O3}=1$, $k_3^{O3}=-0.5$, $k_4^{O3}=-2.2$ and k_5^{O3}=1.7, each spectrometer may customized such parameters (Savastiouk and McElroy, 2005). After estimating X^{O_3}, new weight coefficients are used to solve for X^{SO2}. Finally, the amount of aerosol in the atmosphere (C) is computed by substituting X^{O_3} and X^{SO2} into Eq. (2.38).

This generalised theory can be applied to spectral data gathered by any instrument. The Brewer was carefully designed in the 1970s to provide the best measurement inputs to this

theoretical analysis whilst operating autonomously in a wide range of climatic conditions. Modifications to the Brewer, e.g. the advent of the double monochromator model, have kept it at the forefront of ground-based TOC measurement devices. However, in the intervening 50 years, many technological advances have the potential to provide alternative methods of delivering measurement inputs to the theory, and hence alternatives to the Brewer.

Chapter 3. Acousto-optic tunable filter (AOTF)

The principal components of any spectroradiometer are the input optics, an element to disperse the different wavelengths of radiation, and a detector for the discrete wavelengths. The technology to replace the diffraction grating is the acousto-optic tunable filter (AOTF), which is being applied in a ground-based spectrometer to measure the stratospheric column of ozone. Notice that there is no available literature on other ground-based spectrometers based on the AOTF to measure the total ozone column, apart from vague comments about a Russian prototype senior researchers at Kipp and Zonen. This chapter briefly describes the standard components of an ozone spectrometer and then provides a detailed account of the AOTF (see Figure 3.1).

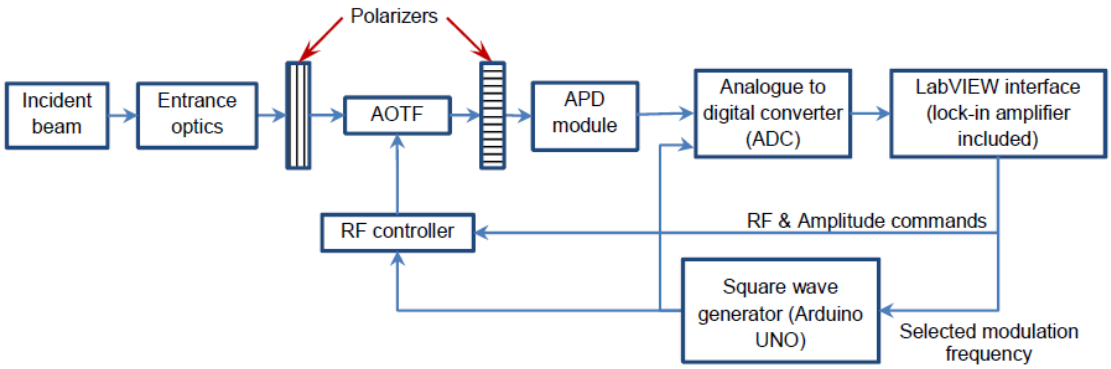

Figure 3.1 Block diagram of the spectrometer used in this work.

3.1. Differences between the proposed spectrometer and current spectrometers

3.1.1. Prisms and diffraction Gratings

The monochromator is considered the core of any spectrophotometer. It disperses the incident beam and focuses light at the desired wavelength into the detector. Prisms and diffraction gratings are the traditional diffractive elements in traditional spectrometry (see Figure 3.2). Most monochromators possess the same internal structure: entrance and exit slits, a prism or diffraction grating, fore-optics and focusing lenses.

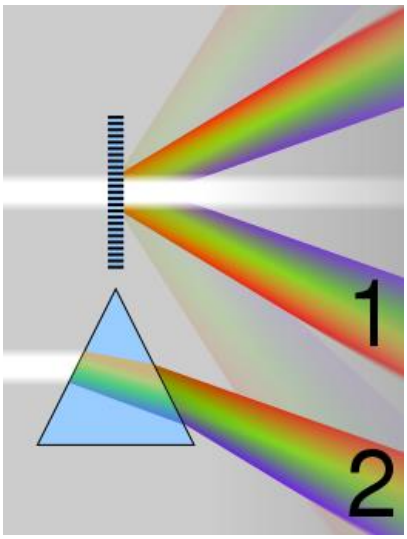

Figure 3.3 Visual representation of a prism and a diffraction grating dispersing a beam of light.

Figure 3.4 illustrates a single monochromator inside the Brewer spectrometer.

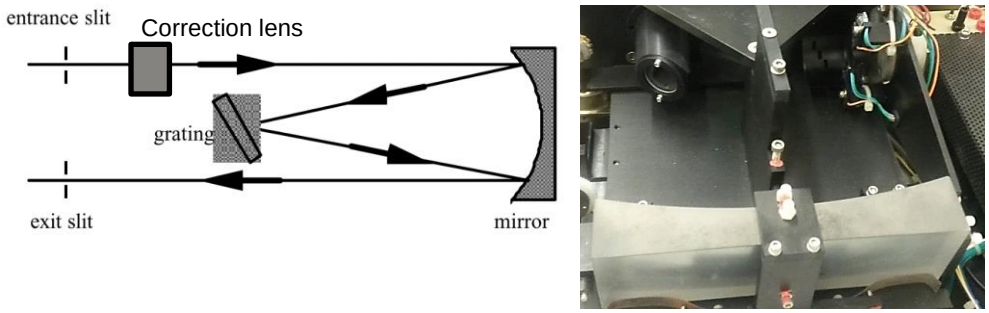

Figure 3.4 Brewer monochromator diagram compared with its exposed parts (taken by the INTA, Spain during intercomparison 2015).

3.1.2. Photodiode arrays and Photomultiplier Tubes (PMTs)

Photomultiplier tube (PMT)

The photomultiplier tubes (PMT) are sensitive photodetectors that produce an electrical current proportional to the intensity of the incident beam. Its high accuracy in transforming photons into a proportional number of electrons is the main reason why specialized spectrophotometers such as the Dobson and the Brewer use them as its detector. Figure 3.5 display the internal diagram of a typical PMT.

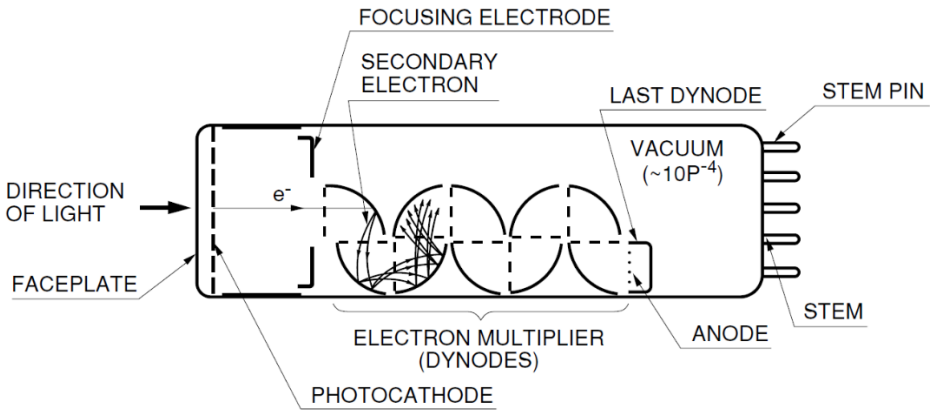

Figure 3.5 Schematic of a typical photomultiplier tube (Hamamatsu Photonics, 2006).

Photodiode Arrays (PDA)

The PDA is a photodetector made from semiconductor materials capable of simultaneously measuring a wide spectral range of wavelengths from a broadband source. They are commonly used in spectrometry due to their versatility in measuring a broad spectrum at once (see Figure 3.6).

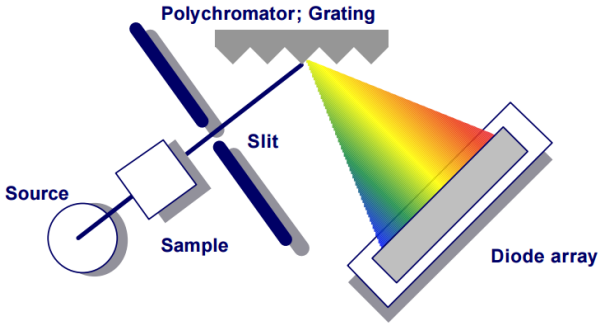

Figure 3.7 Diagram of a photodiode array working in conjunction with a diffraction grating.

PDA detectors use unidimensional arrays (a row) or bidimensional arrays (a 2D matrix) of individual photodiodes, where each photodiode is considered a pixel. However, it is important to mention that pixels in solid state detectors are not individually adjusted to detect specific wavelengths. For this reason, the integration time of the whole detector must be regulated in order to avoid the saturation of any pixel. Otherwise, it may saturate or modify the value of neighbouring pixels.

The detector used in this prototype instrument is a solid-state photodiode (high quantum efficiency, high gain, high sensitivity, fast response, reduced size, breakdown voltages up to 200V, and cheaper than a PMT and a diode array). For further details, see Chapter 4.

3.2. Acousto-optic tunable filter (AOTF)

The acousto optical tunable filter (AOTF) is considered a new-generation monochromator due to its solid-state technology, compact design, and ability to electronically tune and filter a narrow spectral range at high speed. This technology is widely used in various applications, mainly in visible and near-infrared spectra, such as spectral imaging, laser spectroscopy, fibre communications, quality control monitoring, remote sensing, and satellite measurements (see Table 3.1).

Table 3.1 AOTF Devices operated in space (Korablev et al., 2018)

Year	**Spacecraft**	**Instrument name,** **Target**	**Filter material,** **Spectral range**	**Principle, Observation**	**Mass**
1987	Ocean, USSR	Trasser-NHM Oceans, surface	Quartz 0.42–0.78 μm	Pencil beam, nadir	30kg
1999	Ocean, Russia	Trasser-O Oceans, surface	Quartz 0.42–0.78 μm	Pencil beam; nadir	30kg
2003 - Present	Mars Express, ESA	SPICAM-IR Mars atmosphere	TeO_2 0.9–1.65 μm	Pencil beam; nadir, limb, solar occultation	*0.8kg
2005 - 2014	Venus Express, ESA	SPICAV-IR Venus atmosphere	TeO_2 0.65–1.6 μm	Pencil beam; nadir, limb, solar occultation	*0.8kg
2005 – 2014	Venus Express, ESA	SOIR Venus atmosphere	TeO_2 2.2–4.4 μm	Order sorting in echelle-spectrometer, solar occultation	*6.5kg
2009 - 2012	ISS, Russian segment	RUSALKA greenhouse gases	TeO_2 0.7–1.7 μm	Order sorting in echelle-spectrometer; nadir	3.3kg
2013	Chang'e-3 Yutu, CNSA	VNIS-VNIR VNIR-SWIR Moon mineralogy	Quartz 0.45–0.95 μm TeO_2 0.9–2.4 μm	Imaging Pencil beam both in reflection	*4.7kg
2014 - present	Hayabusa-2 MASCOT, JAXA, DLR/CNES M	MicrOmega Mineralogy of asteroid Ryugu	TeO_2 0.9–3.55 μm	Monochromatic illumination of a sample	*1.8kg
2016 - present	ExoMars TGO, ESA/ Roscosmos	ACS-NIRNOMAD-LNO NOMAD-SO Mars atmosphere	TeO_2 0.7–1.65 μm 2.3-3.8 μm 2.2-4.2 μm	Nadir, limb, solar occultation, Order sorting in echelle-spectrometer	*3.2kg 9.4kg 13.5kg

*Mass of a channel (the main electronics not included) NOTE: Hayabusa-2 was in cruise flight, and no space operations of MicrOmega instrument were performed until July 2018. ExoMars TGO started test observations with AOTF instruments when it reached Mars orbit in 2016.

The acousto optical tunable filter is based on the diffraction of a birefringent crystal. The crystal modifies the refraction index of a very narrow wavelength range (fraction of a nanometre)

depending on the frequency of the applied acoustic wave. As a result, it is possible to achieve a fast wavelength tuning, which is only limited by the acoustic wave's transit time across the crystal, plus any control/communication time.

The presented spectrometer is based on the AOTF technology as a diffraction component, using quartz as its birefringence crystal due to its higher transmittance in the ultraviolet spectrum.

3.2.1. Birefringence

The optical, thermal, electrical and mechanical properties of a crystal are intrinsically related to its chemical composition, molecular structure, and chemical bonds. For example, isotropic crystals possess cubic structures with identical mechanical and physical properties in all directions, independent of the orientation along the crystal's molecular axis. On the other hand, anisotropic crystals are direction-dependent mediums with unsymmetrical structures. Therefore, the measurement of its mechanical and physical properties varies if there are changes in the crystal's orientation or external forces are applied to the crystal, such as periodic constraints due to acoustic waves.

Birefringence is an optical property of all anisotropic crystals, such as quartz, sapphire, and calcite, dividing an incident beam into two rays. These crystals can be categorized depending on the material's structural symmetry for having one or two optical axes, also called uniaxial and biaxial, respectively. Uniaxial crystals possess two diffraction indexes that split the unpolarised incident beam into two orthogonal wavefronts, an ordinary and an extraordinary one.

Figure 3.8 shows a double image viewed through a birefringent crystal when it is illuminated with unpolarised light. This phenomenon is also called double refraction. Because of the difference in refractive indexes, one ray will travel slowly through the birefringent crystal compared with the other.

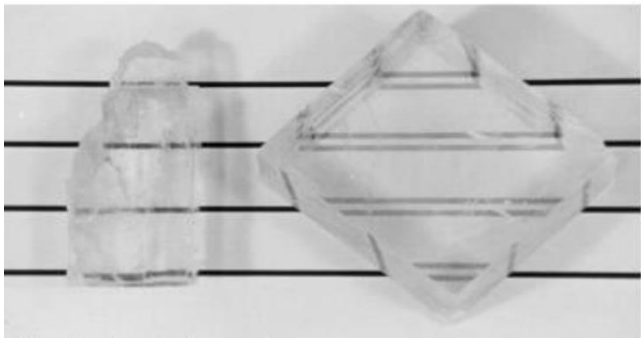

Figure 3.8 Comparison between an isotropic and an anisotropic crystal (calcite), left and right side, respectively. The image is taken from https://www.slideserve.com/vernados/birefringence

The two resulting waves have orthogonal polarization states and two indices of refraction (see Figure 3.9). The polarization of the ordinary beam is perpendicular to the optical axis, while the polarization of the extraordinary ray is parallel to the optical plane of the crystal. The ordinary

refraction index n_o follows the normal refraction (Snell's law) regarding the direction of the input beam. At the same time, the extraordinary ray is dependent on the path and polarization of the incident beam, except when the direction of the incident beam is parallel to the crystal optical axis. In this case, the birefringent crystal behaves like an isotropic material with no double refraction for any direction of the polarization (see right representation in Figure 3.9).

When the incident ray is orthogonal to the optical axis, the trajectories of the ordinary and extraordinary beams are collinear but shifted in phase to one another (circular polarization) due to the dual refraction indexes for ordinary and extraordinary rays (n_o and n_e). Figure 3.9 (c) illustrates this phenomenon.

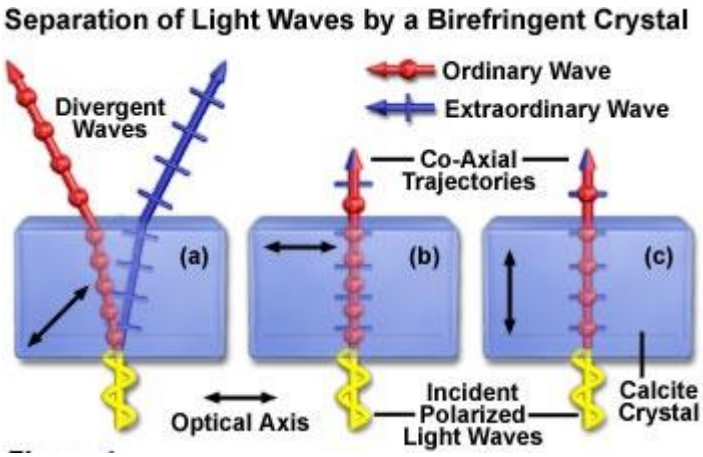

Figure 3.9 Response of a birefringent crystal to three different angles between the input beam and the optical axis: (a) arbitrary, (b) perpendicular, and (c) parallel. The image is taken from https://www.olympus-lifescience.com/ja/microscope-resource/primer/java/polarizedlight/crystalwavefronts/.

When n there is an arbitrary angle between the incident beam and the optical axis, two orthogonal wavefronts with different directions are generated. The first one is caused by the ordinary refraction index n_o, but the second one is not caused entirely by the extraordinary refraction index n_e. Instead, it is a combination of n_o and n_e, it is estimated by Eq. (3.1).

$$n = \frac{1}{\sqrt{\frac{\cos^2\theta}{{n_o}^2} + \frac{\sin^2\theta}{{n_e}^2}}} \tag{3.1}$$

Where θ is the angle between the optical axis and the propagation direction of the incident beam.

It's worth mentioning that birefringence can be induced artificially in isotropic crystals when external forces break their molecular symmetry, with temporary or permanent effects. Such forces could be a strong electric field or mechanical stress caused by bending or compressing.

3.2.2. Quartz as a birefringent crystal

Quartz (SiO_2) is the most common form of silica on Earth. It is transparent, clear, and colourless in pure form. AOTF commonly uses crystalline quartz as birefringent material in UV applications due to its spectral transmittance (see Figure 3.10). However, other materials could be used as a birefringent crystal to work also in the UV spectrum, such as sapphire (Al_2O_3), ammonium dihydro-phosphate (APD), potassium dihydro-phosphate (KPD) or magnesium fluoride (MgF_2) (Gupta and Voloshinov, 2004).

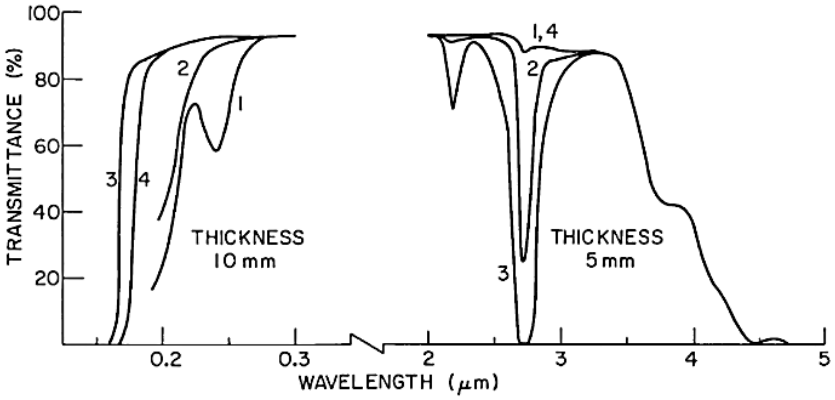

Figure 3.10 Approximate transmittance of four quartz crystals classified by their methods of manufacture. #1 is fused quartz (direct fusion of quartz crystal). #2 is the Heracus process (flame fusing of powdered quartz crystal). #3 is synthetic (vapour-phase hydrolysis of an organosilicon compound). #4 is water-free synthetic. (Elson et al., 1979)

This prototype used quartz as the birefringent crystal because of its commercial availability and spectral transparency range (see Table 3.2). Figure 3.11 compares the refractive indexes of quartz from 400 nm to 1.6 μm.

Table 3.2 Properties of some crystals used in AOTFs.

CRYSTAL	TRANSPARENCY RANGE	AOTF type
α – Quartz	120 nm – 4500 nm	Collinear Non-collinear
$CaMoO_4$ (Calcium molybdate)	400 nm – 4500 nm	Collinear
$LiNbO_3$ (Lithium niobate)	400 nm – 4500 nm	Collinear
TeO_2 (Tellurium dioxide)	350 nm – 4500 nm	Non-collinear
Tl_3AsSe_3	1250 nm – 17000 nm	Collinear Non-collinear
Hg_2Cl_2 (Mercury chloride)	400 nm – 20000 nm	Non-collinear

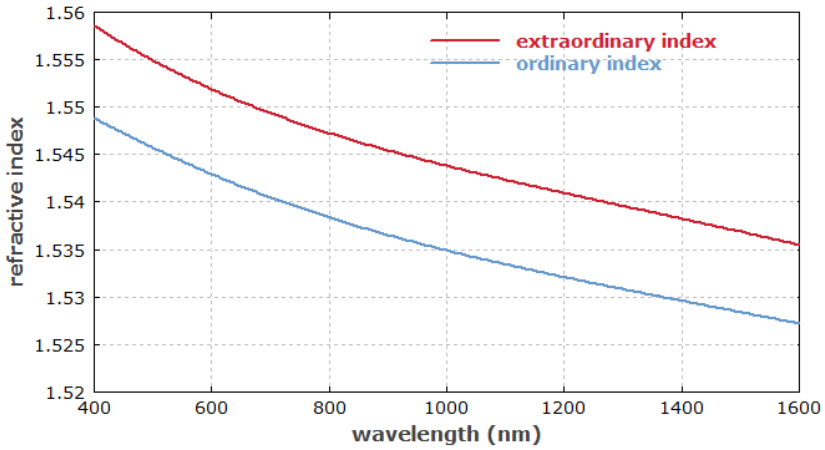

Figure 3.11 Refractive indexes of the ordinary and extraordinary in a quartz crystal along different wavelengths. The image is taken from https://www.rp-photonics.com/birefringence.html

3.2.3. Acousto-optic effect

The acousto-optic effect is the phenomenon that occurs when the propagation of an acoustic wave through crystalline materials modifies the behaviour of light in a crystalline medium. As a result, light diffraction is produced by a periodic modulation of the refractive index caused by the material's temporary deformation. The only requirement is that the length of the crystal must be large enough to allow the generation of wavefronts at a specific frequency.

Depending on the angle of the incident beam, the AOTF can operate on the Braggs or the Raman-Nath regime (see Figure 3.12). When the AOTF is working in the Raman-Nath regime, different orders are diffracted (positives above zero-order and negatives below zero-order). On the other hand, the Bragg regime has a higher diffraction efficiency for the 1st diffraction order and nearly zero scattering into higher orders. For this reason, quasi-collinear configurations are based on the Raman-Nath regime, while the non-collinear configuration is based on Bragg diffraction. Note that for both cases, the optical path of the ordinary ray (also known as zero-order) is not altered by changes in the acoustic wave.

Equation (3.2) describes the critical angle for Bragg diffraction.

$$\theta_i = \frac{\lambda f}{2v} \tag{3.2}$$

Where:

λ= Wavelength of the diffracted beam.
f= Frequency of the acoustic wave in the crystal.
v= Speed of the acoustic wave in the crystal.

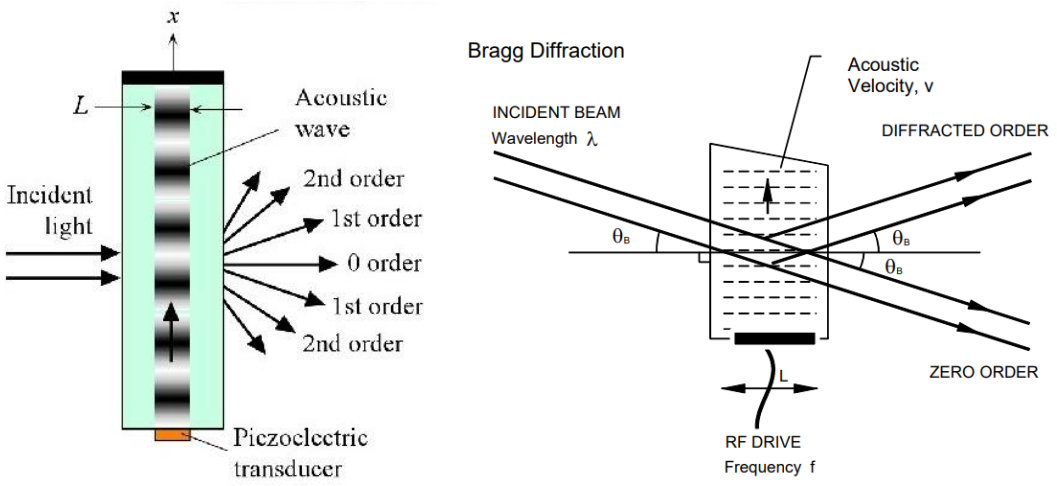

Figure 3.12 Comparison between Raman-Nath (left-diagram) and Bragg regime (right-diagram). Images are taken from https://isomet.com/App-Manual_pdf/AOTF-Notes.pdf and https://slidetodoc.com/acoustooptic-modulators-left-acoustooptic-tunable-filters-right-acoustooptic/.

In the Bragg regime, the acoustic waves applied to a birefringent crystal generate a periodic modulation of the crystal's refractive index. Equation (3.3) describes the relationship between diffracted wavelength and applied RF frequency. Depending on the crystal used, the signal's frequency varies from a few tens of megahertz (MHz) up to some gigahertz (GHz). Therefore, the wavelength and amplitude of the diffracted beam can be electronically selected by varying the frequency and amplitude of the applied electric signal.

$$f(\lambda) = \frac{v\Delta n\sqrt{\sin^4(\theta_i) + \sin^2(2\theta_i)}}{\lambda} \tag{3.3}$$

Where: Δn is Crystal birefringence. It is the difference between the extraordinary and ordinary refractive indexes ($\Delta n = n_e - n_o$).

3.2.4. Collinear and Non-collinear configuration

The diffraction angle of the selected wavelength is more noticeable in soft birefringent crystals such as TeO2, with a higher transmission in the visible and near-infrared spectrum. To select the desired wavelength, an AOTF in a non-collinear set-up uses a physical blocker that only lets the first order of the diffracted beam passes through (see Figure 3.13). Finally, a sensor device is aligned with the output beam to measure the selected wavelength.

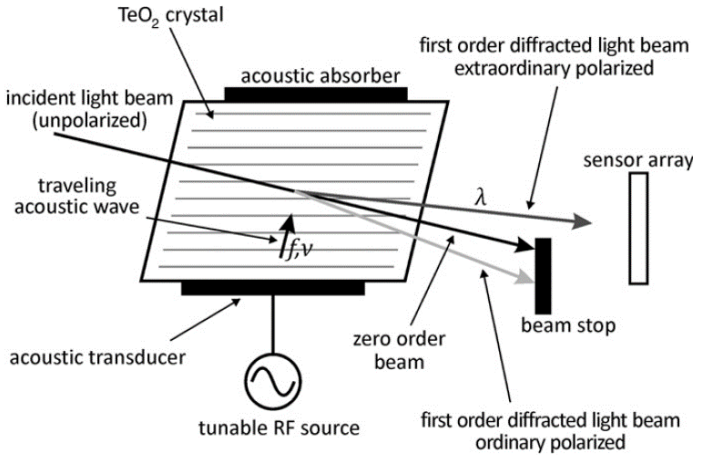

Figure 3.13 Non-collinear AOTF configuration with unpolarized incident light (Katrašnik et al., 2010).

On the other hand, the output beam in a quasi-collinear configuration (Raman-Nath regime) contains the ordinary and extraordinary ray in the same direction of propagation with an angle between the incident and exit beam almost equal to zero. Thus, the system filters the extraordinary component and rejects the zero-order component by placing orthogonal polarizers at each end of the AOTF (see Figure 3.14). The input polarizer is aligned with the optical axis of the birefringent crystal, and the AOTF will act as a circular polarizer only to the selected wavelength. Finally, the second polarizer will extinguish the zero-order beam (ordinary ray) and let through only the extraordinary ray. Thus, this configuration requires a fine rotational adjustment of the polarizers to achieve the maximum extinction coefficient and reduce background noise.

An AOTF in a quasi-collinear configuration is effective as long as the incident angle is lower than 7.5 degrees. On the contrary, the lower the incident angle, the higher the spectral resolution of the AOTF (Mantsevich and Yushkov, 2021). Because the average distance between the Earth and the Sun is approximately 150 million kilometres (1 Astronomical Unit, AU), the solar radiation that reaches the Earth is considered a quasi-collimated beam. Thus, the AOTF is perfect for applications with direct solar radiation as the input beam.

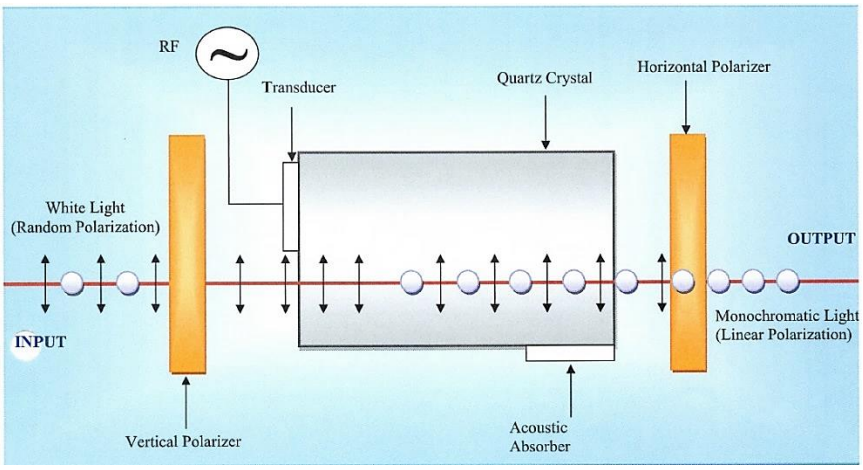

Figure 3.14 Collinear configuration of the AOTF suggested by the manufacturer.

The AOTF used in this work is based on a collinear configuration with a quartz crystal. The following chapter shows how this technology was incorporated into a UV spectrometer.

Chapter 4. The AOTF spectrometer

Most traditional spectrometers use diffraction gratings and prisms as dispersing elements, combined with different detector technologies such as photomultiplier tubes (PMT), photodiodes, avalanche photodiodes, and diode arrays. Thus, monochromatic spectral measurements require rotating the dispersing element, aligning the output beam with the detector or having aligned multiple detectors (diode arrays). This increases the cost and complexity of manufacturing them due to the precise alignment of their optical and mechanical parts. Therefore, having a solid-state monochromator that does not require mechanical parts to perform monochromatic measurements reduces production costs and maintenance.

Acoustic vibrations in Quartz cause variations in the extraordinary refractive index, allowing the crystal to act as a diffraction grating through the whole volume of the crystal. Nonetheless, the AOTF in a collinear configuration acts more like a filter than a diffraction grating. Since the acoustic wave speed (around 5570 m/s) is slow compared to the light speed in quartz (about 193×10^6 m/s at 400 nm), the acousto-optic effect is considered a stationary volume grating.

The output of an AOTF is a narrow spectral range centred at the desired diffracted wavelength and electronically tuned by manipulating an RF signal at the input of the AOTF. Allowing the development of small, fast, light, cheap, and portable devices less susceptible to vibrations and reduced temperature dependence. In comparison, Brewer spectrometers are designed to expand and contract internal elements simultaneously to reduce the temperature. For these reasons, AOTF technology is a suitable alternative to replace the dispersing element in monochromators.

Figure 4.1 and Figure 4.2 display the initial and final design of the AOTF spectrometer. The AOTF with an integrated water-cooling system had to be replaced due to water leakage in the middle of the research. The new AOTF model possesses the same optical properties, but the thermoelectric cooling system replaced the water-cooling system, allowing monitoring and remote temperature control.

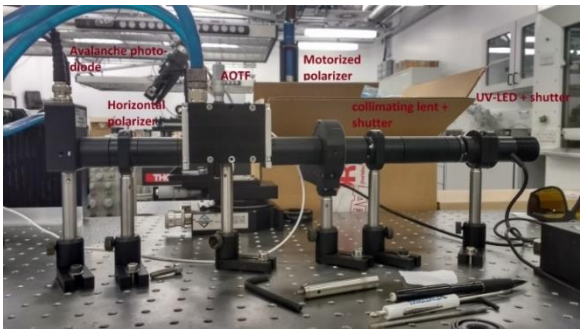

Figure 4.1 Initial design of the prototype using a water-cooling system for the AOTF.

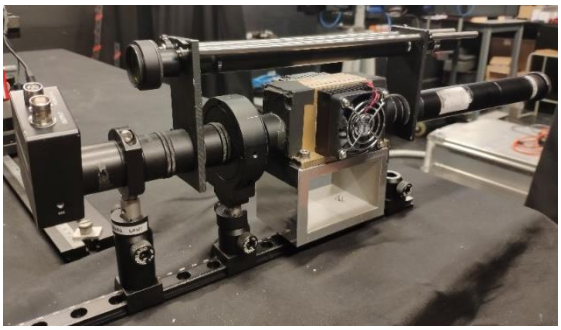

Figure 4.2 Final prototype using the replaced AOTF with thermoelectrical cooling.

4.1. Optical design

Most of the optical parts of the presented spectrometer were acquired from Thorlabs to have uniformity in sizes and threads. Most of the design is fitted in lens tubes of one inch in diameter coated in black to minimize stray light and maintain clean lenses free of grease, dust or fingerprints. Figure 4.3 shows a 3D model of the final spectrometer design.

Figure 4.3 The image displays a 3D model of the AOTF spectrometer.

The spectrometer was designed to be mounted directly into a solar tracker to point directly to the solar disc. However, manual manoeuvring was required to align the optics of the AOTF spectrometer to the solar disc. An additional tube with a neutral density filter was placed parallel to the spectrometer to visually align the centre of the solar disc with the spectrometer's field of view (see Figure 4.2). A set of black aluminium discs, with diameters of 7 mm and 5 mm and a width of 0.5 mm, were collocated along with the spectrometer’s optical path acting as an optical baffle. They limited the size of the input beam to 5 mm (optical aperture of AOTF) and fixed a field of view lower than 2 degrees (see Chapter 6).

4.1.1. Quartz crystal and transductor of AOTF

AOTF spectrometers can measure in different ranges of the spectrum depending on their birefringent crystal. The most common birefringent crystal used in AOTF is Tellurium Dioxide

(TeO_2) in a non-collinear configuration. However, it has high transmission losses in wavelengths shorter than 360 nm. For this reason, quartz is mainly used for UV applications.

This spectrometer uses quartz on a quasi-collinear configuration to operate in a wavelength range from 250 nm to 440 nm. Its transfer function (slit function) varies linearly from 0.25 nm to 0.4 nm. It also possesses a square aperture of 5x5 mm. Moreover, transmission efficiencies of quartz in the UV spectrum are around 98%, with maximum diffracting efficiencies at 406 nm between 15% and 20% (details from manufacturer).

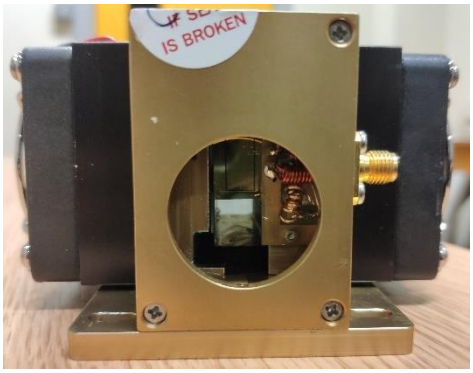

Figure 4.4 Display the 5 mm x 5 mm optical aperture of the AOTF.

Equation (4.1) determines the relationship between the RF signal and the selected diffracted wavelength.

$$\lambda = \Delta n \alpha \frac{V_\alpha}{f_\alpha} \tag{4.1}$$

Where Δn is the absolute difference between the ordinary and the extraordinary refracting index, f_α is the frequency of the acoustic wave (around 5570 m/s), V_α is the velocity of the acoustic wave through quartz, and α is a complex parameter which depends on the AOTF design.

The piezoelectric transducer attached to the crystal (Figure 4.5) generates acoustic waves from an applied electrical signal (RF) with a maximum power of 10 W. The waves will travel through the crystal until they reach the other end, where an absorber is placed to stop the return of such waves. The heat released by the continuous mechanical compression of the crystal increases its temperature, which has to be cooled down either by running water or by a thermo-electric (TE) cooling system. The operating temperature to avoid internal damage to the AOTF is 50° C with a preferable temperature of 25° C, especially at the points where the transducer and absorber are bonded to the crystal.

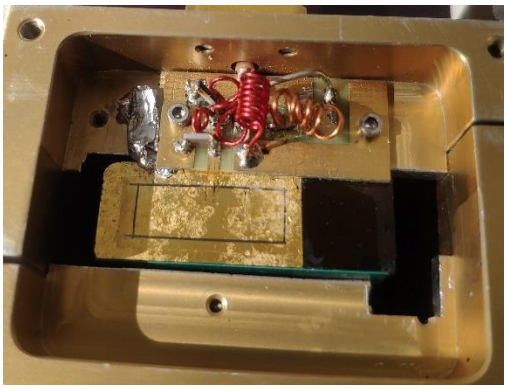

Figure 4.5 Piezoelectric transducer of the AOTF used in this project.

The output wavelength and the intensity of the output beam are controlled by varying the frequency (80 MHz to 165 MHz) and amplitude of the electrical signal applied to the previously described piezoelectric transducer. Therefore, the output beam can be modulated if the electrical signal is convoluted with a periodic signal in the range of kilo Hertz. This characteristic enabled improving the output measurement by using a lock-in amplifier to reduce background noise (see section 4.3).

4.1.2. Band-pass filter

In order to minimize the effect of incident radiation in the wavelengths ranging from 600 nm to 900 nm, it was placed a UV bandpass filter. Filters such as the UG5, UG11, UG11+KGB3, UVC7, and UG11-IBR, among others from Edmund optics, were tested. This section compares the spectral response of the most relevant filters.

In order to reduce undesired measurements of wavelengths from the infrared spectrum, possibly produced due to internal acoustic reflections in the AOTF crystal, a UV band-pass filter is placed as the first element of the input optics. Then, the first polarizer only lets the corresponding component of the unpolarised solar radiation through. Then, the desired wavelength to be measured is selected by applying its corresponding RF signal to the AOTF. Finally, the second polarizer only lets the filtered wavelength through, and a plano-convex spherical lens would focus the output beam into the APD detector.

The initial design of the proposed spectrometer did not include a bandpass filter due to the belief that the extinction coefficient of the orthogonal polarizers, in addition to the lock-in amplifier, would reject most of the background stray light. Moreover, the AOTF could further attenuate the modulated output beam at desired wavelengths to avoid saturating the detector by reducing the amplitude of the applied electrical signal. However, it was found later that a second wavelength in the visible or near-infrared spectral range reaches the detector (see Chapter 6 and Chapter 7). For example, if the AOTF is configured to filter a wavelength at 350 nm, the output beam will contain 350 nm and 700 nm wavelengths. Thus, the use of an input filter became unavoidable.

Most of the direct solar measurements performed by the AOTF spectrometer at Kipp & Zonen facilities were performed using the filter UG11 manufactured by Thorlabs due to its easy accessibility (see Figure 4.6).

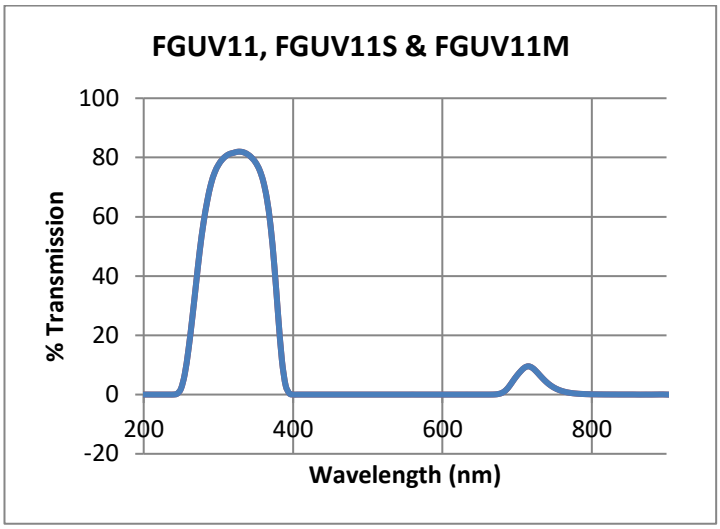

Figure 4.6 Spectral response of the FGUV11 filtered manufactured by Thorlabs.

Initially, the UVC7 filter from Inrad Optics was considered a replacement for the provisional UG11 filter (see Figure 4.7). However, its transmission on the visible spectrum would not block the undesirable wavelength that the AOTF let through at approximately double the selected wavelength. Thus, it was decided to use the filter UG11 with a 2 mm thickness offered by a different manufacturer see (Figure 4.8), which completely attenuates the undesired second wavelength that reaches the detector in the spectral range from 600 nm to 800 nm. Having spectral transmissions of ~0.001% from 420 nm to 799 nm, ~0.05% from 800 nm to 999 nm, and ~0.5% from 100 nm to 1200 nm.

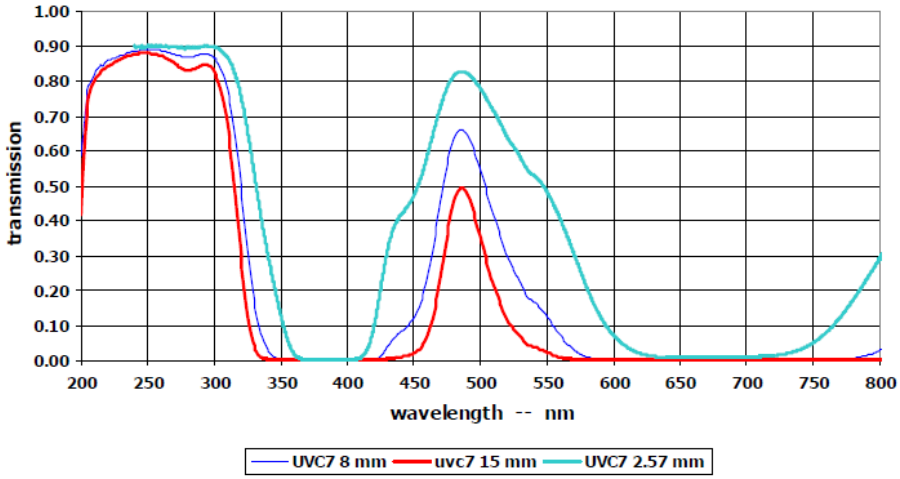

Figure 4.7 Spectral response comparison of the filter UVC7, manufactured by Inrad Optics, at different widths.

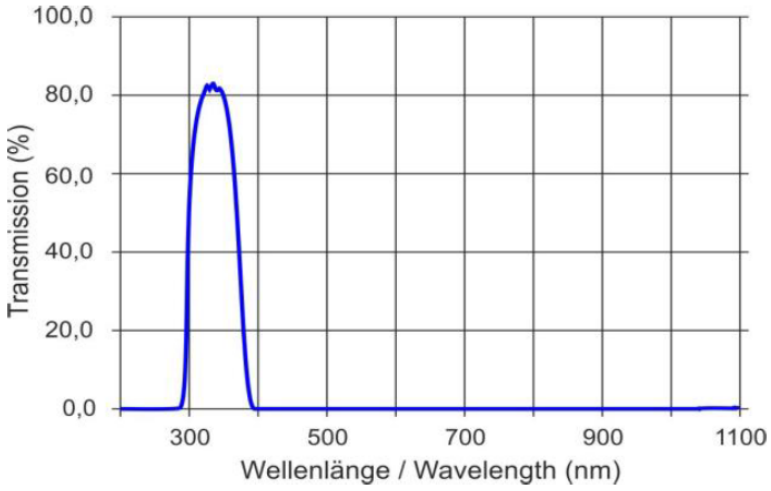

Figure 4.8 Spectral response of the bandpass filter used in this project (UG11 with a thickness of 2mm).

4.1.3. Glan-Tylor polarizers

Glan Tylor polarizers consist of two identical birefringent prisms with a thin air gap in between. The input beam is then divided into two rays with orthogonal polarizations and orthogonal beam directions (ordinary and extraordinary components). The beam of light transmitted through the polarizer consists of the extraordinary polarization component, while the ordinary ray exits the crystal partially polarized. Depending on the application, the polarizer could have an escape window for the output beam that is not collinear with the input beam (ordinary ray). Polarizers without an escape window are suitable for low to medium-power applications where the rejected beam is not required.

The field of view (FOV) of a polarizer depends on the refractive index of the intermediate layer, such as cement or air, and the internal angle of the internal prisms. Therefore, the FOV of ordinary and extraordinary rays varies with wavelength and incident angle, producing that divergent and convergent beams would not exhibit proper polarization if they exceed the polarizer (See Figure 4.9).

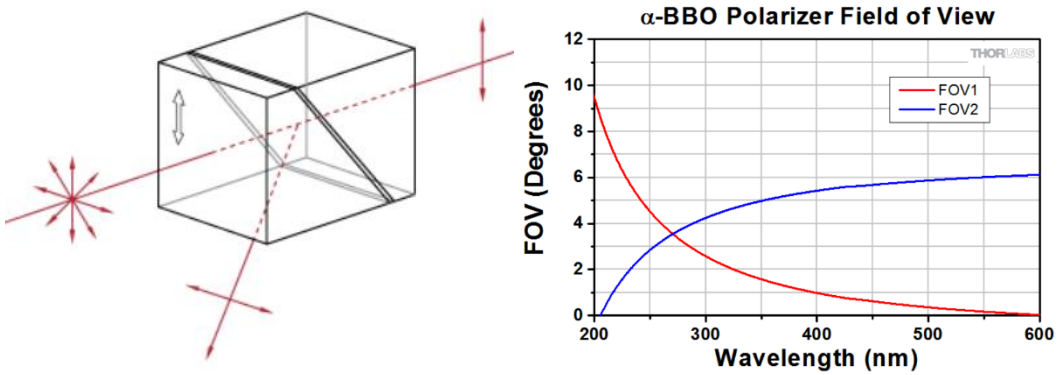

Figure 4.9 The diagram on the left shows the internal parts of a Glan-Taylor polarizer. The right graph displays the typical acceptable field of view values for α-BBO Glan-Taylor polarizers. Where FOV1 is the field of view for ordinary rays escaping the window, and FOV2 is the field of view for extraordinary rays passing through the polarizer (THORLABS, 2017).

The transmittance of the Glan-Taylor polarizers used in this project uses a Laser-Quality α-BBO (Barium borate) crystal with a spectral range from 300 nm to 700 nm. Although the manufacturer states that the extinction ratio of both polarizers is near $5x10^{-6}$, further measurements in Chapter 5 showed an extinction ratio of $1x10^{-4}$. Figure 4.10 displays the transmittance of the polarizers used in this spectrometer.

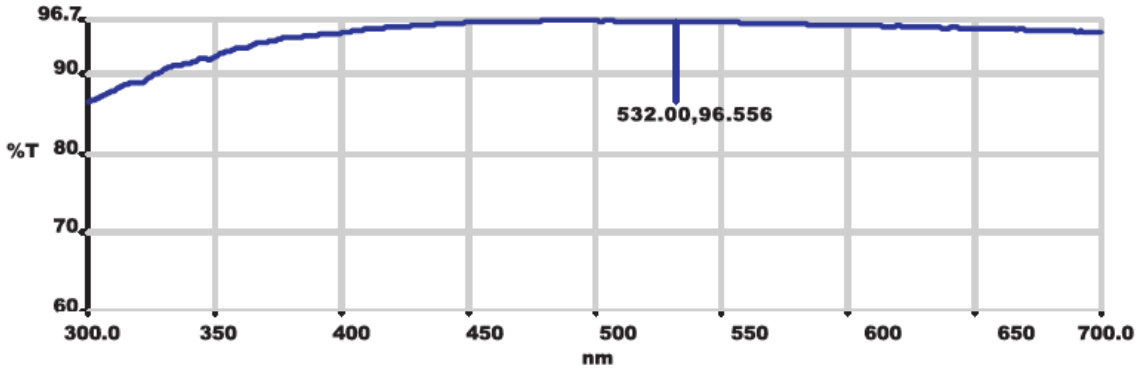

Figure 4.10 Typical spectral response of Glan-Tylor polarizers (THORLABS, 2017).

4.1.4. Plano-convex lens

Plano-convex lenses are commonly used in optical applications to focus a collimated beam or collimate a divergent beam from a focal source. Most of these lenses possess a spherical curvature instead of an elliptic one, generating a spherical aberration. Thus, the collimated beam should be facing the curved surface of the plano-convex lens to minimize such aberration (see Figure 4.11). However, this aberration is negligible in the presented spectrometer due to the diameter of the collimated incident beam (3.5mm) and the size of the detector (1mm).

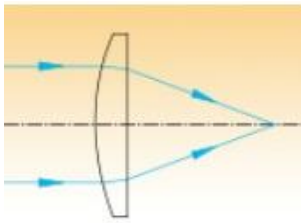

Figure 4.11 Plano-convex lens configured to focus a collimated beam.

UV-grade fused silica lenses offer high transmission on the UV and low thermal expansion compared to other optical UV crystals such as the N-BK7. Additionally, fused silica lenses with an anti-reflective (AR) coating deposited on both optical surfaces are commercially available, providing an average reflectance of less than 0.5% compared with the 4% of the light that is approximately reflected in uncoated surfaces. The spectral range of commercial AR coating products from Thorlabs is 245 to 400 nm or 290 to 370 nm for UV fused silica.

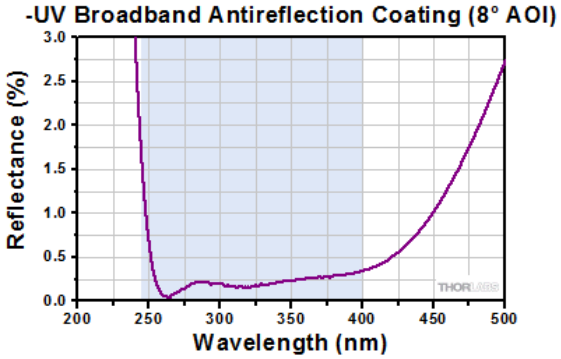

Figure 4.12 Reflectance graph of the AR coating deposited on UV fused silica with a spectral range from 245 nm to 400 nm (THORLABS, 2017).

The collimated beam at the output of the second polarizer is focused by the AR-coated UV-fused silica plano-convex lens from Thorlabs. Note that an additional plano-convex lens was used to collimate the beam from different light sources in the laboratory.

4.2. Electronics

The AOTF spectrometer's electronics were placed together in an independent box on top of the RF generator (see Figure 4.13). All electronic parts were situated on a solid base next to the solar tracker during direct solar measurements, while the optics of the proposed AOTF spectrometer were mounted on top of a solar tracker.

Future work includes placing the AOTF spectrometer into a weatherproof case, with the electronics next to the optics or in a separate container to reduce stray light errors due to dust and condensation. Additionally, the temperature and humidity inside would be controlled and monitored to reduce its temperature dependence.

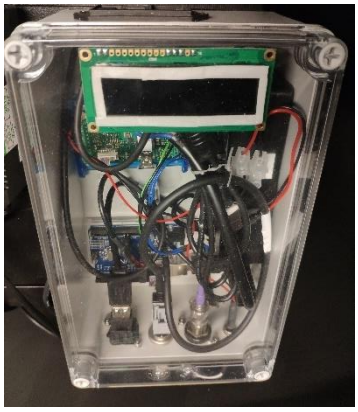

Figure 4.13 Waterproof case contains the TE controller of the AOTF, environmental sensors, and an Arduino as a modulation signal generator.

4.2.1. RF controller

The AOTF manufacturer provided the RF controller unit used in this project to work in conjunction with the AOTF. The customised user interface controls the amplitude and frequency

of the RF output signal, having a frequency range from 80 MHz to 165 MHz ± 5% of tolerance with minimum increments of frequency of 8 ns and maximum output power of 10 W.

Its design is bulky, 30 cm wide, 15 cm high, and 28 cm deep. It possesses a metallic case to avoid electromagnetic radiation leaks, but more than half is empty. Its internal design has three main components: a power supply, a commercial RF amplifier, and an electronic board that generates the RF signal. The PC communication is via serial protocol through an RS232 cable. It possesses an SMA connector for the RF output port and a BNC connector for its digital modulation, with TTL voltages from 0 V for minimum output power to 5 V for 10 W of maximum power (see Figure 4.14).

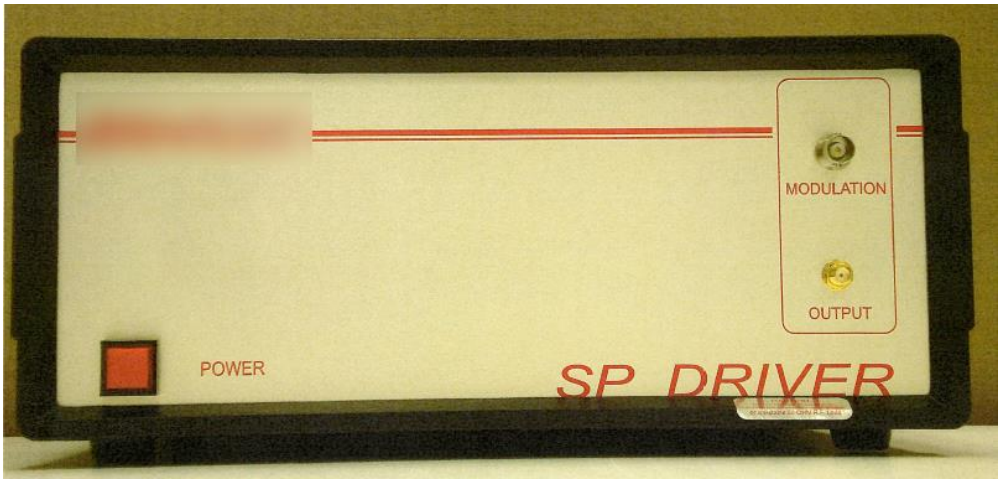

Figure 4.14 Picture of the RF controller used in this project (300 mm wide, 150 mm high, 280 mm deep).

The RF controller unit needs a warm-up of 15 minutes after being turned up to stabilize the driver. And it is suggested to work in a temperature range from 15° C to 75° C for better performance. Additionally, an output load of 50 ohms of impedance must be connected at all times to avoid damage.

4.2.2. Thermo-electric controller of AOTF

The initial AOTF required a water-cooling system to maintain a working temperature below 50° C to avoid internal damage. However, the device suffered from water leaking in the last part of the research, and it had to be replaced by a new model with thermoelectric (TE) cooling instead. The water pipes were removed and replaced by Peltier modules located internally at each side of the birefringent crystal. The new design also included two fans on each side but not an electronic driver to control the system's temperature. So, it was decided to use a commercial model instead of designing and developing it.

The temperature module increases or reduces its output current to maintain a steady temperature of 25° C, with output voltages from 0 to ±21V and output currents from 0 to ±4 A. The user interface monitors the device's status, and it is reset in case there is any unexpected

output. Additionally, the measured temperature of the AOTF and the output values of the TE controller are displayed on an LCD to allow the operator to see these values on site.

4.2.3. Analogue to digital converter (ADC)

After the monochromatic beam filtered by the AOTF hits the APD detector, the signal is digitalized and processed by an analogue to digital converter (ADC). The ADC model used in this research possesses four input channels with resolutions of 24 bits, a maximum sampling rate of 102.4 kS/s (samples per second) and input voltages from -10 V_{pk} to +10 V_{pk}. Furthermore, it is entirely compatible and easy to interact with LabVIEW.

Two input channels of the ADC are used simultaneously to perform the spectral measurements and monitor the frequency of the generated RF modulation.

4.2.4. Avalanche photodiode (APD)

Avalanche photodiodes (APD) (see Figure 4.15) are fast and highly sensitive photodetectors used in optical applications with low-intensity signals. APD and conventional photodiodes are based on the photoelectric effect, transferring energy from light to an electron. However, APDs possess an internal current gain triggered when a reverse bias voltage is applied, producing an internal electric field that accelerates the electrons in the semiconductor material. Then, secondary electrons are produced by the impact-ionization effect, and the avalanche multiplication effect starts. For this reason, the internal gain is regulated by the reverse bias voltage, usually having high reverse voltages of some hundreds of volts (Dunai et al., 2010).

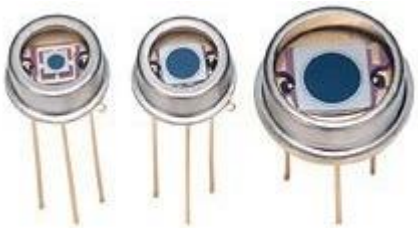

Figure 4.15 Silicon APDs with different photosensitive areas (Hamamatsu, 2004).

The semiconductor material used in APD is chosen depending on the operational wavelengths of the device. Silicon (Si) APD is primarily used from 200 nm to 1100 nm, Germanium (Ge) APD is suitable from 800 nm to 2100 nm, and InGaAs APD is commonly used from 950 nm to 1700 nm. Note that the efficiency and linearity of Si-APDs in the ultraviolet spectrum are lower than those operating in the visible or near-infrared (see Figure 4.16). However, it is expected that this will change as soon as technology progresses.

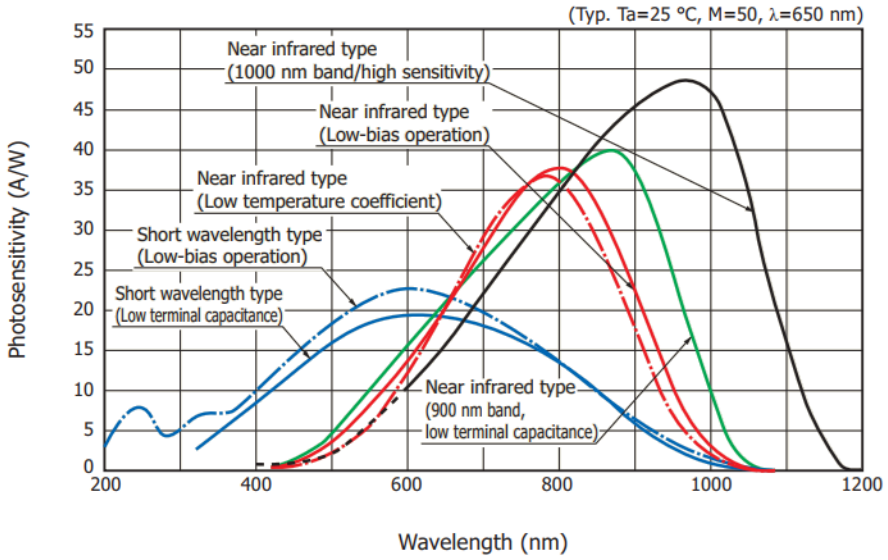

Figure 4.16 Spectral response of different Si APDs, at 25º C and a multiplication factor M of 50 (Hamamatsu, 2004).

The APD is an excellent optical detector for low-intensity light signals. However, noise sources inherent to the APD must be considered (see Figure 4.17). First, the ‘dark current noise’ consists of an undesired and relatively small electric current flowing through the APD with no incident photons. The thermal generation of electron holes primarily generates this noise, and it establishes the minimum amount of light that the device can detect. Second, the non-uniform ionization of individual carriers during the avalanche multiplication process produces the' excess noise'. Third, ’thermal noise’ results from a random motion of electrons through a resistor without an applied voltage (Cherin and Perez, 1995). And finally, the voltage noise generated by amplifiers is located before or after the APD. For these reasons, the current research uses a digital lock-in amplifier algorithm and measurement integrations to attenuate as much undesired noise as possible and reduce random noise.

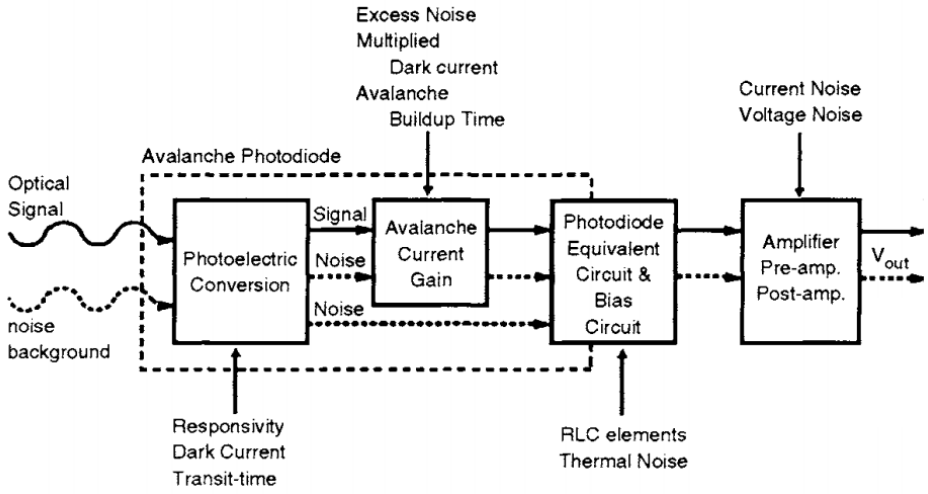

Figure 4.17 Functional block diagram of an APD detector, including the photodetection and the avalanche multiplication stage, as well as the electrical amplification process (Kobayashi and Mikawa, 2002).

The output of APD is temperature-dependent. At a specific reverse voltage, the gain decreases its value as the temperature increases. However, it is possible to avoid gain fluctuations by varying the reverse voltage source as soon as the temperature change. Commercial APD drivers solve this inconvenience by including a thermistor to adjust the bias voltage automatically across the APD. Moreover, those devices also have a current to voltage converter to easily connect the output into a digital acquisition device, plus an ultra-low noise amplifier.

The APD detector used in this research is a temperature-compensated model with a gain factor stability (M) of ±2% to maintain a constant gain at the output (see Figure 4.18).

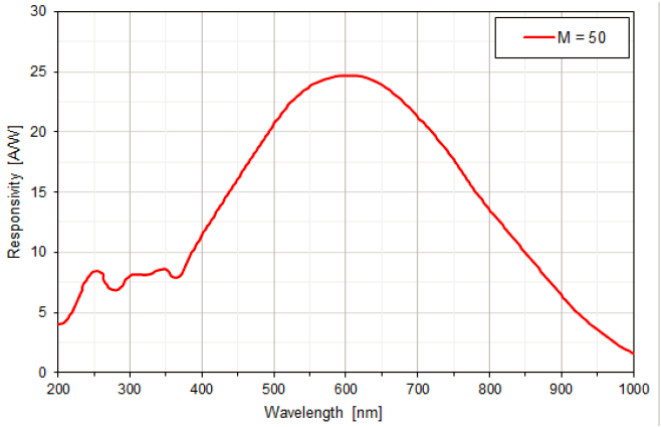

Figure 4.18 Spectral response of an APD at a typical temperature of 25º C, where M is the gain factor of the APDs (THORLABS, 2017).

Some features that make the Si-APD a competitive and cheaper substitute for PTM in some optical instruments are: high quantum efficiency, high gain, high sensitivity, fast response (from 0.4 nm to 1.5 ns depending on the effective surface area), reduced size, breakdown voltages up to 200 V instead of several kilovolts used in PMTs, and an accessible price.

4.3. Locking amplifier

A lock-in amplifier is a phase-sensitive detection technique that detects extremely low modulated signals even when buried in undesired noise hundreds of times larger. This technique can be performed by a dedicated lock-in amplifier instrument or a digital algorithm as long as the modulation frequency is known or the signal is provided. Most of the lock-in amplifiers shift 90º of the modulation signal to have two internal references, obtaining the desired amplitude without operator intervention. However, if the instrument has only one channel, it will be necessary for an operator to manually adjust the phase of internal reference to obtain the same output.

Several optical systems apply this technique to obtain reliable measurements of low-intensity light sources. Thus, they usually use mechanical modulation as a chopper wheel or a digital pulse train to modulate the output beam. Then, it is measured by an optical detector, and the electric

output is connected to the input of the lock-in amplifier (see Figure 4.19). Finally, the result is commonly digitalized by an analogue to digital converter (ADC) and then processed by a PC.

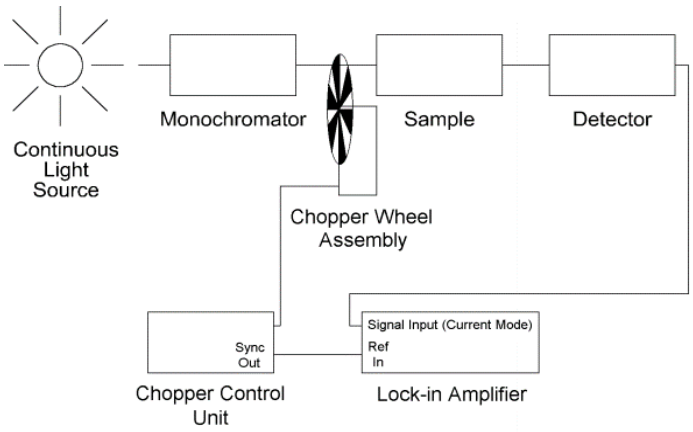

Figure 4.19 Common example of a phase-sensitive detection system using a chopper wheel (PerkinElmer Instruments, 2000).

The algorithm used in digital lock-in amplifiers simulates two identical sinusoidal signals $V_{ref1}(t)$ and $V_{ref2}(t)$ (one is phase shifted $\frac{\pi}{2}$) at the modulation frequency (ω). The amplitude of those internal references signals is commonly one unless it is necessary to pre-amplify the input signal $V_i(t)$. Note that a capacitor between the photodetector and the data acquisition instrument will eliminate the offset of the input signal (V_{offset}). Thus, it is considered $V_{offset} = 0$.

$$V_i(t) = V_i \, sin(\omega t + \phi) \tag{4.2}$$

$$V_{ref1}(t) = V_{ref} \, sin\big(\omega t + \phi_{ref}\big) \tag{4.3}$$

$$V_{ref2}(t) = V_{ref} \, sin\left(\omega t + \phi_{ref} + \frac{\pi}{2}\right) \tag{4.4}$$

Where V_{ref} is the amplitude, and ϕ_{ref} is the phase of the reference signals.

Then, each reference signal in Eq. (4.3) and Eq. (4.4) multiplies the input signal Eq. (4.2). Note that V_{ref} will be substituted by 1 to simplify the following mathematic expressions.

$$X(t) = V_i \, sin(\omega t + \phi) \, sin\big(\omega t + \phi_{ref}\big) \tag{4.5}$$

$$Y(t) = V_i \, sin(\omega t + \phi) \, sin\left(\omega t + \phi_{ref} + \frac{\pi}{2}\right) \tag{4.6}$$

Where $X(t)$ is the product of $V_i(t)$ and $V_{ref1}(t)$, and $Y(t)$ is the product of $V_i(t)$ and $V_{ref2}(t)$.

Equations (4.5) and (4.6) are then simplified by applying the trigonometric identity in Eq. (4.7).

$$sin\,\alpha\,sin\,\beta = \frac{cos(\alpha-\beta)-cos(\alpha+\beta)}{2} \tag{4.7}$$

$$\boldsymbol{X(t) = \frac{V_i}{2}\left[cos\left(\phi-\phi_{ref}\right)-cos\left(2\omega t+\phi+\phi_{ref}\right)\right]} \tag{4.8}$$

Similarly

$$Y(t) = \frac{V_i V_{ref}}{2}\left[cos\left(\phi-\phi_{ref}-\frac{\pi}{2}\right)-cos\left(2\omega t+\phi+\phi_{ref}+\frac{\pi}{2}\right)\right] \tag{4.9}$$

$$\boldsymbol{Y(t) = \frac{V_i}{2}\left[sin\left(\phi-\phi_{ref}\right)+sin\left(2\omega t+\phi+\phi_{ref}\right)\right]} \tag{4.10}$$

At this point, Eq. (4.9) and Eq. (4.10) have a DC component (since $\phi-\phi_{ref}$ is constant) as well as a sinusoidal component with twice the modulation frequency. Thus, a low-pass filter is placed after the multiplication stage to let the DC component through and considerably attenuate all AC components.

Once Eq. (4.8) and Eq. (4.10) are filtered, only the DC component will remain:

$$X(t) = \frac{V_i}{2}cos\left(\phi-\phi_{ref}\right) \tag{4.11}$$

$$Y(t) = \frac{V_i}{2}sin\left(\phi-\phi_{ref}\right) \tag{4.12}$$

Then, solving for the magnitude of V_i, the result does not depend on the phase difference between the signal and the simulated references.

$$\boldsymbol{V_i = \left(\frac{2}{V_{ref}}\right)\sqrt{X^2(t)+Y^2(t)}} \tag{4.13}$$

Figure 4.20 displays the block diagram of the lock-in amplifier algorithm.

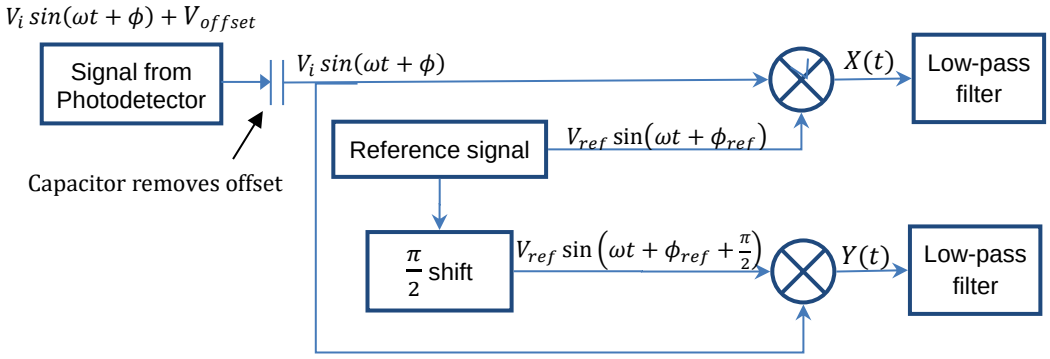

Figure 4.20 Block diagram of a lock-in amplifier algorithm.

The proposed spectrometer produces an external reference signal that modulates the RF controller's output. This signal is controlled and synchronized by the user interface during measurement.

4.4. User interface

Having built the optical instrument requires control and instruction software, provided through a user interface with in-built digital controls. It was designed as a bespoke piece of software using LabVIEW to give the experimental flexibility required in developing the AOTF spectrometer. NI LabVIEW is an engineering software designed by National Instruments (NI), mainly dedicated to acquiring, processing and visualizing data from compatible input /output devices. In addition, LabVIEW reduces programming time by using a graphical code syntax and ready-to-use functions instead of traditional text commands. Additionally, it possesses a dynamic interaction between the block diagram programming and the developed user interface. Thus, LabVIEW was chosen to design the user interface of the presented spectrometer.

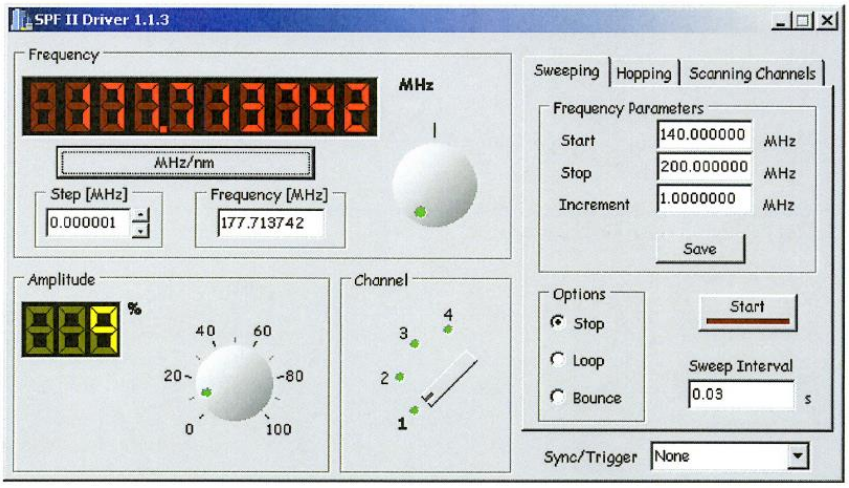

Figure 4.21 User interface provided by the AOTF manufacturer in 2016.

Initially, the user interface used to control the AOTF was provided by its manufacturer, which included a calibration file and a fixed operation routine (see Figure 4.21). However, the need for a flexible and customized user interface became necessary during the development of the prototype. Based on the communication protocols provided by the manufacturer, the author of this thesis programmed an interface with customized routines to cover the needs of this project.

Unfortunately, it was not possible to use the calibration files of the original user interface. Thus, it was necessary to perform a spectral calibration to get the relation between the filtered wavelength and the applied radiofrequency. The customised interface (see Figure 4.22) also displays the spectrometer's spectral measurements in almost real-time, digitally processes the acquired data through a lock-in amplifier algorithm, generates the modulation signal of the RF controller, and monitors external sensors (temperature, humidity, and atmospheric pressure). Additionally, as a safety feature, the interface enables and disables the 10 watts RF signal of the AOTF, avoiding overheating the electronics or the piezoelectric transducer of the AOTF when the spectrometer is in idle mode. The program has been substantially improved along the designing process, achieving its final phase when the operator can efficiently perform spectral measurements by pressing one button.

The final user interface design enables wavelength selection via the RF generator, digital processing of the raw signal, including the lock-in amplifier, temperature control of the crystal, temperature and humidity monitoring of the entire electronic system, display of the measured spectrum, and resulting ozone value.

Because of the nature of parallel programming, one of the challenges is the communication between loops that runs simultaneously. This problem was handled by using a producer/ consumer structure combined with event handling and queue management. The correct applications of such tools avoid the program being stuck in a loop that never will end due to an unexpected error. The user interface's final objective is to have a neat and efficient program that should be intuitive to use by an operator and easy to modify by a third party if necessary.

Although AOTF can move from one wavelength to another in nanoseconds, the processing time of a single spectral measurement depends on the user interface's time to communicate with the RF controller and the number of samples necessary to perform the lock-in amplifier algorithm. Additionally, a single wavelength measurement is integrated several times to reduce random noise and improve the signal-to-noise ratio, adapting the number of integrations when the input signal is too low. The spectrometer takes around 1 minute 15 seconds to integrate twice the measurements from 300 nm to 325 nm with a resolution of 0.05 nm.

Figure 4.22 Customised User interface of the AOTF spectrometer.

The favourable results presented in Chapter 6 and Chapter 7 confirm the reliability of the digital lock-in amplifier in reducing noise and filtering very low-intensity signals.

Chapter 5. Optimization of the initial design

This chapter contains some physical and software adjustments to increase the performance of the proposed spectrometer. It is explained the importance of an accurate alignment of the polarizers to reduce stray light reaching the detector. In addition, it is important to notice that the spectral response of the spectrometer is affected by internal imperfections of the AOTF, which might affect the symmetry along the spectrum when compared with the ideal $sinc^2$ function. Furthermore, each monochromatic measurement made by the AOTF spectrometer should be measured several times and then integrated to minimize background noise. Such considerations will considerably reduce the generated background noise.

5.1. The transfer function of the AOTF spectrometer

The diffracted light wavevectors of an AOTF (K_d) are based on the interaction between the incident light (K_i) and the acoustic wavevectors (K_a), satisfying the momentum matching condition described in (5.1).

$$K_d = K_i + K_a \tag{5.1}$$

The transfer function represents the device's output for each possible input, and it is an inherent property of all kinds of filters, regarding their type (digital, analogue, optical, or mechanical). The transfer function of an AOTF (T), also called the spectral tuning curve, is determined by the phased matching condition expressed in Eq. (5.2) (Katrašnik et al., 2010).

$$T(\lambda) = \alpha(\lambda) sinc^2\left(\frac{\Delta K(\lambda) L}{2\pi}\right) \tag{5.2}$$

Where $\alpha(\lambda)$ is the peak transmission at the exact momentum matching, L is the interaction length between the acoustic and light waves, $\Delta K(\lambda)$ is the momentum vector mismatch ($\Delta K = K_d - K_i - K_a$), and the function sinc symbolizes sin(x)/(x).

The full-width half maximum (FWHM) is a parameter used to describe the width of a curve function. It is the distance between the curve points at the peak half maximum level. In this case, the FWHM of the AOTF describe the width of the transfer function, and it is determined by Eq. (5.3). Note that it is wavelength-dependent, and it describes the spectral resolution of the spectrometer (Katrašnik et al., 2010)

$$FWHM(\lambda) = \frac{1.8\pi\lambda^2}{D(\lambda)Lsin^2(\theta)} \tag{5.3}$$

Where $D(\lambda)$ is the wavelength-dependent optical dispersive constant for the quartz, θ is the incident angle with respect to the optic axis, and L is the interaction length between the acoustic and the light waves.

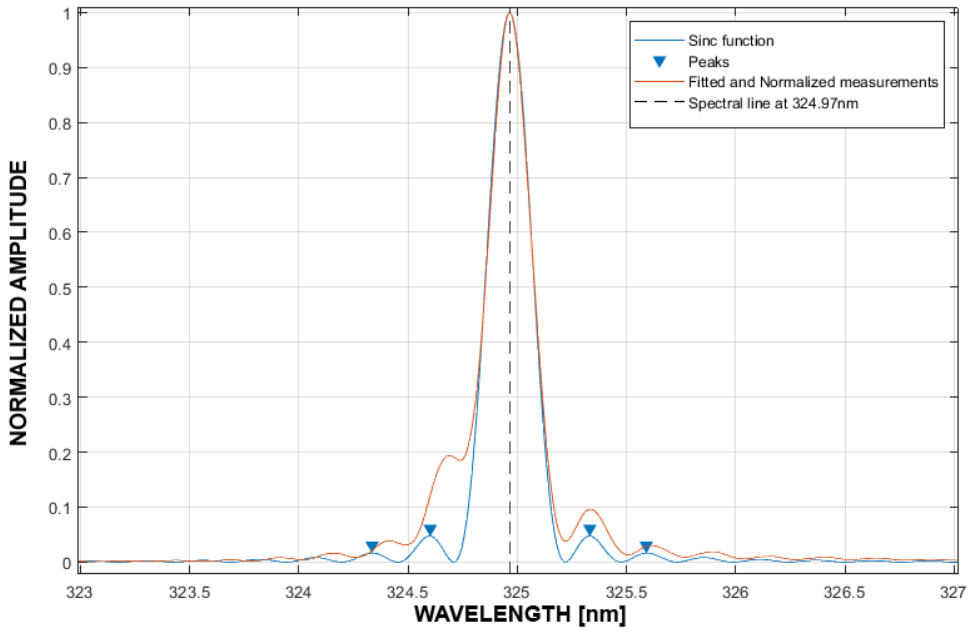

Figure 5.1. This is the measurement made by the AOTF of a spectral line at 324.97 nm using a HeCd laser as a light source. It compares the transfer function of the AOTF with a $sinc^2$ function at the same wavelength. FWHM=0.226 nm.

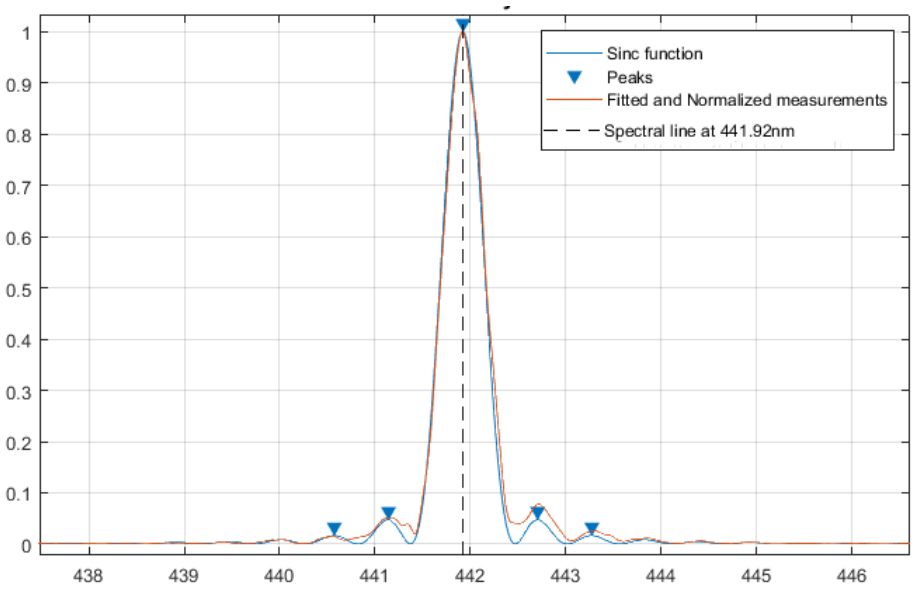

Figure 5.2 This is the measurement made by the AOTF of a spectral line at 441.92 nm using a HeCd laser as a light source. It compares the transfer function of the AOTF with a $sinc^2$ function at the same wavelength. FWHM=0.48 nm.

Figure 5.1 and Figure 5.2 display the spectral line measurements made by the AOTF spectrometer (see section 6.2.4), showing that Eq. (5.2) is an appropriate approximation of the transfer function of the instrument. The asymmetrical side lobes obtained during spectral line measurements by the AOTF spectrometer may be produced by the spectral response of the detector, variations on the profile of the acoustic waves, irregularities in the attachment of the piezoelectric transducer, or imperfections of the AOTF such as the crosstalk effect and inhomogeneous birefringence of the crystal (Katrašnik et al., 2010, Mahieux et al., 2009, Agrawal et al., 2015).

5.2. Alignment of polarizers

The collinear configuration of the AOTF requires aligning perpendicularly two polarizers at the two ends of the AOTF only to let through the ordinary ray or the extraordinary rays. The rejected rays and the undiffracted zero-order beam are attenuated by the extinction coefficient of the polarizers ($5x10^{-6}$). However, it is essential to mention that the latest measurements performed at Kipp and Zonen facilities revealed that wavelengths higher than 600 nm passed as stray light (second-order output of AOTF) unless a UV transmitting filter is placed with the entrance optics.

The purpose of measuring the extinction coefficient of the polarizers as a function of the degree of rotation is to emphasize the importance of setting the polarizers completely perpendicular to each other. Figure 5.3 represents the block diagram of the setup used to measure the extinction coefficients of the polarizers in order to compare it with the theoretical value of $1x10^{-5}$.

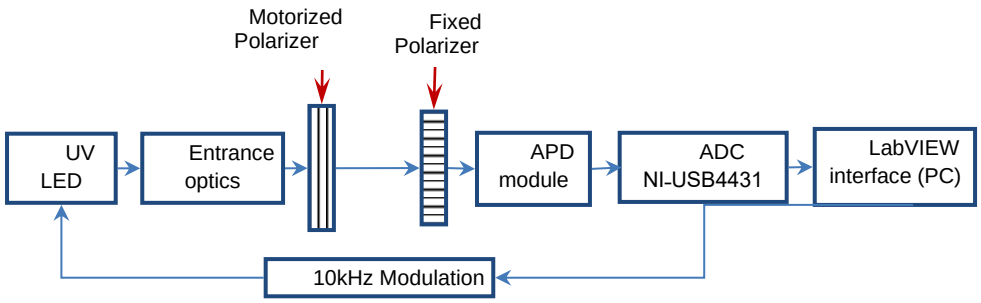

Figure 5.3 Block diagram of the optical system used to test the lock-in and the extinction coefficient of polarizers.

Figure 5.4 shows the measured extinction coefficient, achieving a maximum detectable value of $4x10^{-5}$ when both polarizers are perpendicular. Note that the motorized polarizer rotated with a 0.03-degree step, and the lock-in amplifier algorithm was used to reduce background noise. It is possible to appreciate from Figure 5.5 that maladjustments of 1 degree may decrease the extinction coefficient up to ten times, increasing the background noise generated by stray light. Thus, it is expected that the implementation of a motorized mounting on one polarizer will help to achieve the highest extinction coefficient possible.

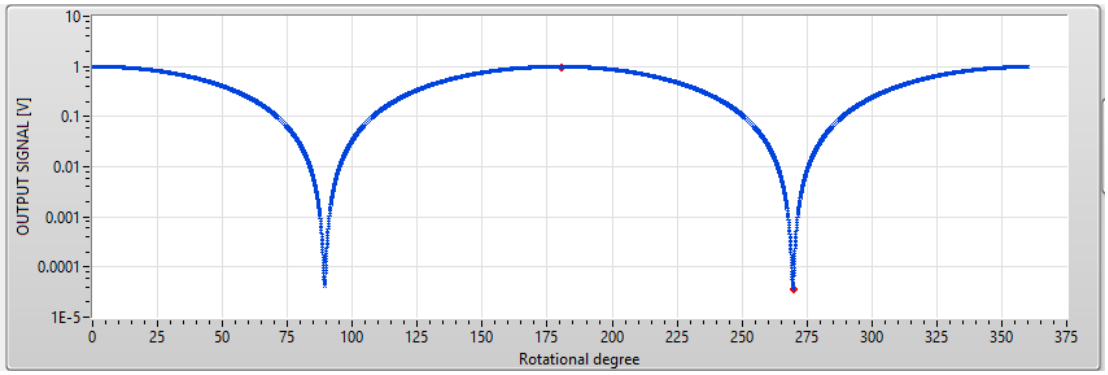

Figure 5.4 Extinction coefficient of polarizers from 0 up to 360 degrees with a step of 0.05 degrees. The detector output was normalized to 1 to compare measurements when the polarizers are parallel and orthogonal to each other without saturating the detector.

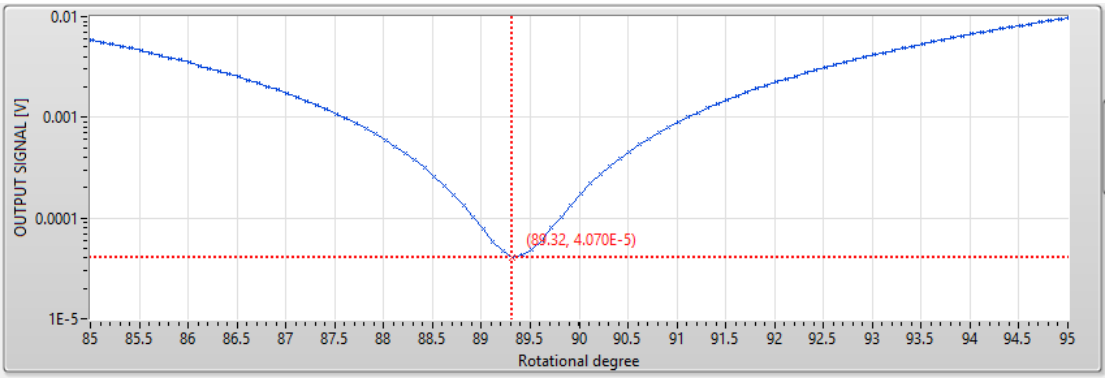

Figure 5.5 Zoom of the extinction coefficient near 90 degrees.

Note that when the rotating polarizer was mounted and fixed, it was initially aligned by eye. Hence the minimum in Figure 5.5 is not exactly 90 degrees. Within the software, the reference alignment becomes 89.32 degrees.

5.3. Importance of lock-in amplifier

The advantages of using a solid-state detector such as the APD (avalanche photodiode detector) instead of a photomultiplier tube (PMT) are its higher sensitivity, its reduced size and its lower cost. However, it possesses a higher dark current that would increase the background noise of the spectrometer. For this reason, it is necessary to place an additional filter and/or further digital signal processing.

The AOTF spectrometer uses a lock-in amplifier algorithm designed in LabVIEW to extract the desired signal from an extremely noisy source, as long as the signal is modulated at a known frequency. It is achieved by modulating the output of the RF controller with train pulses of 10 kHz. Figure 5.6 shows the measurements of a Hg spectral line with and without using the lock-in amplifier algorithm.

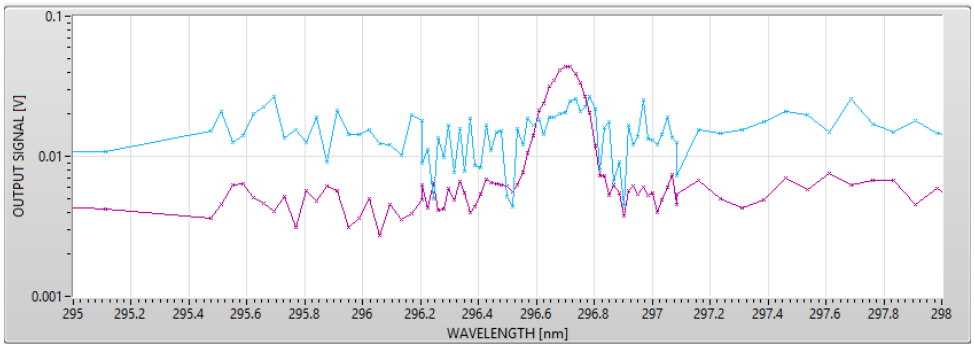

Figure 5.6 Spectral line measurements at 296.67 nm with 100 integrations using the lock-in amplifier algorithm (purple) and without (blue).

5.4. The optimum number of integrations

Measurements of spectral lines near 300 nm are highly attenuated mainly because of the spectral response of the APD detector. Although the lock-in amplifier is able to filter the measured signal, there is still unwanted random noise (see Figure 5.7). Thus, the spectrometer performs the same measurement several times and then integrates them to minimize the noise.

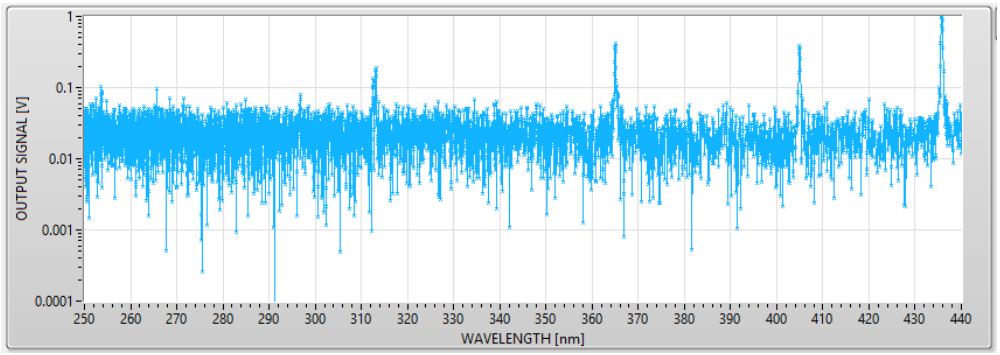

Figure 5.7 Single spectral measurements of a Hg lamp source (100W) (one single integration).

Figure 5.8 shows the spectral measurement of the same lamp after being integrated 100 times. The background noise is significantly reduced, and the peaks below 300 nm are visible compared with those in Figure 5.7. However, the downside is that each measurement takes 6 seconds to be acquired (100 times slower).

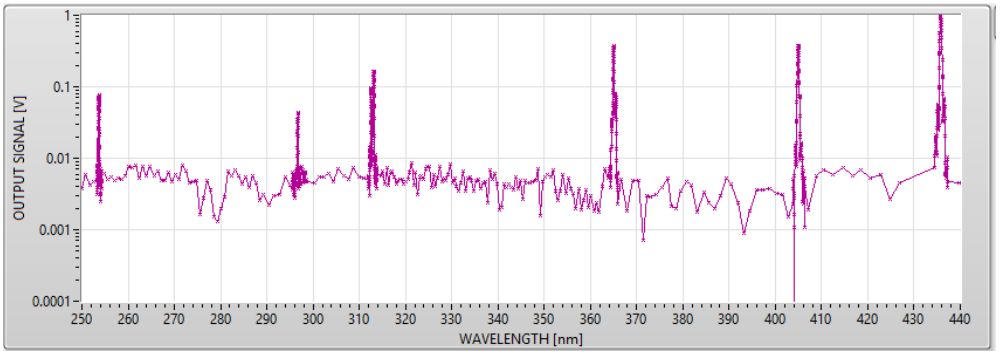

Figure 5.8 Measurement of spectral lines from a Hg lamp source (100W), integrating the signal 100 times and using a higher resolution near its spectral lines.

After the instrument was tested side by side with a Brewer spectrometer, it was found that the integration times should vary depending on wavelength. For example, 25 integrations may be enough for wavelengths higher than 320 nm, but more integrations are necessary for shorter wavelengths to obtain more reliable measurements.

The work thus far was completed in Manchester. For more specialised facilities, access was granted to the laboratories of Kipp and Zonen (in Delft, The Netherlands), the manufacturers of the Brewer spectrometer. Two visits were permitted, each lasting one week. Spectral line measurements of mercury, cadmium and zinc calibration lamps improved the existing wavelength. The detailed spectral response of the proposed spectrometer was obtained by measuring the spectral lines of a HeCd laser. The temperature stability of the instrument was tested in a temperature chamber. And side-to-side measurement comparisons with Brewer #223 were performed. Due to limited time, some of the tests we performed once, but the investigations conducted there are presented in Chapter 6.

Chapter 6. Laboratory characterization and calibration

Having achieved a basic working prototype of the AOTF spectrometer, the next task was to characterise its performance and undertake initial calibrations, particularly for the wavelength scale. These investigations were conducted at various locations that provided different test facilities, including two week-long visits to Kipp and Zonen facilities in Delft, The Netherlands, and the Photon Science Institute laboratories at the University of Manchester. The AOTF-based instrument can measure across a broad spectral range, so results are presented for wavelengths in the whole working range of the AOTF spectrometer, though the main focus is on the UV and comparison with the Brewer performance over the same range.

Many of the tests were conducted multiple times. For example, the initial link between frequency and wavelength was unknown, and an iterative process was required to finesse the wavelength alignment. The results shown here indicate the final performance of the prototype that was then used for solar measurements (Chapter 8), though with a different cooling mechanism for the crystal. The original crystal was water-cooled, but it had to be returned to the manufacturer for repair, and the water cooling was replaced at that point with a Peltier system which has the advantages of being smaller, more compact and portable. The cooling has no impact on the optical pathway, and its purpose is only to prevent the crystal temperature from exceeding 50^{o}C. Therefore we assume the optical characteristics are not affected by this change, which appears to be borne out in Chapter 8. Severe delays at the manufacturer meant that the returned crystal coincided with the long-term closure of laboratories due to Covid-19, and laboratory work could not be repeated.

Sources that were used for wavelength alignment and determining the slit function, specified by the full width half maximum, are mercury (Hg), cadmium (Cd) and zinc (Zn) lamps, a Cd laser and a laser-driven light source. Initial absolute calibration sources that were tested were a 50W halogen lamp from the Brewer calibration kit and a 200W halogen lamp provided by Schreder as a portable field calibration unit. A temperature chamber located at Kipp and Zonen laboratories was used for temperature sensitivity measurements.

A rail system was implemented to fix all optical components in place, and the original water cooling system was in use during the characterisations (as shown in Figure 6.1). Optical shielding was employed for each lamp to protect users and surrounding people from UV radiation.

Figure 6.1 Solid-state spectrometer performing measurements of a 50W halogen lamp at Kipp and Zonen Facilities.

It was still impossible to obtain irradiance measurements at this stage as a full calibration of the spectrometer had not been carried out. Nonetheless, the data allows the spectral lines of several calibration lamps to be plotted, the wavelength scale aligned, and FWHM (half-width half maximum) calculated. Note that the amplitude is not normalized, and it only represents the voltage obtained at the output of the analogue to digital converter.

6.1. Initial wavelength alignment

The AOTF and the RF controller were initially calibrated by the manufacturer when it was bought. However, the relationship between the RF applied to the AOTF, and the filtered wavelength was embedded within their bespoke software, and it was not possible to use it with the newly developed user interface. For this reason, a linear function was initially used to describe the relationship between the RF and the wavelength, according to the graph found in the user manual of the AOTF (see Figure 6.2).

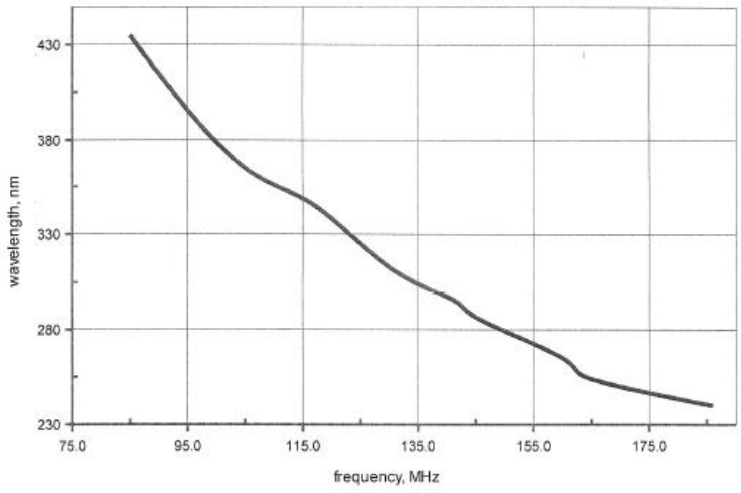

Figure 6.2 Relationship between the radio frequency applied to the AOTF and the filtered wavelength (AOTF manual).

In order to better characterize the instrument, it was necessary to perform measurements of a light source with well-defined wavelengths, such as a mercury lamp. An advantage of a mercury lamp is the emission of ultraviolet radiation at specific wavelengths under 400 nm, with well-defined spectral lines. However, there are two potential hazards in operating such lamps. First, the exposure of operators to UV radiation can cause cell damage or even mutation in eye and skin cells. Thus, in order to avoid ultraviolet exposure and minimize stray light coming from other light sources, the entire path of the beam was enclosed and covered by a black curtain. Additionally, safety UV goggles were worn by the user as well as any person near the working place as long as the lamp was on. Second, the power supply needs to be electrically isolated as it generates a high voltage to operate the mercury lamp. Fortunately, the portable calibration lamp ORIEL model 6025 provides spectral lines under 400 nm while meeting both safety requirements. It provides an enclosure that can be attached to the input optics of the spectrometer, and the internal circuitry, operated with a 9 V battery, is electrically isolated (the internal diagram of the lamp is illustrated in Figure 6.3). Note that due to a mechanical incompatibility between Oriel and Thorlabs optical parts, a customised adaptor was made by Eric Whittaker (senior experimental officer in photonic laboratories).

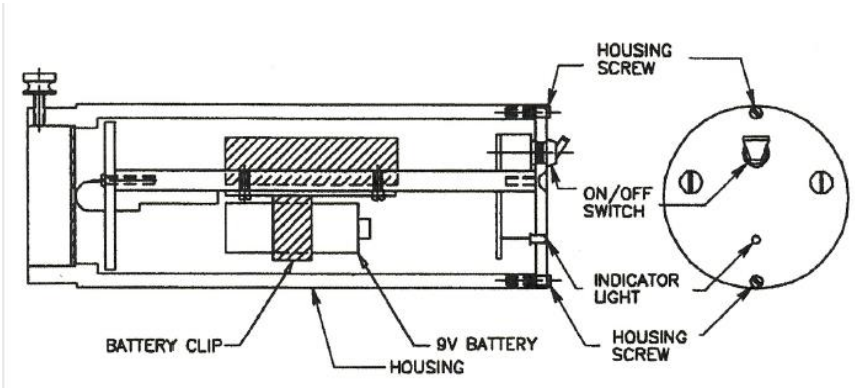

Figure 6.3 Internal diagram of the calibration lamp ORIEL model 6025.

The chosen mercury lamp provides lines in the UV, visible and near-infrared spectra, as shown in Figure 6.5. However, only measurements from 200 nm to 500 nm matched the spectral response of the AOTF. For this reason, only the lines at 253.7 nm, 365 nm, 404 nm and 435.8 nm are considered in further analysis.

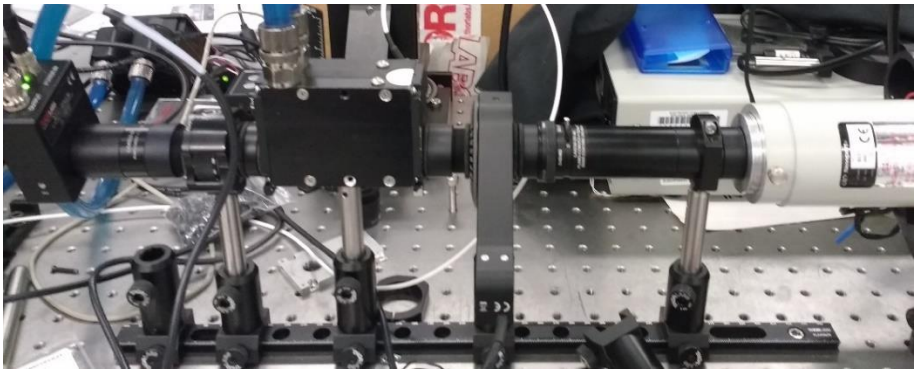

Figure 6.4 Setup during the Hg pencil lamp measurements.

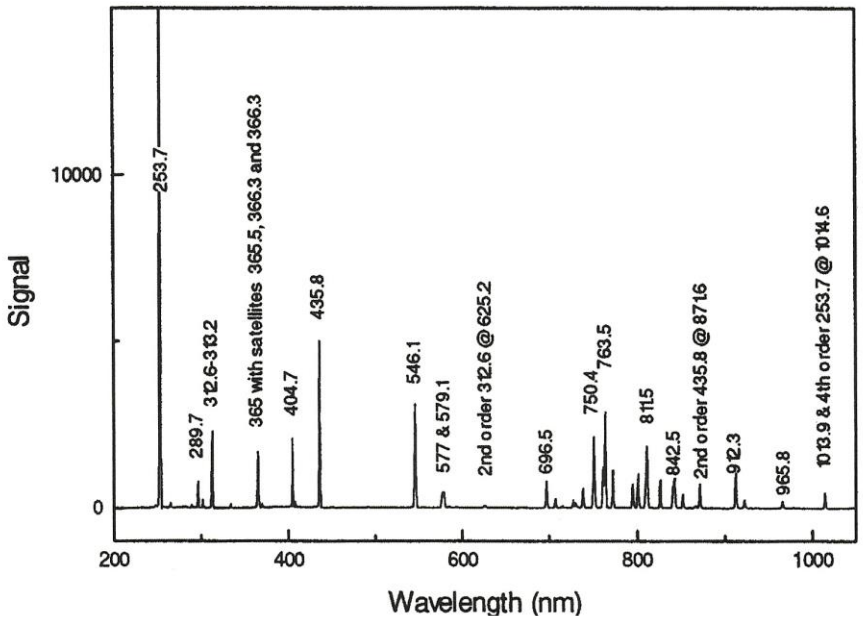

Figure 6.5 Spectral response of the mercury lamp, taken from the user manual (ORIEL model 6025). They were recorded using the manufacturer's spectrograph and an unspecified diode array detector.

Once the mercury lamp was attached and aligned to the spectrometer entrance, the instrument successfully scanned and plotted the nominal spectral lines of the lamp from 240 nm to 500 nm. Further work required the power supply for the lamp to be changed due to inconsistent operation on battery power. Figure 6.6 shows that the relative output of the mercury lamp decreases about 50% after being continuously operated for 140 minutes using a new alkaline 9 volts battery. After such time, the battery becomes unusable, and an immediate replacement is necessary. Thus, the portable lamp was modified to use a continuous DC power supply instead of a 9V battery to obtain consistent results. Note that this lamp was used due to its practicality for wavelength calibrations at the University of Manchester.

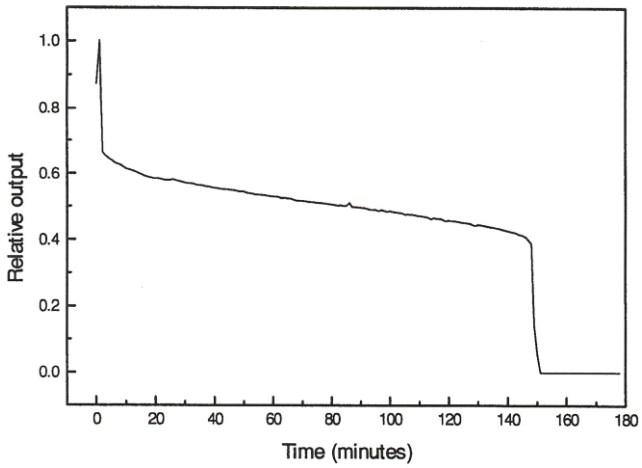

Figure 6.6 Typical performance of the mercury lamp when it is operated continuously using a new alkaline battery. Note that it is possible to achieve longer operating times if the lamp is used intermittently.

The signal and wavelength alignment of the spectrometer then had to be improved. Because there was no previous spectral response of the instrument nor a relationship between wavelengths and the radio frequencies applied to the AOTF, the maximum range of frequencies accepted by the AOTF (75 MHz to 190 MHz) was first scanned with steps of 2 kHz. The frequency-wavelength tuning curve from Figure 6.7 (user manual) was digitized and fitted into a 3rd order polynomial to visualise the wavelength domain.

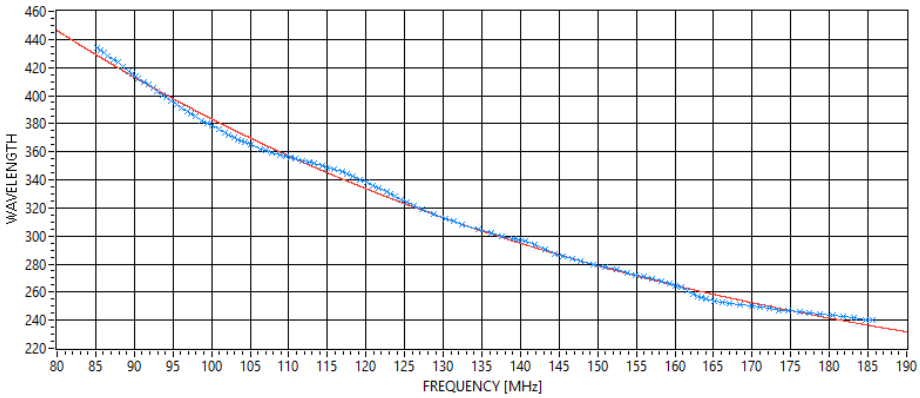

Figure 6.7 Blue graph represents the digitalized graph from the manual, and the red graph displays the polynomial fitting applied to the measurements.

Although digital data processing is a powerful tool to remove undesired noise, it was considered possible that it would hide features of the instrument's performance, and it should be used in the final phase of the research when all the other simpler tools have been tested. For this reason, it was chosen to integrate the signal over multiple samples, aiming to cancel random noise and increase the intensity of the expected signal. Figure 6.8 displays the obtained spectrum of the mercury lamp after each measurement was integrated over 100 samples. Although there is a significant improvement in the noise reduction, an obvious disadvantage of applying this method is that the measuring time increased in relation to the number of integrations (number of times that a measurement of the same wavelength is made). However, later improvements to the spectrophotometer, such as adding a physical band-pass filter and customizing collimating and focusing optics, increased the stray light rejection as well as reducing the required number of integrations.

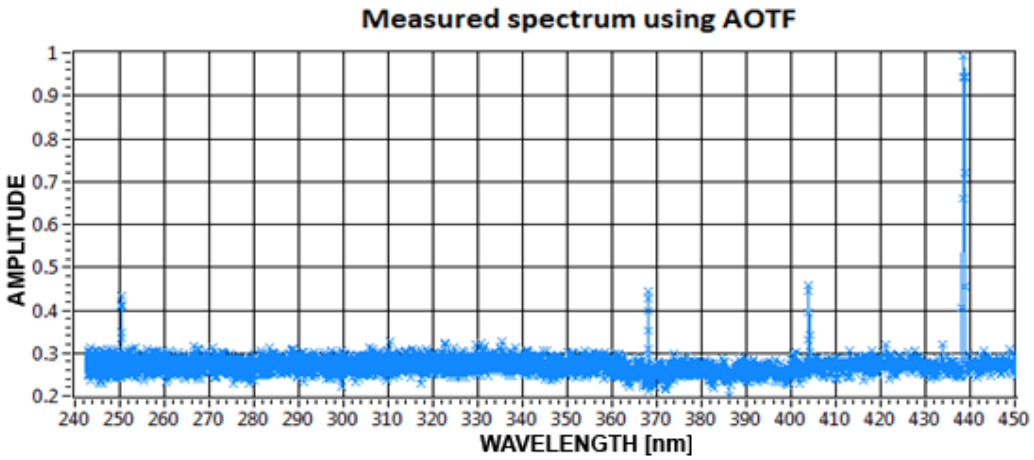

Figure 6.8 Spectral measurement of the mercury pencil lamp at the University of Manchester, integrating 100 times each measurement.

The user manual of the AOTF states that the spectral resolution of the instrument varies from 0.2 nm to 0.8 nm along the spectral range of the spectrometer (250 nm to 450 nm). These parameters can be estimated from Figure 6.9, where the mercury lines at 253 nm and 435.8 nm are separately analysed. The Full Width at Half Maximum (FWHM) at 253 nm is about 0.2 nm, while it is near 0.45 nm at 435.8 nm, matching the expected spectral resolution of the AOTF. Such results also show that there is a greater attenuation of shorter wavelengths. Further work considers applying a tunable laser as an input beam to characterise the proposed spectrometer completely.

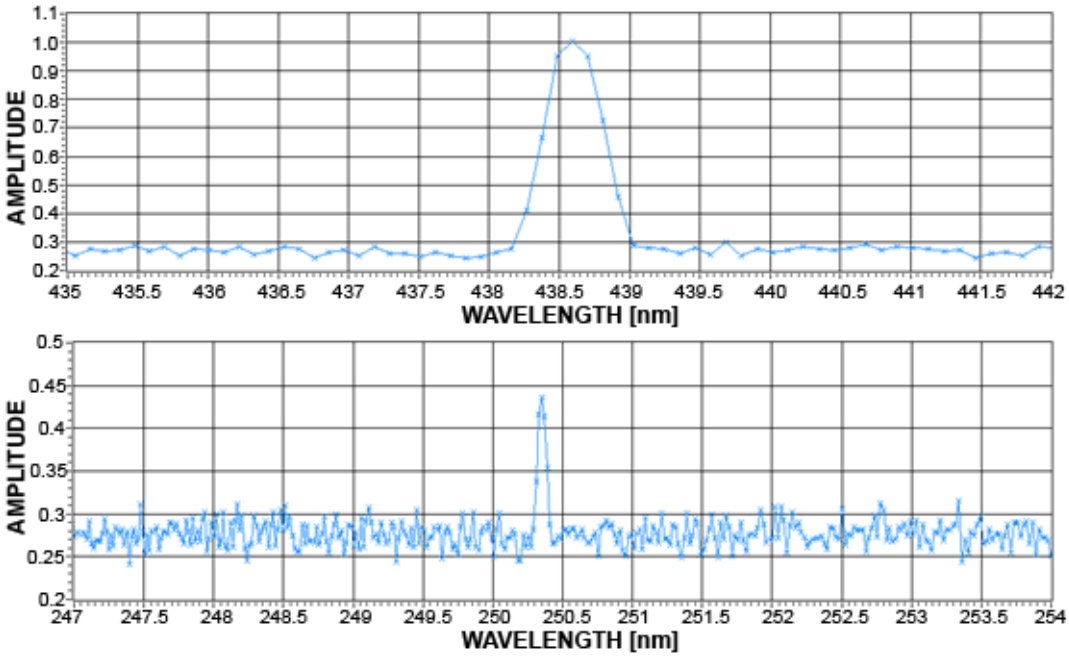

Figure 6.9 FWHM of the mercury lines at 435.8 nm and 253 nm, respectively. Notice that all the spectral measurements were integrated ten times and normalized to 1. Improvements in the polynomial fitting function are necessary to achieve better wavelength calibration.

6.2. Measurement of spectral lines

The following sections show the measurement of spectral lines from a range of lamps to provide good coverage of the wavelength range of the AOTF. All the measurements presented in this section were performed at the Kipp and Zonen facilities, where they facilitated the use of high-intensity spectral light sources such as the HeCd laser to obtain a more accurate wavelength calibration.

6.2.1. Mercury lamp

Figure 6.10 shows the spectral lines of a standard Hg lamp and displays the lines measured by the AOTF spectrometer below 485 nm. Note that multiple peaks in close proximity, around 313 nm and 365 nm, can be distinguished.

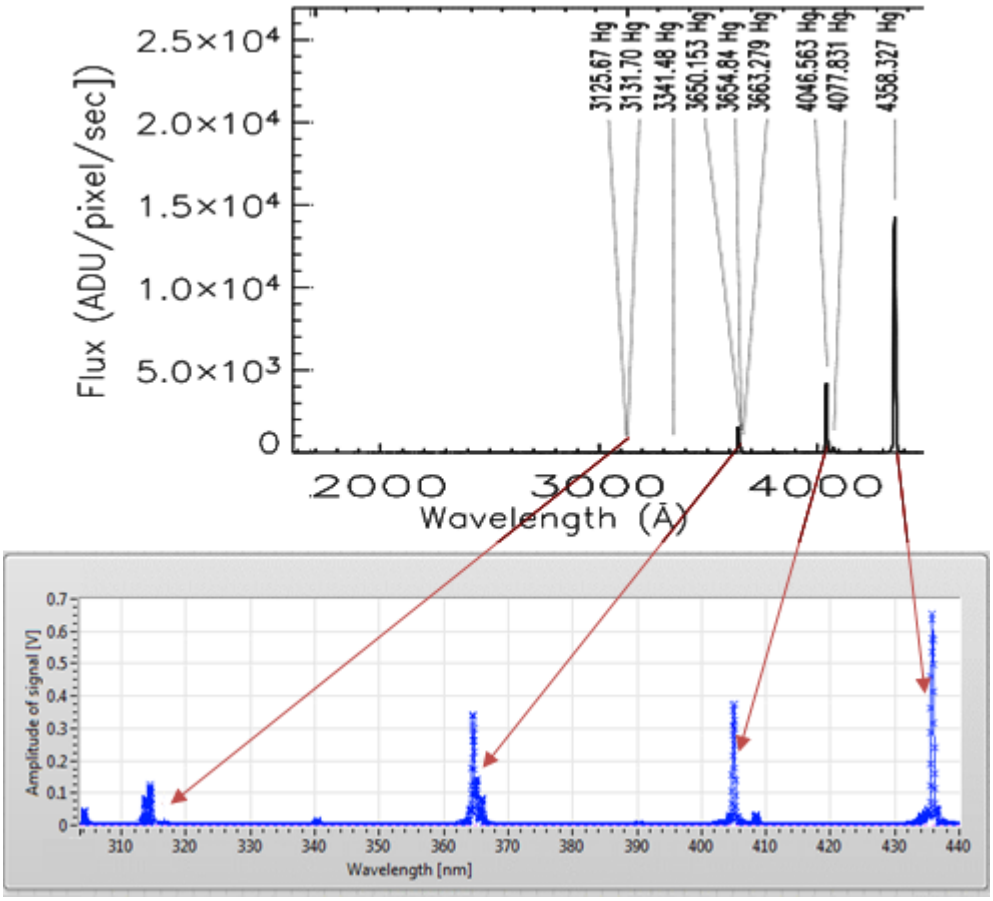

Figure 6.10 Comparison between main spectral lines of a standard Hg lamp and the measured spectral lines of a Hg lamp by the proposed spectrometer (integrated 50 times) (https://www2.keck.hawaii.edu/inst/lris/arc_calibrations.html).

6.2.2. Cadmium lamp

Figure 6.11 shows the spectral lines of a standard Cd lamp and displays the lines measured by the AOTF spectrometer up to 485 nm.

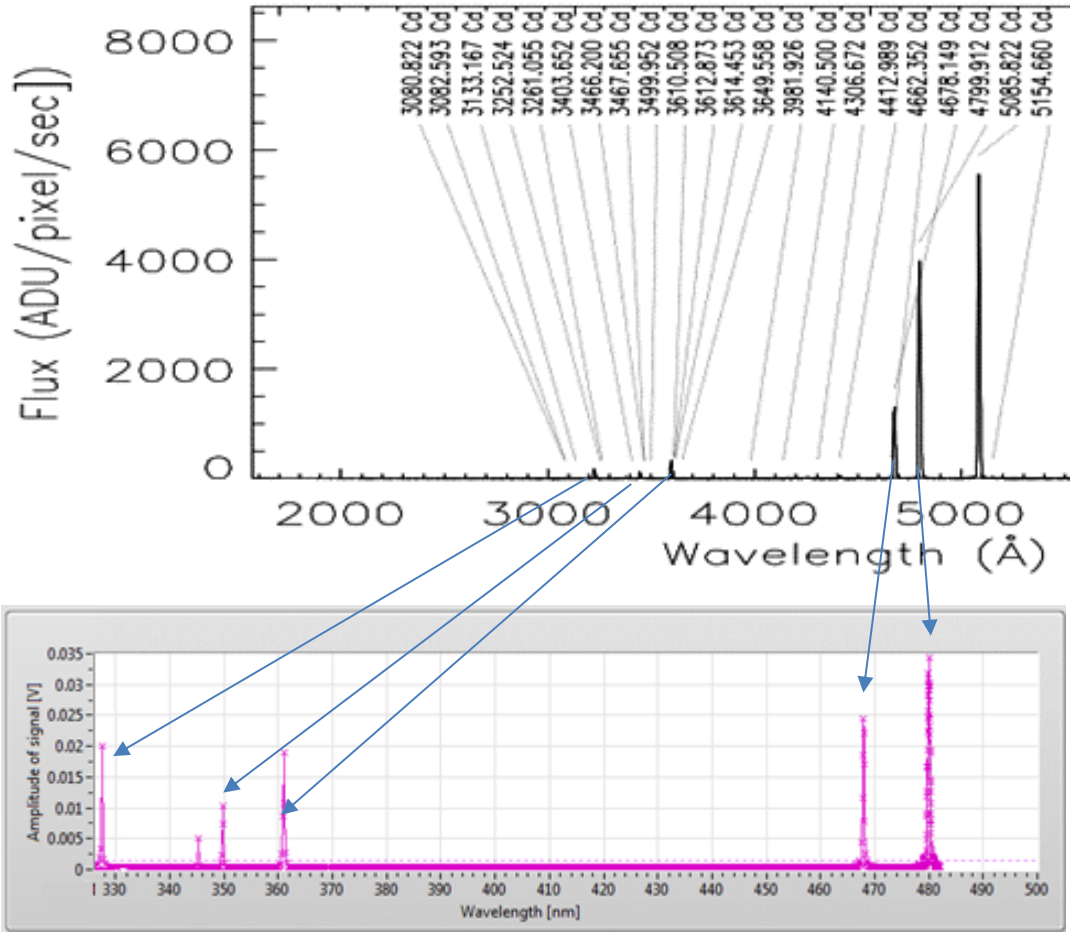

Figure 6.11. Comparison between spectral lines of a standard Cd lamp and the measured spectral lines of a Cd lamp by the prototype AOTF spectrometer (integrated 50 times) (https://www2.keck.hawaii.edu/inst/lris/arc_calibrations.html).

6.2.3. Zinc Lamp

Figure 6.12 shows the spectral lines of a standard Zn lamp and displays the lines measured by the AOTF spectrometer up to 481 nm (integrated 100 times).

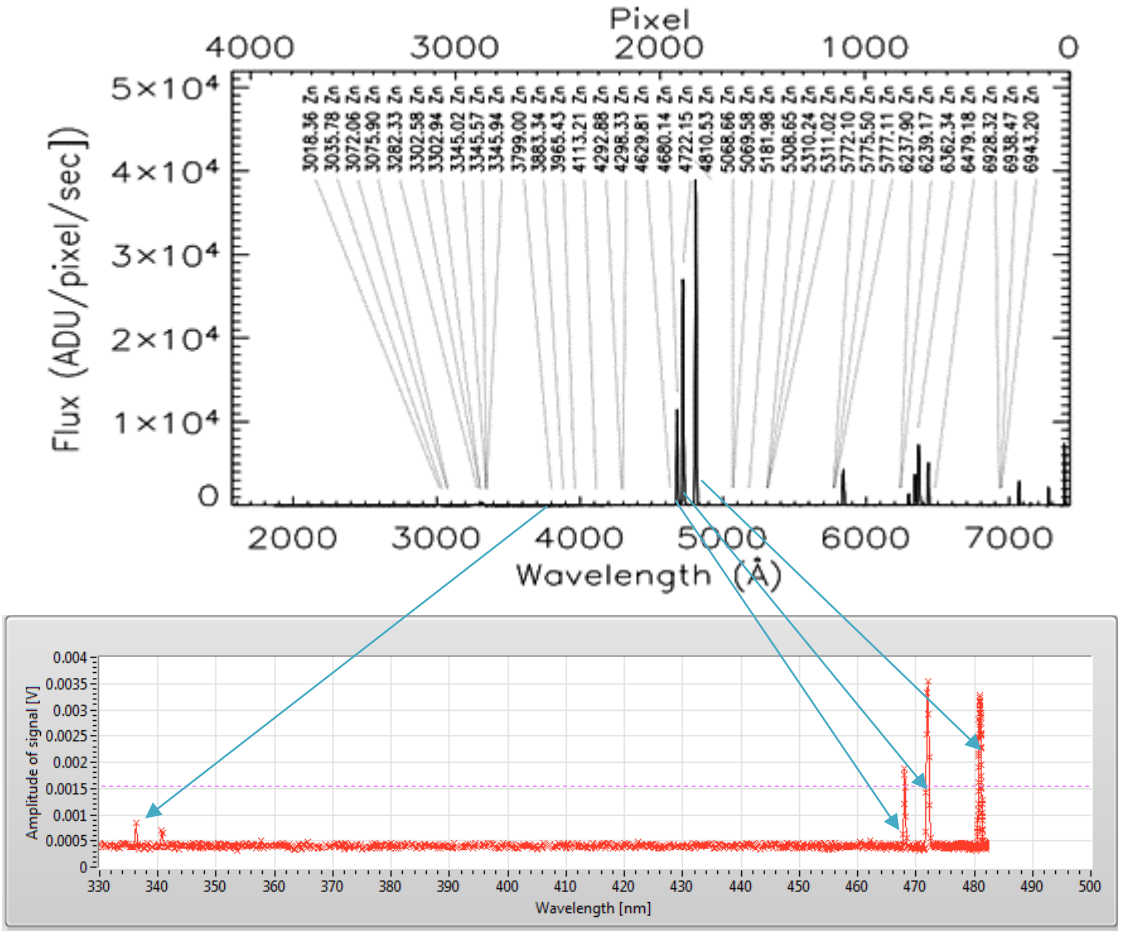

Figure 6.12. Comparison between Spectral lines of a standard Zn lamp and spectral lines of a Zn lamp measured by the proposed spectrometer (integrated 100 times) (https://www2.keck.hawaii.edu/inst/lris/arc_calibrations.html).

6.2.4. Measurement of Helium-Cadmium (HeCd) laser

Indirect measurements of the HeCd laser beam output were made in order to avoid damaging the optics or the detector due to its high intensity (see Figure 6.13). Although the laser provided two spectral lines at 325 nm and 442 nm, the safety mechanism of the laser only allows measuring one wavelength at a time (Figure 6.14 and Figure 6.15, respectively). Note that the measurements possess a shift in wavelength due to the initial correlation between RF and wavelength interpolation of a single spectral Hg lamp.

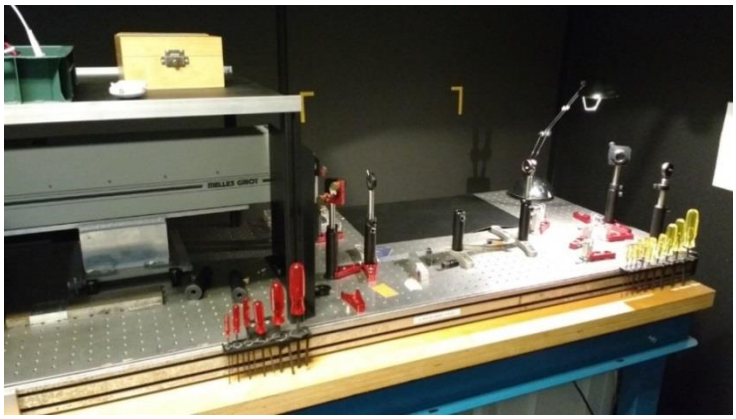

Figure 6.13 Arrangement of optics to perform measurements of the Cd laser.

Spectral line measurements of the Cd laser at 325 nm and 442 nm were measured several times, showing almost symmetrical side lobes at 442 nm (Figure 6.15) and asymmetrical side lobes at 325 nm (Figure 6.14), representing the transfer function of the AOTF. Compared to the 325 nm line measurement made by a Brewer spectrophotometer (Figure 6.16), it is clear that the Brewer does not show any side lobes. However, the full width half maximum (FWHM) of Brewer spectrometers is 0.6 nm at this wavelength, while that of the AOTF is 0.3 nm.

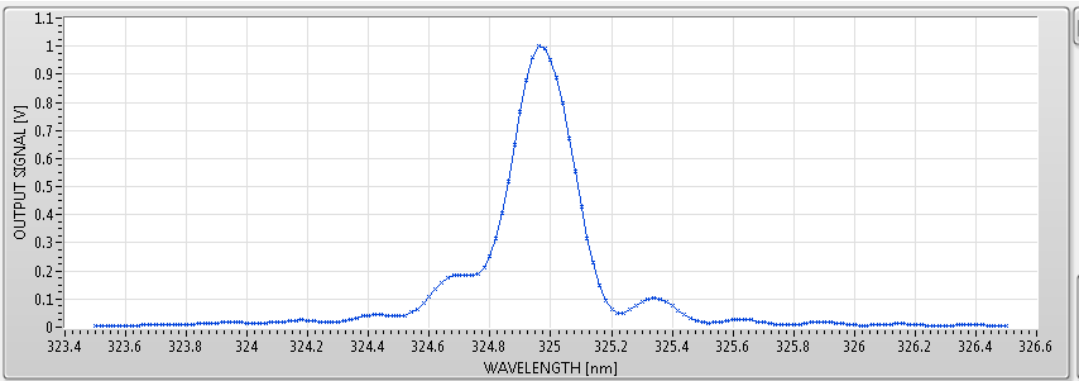

Figure 6.14 Spectral measurements of the HeCd laser at 325 nm using the AOTF spectrometer.

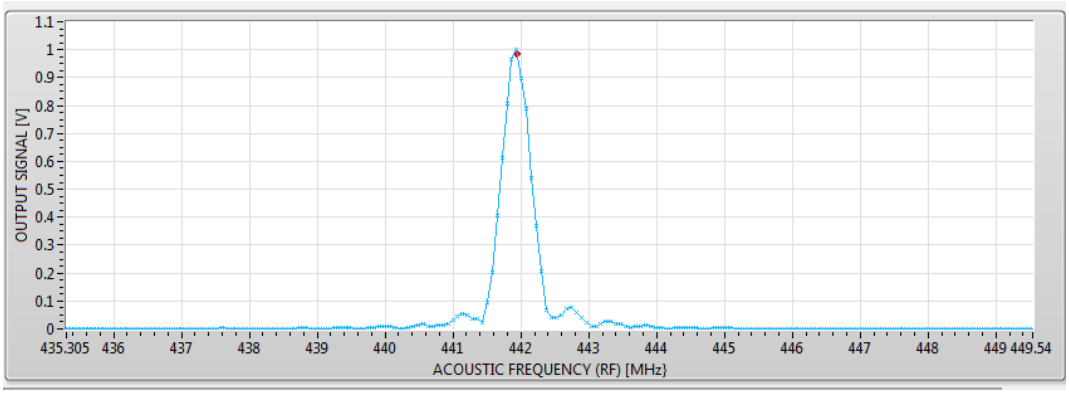

Figure 6.15 Spectral measurements of the HeCd laser at 442 nm using the AOTF spectrometer.

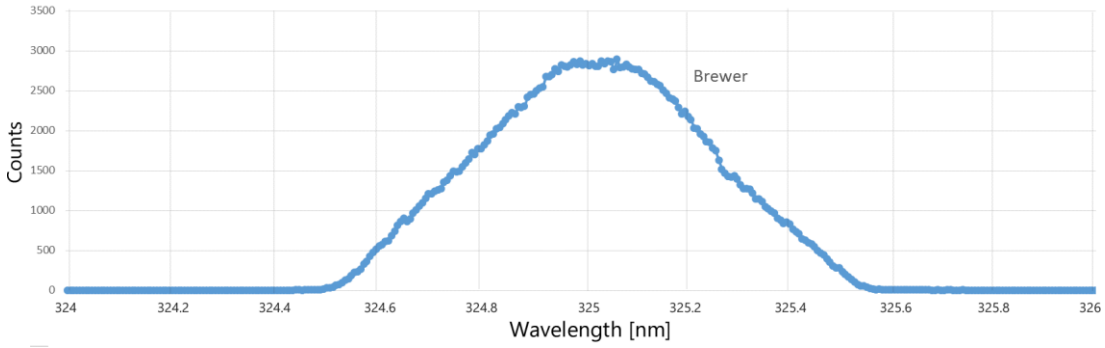

Figure 6.16 Spectral line of Cd laser at 325 nm with an FWHM of 0.6 nm measured by the Brewer spectrophotometer (plot provided by K&Z).

The measurement of the HeCd laser at 442 nm using the AOTF spectrometer indicates an FWHM near 0.5 nm at this wavelength. This measurement could not be compared with a Brewer spectrophotometer since the Brewer cannot perform measurements at 442 nm.

6.3. Full width half maximum

The measurement of a further range of spectral lines by the Brewer and the resulting FWHM indicated were compared with similar data from the AOTF from spectral lines such as those in the previous section. Figure 6.17 shows spectral line measurements of Hg and Cd lamps performed by Brewer #223 (belonging to Kipp and Zonen) from 286.5 nm to 363 nm.

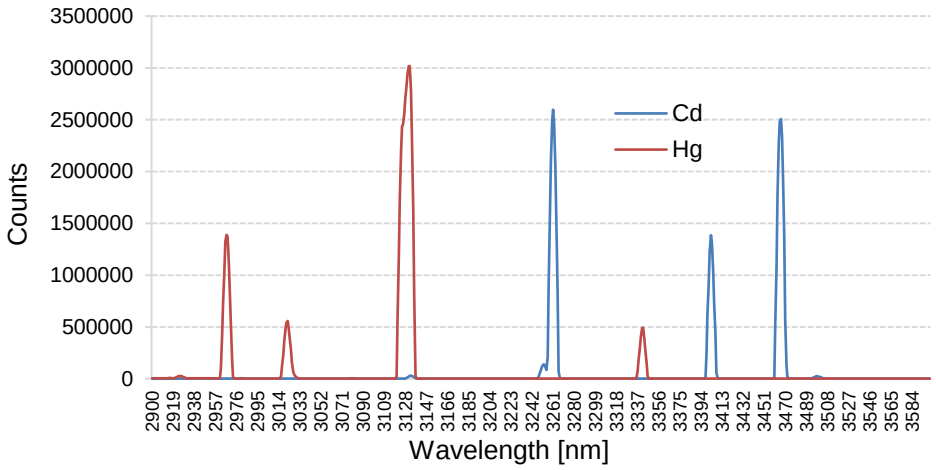

Figure 6.17 Measurements of Hg lamp and Cd lamps performed by the Brewer spectrophotometer #223 (courtesy of Kipp and Zonen).

Figure 6.18 and Figure 6.19 display two Hg spectral lines measured by the Brewer #223 at 296.728 nm and 334.138 nm, with an FWHM of 0.6 nm and 0.56 nm, respectively.

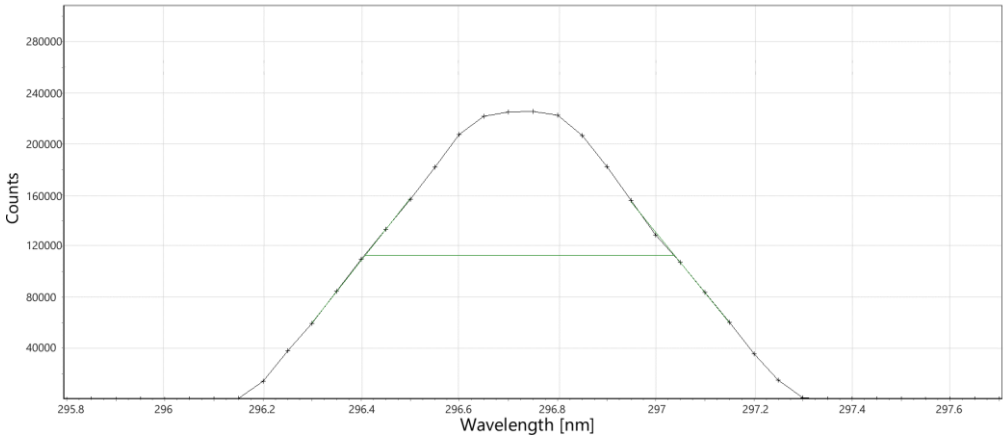

Figure 6.18 Displays the Hg spectral line at 296.728 nm measured by Brewer #223, having an FWHM of 0.6 nm (plot provided by K&Z).

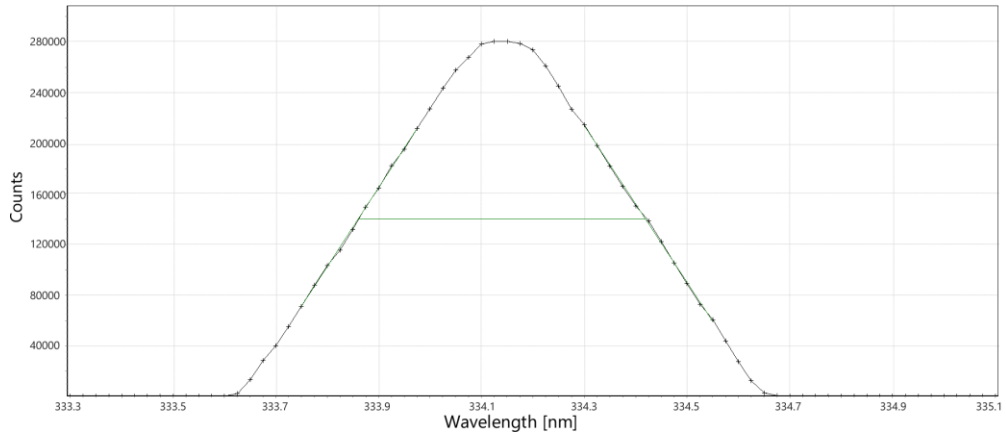

Figure 6.19 Displays the Hg spectral line at 334.138 nm measured by Brewer #223, having an FWHM of 0.56 nm (plot provided by K&Z).

Table 6.1. FWHM comparison as a function of wavelength between the AOTF spectrometer and Brewer #223.

Hg lines(nm)	**Cd lines(nm)**	**FWHM AOTF [nm]**	**FWHM Brewer [nm]**
292.541 nm			
	298.062 nm		
296.728 nm			0.6 nm
	308.082 nm		
312.56 nm		~0.2 nm	
313.17 nm		~0.2 nm	
334.14 nm			0.56 nm
	349.99 nm	~0.25 nm	
	361.20 nm	~0.25 nm	
365.01 nm		~0.3 nm	
365.48 nm		~0.3 nm	
366.32 nm		~0.3 nm	

404.65 nm		~0.35 nm	
407.78 nm		~0.35 nm	
435.83 nm		~0.45 nm	
	468.01 nm	~0.5 nm	
	480 nm	~0.5 nm	

At the short UV wavelengths used to measure ozone, the FWHM of the AOTF is about half that of the Brewer, improving stray light from nearby wavelengths and resolution. Note that the FWHM of the AOTF increases with wavelength but is reasonably consistent over the wavelengths used to measure ozone – as is the Brewer, although there is an indication from these data that the Brewer FWHM may decrease slightly with increasing wavelength.

6.4. 50W and 200W Halogen lamp

The broad spectrum of calibrated halogen lamps is widely used to measure the absolute stability of UV spectrometers with time. For example, the Brewer spectrophotometer uses a small 20W halogen lamp for this purpose, mounted inside the casing of the instrument. Figure 6.20 displays the spectrum of a common halogen lamp.

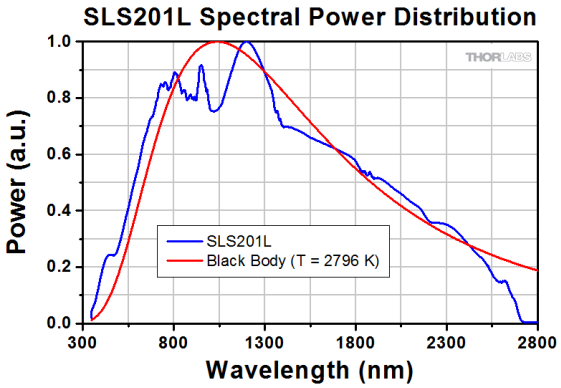

Figure 6.20 Spectral power distribution of a 200W halogen lamp (SLS201L from Thorlabs) compared with a black body.

Two low power field calibration units were tested, one 50W halogen lamp and one 200W halogen lamp. Since they have to be placed close to the input optics, a diffuser is required to provide a uniform light distribution, avoiding imaging the filament at the instrument input. The diffuser was adapted to the entrance optics of the proposed spectrometer only for this test. However, the diffuser significantly reduces the signal. When combined with the necessary bandpass filter to reduce stray light from visible wavelengths within the AOTF system, the output beam was too low to be detected by the APD. Even after integrating 200 times one single measurement, the AOTF spectrometer was not able to recover the signal from the lamp. This is one of several indications that a more sensitive detector is required (see further work in Chapter 8).

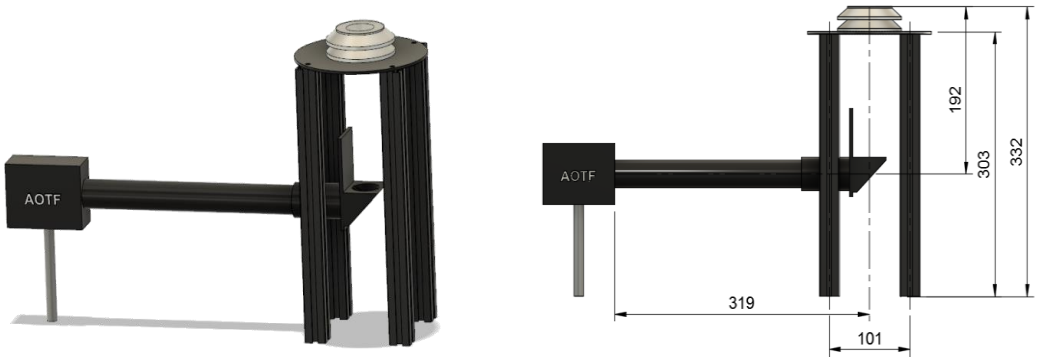

Figure 6.21 Setup of the mounting used to measure Schreder UV stability kit

6.5. Temperature stability test using a temperature chamber

A temperature chamber at the Kipp and Zonen facilities in The Netherlands was used to assess the temperature sensitivity of the AOTF spectrometer and some of its component parts.

The first temperature test was performed with all the electronic and optical parts of the proposed spectrometer inside the temperature chamber (including the HG lamp and its power supply), see Figure 6.25. A second temperature test was performed with only optical parts of the spectrometer inside the temperature chamber to determine whether the electronics or the optics were the most temperature-sensitive parts. The result of such tests is described in the following paragraphs.

In the initial experiment, the light source (Hg lamp), the detector and the AOTF were placed outside the chamber, while the RF generator was located inside the temperature chamber (see Figure 6.22). A mercury lamp from the Brewer was used as a light source during this test to identify any shift in wavelength by varying the temperature of the RF controller.

Figure 6.22 Setup of the temperature chamber test, where the RF generator was the only device inside the temperature chamber.

The temperature chamber was set up to start from 0 °C and gradually increase the temperature up to 50° C. There was not any noticeable shift in wavelength during all the tests. Figure 6.23 shows multiple scans of the Hg lamp across the temperature range, while Figure 6.24 is an expanded view of the mercury lines. There was no wavelength shift associated with changing the temperature of the RF controller, but there was a very significant attenuation of the signal when the temperature was at either extreme (cold or hot). The maximum signal was achieved with the RF controller at a temperature of ~20^{o} C, indicating that this would be the optimum temperature at which to stabilise this element of the instrument.

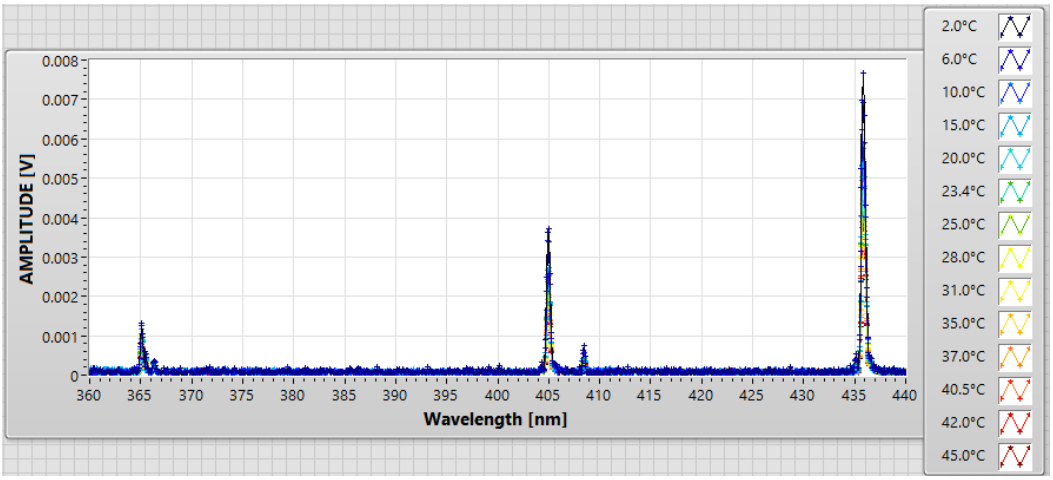

Figure 6.23 Plot of Hg spectral lines measured during the temperature chamber test. These variations are the result of temperature changes in the RF generator.

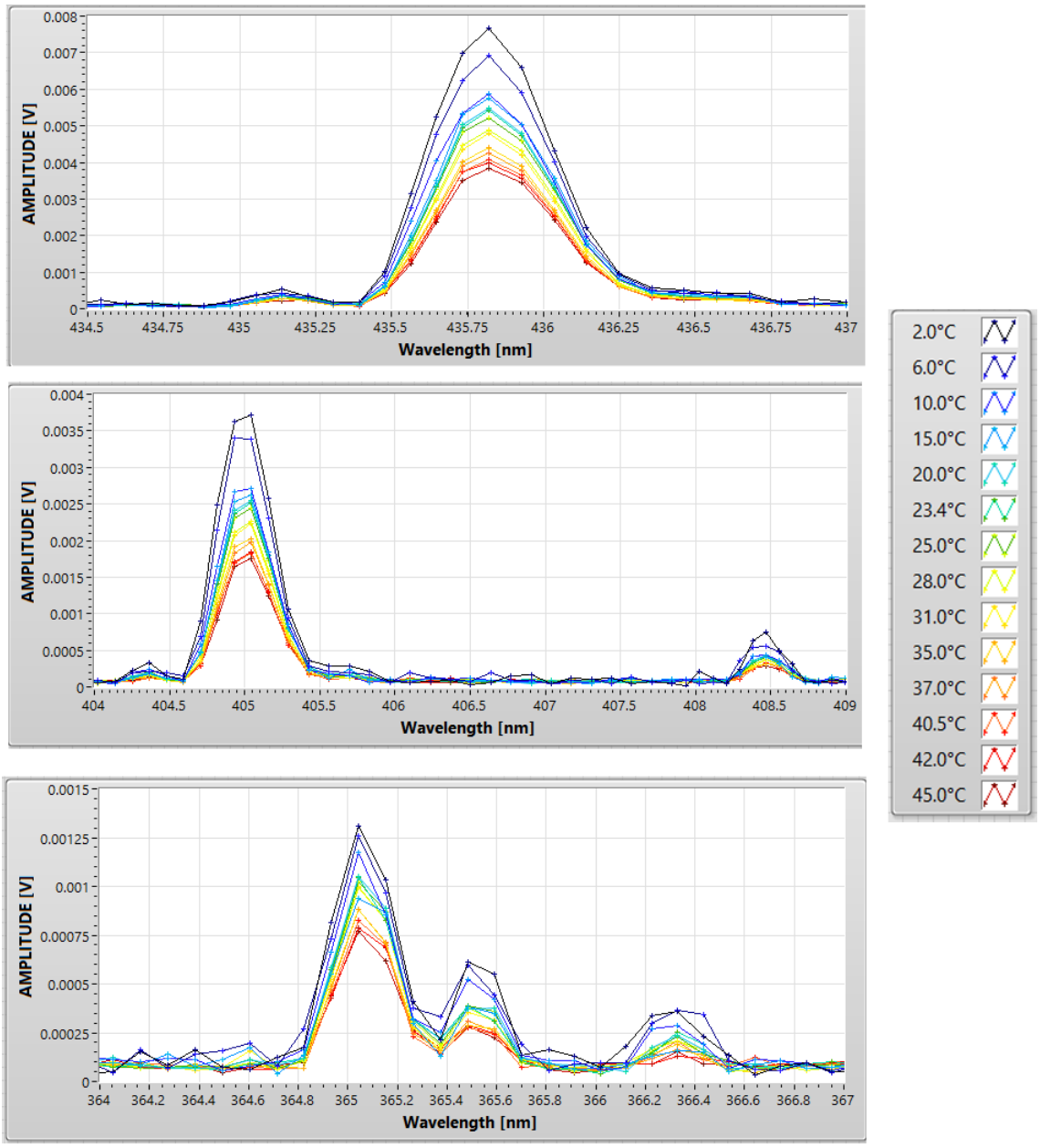

Figure 6.24 Measurements of mercury spectral lines during temperature chamber tests. These variations are the result of temperature changes in the RF generator.

The temperature stability test was then made by placing the entire optics of the AOTF spectrometer inside the temperature chamber (see Figure 6.25), with the RF generator outside. Unfortunately, this meant the mercury lamp and its power supply were also placed inside as the chamber window does not transmit UV wavelengths. For this reason, this test is not 100% reliable as it incorporates any effects of temperature variations on the Hg lamp and its power supply. The wavelength of the Hg lamp output should not change with temperature, but its amplitude might.

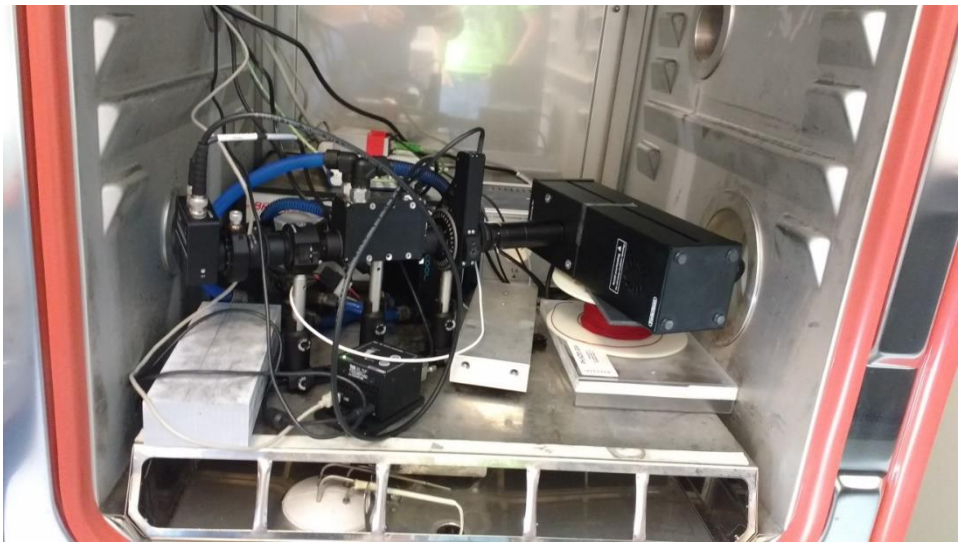

Figure 6.25 Setup used during the temperature stability test. The whole optics of the AOTF spectrometer are placed inside the temperature chamber.

The temperature inside the chamber was set to stabilize at 50º C and then steadily decrease until it reached -10º C, a process lasting approximately 6 hours. During this time, the AOTF spectrometer performed periodic measurements of 7 Hg spectral lines every 10 minutes. Figure 6.26 displays the results obtained from this test, showing a slight shift in wavelength of ±0.15 nm when comparing measurements at 50º C and measurements at -10º C. Such a shift is positive at wavelengths below 365 nm, null near 365 nm and negative for wavelengths higher than 365 nm.

The amplitude axis in Figure 6.26 represents the output of the lock-in amplifier in volts. Note that these measurements are not normalized in order to visualise amplitude variations because of the temperature. Such measurements show the lowest output near 50º C and the highest one near -10º C, so a consistent decline in signal as the temperature increases: the AOTF optics are best operated at low temperatures. If all components of the instrument have to be stabilised at a single temperature, then 25º C would optimise the RF sensitivity and give reasonable sensitivity from the optical components whilst not being extreme with respect to environmental temperatures within which the instrument might operate. Additionally, this is the recommended operating temperature for the AOTF is 25º C, according to the manufacturer.

Note that the wavelength shift between -10 to +50º C is between 0.1 and 0.2 nm – in the same direction. Therefore, the relative shift for a ratio of wavelengths is < 0.1 nm. The change with wavelength is also linear, so it was possible to apply such corrections to the performed measurements presented in Chapter 7.

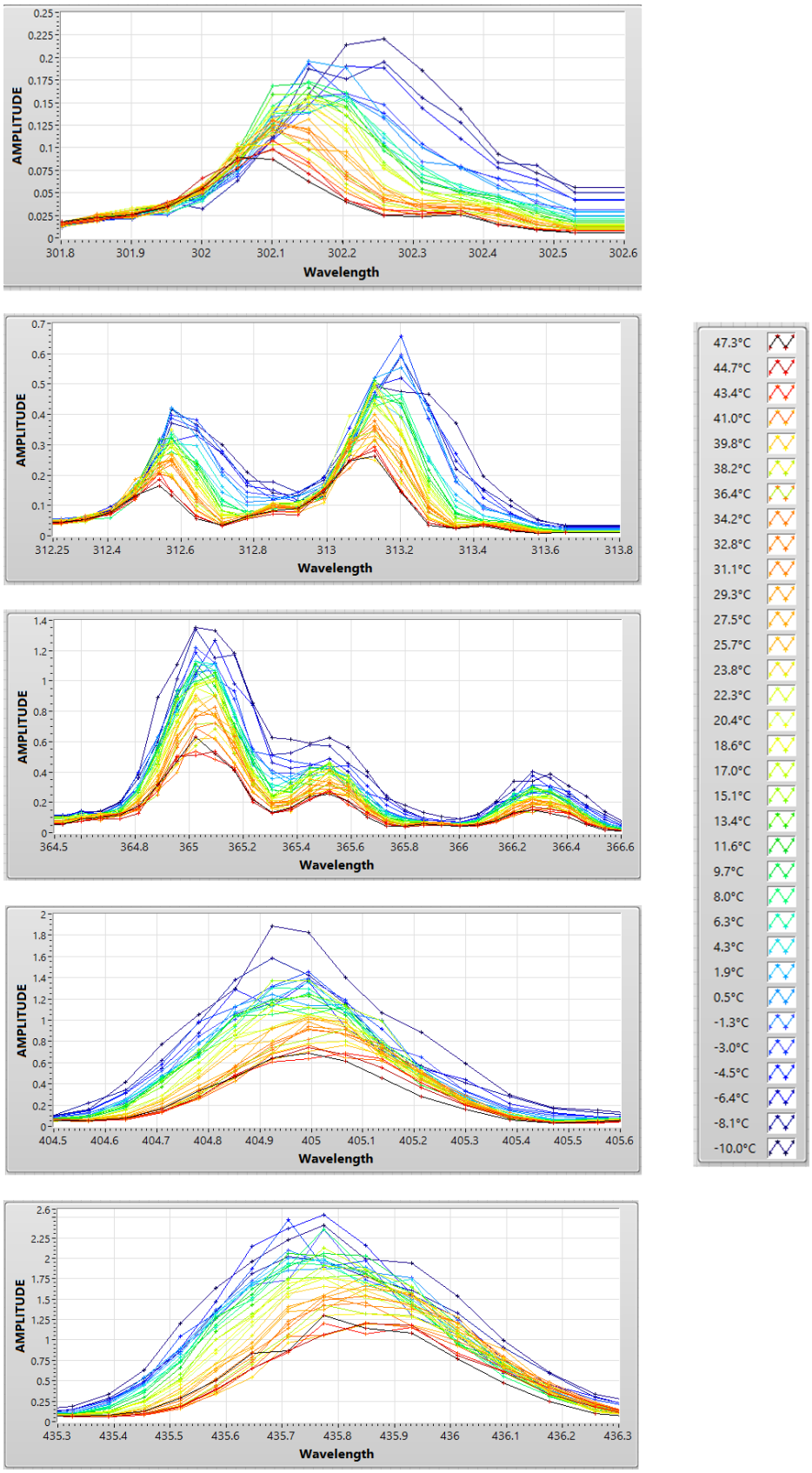

Figure 6.26 Illustration of measurements performed during the temperature stability test for each spectral line. Each colour line represents one measurement at the indicated temperature, starting at 47.3º C (red) and finishing at -10º C (blue). The Amplitude was normalized based on the measurements at 47.3º C.

6.6. Broadband sources and fine-scale modulation

Early in the development of the AOTF spectrometer, two LED sources (UV and white light) were employed for initial tests of the spectrometer performance, and in doing so, long wavelength stray light and an unexplained modulation were identified in the spectrometer performance. The modulation is at a very fine scale and is not identifiable in the general characterisation tests in the previous parts of this chapter. Nevertheless, the feature is included here for the sake of completeness. The preliminary measurements were made before the wavelength alignment had been completed, so there is a wavelength shift between the theoretical spectra and those measured.

6.7. White LED (6500K)

A high-Power white LED (MCWHL2) with a correlated colour temperature of 6500 K was used to prove that the solid-state spectrometer was able to measure the spectrum of a light source above 400 nm. Figure 6.27 shows a comparison between the spectral response of the white LED, obtained from its manufacturer Thorlabs, and the spectral response obtained from the measurements with the AOTF. Note that the AOTF spectrum is a raw signal and does not include calibrations for the spectral response of the AOTF. In addition, those measurements were based on scanning the RF frequency applied to the AOTF and then fitted into a polynomial function to obtain their respective wavelength (see Figure 6.28). Thus, it is understandable at this stage that the wavelengths do not precisely match.

Although measurements were repeated several times and the dark measurements were close to zero, the spectral measurements from 250 nm to 350 nm were constants, yet these would not be permitted in a ‘white light’ source. This issue of apparent short wavelength radiation where none should exist arose several times throughout the testing of the AOTF spectrometer, both indoors and outdoors, although chronologically close in time. Note that the results are not presented in chronological order, and neither is the explanation of this phenomenon. Due to Thorlabs does not provide information about any radiation below 400 nm, this report cannot offer any other explanations than it is due to the second refracting order of the AOTF or that the white LED possesses a spectral response that is not included in its specifications.

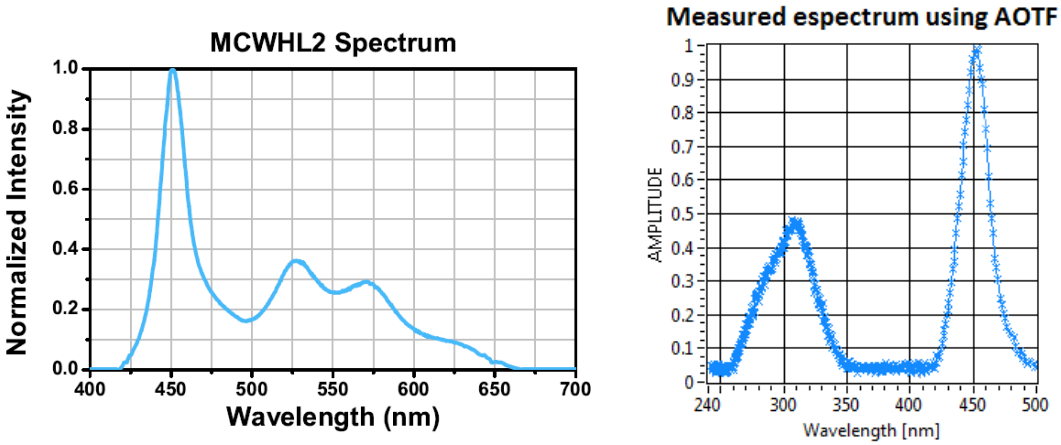

Figure 6.27 The spectrum of the white-LED manufacturer is shown on the left, and the spectrum measured using the AOTF is shown on the right.

6.8. UV LED (365 nm)

An UV LED (M365L2) with a nominal peak wavelength of 365 nm and an FWHM of 7.5 nm was widely used in early tests. Figure 6.28 shows a comparison between the spectral responses from the UV-LED obtained from its manufacturer Thorlabs and the spectral response obtained from the measurements using the AOTF. Note that the wavelengths do not perfectly match because the relationship between RF and wavelength was not defined at that moment.

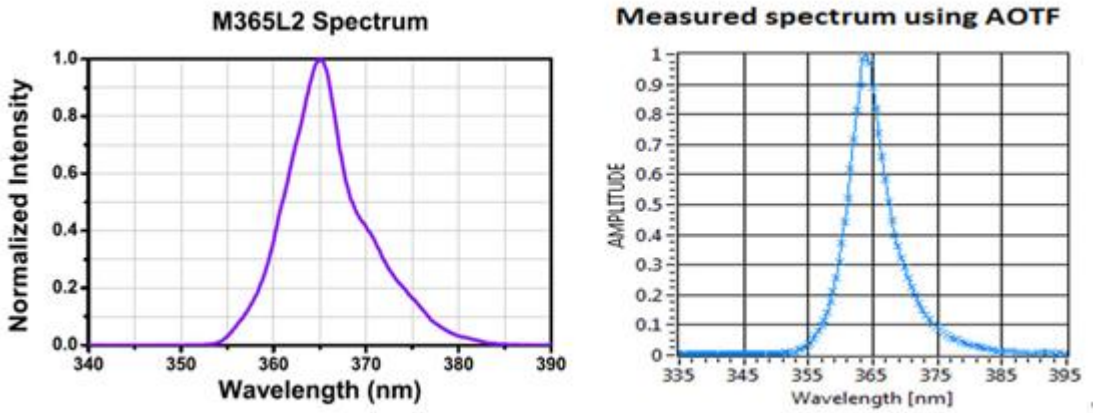

Figure 6.28 The spectrum of UV-LED provided by the manufacturer (Thorlabs) is shown on the left, and the measurements of the proposed solid-state spectrometer are shown on the right. The measurements were integrated ten times and normalized to 1.

6.9. Undesired second wavelength reaching the detector.

The issue of spurious radiation at wavelengths shorter than the source, first seen in section 6.7 (white LED), was also observed with early measurements of a Hg lamp, as shown in Figure 6.29. The two bumps observed near 273 nm and 288 nm indicate the source of this unwanted radiation,

being at wavelengths half those of the Hg spectral lines at 546 nm and 579 nm, respectively. The FWHM of such undesired wavelengths is more significant because it increases with wavelength. We hypothesise that the measurement of the undesired second wavelength is due to internal acoustic interference inside the AOTF crystal, or rather the traditional explanation of refraction orders does not apply to the AOTF.

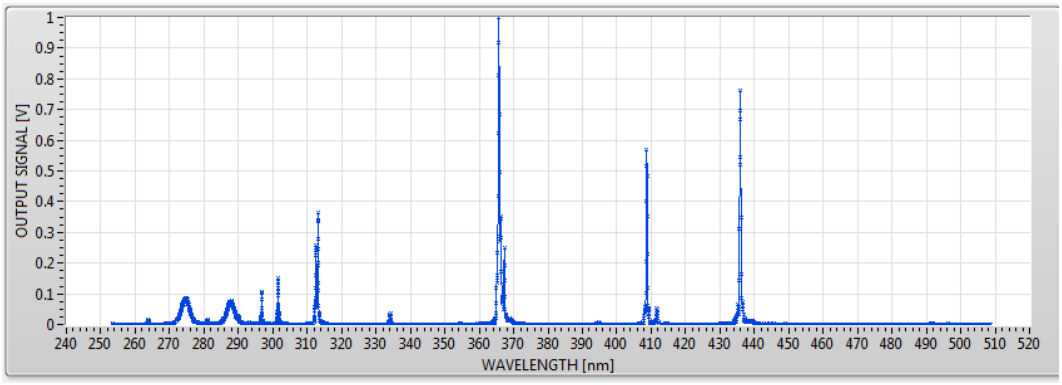

Figure 6.29 Linear representation of Hg spectral measurements.

This phenomenon was also noticeable during solar UV measurements within a similar timeframe. The first solution was placing the UG11 filter from Thorlabs, which was at hand during outdoor measurements in Delft (see Chapter 7). All final measurements with the instrument, i.e. those earlier in this chapter, employed the UG11 filter described in section4.1.2.

6.10. Summary

The purpose of this chapter was to present the calibration and characterization processes of the proposed spectrometer. The initial spectral measurements performed by the instrument used the wavelength calibration provided by the AOTF manufacturer. Because the relation between frequency and wavelength is not linear, it was necessary to perform spectral line measurements from different light sources to generate a customized polynomial fitting.

Additionally, the performed spectral line measurements allowed us to compute the transfer function of the AOTF across its operating spectral range, getting the relation between FWHM with wavelength. It was also found that there are variations in the amplitude and the central wavelength of the transfer function at different temperatures. These measurements were performed with the previous AOTF using a water-cooling system, and it was not possible to repeat such tests with the new AOTF that is TE-cooling controlled. However, it can be observed in Figure 6.23 and Figure 6.24 that there are only linear variations in amplitude when the RF generator is subject to changes in temperature while the AOTF remain at a stable temperature. Therefore, measurement corrections are applied to compensate for temperature changes in the RF generator when the AOTF is temperature stabilized at 25° C.

It was identified in section 6.4 that even after increasing the number of measurements to reduce background noise to 300 times, it was not possible to perform successful spectral measurements using the halogen lamps as a light source.

Furthermore, it was also discovered that two monochromatic light beams reach the detector, the unwanted one located at twice the selected wavelength. Therefore, according to Figure 6.7, it is assumed that there are stray acoustic waves with half the frequency in the AOTF crystal. The RF generator output measurements did not show harmonics or frequencies other than the selected one. The manufacturer did not provide information about this phenomenon.

Chapter 7. Direct solar measurements

The ultimate test of the new instrument design was to set it up outside and make atmospheric measurements. The original intention was to undertake a rigorous test at the Regional Brewer Calibration Campaign at El Arensillo in Spain in 2019. Unfortunately, this was not possible in the end, and the field tests of the instrument were limited to those made in Delft against Brewer #223 and Manchester against Brewer #172, both of which are MkIII double monochromator Brewer instruments. The AOTF spectrometer was mounted on an aluminium base, attached to a solar tracker, and it was synchronized with the appropriate Brewer spectrometer. The distance between the two instruments was about 3 meters when the field measurements were performed at Kipp and Zonen facilities (Delft, The Netherlands 4.38° lat, 51.99° long, 6 m altitude), and about 500 meters when the calibration was performed at Manchester, UK (-2.23° lat, 53.47° long, 63 m altitude) when the Brewer was in its standard monitoring position on the roof of another nearby building. The measurements were performed during clear-sky conditions at Delft (see Figure 7.1), but conditions were less than ideal in Manchester, though there were periods with a clear solar disc. In both cases, solar scans were performed from 293 nm to 363.5 nm.

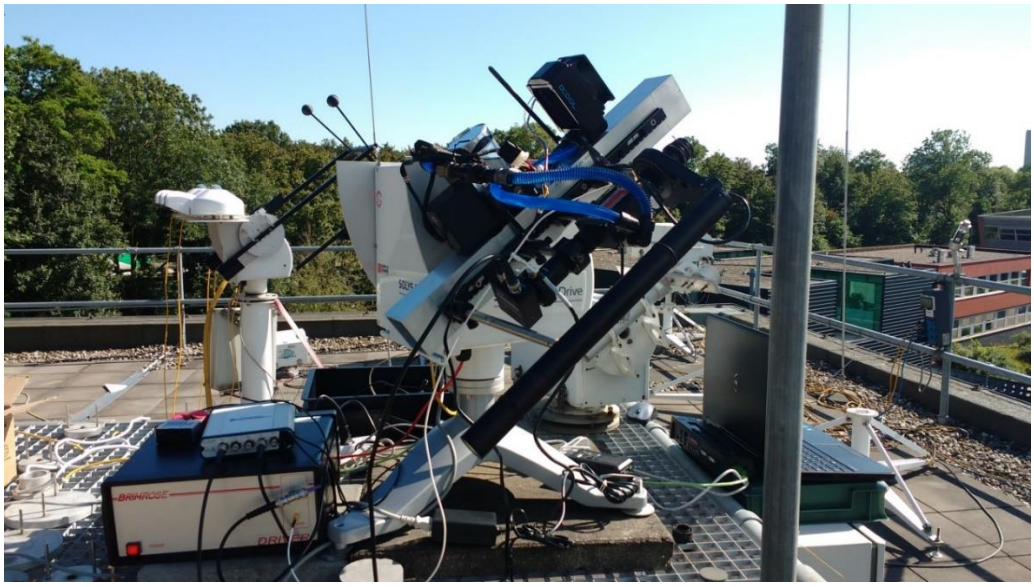

Figure 7.1 Setup used during direct solar radiation measurements at Delft June 2018.

7.1. Direct solar measurements at Kipp and Zonen facilities in Delft, The Netherlands

The number of times a single measurement was integrated to reduce random noise was modified during each comparison to allow synchronization with the Brewer spectrometer. The minimum step that the Brewer is allowed to perform is 0.025 nm, while the minimum tuning of the AOTF is given by the minimum frequency step that the RF unit can generate (18 Hz), equivalent

to ~0.00003 nm. The maximum resolution of the AOTF is determined by the width of a measured spectral line, which varies from 0.2 nm to 0.4 nm. On average, the AOTF spectrometer performs 18 integrations of the same measurement, while the Brewer realizes one. Most of the UV scanning comparisons have been normalised to the peak value for the scan because neither instrument needs an irradiance calibration to perform TOC measurements. Note that the different spectral response of the AOTF spectrometer and the Brewer affects the comparison of uncalibrated solar scans.

The first direct solar scan performed by the AOTF spectrometer shown in Figure 8.2 was not very promising, but applying a UV bandpass filter to attenuate wavelengths in the visible and near-infrared spectrum solved the issue. After the analysis of several measurements without using any input filter (including spectral line measurements), it was discovered that wavelengths in the visible and near-infrared from ~580 nm to ~720 nm pass through the AOTF crystal, apart from the desired wavelength. The cause of this effect is still unknown, with two possible explanations. The first is that the RF applied to the AOTF is not pure, and there is an attenuated lower frequency mixed with the principal one. However, the output of the RF unit was analysed using the FFT function of an oscilloscope without showing a prominent peak at any frequency other than the selected one. Harmonics does not explain this phenomenon because higher frequencies are linked to lower wavelengths (see Figure 6.2). The second possible explanation is that the acoustic waves inside the crystal generate interference at lower frequencies, allowing the filtering of two wavelengths simultaneously. Note that the second wavelength seems to be double in value of the selected one.

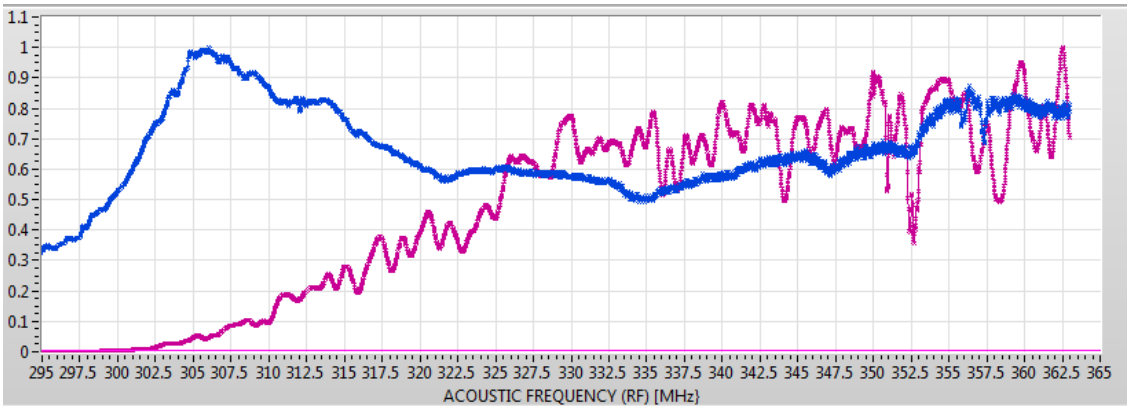

Figure 7.2. Normalized measurement comparison between the AOTF spectrometer (blue) and the Brewer #223 (pink) without UG11 on 26th June 2018. The wavelength step of Brewer and the AOTF spectrometer is 0.05 nm from 290 nm to 363 nm (CZ scan). The AOTF had to integrate about 18 times to match the speed of the Brewer of ~0.5 seconds per wavelength.

Once the bandpass filter UG11 was placed within the AOTF input optics, its spectral measurements were in much better agreement with those made by the Brewer (see Figure 7.3).

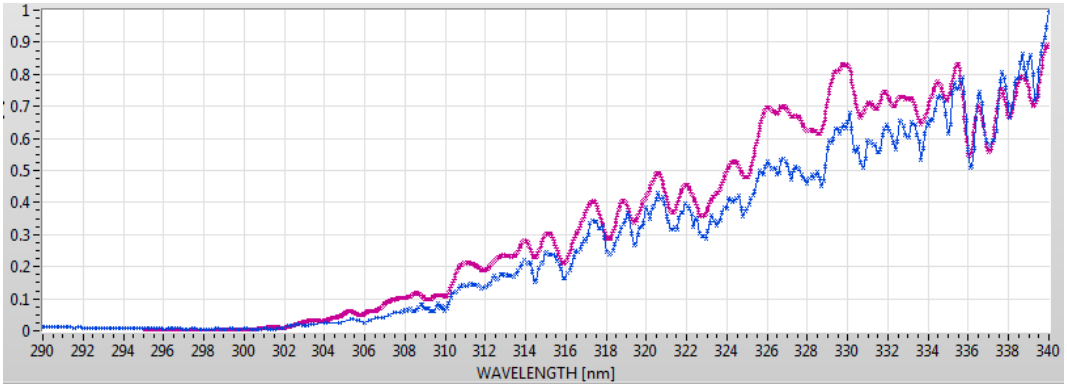

Figure 7.3 Normalized measurement comparison between the AOTF spectrometer (blue) and the Brewer #223 (pink) using UG11 filter on 27th June 2018 (integration value=10). The wavelength step of Brewer is 0.05 nm (CZ scan), and the AOTF spectrometer is 0.1 nm from 290 nm to 340 nm.

Figure 7.4 and Figure 7.5 display a comparison made on 29th June 2018 between the AOTF spectrometer and Brewer under clear-sky conditions.

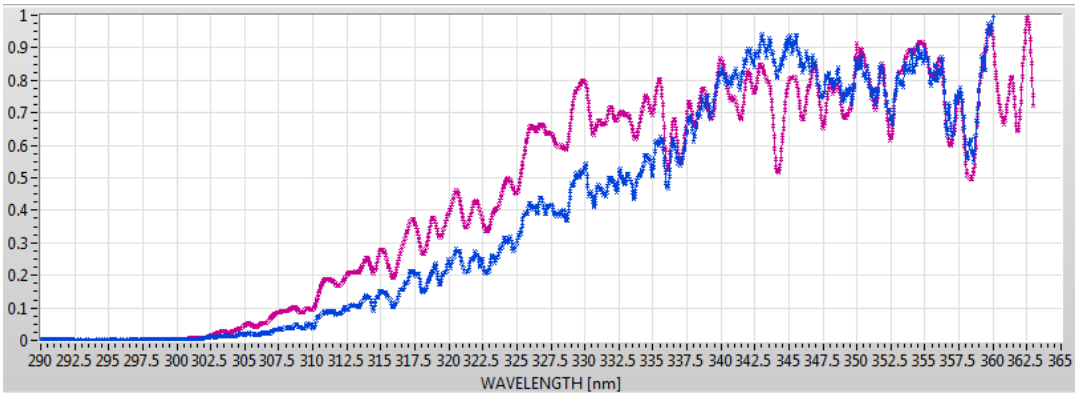

Figure 7.4. It displays a clear sky measurement comparison between the AOTF spectrometer with an integration value of 20 times (blue) and the Brewer #223 (pink) on 29th June 2018 across the entire wavelength range of the Brewer (CZ scan from 290 nm to 363 nm with a step of 0.05 nm).

The differences between the solar spectrum measured by the AOTF spectrometer and the Brewer #223, presented in Figure 7.3 and Figure 7.4, are produced because the two spectrometers have different spectral responses. However, their measurements should match perfectly if both instruments provide irradiance values, assuming they are properly calibrated.

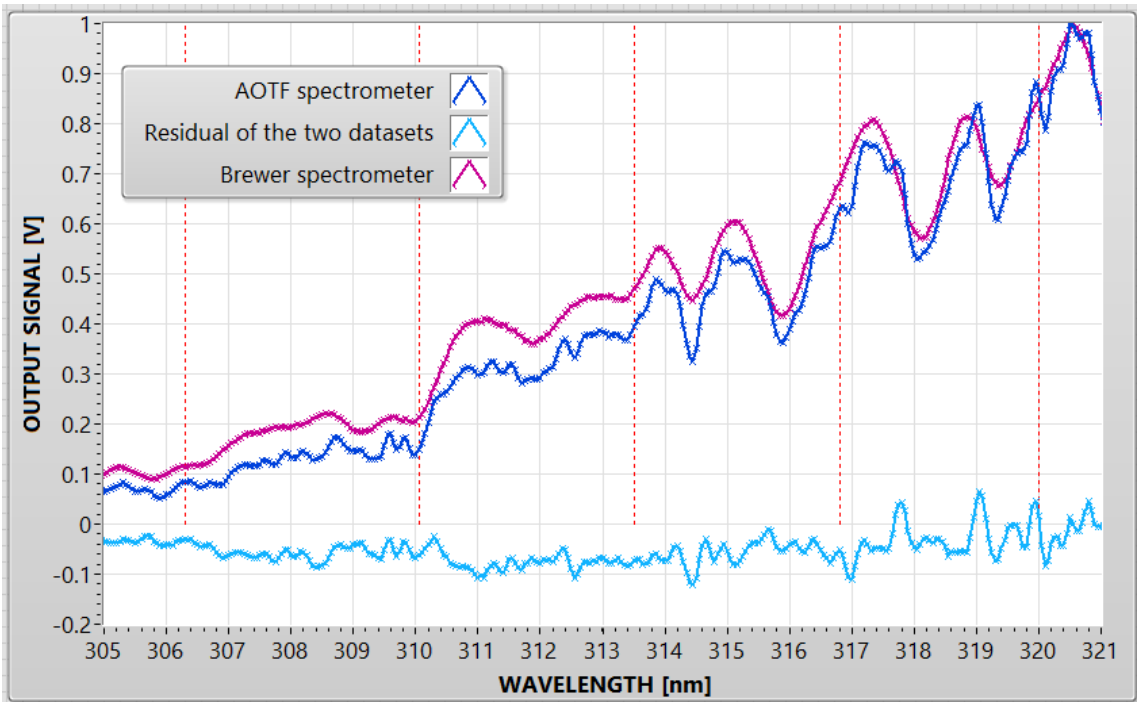

Figure 7.5. Zoom of the figure Figure 7.4 to cover the wavelength range used for TOC measurements from 305 nm to 321 nm on 29th June 2018 at 15:26 UTC. It displays normalized comparison measurements between the AOTF spectrometer (blue) and the Brewer #223 (pink), as well as the residual between the two datasets. The red lines show the wavelengths used for TOC estimations from Brewer's manual (306.3 nm, 310 nm, 313.5 nm, 316.8 nm and 320 nm). The amplitude of both datasets was normalized.

The first solar UV measurements of the AOTF spectrometer (displayed in Figure 7.5) were performed without an absolute calibration. It clearly shows its wavelength alignment and its higher spectral resolution compared to the Brewer. The peaks and valleys of Fraunhofer lines in the solar spectrum are well reproduced, while the signal values are normalised to the peak wavelength in each scan. The output signal is not calibrated for absolute irradiance in both spectrometers: the Brewer values are photon counts per wavelength, while the AOTF values are output voltages from the APD. Thus, the agreement or divergence between the normalised output signals represents the differences in the spectral response of the two instruments.

7.2. Direct measurements at The University of Manchester, UK

Further direct solar scans provided solid evidence that the AOTF spectrometer can successfully measure a narrow range of wavelengths across its operating spectral range (280 nm to 460 nm). The following paragraphs will describe the performance of the AOTF performing UV scans at a different location (Manchester) and its first ozone calibration. Figure 7.6 shows the AOTF spectrometer (on its optical rail) mounted on an EKO solar tracker and pointing at the sun, while Figure 7.7 shows it in the zenith sky mode. The AOTF was located on a platform at the side of the Simon Building, University of Manchester, while the Brewer #172 remained at its standard

monitoring position on the Pariser Building rooftop, at ~ 500m from the measuring site and ~ 50m higher.

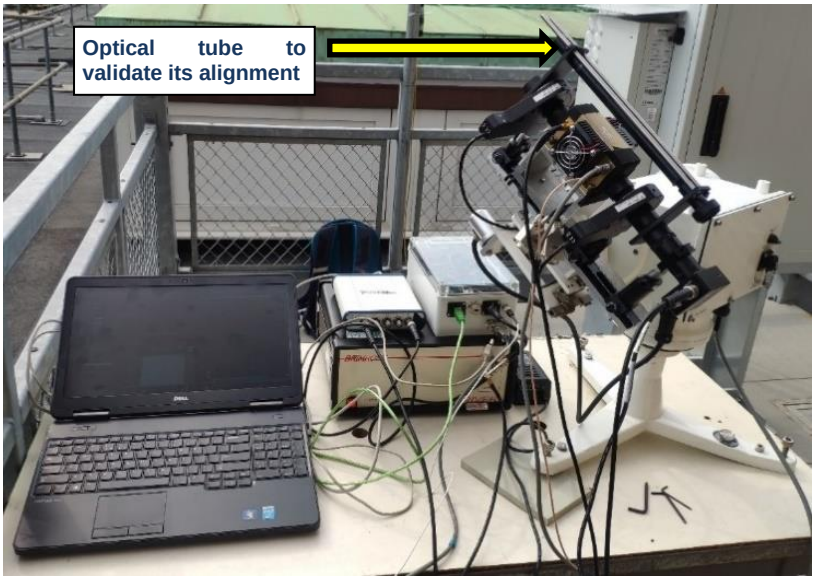

Figure 7.6 Picture of the AOTF mounted on a solar tracker while performing direct solar measurements (Manchester, UK).

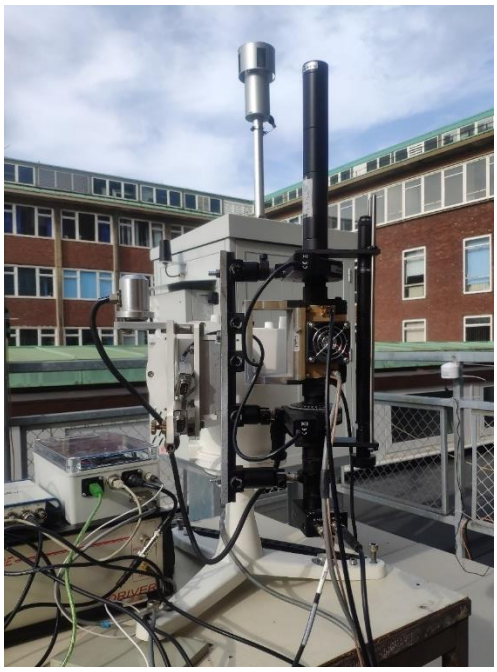

Figure 7.7 The AOTF is mounted on a solar tracker and pointing at the zenith sky (Manchester, UK). Note that the silver pole that appears to be protruding from the top of the tracker is another instrument mounted further back on the platform.

The AOTF spectrometer performed zenith sky measurements on several occasions, but the signal was too low to be distinguished from the background noise, even with the lock-in amplifier. As a result, it can be concluded that the spectrometer's sensitivity is not enough to perform such measurements, and either an improved throughput or a more sensitive detector would be required

for this type of measurement. Therefore, the AOTF spectrometer is used exclusively to measure direct solar radiation.

The best performance of the AOTF spectrometer occurs when measuring direct scans of the solar spectrum, where the AOTF spectrometer showed a good correlation with the Brewer measurements. Figure 7.5 and Figure 7.8 compare in the same graph the relative output of the Brewer spectrometer with the AOTF spectrometer, which is not calibrated to measure direct irradiance. Measurements at Delft and Manchester showed consistency with the same optimistic output, even when the TE-AOTF and the RF unit were replaced after the Brewer comparisons performed in Delft.

Notice that the water-cooling system was replaced by thermoelectric cooling (TE-AOTF) after the Brewer comparisons performed in Delft. The instrument characterization of the AOTF before and after such changes does not show significant differences that might impact the AOTF spectrometer's performance. Additionally, the initial bandpass filter UG11 produced by Thorlabs and used to exclude the interference/stray-light from longer wavelengths was substituted with an improved version from a different manufacturer (see Chapter 4).

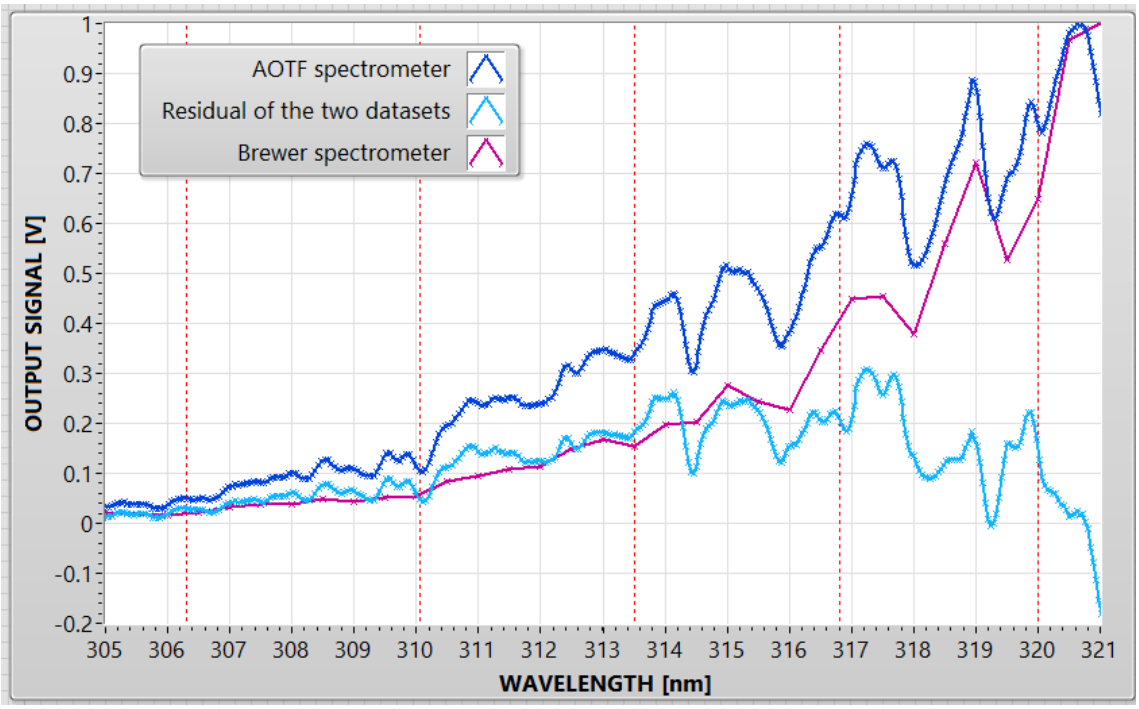

Figure 7.8 Spectral comparison of direct solar measurements on 25th September 2020 at 15:14 UTC, SZA equals 67.76° from 300 nm to 320 nm. The blue line represents the AOTF scan measurements (0.05 nm resolution), the pink graph displays the measurements of Brewer 172 (0.5 nm resolution), and the light blue line indicates the residual between the two datasets. The red lines show the wavelengths used for TOC estimations from Brewer's manual (306.3 nm, 310 nm, 313.5 nm, 316.8 nm and 320 nm). Note that after the return of the AOTF, the detailed wavelength calibration from Delft could not be assumed to remain. It was checked for the returned system, but only with a number of Hg lines. These indicated that the wavelength calibration was still viable and matched Figure 6.7.

The Brewer spectrometers perform internal calibrations to keep the micrometres that rotate the slit mask and the diffraction grating in the correct position (0.05 nm steps). As a result, each Brewer has customized operating wavelengths to measure TOC close to those specified in Brewer's manual: 306.3 nm, 310 nm, 313.5 nm, 316.8 nm and 320 nm (see Figure 7.8). The wavelengths used by Brewer #172 are 306.287 nm, 310.031 nm, 313.480 nm, 316.779 nm, and 319.976 nm. Clearly, the performance of the AOTF in this regard is commensurate with that of the Brewer, whose procedures are being mimicked during this research. Since mechanical parts do not restrict the AOTF, the proposed spectrometer can perform spectral scans faster and at a higher resolution than the Brewer. Thus, one future option for calibrating the AOTF might consist of taking high-resolution scans and processing measurements at slightly different wavelengths to optimise the ozone column retrieval during post-processing.

Table 7.1 Minimum and maximum values of SZA during measurements with the presented spectrometer

DATE	FIRST MEASUREMENT OF THE DAY		MEASUREMENT CLOSEST TO NOON		LAST MEASUREMENT OF THE DAY	
	HOUR (UTC)	SZA	HOUR (UTC)	SZA	HOUR (UTC)	SZA
17th September 2020	12:20:15	51.61367	12:20:15	51.61367	15:34:23	67.22945
18th September 2020	9:28:15	-60.8142	11:59:36	-51.8801	15:39:53	68.31679
25th September 2020	9:16:05	-64.3082	12:00:01	54.59636	14:19:52	61.8283

Total ozone column measurements were attempted on three days in September 2020 from the roof platform to the Simon Building in Manchester, UK, at times described in Table 7.1. As shown in Figure 8.6, the instrument was mounted with the tracker aligned and set to track the sun for direct sun measurements of ozone. The alignment of the AOTF was manually and visually validated with an optical tube attached to the AOTF spectrometer (Figure 7.6). It is parallel to the instrument's optical path, has a neutral density filter to attenuate solar radiation (for eye safety), and has a circular graticule to centre the sun's image correctly. Note that zenith sky measurements are not possible with the existing detector. Thus, only direct sun measurements are reported in the following paragraphs. Since the whole set-up was temporary and less stable than a routine monitoring instrument, the alignment to the sun was frequently monitored.

7.3. Measurements of Total ozone column at The University of Manchester, UK

7.3.1. Instrument intercomparison-calibration with Brewer #172

There were several modifications to the AOTF spectrometer since it performed field measurements at Kipp and Zonen facilities in Delft, the Netherlands. The AOTF crystal used at the beginning of this research suffered from water leaking and was replaced with an updated version with thermoelectric cooling instead of a water-cooling system. Additionally, the RF unit was damaged during transportation, and it had to be repaired by its manufacturer. Due to the pandemic and the deadline for this PhD, it was impossible to repeat all the previous characterizations of the instrument. However, the function describing the relationship between RF and wavelength remained constant (see Chapter 6), and the temperature dependence of the crystal is expected to be reduced because the TE cooling keeps the AOTF's crystal at a constant temperature of 25° C ± 1%.

The first measurement of direct solar radiation using the new TE-AOTF was performed on September 17th, 2020, which was a cloudless day and ideal for measurements that could act as the basis for calibration. However, the whole direct sun alignment setup and configuration had to be installed on the roof platform during the morning, so measurements started early in the afternoon. As the proposed spectrometer does not have a weatherproof case and it was exposed to weather conditions, it could not be left outside and unattended during the night. Thus, all the setup had to be repeated on each measurement day.

The left graph in Figure 7.9 displays the time and SZA of ozone measurements performed by the Brewer (blue dots) and the AOTF spectrometer (red dots) throughout the day. The right graph plots the estimated ozone values by the Brewer. These Brewer O_3 values were used to transfer the calibration from the Brewer to the proposed spectrometer.

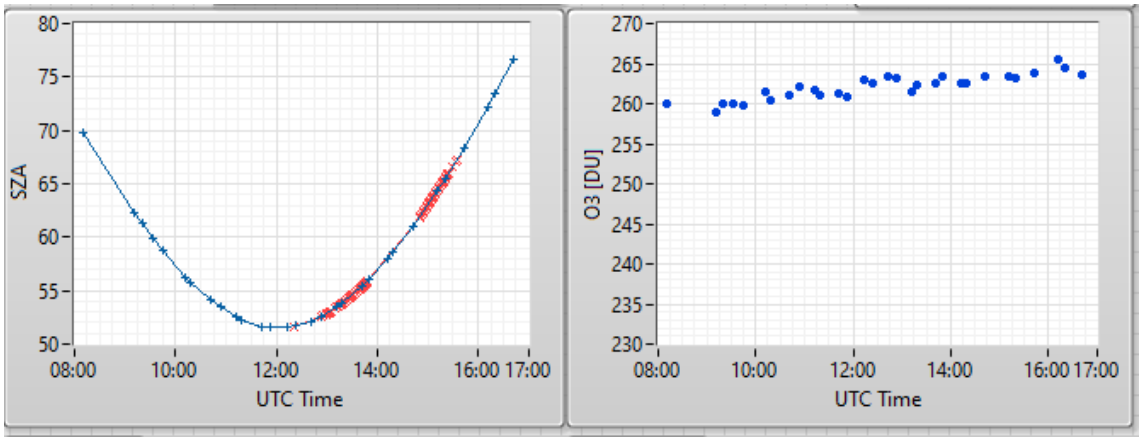

Figure 7.9 Solar zenith angles and direct ozone measurements on 17th September 2020. The left graph compares the total number of measurements performed by the Brewer (Blue) and the AOTF (red) at different times during the day with their respective SZA. The diagram

on the right displays the Brewer ozone measurements with a standard deviation below 2.5 (blue dots).

The process of transferring the Brewer calibration to the proposed spectrometer followed the same procedure as any other Brewer. First, the direct measurements of the spectrometer have to be compensated by the effect of Rayleigh optical depth $\tau(\lambda)$ and its relative optical air mass, $m_\lambda(\theta)$ see Eq. (2.37) and Eq. (2.20).

$$F_i = F_i + \tau(\lambda) x \, m_\lambda(\theta) \qquad i = 2,3,4,5,6 \tag{7.1}$$

Where $F_i = In(I_i)$, θ_0= apparent solar zenith angle and λ represents the Brewer operating wavelengths ($F_2 \rightarrow$ 306.3 nm, $F_3 \rightarrow$ 310 nm, $F_4 \rightarrow$ 313.5 nm, $F_5 \rightarrow$ 316.8 nm and $F_6 \rightarrow$ 320 nm). Notice that most of the Rayleigh scattering occurs at the centre of mass of the atmosphere around 5 km over sea level.

Then the single and double ratios are computed following the procedure described in Brewer's manual.

The following equation estimates the single ratios:

$$MS4 = R1 = F5 - F2 \tag{7.2}$$

$$MS5 = R2 = F5 - F3 \tag{7.3}$$

$$MS6 = R3 = F5 - F4 \tag{7.4}$$

$$MS7 = R4 = F6 - F5 \tag{7.5}$$

Notice that direct solar measurements at 306.3 nm (represented by F2) are significantly affected by SO_2, while the measurements at the other wavelengths are predominantly affected by O_3.

Then, the double ratios are estimated by the following equations, considering that R6 is used for ozone and R5 for SO2 estimations.

$$R5 = MS4 - 3.2 * MS7 \tag{7.6}$$

$$R6 = MS5 - 0.5 * MS6 - 1.7 * MS7 \tag{7.7}$$

Figure 7.10 displays the single and double ratios obtained from the measurements performed by the AOTF spectrometer on 17th September 2020. According to Brewer's manual, the R6 measures the weighted ratio of ozone absorbance between the 310.1 nm, 313.5 nm, 316.8 nm, and 320.1 nm wavelengths.

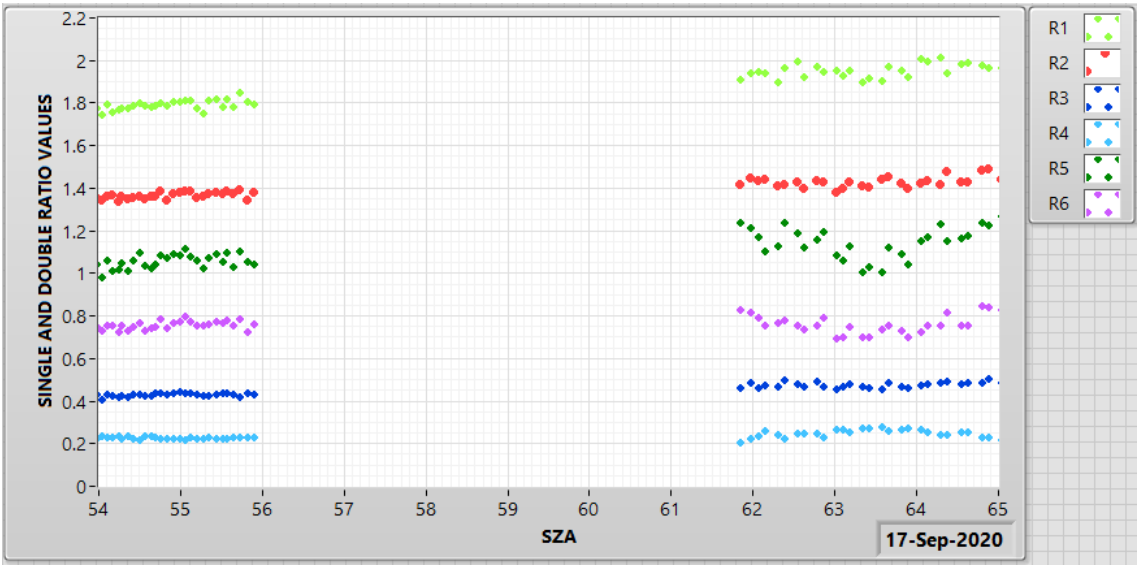

Figure 7.10 Displays AOTF measurements on 17th September 2020 of single and double ratios used for ozone (R2, R3, R4 and R6) and SO_2 estimations (R1 and R5). The plot shows the single ratios: R1 in light green, R2 in red, R3 in blue, and R4 in light blue; and the double ratios: R5 in green and R6 in purple.

Figure 7.11 displays the single and double ratios used for ozone calculations obtained by Brewer #172 on 17th September 2020. It is observed that these values increase with SZA, as the ones obtained with the AOTF spectrometer in Figure 7.10. Note that the double ratio (R6) values estimated by both spectrometers are not identical because both spectrometers have a different spectral response, and the Brewer values are scaled by 10 000.

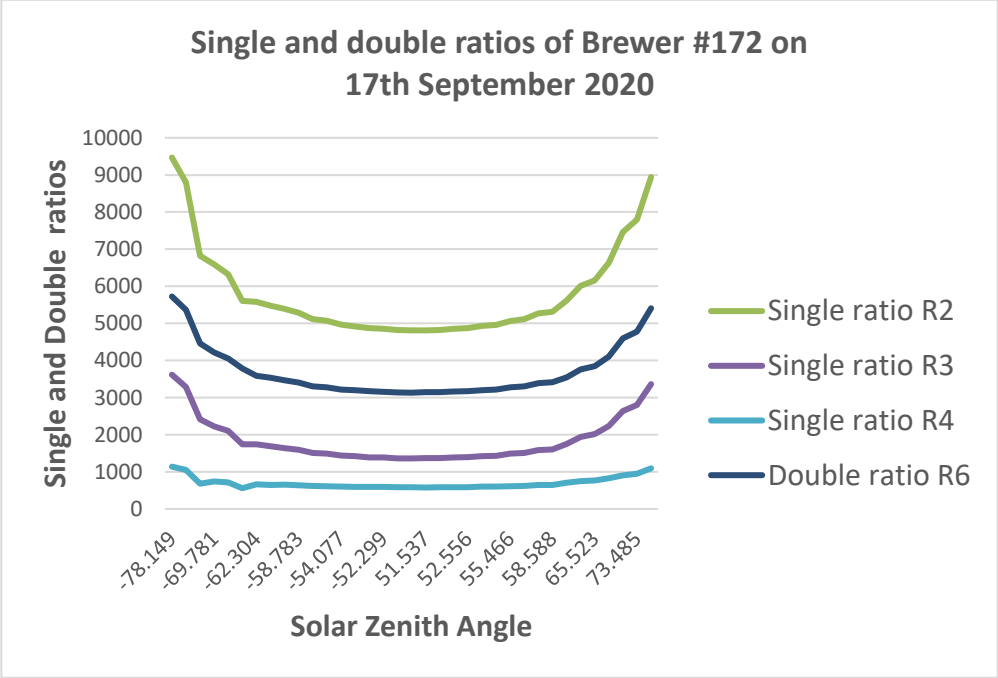

Figure 7.11 Displays measurements on 17th September 2020 of single and double ratios used for ozone (R2, R3, R4 and R6) obtained by Brewer #172. R2, R3, R4 and R6 are represented by a green, purple, light blue and dark blue line, respectively. Negative SZA represents values obtained before noon.

Lastly, the total ozone column (TOC) can be estimated by Eq. (7.8).

$$O_3 = \frac{R6 - ETC_{O3}}{\mu * \ Differential\ absorption\ coefficient\ for\ ozone} \quad (7.8)$$

Where μ is the relative optical air mass corresponding to O_3absorption at 22 km of height.

To transfer the calibration of Brewer #172 into the AOTF spectrometer, the values of TOC measured by Brewer #172 are substituted in Eq. (7.8). Then, the equation is arranged into the form Y=mx+b, where the X-axis represents the ozone slant column and Y-axis the ratio R6. A linear fitting is applied to the plotted data, with a slope equal to the differential absorption coefficient for ozone. The Y-interception of the line represents ETC values for ozone.

Transferring calibration coefficients from the Brewer to the AOTF spectrometer is possible because the wavelengths for deriving the TOC are the same ones that the Brewer spectrometer uses. Therefore, it is possible to use the R6 ratios to get the differential absorption coefficient and the ETC coefficient for ozone.

An initial calibration plotted all the measured data with a Y-axis representing the double ratios R6 and the X-axis representing the product of TOC values multiplied by their air mass factor (see Figure 7.12). However, this resulted in a poor fit because it is necessary to have a more extensive data set with more SZA values to characterize the slant of R6 properly and derive statistically robust results.

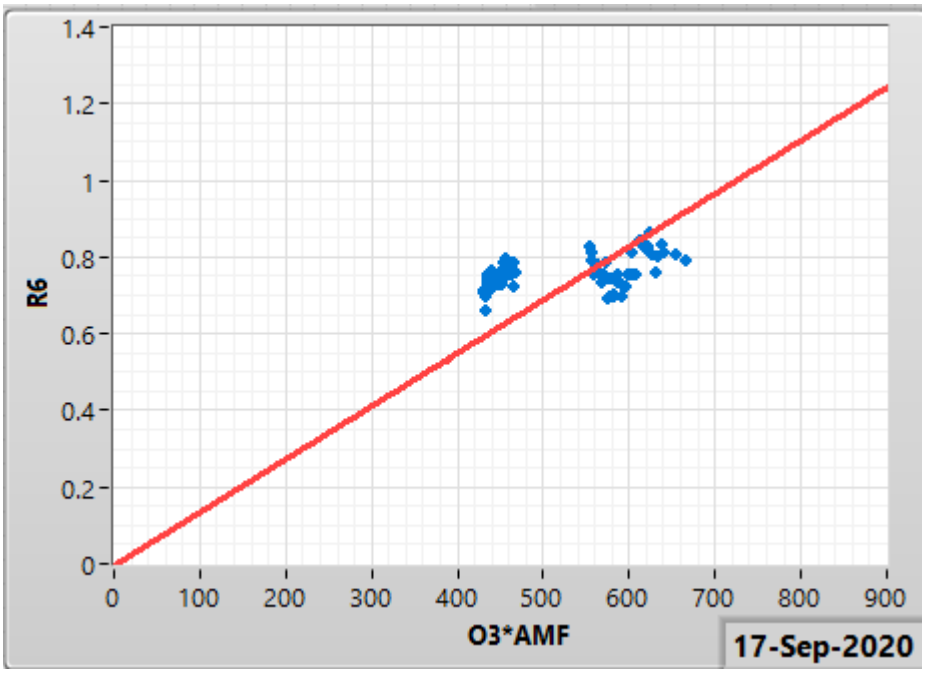

Figure 7.12 The equation y= 0.0013858669x - 0.00558188025 represents the linear fitting (red line) used for the calibration of the AOTF instrument (differential absorption coefficient for ozone=0.0013858669 and ETC for ozone=0.00558188025). Blue dots stand for direct solar measurements of the AOTF.

The calibration described in Figure 7.12 was applied to all raw data of the AOTF obtained during the three days of direct solar measurements at the University of Manchester (17, 18 and

25th September 2020). The calculated R6 does not accurately follow the variability of ozone. One possible reason is background noise plus the mismatch displayed in Figure 7.5 and Figure 7.6 between the wavelengths measured by the AOTF and the Brewer spectrometer. The wavelengths measured by Brewer #172 are 306.287 nm, 310.031 nm, 313.48 nm, 316.779 nm and 319.976 nm (data from Brewer's internal file). On the other hand, the AOTF's wavelengths are 306.3 nm, 310.05 nm, 313.48 nm, 316.74 nm and 320.05 nm to compensate for minimal errors in the wavelength calibration. However, such corrections were made from the interpolation of UV scans, such as the one displayed in Figure 7.13.

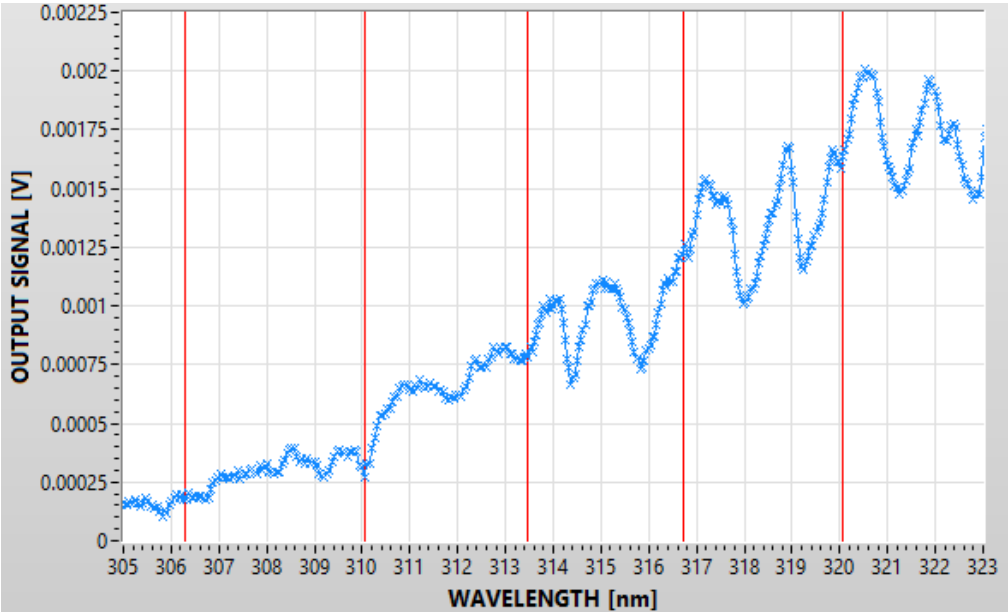

Figure 7.13 Output of the AOTF spectrometer during a solar scan on 17th September 2020 at 13:18 UTC (blue line). The red lines display the wavelengths that the spectrometer uses for ozone measurements (306.3 nm, 310.05 nm, 313.48 nm, 316.74 nm and 320.05 nm).

The AOTF ozone data at around 15:00 UTC on 17th September 2020 is now -matched to the Brewer, with scattered ozone measurements of the order +/- 10DU, albeit a somewhat circular argument (Figure 7.14). The calibration used on data during midday is not in such good agreement, and more data is required to determine why. Unfortunately, it was found that measurements made on 18th September were affected by condensation on the surfaces of the AOTF crystal due to errors in the program controlling the TE cooling system. Therefore, with only two days of valuable measurements, the data on the 17th of September was used to calibrate the AOTF spectrometer.

Figure 7.14 presents relatively stable ozone retrieval values in the morning (± 10 DU), but it differs from Brewer values by ~ 50 DU. The later data is in better agreement with the Brewer but has a few outliers. Figure 7.12 shows that the slope of the calibration line is reasonable for both sets of data, but the offset is a better fit for the afternoon data, which is reflected in the absolute ozone results. Ideally, the transferred calibration (red line) would be a good fit through all the data and not only one section. However, a large dataset with a more extensive range of SZA values is necessary to provide a better calibration.

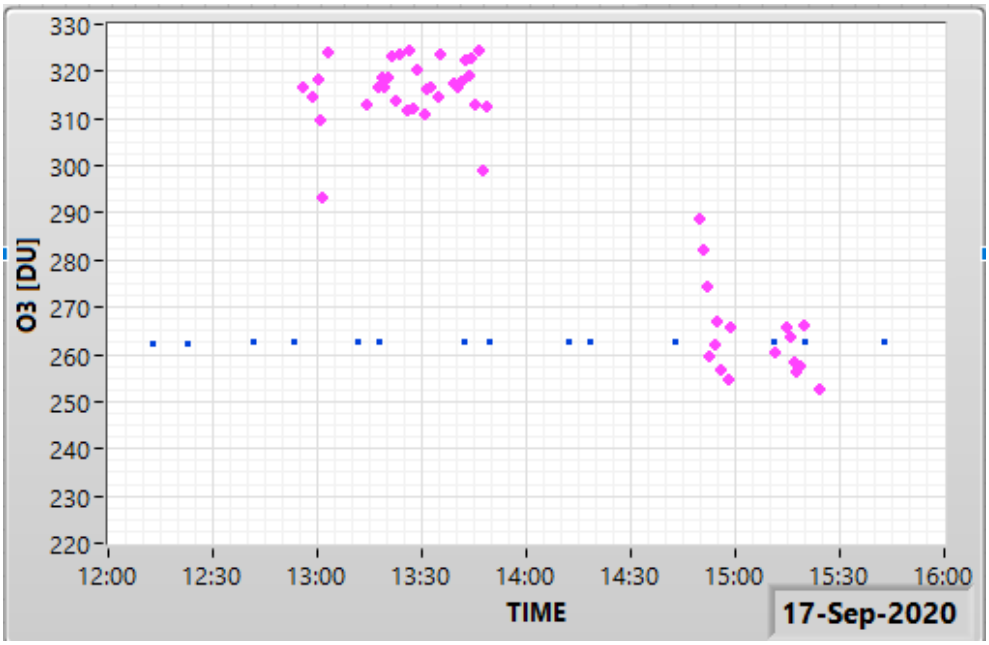

Figure 7.14 Estimated TOC values on 17th September 2020 based on the linear fitting displayed in Figure 7.12. Blue symbols plot the Brewer data in its daily routine monitoring mode, while pink plots represent data associated with the AOTF.

7.3.2. TOC measurements on 18th September 2020

The day after the calibration (18th September 2020), the AOTF spectrometer was reinstalled on the platform in the morning and measurements were performed throughout the day until 16:00 UTC. Unfortunately, the weather was not as good on this day, with periods when the solar disc was clear of cloud and significant periods when the sun was cloud-covered. On this day, zenith sky measurements were attempted and found to be unsuccessful. The series of measurements by both Brewer and AOTF on this day are shown in the right plot in Figure 7.15. Unfortunately, some issues with the tracker and its connections caused the break in afternoon data. Moreover, covid working hours in force precluded later access to university property.

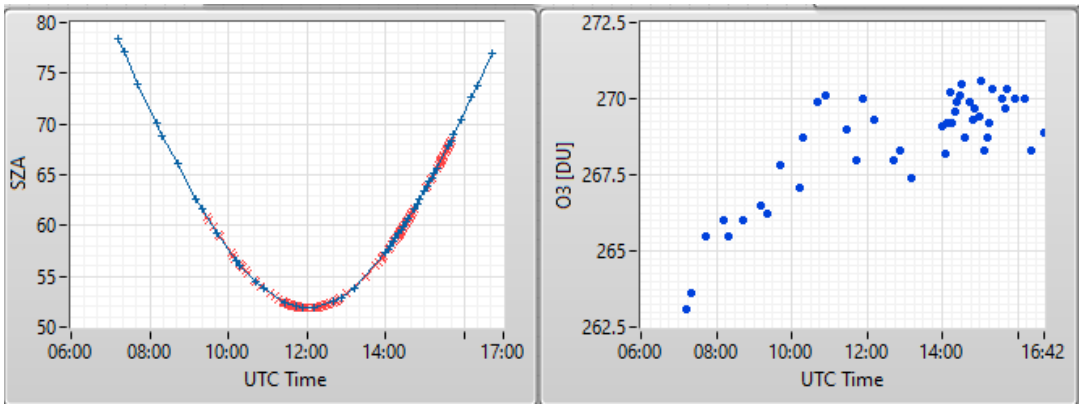

Figure 7.15 Solar zenith angles and direct ozone measurements on 18th September 2020. The left graph compares the total number of measurements performed by the Brewer (Blue) and the AOTF (red) at different times during the day with their respective SZA. The diagram on the right displays the Brewer ozone measurements with a standard deviation below 2.5 (blue dots).

While the Brewer data is mainly within 2.5 DU as determined by the processing quality control, the scatter in both raw and calibrated data from the AOTF is rather large for this day (see Figure 7.16 and Figure 7.17). Some of this can be attributed to the difficult conditions and the clouds. However, after inspecting the instrument between 1300-1400 UTC (when it was overcast), condensation was noticed on the AOTF quartz crystal. This was a result of a safety feature in the cooling of the crystal, which applied a fixed electrical current to the Peltier module if any error occurred in the thermoelectric cooling circuit. As a result, the temperature of the crystal achieved temperatures of ~5^0 C instead of the expected 25^0 C.

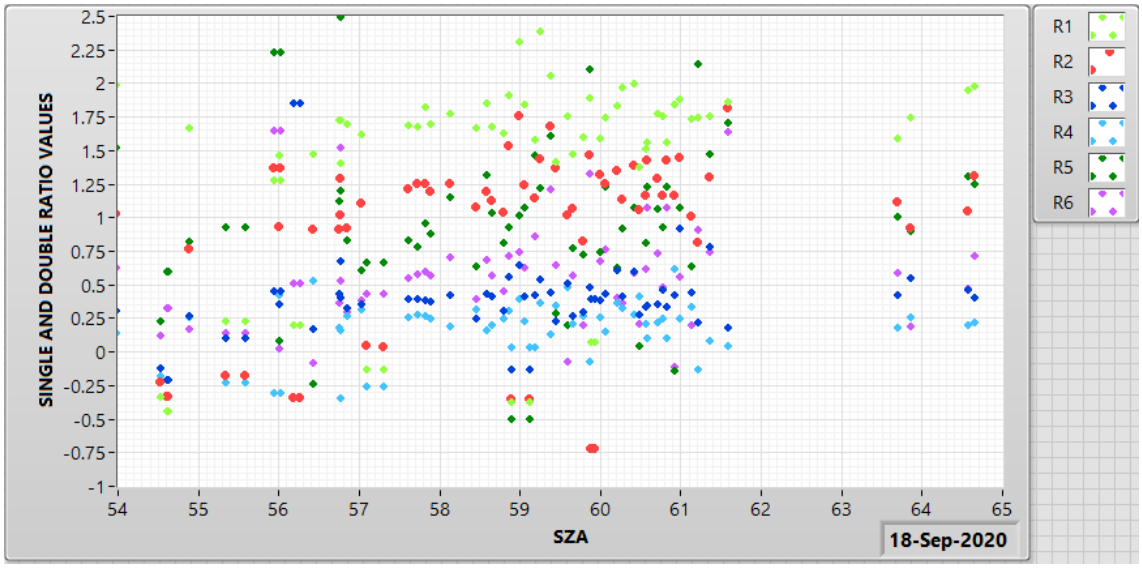

Figure 7.16 Displays AOTF measurements on 18th September 2020 of single and double ratios used for ozone (R2, R3, R4 and R6) and SO_2 estimations (R1 and R5). The panel as described in Figure 7.10.

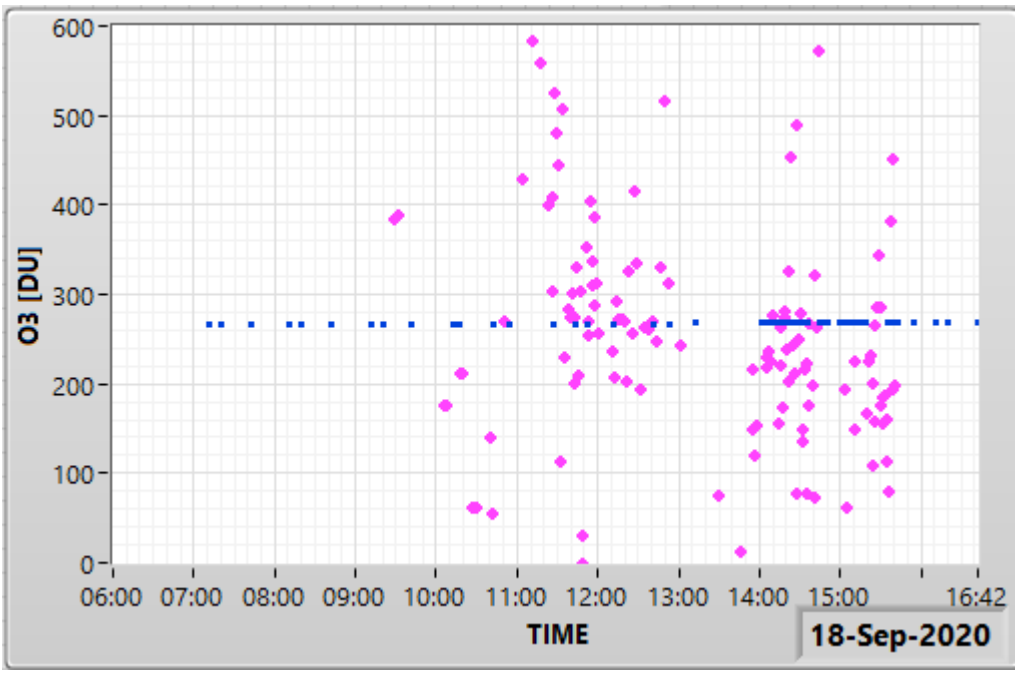

Figure 7.17 Estimated TOC values on 18th September 2020 based on the linear fitting displayed in Figure 7.12. Blue symbols plot the Brewer data in its daily routine monitoring mode, while pink plots represent data associated with the AOTF.

Data records indicated that this incident started in the morning at ambient temperatures of ~14^0 C and up to ~18^0 C at noon. Thus, condensation might have been expected due to the difference in temperature. The system was reset to enable more data to be gathered, but the crystal could not be wiped dry, so it was hoped that increasing the temperature to a more normal operating range (above ambient) would dry things out. The results indicate that this was not effective within the time frame of the remaining few hours of measurements. After this unfortunate incident, the AOTF user interface was updated to maintain a temperature of 25^0 C, even if an internal error occurs in the electronic board of the TE controller. By doing so, it is expected to reduce the possibility of producing condensation on the crystal surfaces.

7.3.3. TOC measurements on 25th September 2020

The final day when field measurements were possible was 25th September 2020. The thermoelectric programming had been modified to prevent excessive cooling of the crystal and the resultant condensation. The weather conditions on this day were clear sky in the morning with some cloudy periods in the afternoon, achieving a maximum temperature of 14° C at noon. Figure 7.18 shows the SZA values at the time of the ozone retrieval measurements performed by the AOTF spectrometer and the TOC values obtained by Brewer 172 on 25th September 2020.

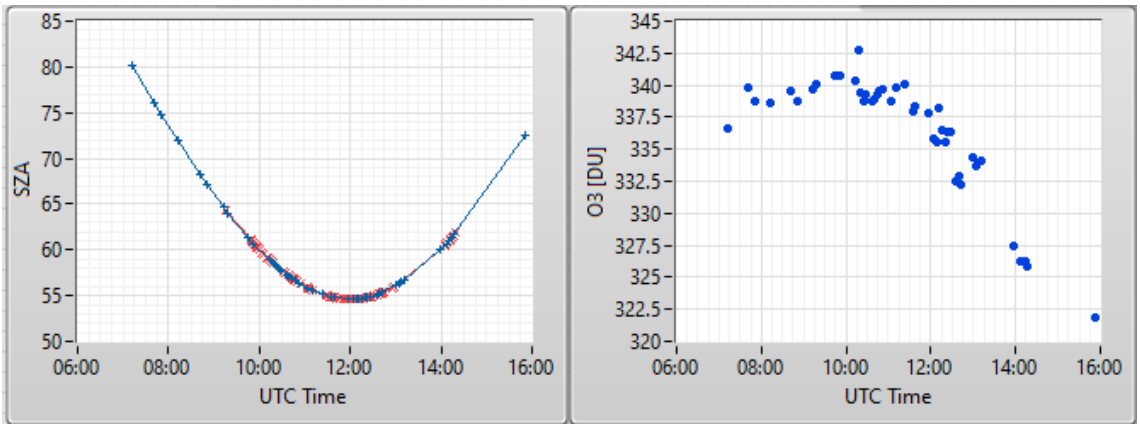

Figure 7.18 Solar zenith angles and direct ozone measurements on 25th September 2020. Panels are as described in Figure 7.15.

The AOTF instrument performed direct measurements of the solar beam throughout the middle of the day from 0900-1500 UTC. Figure 7.19 displays the agreement between the calibration obtained on 17th September and the measurements performed on 25th September.

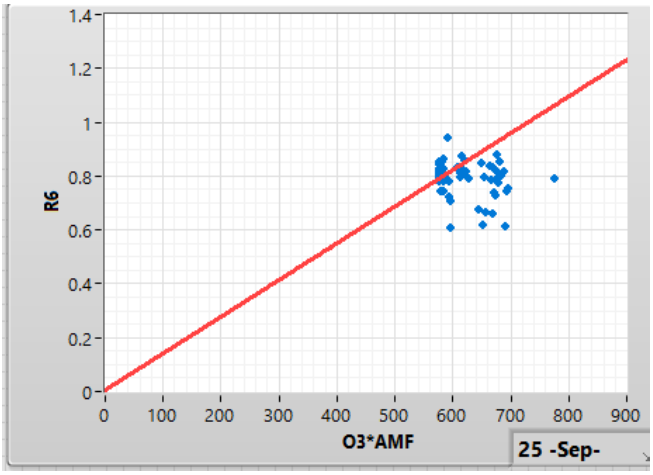

Figure 7.19. It compares the R6 ratios obtained on 25th September and the fitting R6 slant obtained on 17th September by the AOTF spectrometer (see Figure 7.12).

The results of plotting the ratios that lead to the ozone retrieval are shown in Figure 7.20, indicating the stability of the measurements. Although the ozone ratios R2, R3, R4 and R6 are stable during the day, these values are more scattered than desirable. Unfortunately, the source has not yet been identified.

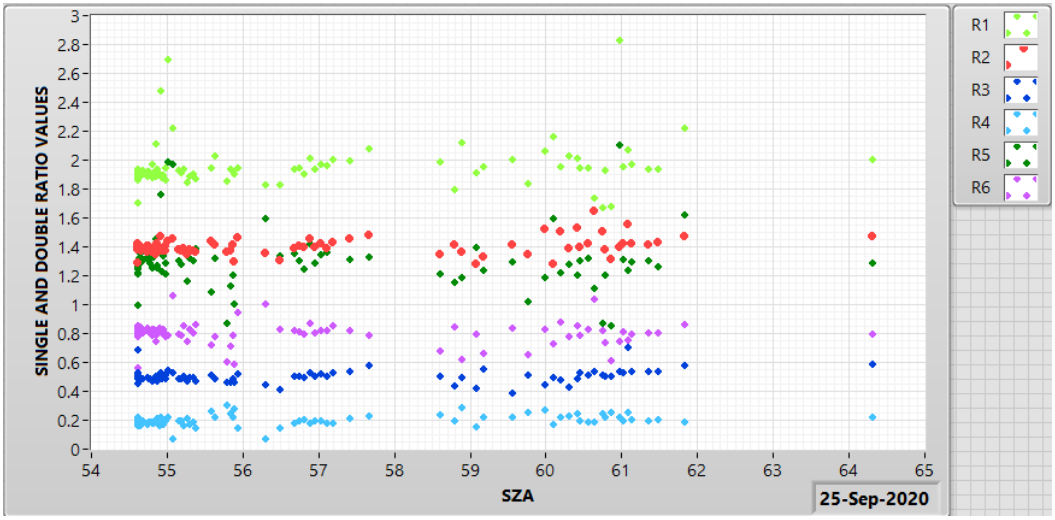

Figure 7.20 Displays AOTF measurements on 25th September 2020 of single and double ratios used for ozone (R2, R3, R4 and R6) and SO_2 estimations (R1 and R5). Panel as described in Figure 7.10.

An arc can be identified in Figure 7.21, with data gathered near noon being close to the Brewer values, while those at more significant SZA measure too low compared to the Brewer (as did the larger SZA measurements on the calibration day itself). This shows consistency in the AOTF operation from day to day, and it displays an agreement with Brewer measurements of ± 20 DU.

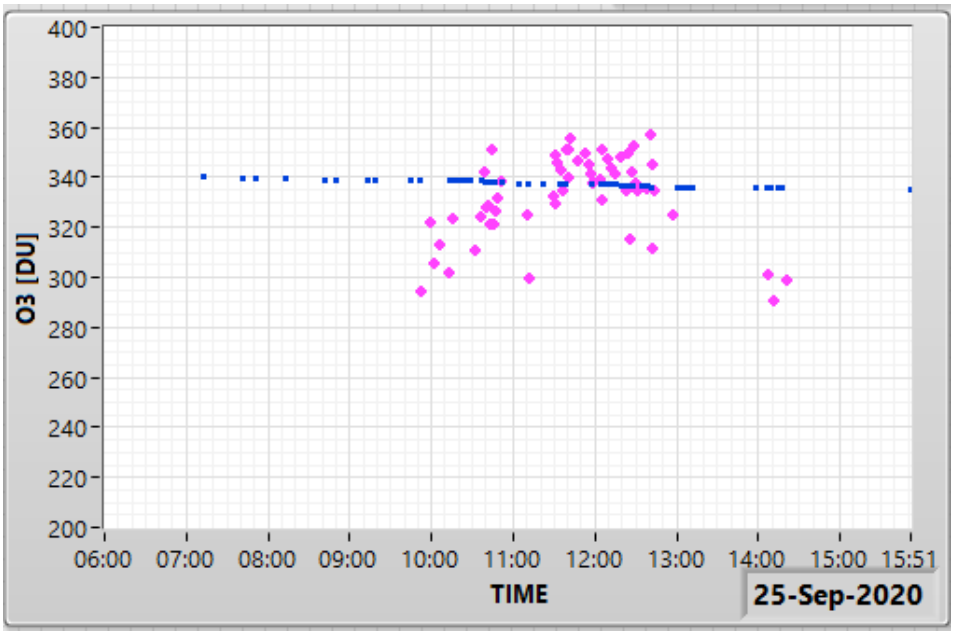

Figure 7.21 Estimated TOC values on 25th September 2020 based on the linear fitting displayed in Figure 7.12. Blue symbols plot the Brewer data in its daily routine monitoring mode, while pink plots represent data associated with the AOTF.

As a further confirmation of performance, the ozone was retrieved from the AOTF scans using a simple two-wavelength DOAS technique (i.e. one wavelength strongly absorbed at 310.1 nm and another weakly absorbed at 320.1 nm). This basic technique does not exclude the influence of SO2 or aerosols (as removed by Brewer processing), but it gives an indication of whether the measurements are plausible without invoking some of the complexities of the Brewer processing.

This was intended to indicate whether the cause of the uncertainties seen above could be identified in the data or the processing.

7.3.4. Simple two-wavelength DOAS technique to retrieve TOC

The Eq. (7.8), which is employed to estimate the TOC from double ratio values, can also be used to retrieve TOC values from single ratio values, see Eq. (7.9).

$$O_3 = \frac{R - ETC_{O3}}{\mu * \ Differential\ absorption\ coefficient\ for\ ozone} \tag{7.9}$$

Where R is the single ratio between two measurements at wavelengths that are attenuated by ozone. The following results use the same four wavelengths the Brewer spectrometer uses to retrieve TOC values to get all the single ratio combinations. Notice that the values F3, F4, F5 and F6, are obtained after applying the natural logarithm to the AOTF measurements at 310 nm, 313.5 nm, 316.8 nm and 320 nm, respectively.

The single ratios R6-R5, R6-R3, R5-R4 and R4-R3 consider one wavelength strongly absorbed by ozone and another weakly absorbed by ozone, peaks and valleys on the ozone cross-section see Figure 2.9. All other single ratios (R6-R4, R5-R3) compare two wavelengths at the peaks or valleys of the ozone cross-section.

Figure 7.22 and Figure 7.23 display the comparison between the single ratios used in this section, which were obtained on 17th September 2020 and 25th September 2020, and the SZA. This plot shows agreement with the double and single ratios used for TOC estimations (R2, R3, R4 and R6) in Figure 7.10 and Figure 7.20.

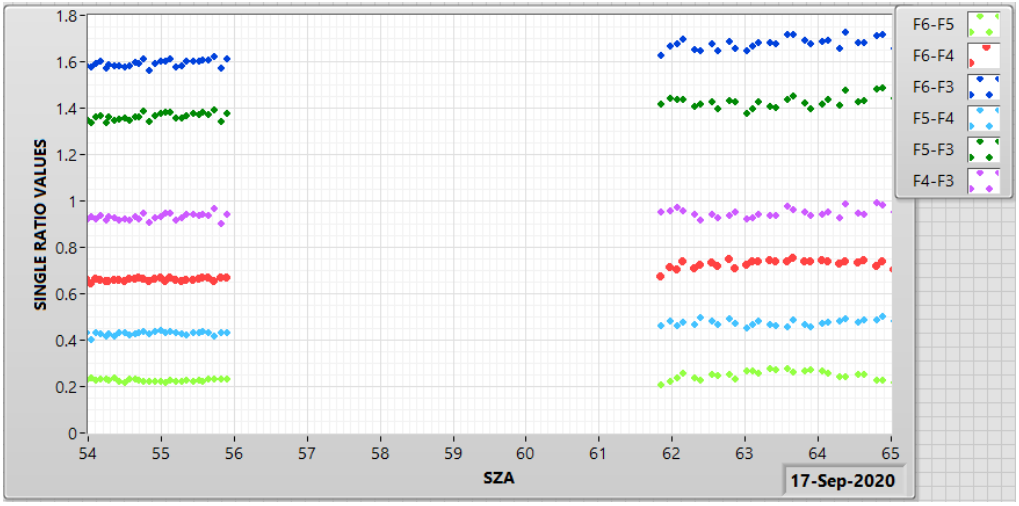

Figure 7.22 Displays AOTF measurements on 17th September 2020 of single ratios used for TOC estimations. The analysed ratios are obtained from measurements at the four wavelengths used by the Brewer algorithm to retrieve TOC ($F_2 \rightarrow$ 306.3 nm, $F_3 \rightarrow$ 310 nm, $F_4 \rightarrow$ 313.5 nm, $F_5 \rightarrow$ 316.8 nm and $F_6 \rightarrow$ 320 nm), and compared with the SZA. The plot shows single ratios R4=F6-F5 in light green, F6-F4 in red, F6-F3 in blue, R3=F5-F4 in light blue, R2=F5-F3 in green, and F4-F3 in purple marks.

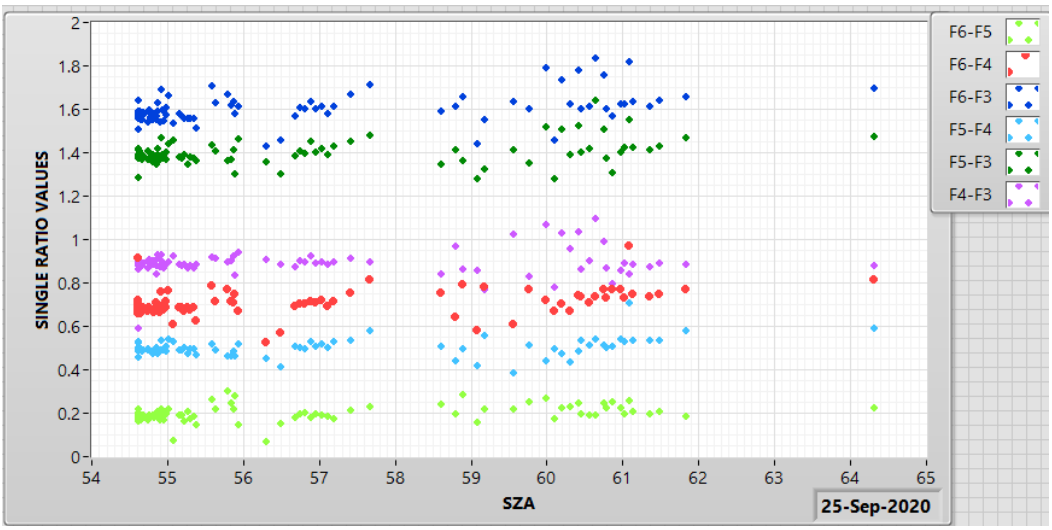

Figure 7.23 Displays AOTF measurements on 25th September 2020 of single ratios used for TOC estimations. Panel as described in Figure 7.22.

To transfer the calibration of Brewer #172 into the AOTF spectrometer using only a single ratio of wavelengths, the TOC values measured by Brewer #172 are then substituted in Eq. (7.9). Then, the equation is arranged into the form Y=mx+b, where the X-axis represents the ozone slant column and Y-axis the single ratio R. A linear fitting is applied to the plotted data, with a slope equal to the differential absorption coefficient for ozone, and the Y-interception of the line representing ETC values for ozone. Notice that the ozone values estimated by this method do not consider the effect of SO_2 and aerosols compared with the double ratio measurements that include the weighting coefficients to minimize their impact on TOC measurements.

Single ratio R4= F6-F5

The single ratio F6-F5 represents the measurements at 320 nm and 316.8 nm. The TOC estimations after applying the calibration displayed in the left plot of Figure 7.24 shows a variation of ±80 DU with the TOC values obtained by the Brewer 172 on the same day (17th September 2020). But, it did not show an agreement after applying the same calibration (red line) to the TOC measurements on 25th September 2020 (see Figure 7.25).

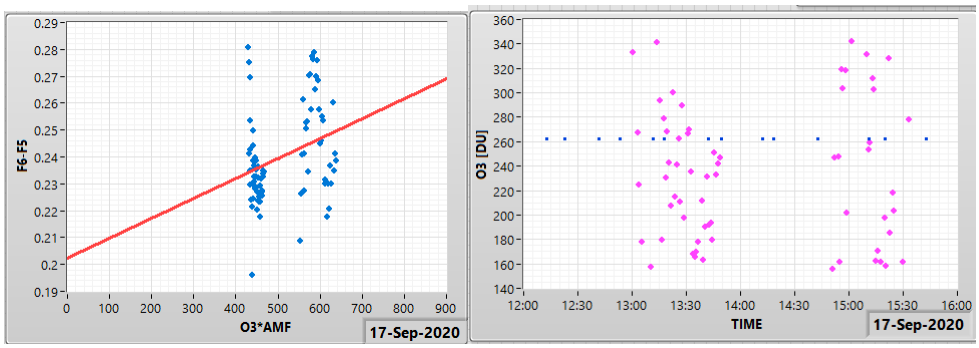

Figure 7.24 Calibration transferred to the AOTF on 17th September 2020, considering the TOC values from the Brewer 172 and the single ratio F6-F5 (320 nm and 316.8 nm) obtained by the presented spectrometer. The left figure shows the single ratios (blue dots) and the fitting equation (red line), with the differential absorption coefficient for ozone equals

0.000079987775, and the ETC for ozone equals 0.202313273. The right figure displays the estimated TOC values based on the linear fitting shown on the left chart, see Eq. (7.9). Blue symbols plot the Brewer data in its daily routine monitoring mode, while pink plots represent data associated with the AOTF measurements.

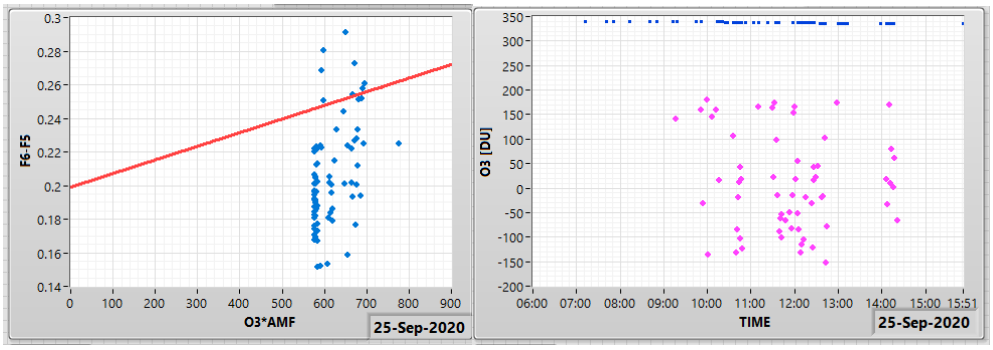

Figure 7.25 TOC Measurements obtained on 25th September 2020 using the single ratios F6-F5 and the calibration shown in Figure 7.24. The left figure compares the fitting calibration (red line) on 17th September 2020 with the single measured ratios (blue dots). The right figure displays the estimated TOC values found from Eq. (7.9), where blue symbols represent Brewer data in its daily routine monitoring mode, and pink plots represent data associated with the AOTF measurements.

Single ratio F6-F4

The single ratio F6-F4 represents the measurements at 320 nm and 313.5 nm. Although the single ratio values are located close to the linear calibration fitting (see red line in Figure 7.26), the obtained TOC values (pink symbols) do not match the TOC values from the Brewer spectrometer on 17th September 2020 nor the ones on 25th September 2020 (see Figure 7.27).

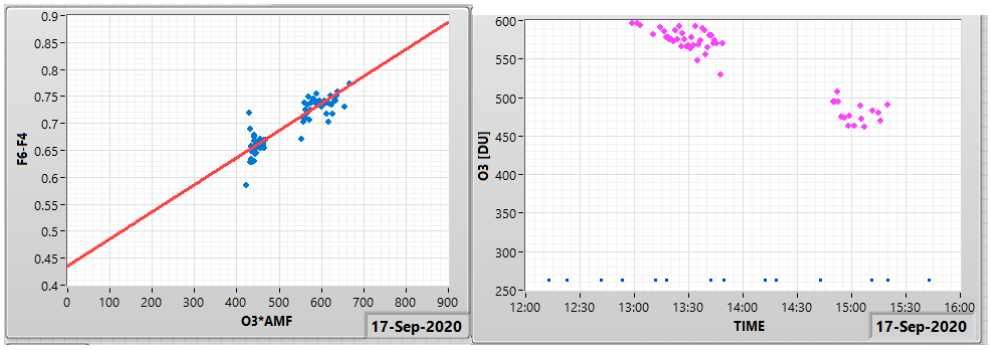

Figure 7.26 Calibration transferred to the AOTF on 17th September 2020, considering the TOC values from the Brewer 172 and the single ratio F6-F4 (320 nm and 313.5 nm) obtained by the presented spectrometer. Panels as described in Figure 7.24. The differential absorption coefficient for ozone equals 0.00050226608, and the ETC for ozone equals 0.435349404.

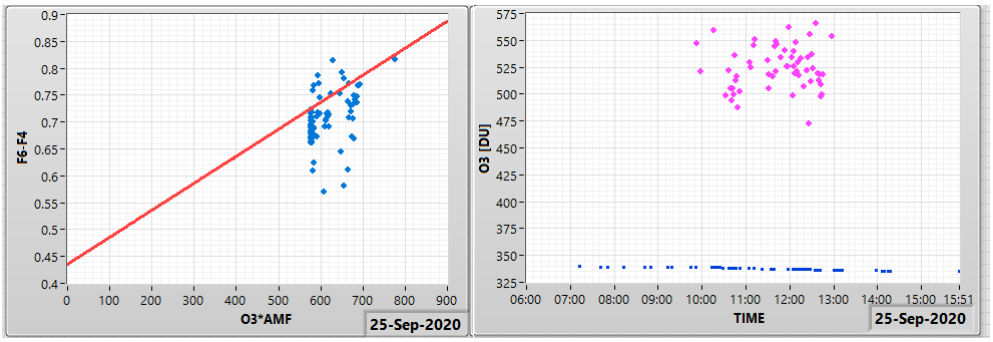

Figure 7.27 Measurements obtained on 25th September 2020 using the single ratio F6-F4 and the calibration shown in Figure 7.26. Panels as described in Figure 7.25.

Single ratio F6-F3

The single ratio F6-F5 represents the measurements at 320 nm and 310 nm. Such values in Figure 7.28 are in line with linear calibration fitting (red line). Also, the TOC estimations obtained by the AOTF spectrometer (pink marks) agree with the ones from the Brewer 172 on 17th September 2020 (blue marks on the right plot in Figure 7.28). However, the TOC values on 25th September 2020 show an offset of ~100 DU regarding the ones from the Brewer spectrometer (see Figure 7.29).

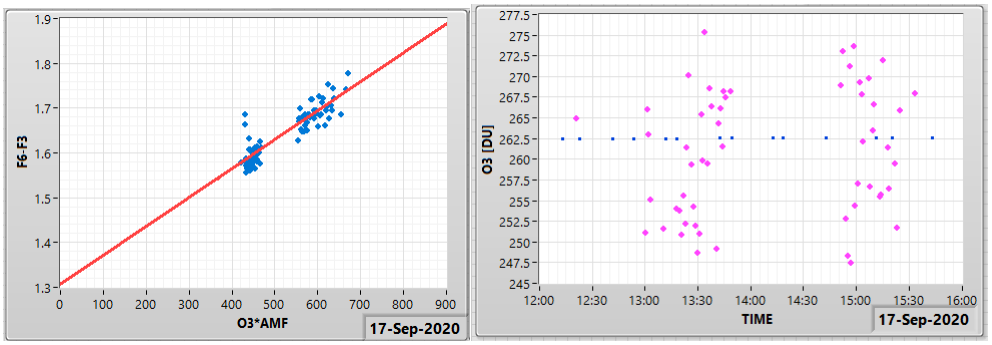

Figure 7.28 Calibration transferred to the AOTF on 17th September 2020, considering the TOC values from the Brewer 172 and the single ratio F6-F3 (320 nm and 310 nm) obtained by the presented spectrometer. Panels as described in Figure 7.24. The differential absorption coefficient for ozone equals 0.0006459861, and the ETC for ozone equals 1.30661416.

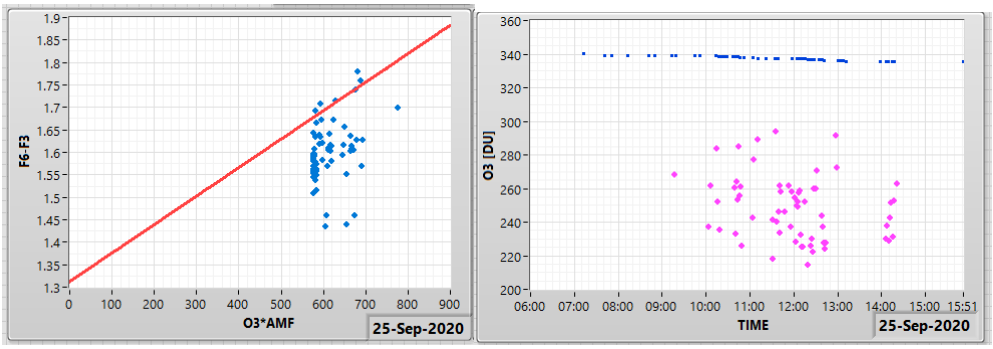

Figure 7.29 Measurements obtained on 25th September 2020 using the single ratio F6-F3 and the calibration shown in Figure 7.28. Panels as described in Figure 7.25.

Single ratio R3= F5-F4

The single ratio F5-F4 represents the measurements at 316.8 nm and 313.5 nm. Such values in Figure 7.30 are in line with linear calibration fitting (red line). Also, the TOC estimations obtained by the AOTF spectrometer (pink marks) have an agreement of ~±15 DU with the Brewer on 17th September 2020 (blue marks on the right plot in Figure 7.30). Additionally, the TOC values on 25th September 2020 show an agreement of ~±35 DU with the Brewer spectrometer (see Figure 7.31).

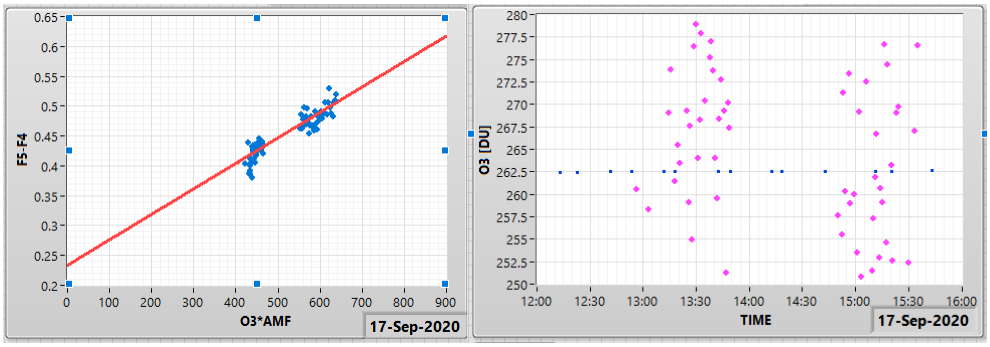

Figure 7.30 Calibration transferred to the AOTF on 17th September 2020, considering the TOC values from the Brewer 172 and the single ratio F5-F4 (316.8 nm and 313.5 nm) obtained by the presented spectrometer. Panels as described in Figure 7.24. The differential absorption coefficient for ozone equals 0.00042642659, and the ETC for ozone equals 0.233452818.

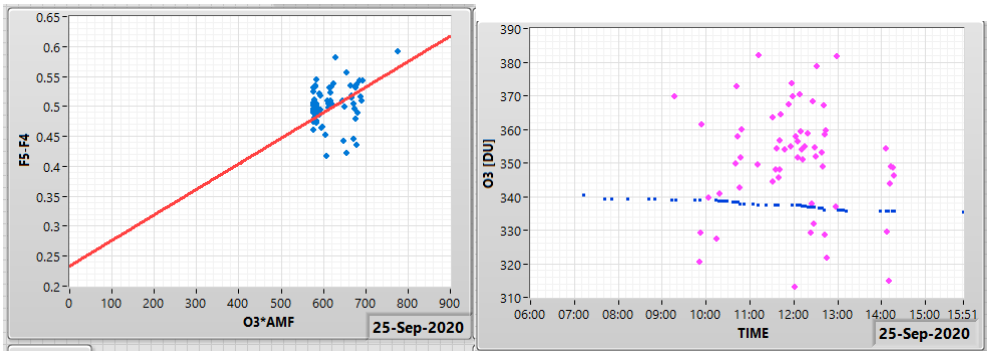

Figure 7.31 Measurements obtained on 25th September 2020 using the single ratio F5-F4 and the calibration shown in Figure 7.30. Panels as described in Figure 7.25.

Single ratio R2= F5-F3

The single ratio F5-F3 represents the measurements at 316.8 nm and 310 nm. These single ratios in Figure 7.32 agree with the estimated linear calibration fitting (red line). Also, the TOC calculations obtained by the AOTF spectrometer (pink marks) have an agreement of ~±18 DU with the Brewer on 17th September 2020 (blue marks on the right plot in Figure 7.32). The TOC values on 25th September 2020 (see Figure 7.33) indicates an offset of ~±50 DU with the Brewer spectrometer, which can be corrected by adjusting the ETC values for ozone and the ozone differential coefficient of the calibration.

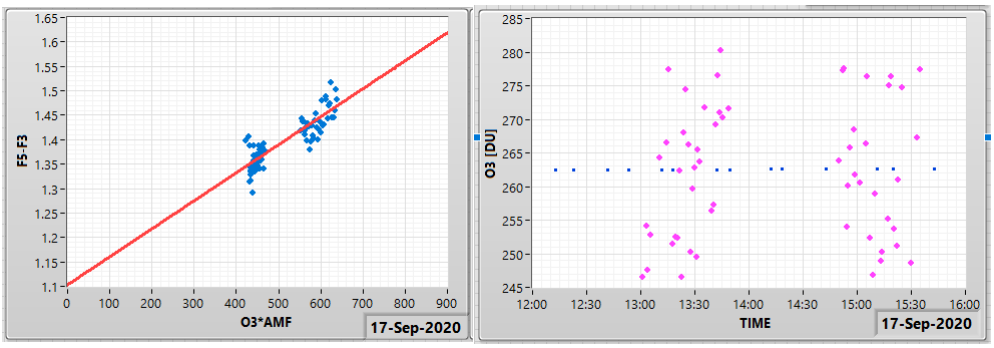

Figure 7.32 Calibration transferred to the AOTF on 17th September 2020, considering the TOC values from the Brewer 172 and the single ratio F5-F3 (316.8 nm and 310 nm) obtained by the presented spectrometer. Panels as described in Figure 7.24. The differential absorption coefficient for ozone equals 0.00057320005, and the ETC for ozone equals 1.10286999.

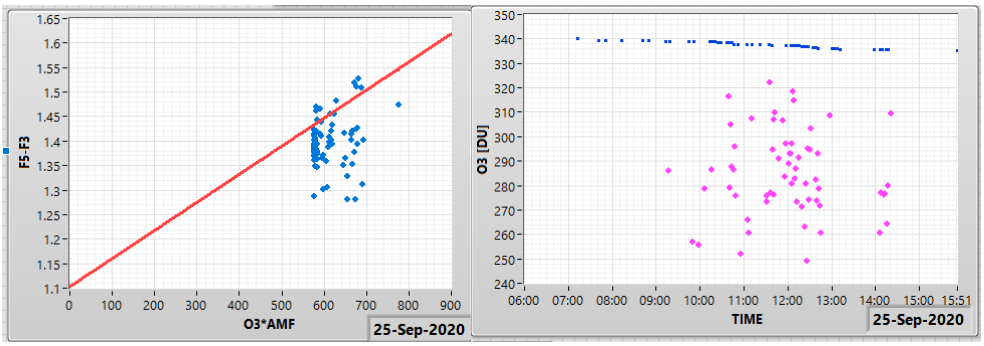

Figure 7.33 Measurements obtained on 25th September 2020 using the single ratio F5-F3 and the calibration shown in Figure 7.32. Panels as described in Figure 7.25.

Single ratio F4-F3

The single ratio F4-F3 represents the measurements at 313.5 nm and 310 nm. The single ratios in Figure 7.34 seem to agree with the linear calibration fitting (red line). The TOC estimations obtained by the AOTF spectrometer on 17th September 2020 (pink marks) are centred with the Brewer values (blue marks on the right plot in Figure 7.34). However, the TOC values on 25th September 2020 (see Figure 7.35) disagree with the Brewer values.

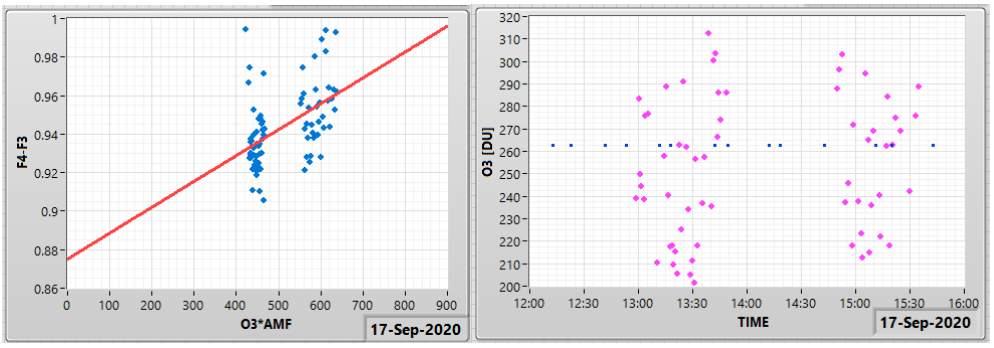

Figure 7.34 Calibration transferred to the AOTF on 17th September 2020, considering the TOC values from the Brewer 172 and the single ratio F4-F3 (313.5 nm and 310 nm) obtained by the presented spectrometer. Panels as described in Figure 7.24. The differential

absorption coefficient for ozone equals 0.00013436294, and the ETC for ozone equals 0.875095412.

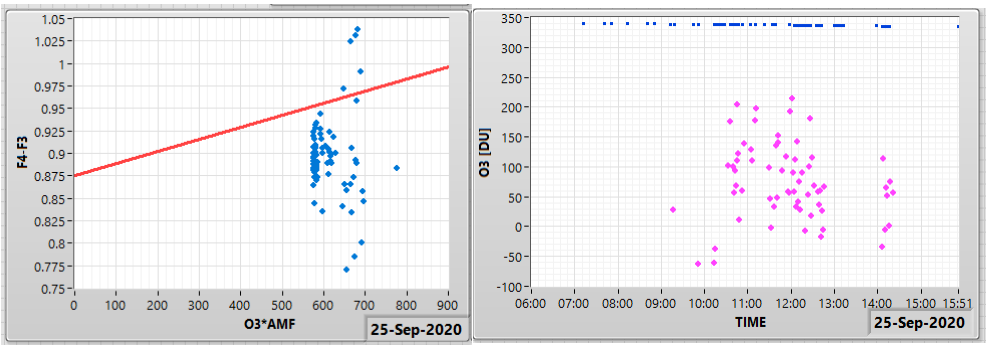

Figure 7.35 Measurements obtained on 25th September 2020 using the single ratio F4-F3 and the calibration shown in Figure 7.34. Panels as described in Figure 7.25.

It is important to mention that adjustments to the linear fittings used during the calibration in this section might improve the agreement between the TOC values of the AOTF and the Brewer spectrometers. However, the purpose of using single ratio values to retrieve ozone measurements was to identify if the problem was related to the data acquisition or the data processing. At this stage, the stability of the AOTF spectrometer still needs to be tested to provide a better understanding of its capabilities in measuring TOC without disturbing the mechanical alignment of the whole system.

Note that the measurements described above are exclusively used to verify the ozone retrieval algorithm. The ozone retrieval values obtained in sections 7.3.2 and 7.3.3 are calculated using the procedure described in Brewer's manual using double ratios.

7.4. Discussion of results

The initial field tests of the AOTF spectrometer were very encouraging. The ability to reproduce a high-resolution direct beam solar spectrum has been clearly shown in Figure 7.5 and Figure 7.8, where the total column of ozone can be theoretically extracted from these measurements. The retrieval of TOC requires either a high-quality absolute radiance calibration or a system that relies on ratios like that of the Brewer and Dobson spectrometers, requiring a different kind of calibration (see section 7.3.1). To date, the processing has mimicked that of the Brewer, and while promising initial results for TOC have been achieved, there are further improvements to be made to the processing that could be instrument-specific, as well as physical improvements to the instrument to enable outdoor use.

The Brewer-style TOC calculation was applied to 5 wavelengths selected from a full scan rather than measurements of only five wavelengths. This was done because the AOTF spectrometer still needs a fine adjustment of each wavelength, similar to the scan test on the direct sun of the Brewer spectrometer, where its five wavelengths are shifted simultaneously to find their optimum values. As a result, each wavelength was a single-point measurement and not

an average or integration over a short time as the Brewer does. This alone may have impacted the results, especially at shorter wavelengths. It also increased the time between measuring the five individual wavelengths, which might have been significant (see below).

There are multiple possible reasons for the apparent lack of stability in the AOTF TOC measurements compared to the Brewer. These can be roughly divided into instrument issues and processing issues, given the processing method for a very different instrument has been applied here to a limited dataset. In an attempt to identify the ozone measurement issues, the simple DOAS technique (2 wavelengths) was used to calculate TOC values (see section 7.3.4). Additionally, the single and double wavelength ratios in the AOTF measurements were plotted against the SZA, proving that the day chosen for calibration was the one with more stable measurements (see Figure 7.10). However, the non-linearity of such measurements might be caused by minor misalignments of the AOTF spectrometer with the solar tracker. Such alignments were done manually because the spectrometer does not possess a customised base attached to the solar tracker. It was a provisional set-up that had to be taken apart at the end of each day due to the lack of a weather-proof case.

The single ratio analysis presented in section 7.3.4 showed consistency with the TOC measurements obtained using double ratios (R6). In that case, it is not the overall conclusion that some of the single ratios (F6-F3, F5-F4, F5-F3) give a reasonable result on a single day (17th September 2020), the best being F5-F4 because its linear fitting agrees with the collected data and it has an agreement with Brewer ~±15 DU. When its calibration was applied to the data obtained on 25th September, the agreement with Brewer 172 was ~±30 DU. However, after comparing the results from the other single ratios, the calibration does not always appear valid when applied to data from another day. It cannot be determined at this stage whether this is an intrinsic instability in the instrument or whether moving an unsecured set of optical parts in and out on different days could have disturbed the mechanical alignment of the whole system. Applying the double ratio methodology does not improve matters. The double ratio should remove SO_2 and AOD effects from the analysis, which otherwise produce some scatter in the data. However, these would appear to be minor contributions to the overall uncertainties in this very first outdoor test of the system.

The ozone single ratios R2, R3, and R4 all appear very stable in the first part of day one (17th September 2020). After the break in data collection, R2 and R3 perform as expected, though slightly noisier, while R4 declines at the highest SZA when it is not expected to do so. This ratio feeds into R6, which also displays a more noisy signal and an unexpected curvature given the constant ozone measured by the Brewer. This implies that in the latter half of the day, the instrument rather than the processing is less stable. Repeated measurements may have improved this performance.

Furthermore, given the flexibility of the AOTF, in terms of speed and resolution of data gathering, a more bespoke system optimised to the strengths of the AOTF should be possible. It is also clear that the instrument would perform better if mounted correctly and enclosed in a

weatherproof case. Temperature stabilisation should be further investigated for absolute UV measurements. However, the impact of temperature dependency of the various elements of the instrument on the signal ratios used for ozone determination is not clear after the AOTF was replaced with the thermoelectric cooling version, which is programmed to stabilize the temperature of the crystal at 25°C.

Chapter 8. Conclusions and further work

This chapter will provide the conclusions from the measurements discussed in Chapter 6 and Chapter 7, including recommended improvements and proposed further research.

8.1. Conclusions

The work described in this thesis has demonstrated the general performance of the AOTF technology for use as a replacement for the diffracting element in a classical spectrometer (diffraction gratings and prisms) and, more specifically, at UV wavelengths both for full spectral measurements and at selective wavelengths for determination of total ozone column by the DOAS technique.

Traditional spectrometers, most usually using diffraction gratings to disperse the spectrum and determine one wavelength of radiation from another, measure a monochromatic beam by rotating the diffraction element, moving the position of the detector, or using slit masks. The motion requires precision engineering to ensure repeated alignment at every scan. However, by replacing the diffraction grating with the proposed AOTF in a collinear configuration, the direction of the acoustically-filtered beam remains aligned with the detector regardless of the filtered wavelength within the range of ~250 nm to ~440 nm.

The distinct advantage of the AOTF spectrometer is thus the absence of moving parts within the instrument, achieving speeds of 0.14 seconds per filtered wavelength when performing a single scan. For example, the instrument performed UV scans from 300 nm to 325 nm with a step of 0.05 nm in around 70 seconds. The maximum speed reached by an AOTF is equal to the time required for the RF signal generation, plus the time the acoustic wave requires to pass through the crystal. This time is usually tens of nanoseconds. However, it is necessary to consider the acquisition time and digital data processing to assess a scan duration fully. Nonetheless, this is considerably faster than a scanning instrument.

The current version of the instrument had limited testing due to covid restrictions. In addition, errors and delays by the manufacturer resulted in a loss of some of the characterisations that could not be fully repeated in the available time. Thus, some characteristics of the instrument were applied with less confidence than they should have been (mainly wavelength and temperature calibration). Despite this, the AOTF spectrometer has proved capable of measuring solar UV radiation and shows promise for TOC. There are, however, a number of practical

improvements that should be made to the next generation of such an instrument to overcome some of the issues identified with the existing version.

After performing several zenith sky measurements, it was found that the current AOTF spectrometer design cannot detect scattered solar UV radiation (i.e. zenith sky measurements). The same issue was observed when measuring the 50W and 200W halogen lamps in the setup shown in Chapter 6. A more sensitive detector is required to remedy this issue, such as solid-state photomultipliers now available on the market. Nonetheless, in this thesis, only relevant measurements are derived from direct solar radiation.

Temperature tests presented in section 6.5 were performed with a water-cooled AOTF, which was not temperature controlled. This AOTF was damaged and replaced with a TE-controlled version whose electronic temperature controller was missing. This problem was addressed by adapting a TE controller that was at hand and adding a routine to the user interface to stabilize the temperature of the new AOTF to 25° C. . Although amplitude corrections observed in Figure 6.23 and Figure 6.24 were considered to compensate for temperature changes in the RF controller, the RF controller remains temperature sensitive and is not temperature stabilised in the current instrument. In future, it would be preferable to have a customised, compact and temperature stabilised (or temperature insensitive) RF controller.

The condensation produced on the surfaces of the AOTF crystal during one day of measurements disperses the collimated beam and generates stray light. This was the consequence of a programming bug that controlled the temperature of the AOTF crystal, which reduced its temperature below 10° C during ambient temperatures of ~20° C.

It is important to mention that the wavelength calibration performed with the previous AOTF version was transferred to the new model because it was found that there were no differences in their spectral responses for the limited available wavelengths at the time the crystal was returned. However, it is necessary to repeat measurements of high-intensity spectral lines (see section 6.2) to corroborate that the shape of the secondary lobes in the transfer function of the AOTF remains the same.

The RF generator provided by the manufacturer of the AOTF allows a digital modulation (pulse wave) of the RF output signal, the frequency used was 10 kHz for practical purposes. However, this means that harmonics of the 10 kHz fundamental frequency also reach the piezoelectric transducer attached to the AOTF because a square signal is the sum of the fundamental wave plus all its harmonics. Although its frequencies are far from MHz values, it is unknown whether this affects the spectrometer. Thus, it is suggested to update the RF modulator to replace digital modulation (square wave) with an analogue one (sinusoidal wave) in the future.

It is still unknown what causes the second wavelength in spectral measurements with nearly double the value of the selected wavelength. Because of the inverse relationship between wavelength and frequency (see Figure 6.7), there is no straightforward explanation for the origin of the acoustic wave that produces such output.

As with any new instrument, the operational stability of the proposed spectrometer still needs to be tested for extended periods to ensure that only atmospheric changes will influence its measurements. This stability test needs to be done once the spectrometer has been appropriately calibrated and preferably performing side-by-side comparisons with a calibrated Brewer spectrometer during clear sky conditions. This way, it would be possible to compare irradiance ratios at different wavelengths in both instruments assuming small stable values of TOC. A smooth variation of such ratios with time would be an initial indication of the stable operation of the AOTF spectrometer concerning its ability to perform reliable ozone measurements.

Although the designed solid-state spectrometer still needs proper calibration to accurately describe its performance in measuring the total ozone column, there are clear advantages compared with the Brewer spectrometer. For example, portability, compact and robust design, no moving parts, lower power consumption with no high voltages, the possibility of onboard processing, and the ability to perform monochromatic measurements at higher speeds, reducing the influence of weather conditions under clear sky circumstances.

8.2. Further work

Although the research described in this thesis has revealed the promising potential of the AOTF technology in atmospheric spectrometry, there are some areas of improvement and further ideas to be tested. The following paragraphs will describe the proposed improvements as well as possible future research.

8.2.1. Characterization and calibration improvements

In order to achieve complete spectral characterization of the spectrometer, the AOTF spectrometer should be tested using a tunable laser. It will provide an accurate frequency to wavelength calibration across the operational spectrum of the AOTF, having a calibration file that does not rely purely on a polynomial fitting of measurements at some wavelengths. Additionally, the transfer function of the AOTF will provide more data about the lateral lobes across the spectrum discussed in section 5.1. Unfortunately, this test was not possible during this research because the operating spectral range of the available tunable lasers did not cover the ultraviolet spectrum.

8.2.2. Replacing the detector

The performance of commercial technology for detecting ultraviolet radiation, in general, is low compared with its performance in the visible or near-infrared spectrum. When combined with the low levels of solar UV radiation, especially at UVB wavelengths, this has provided a long-standing challenge to atmospheric measurements of, or based on, solar UV. However, rapid advancements in science and technology might close that gap in a matter of years.

The Silicon Avalanche Photodetector (APD), which is used in this prototype, is a leading solid-state technology used to manufacture state-of-the-art detectors in the ultraviolet and visible spectrum. However, its performance in the UV spectrum is still well below that at longer wavelengths and has proved a limitation for some of the available field calibration tools (halogen lamps). One alternative is a solid-state photomultiplier (SiPM) from Hamamatsu, which uses the APD in its Geiger mode to get a solid-state photon-counting detector. However, its spectral operating ranges are specified from 320 nm to 900 nm, no guarantee of success when operating beyond this range. If its performance can be extended to the UVB waveband, then these detectors would be an ideal match for the AOTF spectrometer proposed here.

Another alternative is a hybrid photodetector, which is a new PMTs with a semiconductor detector in a vacuum tube and operating voltages similar to the PMT (up to 10 kV). In comparison, the operating voltages of APDs and SiPMs are lower than 200 V.

If a photon-counting detector replaces the current APD detector, additional electronics would be needed to detect current peaks, amplify them, filter peaks below a certain threshold to get rid of noise level, convert the peaks into logic pulses, and finally count such pulses. Due to the high sensitivity of these devices, the filtered output beam might need to be attenuated to be able to measure one photon at a time. Fortunately, it can be done by attenuating the RF signal applied to the AOTF instead of adding a wheel with neutral density filters. Additionally, the monochromatic photons reaching the detector can be modulated in the same way as the presented AOTF spectrometer does, allowing the use of the same digital lock-in amplifier with minor adjustments.

8.2.3. Addition of a mounting case and mechanical improvements

The optical parts of the spectrometer need to be sealed to reduce the potential condensation as much as possible since this was demonstrably an issue with the open system tested in Chapter 7. Moreover, it would be ideal to have both polarizers fixed perfectly orthogonal to each other at both ends of the AOTF instead of relying on motorized mountings (Thorlabs model PRM1Z8) with a repeatable incremental motion of 0.03° and an 0.1% accuracy that can lead to slight misalignments. As described in Chapter 5, the orthogonality of the polarizers is essential to attenuate stray light from the ordinary ray (zero-order), and while the motorized mountings have been an essential development tool, a final instrument would be better served with precisely fixed polarizers.

It is also necessary to develop a weatherproof case to protect the spectrometer from dust particles, keeping humidity low and maintaining a stable temperature. And it has to be designed to be firmly mounted on solar trackers or include its own. Alternatively, some electronics could be placed in a separate weatherproof box next to the optical part of the AOTF spectrometer.

8.2.4. New RF controller and customized electronics

The RF controller unit could also be redesigned to be more compact and have faster PC communication (USB-C). Specific routines could be included in the control board of the new RF unit to perform automatic scans of wavelengths once it is synchronized with the PC, decreasing the communication time and increasing the data acquisition speed.

The analogue to digital converter could also be redesigned to scan only two channels to reduce costs, weight, and size. By doing so, the whole instrument is expected to fit into a small customised weatherproof case.

Additionally, a tactile screen, a Raspberry Pi and some control buttons could be added to facilitate on-site maintenance.

8.2.5. User interface improvements

The user interface could also be programmed in free programming software such as Python and installed into a Raspberry Pi—allowing the processing of all data in-situ instead of using a traditional laptop to run LabVIEW. Then, all the data could be transferred wirelessly or through an Ethernet cable to a workstation for monitoring and further processing.

8.2.6. Additional side-to-side comparisons with calibrated spectrometers

The current instrument still needs proper calibration, based on a large set of data at different zenith angles during clear-sky conditions, an exercise that was repeatedly denied to us by technical delays at the AOTF manufacturer, the global pandemic and the UK weather. A fine-tuning of the standard Brewer's five wavelengths used to measure TOC might be needed to improve the instrument's accuracy.

So far, the AOTF spectrometer has tried to mimic the Brewer spectrometer in data processing and performance. However, it would be interesting to do further research into measuring at more than five wavelengths to retrieve ozone and other trace gases in the atmosphere since the AOTF has a far superior spectral range and optical performance. Furthermore, an absolute calibration of UV measurements would provide further benefits from its promising performance.

While the improvement of described above could not be performed during this research because of time, monetary funds or the lack of available commercial technology, this work provided evidence of the potential of the AOTF technology as the dispersion element in atmospheric UV applications.

8.2.7. Adding a second AOTF to the spectrometer

Another option to reduce stray light measurements is adding a second AOTF to get a double monochromator. In addition to the reduced stray light, the FWHM of the spectrometer will be smaller, and the impact of the imperfect orthogonal polarizers will be minimized. This can be achieved by splitting the output of an RF generator into two with 10 W each if both AOTFs share the exact wavelength-frequency calibration; otherwise, an RF signal would be necessary for each AOTF. As a result, two AOTFs in series will attenuate the stray light reaching the detector, challenging the Brewer double monochromator. It will, however, reduce the throughput, so a more sensitive sensor will be required, and to retain some of the current advantages of an AOTF-based spectrometer, a PMT should be avoided.

This thesis describes the use of the AOTF for total ozone column measurements by repeating the procedure used by Brewer spectrometers. However, the AOTF is not limited to only performing measurements at five monochromatic wavelengths. Therefore, other ozone retrieval methods can be tested, and measurements of other atmospheric compounds could also be achieved.

References

ACE 2007. *BS ISO 21348:2007 - Space environment (natural and artificial). Process for determining solar irradiances*.

AGRAWAL, P., NANDI, A., SUDHAKAR, M., JAISWAL, B., TYAGI, A., SANKARASUBRAMANIAN, K. & AGARWAL, A. 2015. Characterization of an Acousto-optic tunable filter for development of a near-IR spectrometer for planetary science. *Experimental Astronomy,* 39**,** 445-460.

ANALYTICAL METHODS COMMITTEE, A. N. 2019. Revision of the International System of Units (Background paper). *Analytical Methods,* 11**,** 1577-1579.

AVNERY, S., MAUZERALL, D. L., LIU, J. & HOROWITZ, L. W. 2011. Global crop yield reductions due to surface ozone exposure: 2. Year 2030 potential crop production losses and economic damage under two scenarios of O3 pollution. *Atmospheric Environment,* 45**,** 2297-2309.

BERNHARD, G., EVANS, R. D., LABOW, G. J. & OLTMANS, S. J. 2005. Bias in Dobson total ozone measurements at high latitudes due to approximations in calculations of ozone absorption coefficients and air mass. *Journal of Geophysical Research-Atmospheres,* 110.

BODHAINE, B. A., WOOD, N. B., DUTTON, E. G. & SLUSSER, J. R. 1999. On Rayleigh Optical Depth Calculations. *Journal of Atmospheric and Oceanic Technology,* 16**,** 1854-1861.

BOUCHER, O. 2015. *Atmospheric aerosols : properties and climate impacts,* Dordrecht, Springer.

BRÖNNIMANN, S., CAIN, J. C., STAEHELIN, J. & FARMER, S. F. G. 2003a. Total ozone observations prior to the IGY. II: Data and quality. *Quarterly Journal of the Royal Meteorological Society,* 129**,** 2819-2843.

BRÖNNIMANN, S., STAEHELIN, J., FARMER, S. F. G., CAIN, J. C., SVENDBY, T. & SVENØE, T. 2003b. Total ozone observations prior to the IGY. I: A history. *Quarterly Journal of the Royal Meteorological Society,* 129**,** 2797-2817.

BUCHOLTZ, A. 1995. Rayleigh-scattering calculations for the terrestrial atmosphere. *Applied Optics,* 34**,** 2765-2773.

BURROWS, J. P., RICHTER, A., DEHN, A., DETERS, B., HIMMELMANN, S., VOIGT, S. & ORPHAL, J. 1999. Atmospheric remote-sensing reference data from GOME—2. Temperature-dependent absorption cross sections of O3 in the 231–794 nm range. *Journal of Quantitative Spectroscopy and Radiative Transfer,* 61**,** 509-517.

CALVO, M. S., BARTON, C. N. & WHITING, S. J. 2005. Vitamin D intake: A global perspective of current status.

CHAPMAN, S. 1930. On ozone and atomic oxygen in the upper atmosphere. *Philosophical Magazine,* 10**,** 369-383.

CHERIN, A. & PEREZ, R. 1995. 25 - Fiber Optics for EMC. *Handbook of Electromagnetic Compatibility.* San Diego: Academic Press.

CHRISTIE, M. 2001. *The Ozone Layer: A Philosophy of Science Perspective,* Cambridge, Cambridge University Press.

CORNU, A. 1881. Sur l'absorption atmosphérique des radiations ultra-violettes. *J. Phys. Theor. Appl.,* 10**,** 5-17.

CZERNY, M. & TURNER, A. F. 1930. Über den Astigmatismus bei Spiegelspektrometern. *Zeitschrift für Physik,* 61**,** 792-797.

DOBSON, G. M. B. 1968. 40 years research on atmospheric ozone at oxford - A history. *Applied Optics,* 7**,** 387-&.

DUNAI, D., ZOLETNIK, S., SÁRKÖZI, J. & FIELD, A. R. 2010. Avalanche photodiode based detector for beam emission spectroscopy. *Review of Scientific Instruments,* 81**,** 103503.

EBERT, H. 1889. H. Ebert: Wied. Ann. 38, 489.

EBI, K. L. & MCGREGOR, G. 2008. Climate Change, Tropospheric Ozone and Particulate Matter, and Health Impacts. *Environmental Health Perspectives,* 116**,** 1449-1455.

ELSON, J. M., BENNETT, H. E. & BENNETT, J. M. 1979. CHAPTER 7 - Scattering from Optical Surfaces. *In:* ROBERT R, S. & JAMES C, W. (eds.) *Applied Optics and Optical Engineering.* Elsevier.

FABRY, C. & BUISSON, H. 1921. A study of the ultra-violet end of the solar spectrum. *Astrophysical Journal,* 54**,** 297-322.

FARMAN, J. C., GARDINER, B. G. & SHANKLIN, J. D. 1985. Large losses of total ozone in Antarctica reveal seasonal ClOX/NOX interaction. *Nature,* 315**,** 207-210.

FASTIE, W. G. 1952. A Small Plane Grating Monochromator. *Journal of the Optical Society of America,* 42**,** 641-647.

FASTIE, W. G. 1991. Ebert spectrometer reflections. *Phys. Today,* 44**,** 37-43.

FRÖHLICH, C. & SHAW, G. E. 1980. New determination of Rayleigh scattering in the terrestrial atmosphere. *Applied Optics,* 19**,** 1773-1775.

GORSHELEV, V., SERDYUCHENKO, A., WEBER, M., CHEHADE, W. & BURROWS, J. P. 2014. High spectral resolution ozone absorption cross-sections - Part 1: Measurements, data analysis and comparison with previous measurements around 293 K. *Atmospheric Measurement Techniques,* 7**,** 609-624.

GREEN, A. C., BARTLETT, L. M. & VAUGHAN, G. 2001. SAOZ measurements of total ozone at Aberystwyth. *Journal of Quantitative Spectroscopy and Radiative Transfer,* 69**,** 231-243.

GUPTA, N. & VOLOSHINOV, V. 2004. Hyperspectral imager, from ultraviolet to visible, with a KDP acousto-optic tunable filter. *Applied Optics,* 43**,** 2752-2759.

HAMAMATSU 2004.

HAMAMATSU PHOTONICS 2006. Photomultipliers tubes - Basic applications. Third Edition ed.

HARRISON, D. N. & DOBSON, G. M. B. 1925. Measurements of the amount of ozone in the upper atmosphere. *Quarterly Journal of the Royal Meteorological Society,* 51**,** 363-370.

HARTLEY, W. N. 1881. XXI.—On the absorption of solar rays by atmospheric ozone. *Journal of the Chemical Society, Transactions,* 39**,** 111-128.

HAUTEFEUILLE, M. P. & CHAPPUIS, J. 1880. On the liquefaction of ozone, and on its color in the gaseous state. *Journal of the Franklin Institute,* 110**,** 345-347.

HENDRICK, F., POMMEREAU, J. P., GOUTAIL, F., EVANS, R. D., IONOV, D., PAZMINO, A., KYRO, E., HELD, G., ERIKSEN, P., DOROKHOV, V., GIL, M. & VAN ROOZENDAEL, M. 2011. NDACC/SAOZ UV-visible total ozone measurements: improved retrieval and comparison with correlative ground-based and satellite observations. *Atmospheric Chemistry and Physics,* 11**,** 5975-5995.

HERMAN, J., ABUHASSAN, R., EVANS, A., PETROPAVLOVSKIKH, N., MCCONVILLE, I. & CEDE, G. 2015. Comparison of ozone retrievals from the Pandora spectrometer system and Dobson spectrophotometer in Boulder, Colorado. *Atmospheric Measurement Techniques,* 8**,** 3407-3418.

HERMAN, J., CEDE, A., SPINEI, E., MOUNT, G., TZORTZIOU, M. & ABUHASSAN, N. 2009. NO2 column amounts from ground-based Pandora and MFDOAS spectrometers using the direct-sun DOAS technique: Intercomparisons and application to OMI validation. *Journal of Geophysical Research-Atmospheres,* 114.

HOFMANN, D. J., DESHLER, T. L., AIMEDIEU, P., MATTHEWS, W. A., JOHNSTON, P. V., KONDO, Y., SHELDON, W. R., BYRNE, G. J. & BENBROOK, J. R. 1989. Stratospheric clouds and ozone depletion in the Arctic during January 1989. *Nature,* 340**,** 117.

HUGGINS, W. 1890. On a New Group of Lines in the Photographic Spectrum of Sirius. *Proceedings of the Royal Society of London,* 48**,** 216-217.

INN, E. C. Y. & TANAKA, Y. 1953. Absorption Coefficient of Ozone in the Ultraviolet and Visible Regions. *Journal of the Optical Society of America,* 43**,** 870-873.

JACOBSON, M. Z. 2005. *Fundamentals of Atmospheric Modeling,* Cambridge, Cambridge University Press.

JONES, A., URBAN, J., MURTAGH, D. P., SANCHEZ, C., WALKER, K. A., LIVESAY, N. J., FROIDEVAUX, L. & SANTEE, M. L. 2010. *Analysis of HCl and ClO time series in the upper stratosphere using satellite data sets*.

JOSEFSSON, W. A. P. 1986. Solar ultraviolet radiation in Sweden. Sweden: SMHI.

JUZENIENE, A. & MOAN, J. 2012. Beneficial effects of UV radiation other than via vitamin D production. *Dermato-endocrinology,* 4**,** 109-117.

KATRAŠNIK, J., BÜRMEN, M., PERNUŠ, F. & LIKAR, B. 2010. Spectral characterization and calibration of AOTF spectrometers and hyper-spectral imaging systems. *Chemometrics and Intelligent Laboratory Systems,* 101**,** 23-29.

KAYSER, H. 1910. *Handbuch der Spectroscopie / von H. Kayser. 5.Band : mit 2 Tafeln und 3 Figuren,* Leipzig, Leipzig : S. Hirzel.

KERR, J. B., MCELROY, C. T., WARDLE, D. I., OLAFSON, R. A. & EVANS, W. F. J. 1981. The Automated Brewer Spectrophotometer. *In:* ZEREFOS, C. S. & GHAZI, A. (eds.) *Atmospheric Ozone: Proceedings of the Quadrennial Ozone Symposium held in Halkidiki, Greece 3–7 September 1984.* Dordrecht: Springer Netherlands.

KHALIL, M. A. K., MOORE, R. M., HARPER, D. B., LOBERT, J. M., ERICKSON, D. J., KOROPALOV, V., STURGES, W. T. & KEENE, W. C. 1999. Natural emissions of chlorine-containing gases: Reactive Chlorine Emissions Inventory. *Journal of Geophysical Research: Atmospheres (1984–2012),* 104**,** 8333-8346.

KIPP & ZONEN 2014. Brewer MkIII photometer - Operator's Manual for Single Board. Revision E ed.

KOBAYASHI, M. & MIKAWA, T. 2002. Chapter 9 - Avalanche Photodiodes A2 - Dutta, Achyut K. *In:* DUTTA, N. K. & FUJIWARA, M. (eds.) *WDM Technologies.* San Diego: Academic Press.

KOMHYR, W. D. 1980. Operations handbook - Ozone observations with a Dobson spectrophotometer. *In:* 1469, W. T.-N. (ed.).

KOMHYR, W. D., GRASS, R. D. & LEONARD, R. K. 1989. Dobson spectrophotometer-83 - A standard for total ozone measurements, 1962-1987. *Journal of Geophysical Research-Atmospheres,* 94**,** 9847-9861.

KONDRATYEV, K. Y. 1969. *Radiation in the atmosphere*.

KORABLEV, O. I., BELYAEV, D. A., DOBROLENSKIY, Y. S., TROKHIMOVSKIY, A. Y. & KALINNIKOV, Y. K. 2018. Acousto-optic tunable filter spectrometers in space missions [Invited]. *Applied optics. Optical technology and biomedical optics,* 57**,** C103-C119.

KOUREMETI, N., BAIS, A. F., BALIS, D. & ZYRICHIDOU, I. 2013. Phaethon: A System for the Validation of Satellite Derived Atmospheric Columns of Trace Gases. *In:* HELMIS, G. C. & NASTOS, T. P. (eds.) *Advances in Meteorology, Climatology and Atmospheric Physics.* Berlin, Heidelberg: Springer Berlin Heidelberg.

KYRÖ, E. 1993. Intercomparison of total ozone data from Nimbus 7 TOMS, the Brewer UV Spectrophotometer and SAOZ UV-Visible Spectrophotometer at High Latitudes Observatory, Sodankylä. *Geophysical Research Letters,* 20**,** 571-574.

LIOU, K.-N. & HANSEN, J. E. 1971. Intensity and Polarization for Single Scattering by Polydisperse Spheres: A Comparison of Ray Optics and Mie Theory. *Journal of the Atmospheric Sciences,* 28**,** 995-1004.

LIPPMANN, M. 1991. Health effects of tropospheric ozone. *Environmental Science & Technology,* 25**,** 1954-1962.

MAHIEUX, A., WILQUET, V., DRUMMOND, R., BELYAEV, D., FEDEROVA, A. & VANDAELE, A. C. 2009. A new method for determining the transfer function of an acousto optical tunable filter. *Optics express,* 17**,** 2005.

MANSOORI, S. & MITCHELL, A. 2004. RF transversal filter using an AOTF. *Photonics Technology Letters, IEEE,* 16**,** 879-881.

MASTERS, G. M. 2013. *Renewable and efficient electric power systems,* Hoboken, NJ, John Wiley & Sons Inc.

MATSUMURA, Y. & ANANTHASWAMY, H. N. 2004. Toxic effects of ultraviolet radiation on the skin. *Toxicology and Applied Pharmacology,* 195**,** 298-308.

MCCORMICK, M. P., STEELE, H. M., HAMILL, P., CHU, W. P. & SWISSLER, T. J. 1982. Polar Stratospheric Cloud Sightings by SAM II. *Journal of the Atmospheric Sciences,* 39**,** 1387-1397.

MIELENZ, K. D. 1964. Theory of mirror spectographs .3. Focal surfaces + slit curvature of Ebert + Ebert-Fastie spectographs. *Journal of Research of the National Bureau of Standards Section C-Engineering and Instrumentation,* C 68**,** 205-+.

MIYAZAKI, K., IWASAKI, T., SHIBATA, K. & DEUSHI, M. 2005. Roles of transport in the seasonal variation of the total ozone amount. *Journal of Geophysical Research-Atmospheres,* 110.

MÖLDERS, N. 2014. *Lectures in Meteorology,* Cham, Springer International Publishing.

MOLINA, M. J. & ROWLAND, F. S. 1974. Stratospheric sink for chlorofluoromethanes: chlorine atomic-catalysed destruction of ozone. *Nature,* 249**,** 810-812.

MORISON, W. L. 1989. Effects of ultraviolet-radiation on the immune-system in humans. *Photochemistry and Photobiology,* 50**,** 515-524.

NASA 1996. Nimbus–7 Total Ozone Mapping Spectrometer (TOMS) Data Products User's Guide.

NASA. 2021. *Ozone Hole Watch* [Online]. Available: https://so2.gsfc.nasa.gov/so2intro.html#:~:text=If%20you%20were%20to%20compress,SO2%20per%20square%20meter. [Accessed 3 September 2021].

NATIONAL INSTRUMENTS 2009. Sound and Vibration Data Acquisition NI-USB4431.

NICOLET, M. 1984. On the molecular scattering in the terrestrial atmosphere : An empirical formula for its calculation in the homosphere. *Planetary and Space Science,* 32**,** 1467-1468.

NIST. 1994. *NIST Standard Reference Database 121* [Online]. Available: https://physics.nist.gov/cuu/Constants/index.html [Accessed 18 April 2019].

OWEN, B. T. & RICHARD, P. T. 1991. Polar Stratospheric Clouds and Ozone Depletion. *Scientific American,* 264**,** 68.

PALMER, C. A. & LOEWEN, E. G. 2005. *Diffraction grating handbook*, NEWPORT CORPORATION.

PENNDORF, R. 1957. Tables of the Refractive Index for Standard Air and the Rayleigh Scattering Coefficient for the Spectral Region between 0.2 and 20.0 μ and Their Application to Atmospheric Optics. *Journal of the Optical Society of America,* 47**,** 176-182.

PERKINELMER INSTRUMENTS 2000. Low level optical detection using lock-in amplifier techniques.

PHOTONIS 2002. PHOTOMULTIPLIER TUBES principles & applications. Brive, France.

PINTO, D. M., BLANDE, J. D., SOUZA, S. R., NERG, A.-M. & HOLOPAINEN, J. K. 2010. Plant Volatile Organic Compounds (VOCs) in Ozone (O3) Polluted Atmospheres: The Ecological Effects. *Journal of Chemical Ecology,* 36**,** 22-34.

POOLE, L. R., SOLOMON, S., MCCORMICK, M. P. & PITTS, M. C. 1989. The interannual variability of polar stratospheric clouds and related parameters in Antarctica during September and October. *Geophysical Research Letters,* 16**,** 1157-1160.

R. & J. BECK LTD Instructions for use of dr. Dobson's spectrophotometer. London.

RAI, R. & AGRAWAL, M. 2012. Impact of Tropospheric Ozone on Crop Plants. *Proceedings of the National Academy of Sciences, India Section B: Biological Sciences,* 82**,** 241-257.

RAVANAT, J. L., DOUKI, T. & CADET, J. 2001. Direct and indirect effects of UV radiation on DNA and its components. *Journal of Photochemistry and Photobiology B-Biology,* 63**,** 88-102.

ACE 2007. *BS ISO 21348:2007 - Space environment (natural and artificial). Process for determining solar irradiances*.

AGRAWAL, P., NANDI, A., SUDHAKAR, M., JAISWAL, B., TYAGI, A., SANKARASUBRAMANIAN, K. & AGARWAL, A. 2015. Characterization of an Acousto-optic tunable filter for development of a near-IR spectrometer for planetary science. *Experimental Astronomy,* 39**,** 445-460.

ANALYTICAL METHODS COMMITTEE, A. N. 2019. Revision of the International System of Units (Background paper). *Analytical Methods,* 11**,** 1577-1579.

AUCAMP, P. J., BJÖRN, L. O. & LUCAS, R. 2020. Questions and answers about the environmental effects of ozone depletion and its interactions with climate change: 2010 assessment. *Photochemical & photobiological sciences,* 10**,** 301-316.

AVNERY, S., MAUZERALL, D. L., LIU, J. & HOROWITZ, L. W. 2011. Global crop yield reductions due to surface ozone exposure: 2. Year 2030 potential crop production losses and economic damage under two scenarios of O3 pollution. *Atmospheric Environment,* 45**,** 2297-2309.

BERNHARD, G., EVANS, R. D., LABOW, G. J. & OLTMANS, S. J. 2005. Bias in Dobson total ozone measurements at high latitudes due to approximations in calculations of ozone absorption coefficients and air mass. *Journal of Geophysical Research-Atmospheres,* 110.

BODHAINE, B. A., WOOD, N. B., DUTTON, E. G. & SLUSSER, J. R. 1999. On Rayleigh Optical Depth Calculations. *Journal of Atmospheric and Oceanic Technology,* 16**,** 1854-1861.

BOUCHER, O. 2015. *Atmospheric aerosols : properties and climate impacts,* Dordrecht, Springer.

BRÖNNIMANN, S., CAIN, J. C., STAEHELIN, J. & FARMER, S. F. G. 2003a. Total ozone observations prior to the IGY. II: Data and quality. *Quarterly Journal of the Royal Meteorological Society,* 129**,** 2819-2843.

BRÖNNIMANN, S., STAEHELIN, J., FARMER, S. F. G., CAIN, J. C., SVENDBY, T. & SVENØE, T. 2003b. Total ozone observations prior to the IGY. I: A history. *Quarterly Journal of the Royal Meteorological Society,* 129**,** 2797-2817.

BUCHOLTZ, A. 1995. Rayleigh-scattering calculations for the terrestrial atmosphere. *Applied Optics,* 34**,** 2765-2773.

BURROWS, J. P., RICHTER, A., DEHN, A., DETERS, B., HIMMELMANN, S., VOIGT, S. & ORPHAL, J. 1999. Atmospheric remote-sensing reference data from GOME—2. Temperature-dependent absorption cross sections of O3 in the 231–794nm range. *Journal of Quantitative Spectroscopy and Radiative Transfer,* 61**,** 509-517.

CALVO, M. S., BARTON, C. N. & WHITING, S. J. 2005. Vitamin D intake: A global perspective of current status.

CHAPMAN, S. 1930. On ozone and atomic oxygen in the upper atmosphere. *Philosophical Magazine,* 10**,** 369-383.

CHERIN, A. & PEREZ, R. 1995. 25 - Fiber Optics for EMC. *Handbook of Electromagnetic Compatibility.* San Diego: Academic Press.

CHRISTIE, M. 2001. *The Ozone Layer: A Philosophy of Science Perspective,* Cambridge, Cambridge University Press.

CORNU, A. 1881. Sur l'absorption atmosphérique des radiations ultra-violettes. *J. Phys. Theor. Appl.,* 10**,** 5-17.

DOBSON, G. M. B. 1968. 40 years research on atmospheric ozone at oxford - A history. *Applied Optics,* 7**,** 387-&.

DUNAI, D., ZOLETNIK, S., SÁRKÖZI, J. & FIELD, A. R. 2010. Avalanche photodiode based detector for beam emission spectroscopy. *Review of Scientific Instruments,* 81**,** 103503.

EBI, K. L. & MCGREGOR, G. 2008. Climate Change, Tropospheric Ozone and Particulate Matter, and Health Impacts. *Environmental Health Perspectives,* 116**,** 1449-1455.

EISINGER, M. & BURROWS, J. P. 1998. Tropospheric sulfur dioxide observed by the ERS-2 GOME instrument. *Geophysical research letters,* 25**,** 4177-4180.

ELSON, J. M., BENNETT, H. E. & BENNETT, J. M. 1979. CHAPTER 7 - Scattering from Optical Surfaces. *In:* ROBERT R, S. & JAMES C, W. (eds.) *Applied Optics and Optical Engineering.* Elsevier.

FABRY, C. & BUISSON, H. 1921. A study of the ultra-violet end of the solar spectrum. *Astrophysical Journal,* 54**,** 297-322.

FARMAN, J. C., GARDINER, B. G. & SHANKLIN, J. D. 1985. Large losses of total ozone in Antarctica reveal seasonal ClOX/NOX interaction. *Nature,* 315**,** 207-210.

FONTANI, D., SANSONI, P., SANI, E., CORAGGIA, S., JAFRANCESCO, D. & MERCATELLI, L. 2013. Solar Divergence Collimators for Optical Characterisation of Solar Components. *International journal of photoenergy,* 2013**,** 1-10.

FOUNTOULAKIS, I., REDONDAS, A., LAKKALA, K., BERJON, A., BAIS, A. F., DOPPLER, L., FEISTER, U., HEIKKILA, A., KARPPINEN, T., KARHU, J. M., KOSKELA, T., GARANE, K., FRAGKOS, K. & SAVASTIOUK, V. 2017. Temperature dependence of the Brewer global UV measurements. *Atmospheric Measurement Techniques,* 10**,** 4491-4505.

FRÖHLICH, C. & SHAW, G. E. 1980. New determination of Rayleigh scattering in the terrestrial atmosphere. *Applied Optics,* 19**,** 1773-1775.

GORSHELEV, V., SERDYUCHENKO, A., WEBER, M., CHEHADE, W. & BURROWS, J. P. 2014. High spectral resolution ozone absorption cross-sections - Part 1: Measurements, data analysis and comparison with previous measurements around 293 K. *Atmospheric Measurement Techniques,* 7**,** 609-624.

GRÖBNER, J., KRÖGER, I., EGLI, L., HÜLSEN, G., RIECHELMANN, S. & SPERFELD, P. 2017. The high-resolution extraterrestrial solar spectrum (QASUMEFTS) determined from ground-based solar irradiance measurements. *Atmospheric measurement techniques,* 10**,** 3375-3383.

GUPTA, N. & VOLOSHINOV, V. 2004. Hyperspectral imager, from ultraviolet to visible, with a KDP acousto-optic tunable filter. *Applied Optics,* 43**,** 2752-2759.

HAMAMATSU 2004.

HAMAMATSU PHOTONICS 2006. Photomultipliers tubes - Basic applications. Third Edition ed.

HARRISON, D. N. & DOBSON, G. M. B. 1925. Measurements of the amount of ozone in the upper atmosphere. *Quarterly Journal of the Royal Meteorological Society,* 51**,** 363-370.

HARTLEY, W. N. 1881. XXI.—On the absorption of solar rays by atmospheric ozone. *Journal of the Chemical Society, Transactions,* 39**,** 111-128.

HAUTEFEUILLE, M. P. & CHAPPUIS, J. 1880. On the liquefaction of ozone, and on its color in the gaseous state. *Journal of the Franklin Institute,* 110**,** 345-347.

HOFMANN, D. J., DESHLER, T. L., AIMEDIEU, P., MATTHEWS, W. A., JOHNSTON, P. V., KONDO, Y., SHELDON, W. R., BYRNE, G. J. & BENBROOK, J. R. 1989. Stratospheric clouds and ozone depletion in the Arctic during January 1989. *Nature,* 340**,** 117.

HÖNNINGER, G., VON FRIEDEBURG, C. & PLATT, U. 2004. Multi axis differential optical absorption spectroscopy (MAX-DOAS). *Atmospheric chemistry and physics,* 4**,** 231-254.

HUGGINS, W. 1890. On a New Group of Lines in the Photographic Spectrum of Sirius. *Proceedings of the Royal Society of London,* 48**,** 216-217.

JACOBSON, M. Z. 2005. *Fundamentals of Atmospheric Modeling,* Cambridge, Cambridge University Press.

JONES, A., URBAN, J., MURTAGH, D. P., SANCHEZ, C., WALKER, K. A., LIVESAY, N. J., FROIDEVAUX, L. & SANTEE, M. L. 2010. *Analysis of HCl and ClO time series in the upper stratosphere using satellite data sets*.

JOSEFSSON, W. A. P. 1986. Solar ultraviolet radiation in Sweden. Sweden: SMHI.

JUZENIENE, A. & MOAN, J. 2012. Beneficial effects of UV radiation other than via vitamin D production. *Dermato-endocrinology,* 4**,** 109-117.

KALOGIROU, S. A. 2014. *Solar energy engineering : processes and systems,* Amsterdam, Elsevier/Academic Press.

KATRAŠNIK, J., BÜRMEN, M., PERNUŠ, F. & LIKAR, B. 2010. Spectral characterization and calibration of AOTF spectrometers and hyper-spectral imaging systems. *Chemometrics and Intelligent Laboratory Systems,* 101**,** 23-29.

KERR, J. B., MCELROY, C. T., WARDLE, D. I., OLAFSON, R. A. & EVANS, W. F. J. 1981. The Automated Brewer Spectrophotometer. *In:* ZEREFOS, C. S. & GHAZI, A. (eds.) *Atmospheric Ozone: Proceedings of the Quadrennial Ozone Symposium held in Halkidiki, Greece 3–7 September 1984.* Dordrecht: Springer Netherlands.

KHALIL, M. A. K., MOORE, R. M., HARPER, D. B., LOBERT, J. M., ERICKSON, D. J., KOROPALOV, V., STURGES, W. T. & KEENE, W. C. 1999. Natural emissions of chlorine-containing gases: Reactive Chlorine Emissions Inventory. *Journal of Geophysical Research: Atmospheres (1984–2012),* 104**,** 8333-8346.

KIPP & ZONEN 2014. Brewer MkIII photometer - Operator's Manual for Single Board. Revision E ed.

KOBAYASHI, M. & MIKAWA, T. 2002. Chapter 9 - Avalanche Photodiodes A2 - Dutta, Achyut K. *In:* DUTTA, N. K. & FUJIWARA, M. (eds.) *WDM Technologies.* San Diego: Academic Press.

KOMHYR, W. D. 1980. Operations handbook - Ozone observations with a Dobson spectrophotometer. *In:* 1469, W. T.-N. (ed.).

KOMHYR, W. D., GRASS, R. D. & LEONARD, R. K. 1989. Dobson spectrophotometer-83 - A standard for total ozone measurements, 1962-1987. *Journal of Geophysical Research-Atmospheres,* 94**,** 9847-9861.

KORABLEV, O. I., BELYAEV, D. A., DOBROLENSKIY, Y. S., TROKHIMOVSKIY, A. Y. & KALINNIKOV, Y. K. 2018. Acousto-optic tunable filter spectrometers in space missions [Invited]. *Applied optics. Optical technology and biomedical optics,* 57**,** C103-C119.

LEÓN-LUIS, S. F., REDONDAS, A., CARREÑO, V., LÓPEZ-SOLANO, J., BERJÓN, A., HERNÁNDEZ-CRUZ, B. & SANTANA-DÍAZ, D. 2018. Internal consistency of the Regional Brewer Calibration Centre for Europe triad during the period 2005-2016. *Atmospheric measurement techniques,* 11**,** 4059-4072.

LIOU, K.-N. & HANSEN, J. E. 1971. Intensity and Polarization for Single Scattering by Polydisperse Spheres: A Comparison of Ray Optics and Mie Theory. *Journal of the Atmospheric Sciences,* 28**,** 995-1004.

LIPPMANN, M. 1991. Health effects of tropospheric ozone. *Environmental Science & Technology,* 25**,** 1954-1962.

MAHIEUX, A., WILQUET, V., DRUMMOND, R., BELYAEV, D., FEDEROVA, A. & VANDAELE, A. C. 2009. A new method for determining the transfer function of an acousto optical tunable filter. *Optics express,* 17**,** 2005.

MANTSEVICH, S. N. & YUSHKOV, K. B. 2021. Optimization of piezotransducer dimensions for quasicollinear paratellurite AOTF. *Ultrasonics,* 112**,** 106335-106335.

MASTERS, G. M. 2013. *Renewable and efficient electric power systems,* Hoboken, NJ, John Wiley & Sons Inc.

MATSUMURA, Y. & ANANTHASWAMY, H. N. 2004. Toxic effects of ultraviolet radiation on the skin. *Toxicology and Applied Pharmacology,* 195**,** 298-308.

MCCORMICK, M. P., STEELE, H. M., HAMILL, P., CHU, W. P. & SWISSLER, T. J. 1982. Polar Stratospheric Cloud Sightings by SAM II. *Journal of the Atmospheric Sciences,* 39**,** 1387-1397.

MIYAZAKI, K., IWASAKI, T., SHIBATA, K. & DEUSHI, M. 2005. Roles of transport in the seasonal variation of the total ozone amount. *Journal of Geophysical Research-Atmospheres,* 110.

MÖLDERS, N. 2014. *Lectures in Meteorology,* Cham, Springer International Publishing.

MOLINA, M. J. & ROWLAND, F. S. 1974. Stratospheric sink for chlorofluoromethanes: chlorine atomic-catalysed destruction of ozone. *Nature,* 249**,** 810-812.

MORISON, W. L. 1989. Effects of ultraviolet-radiation on the immune-system in humans. *Photochemistry and Photobiology,* 50**,** 515-524.

NASA 1996. Nimbus–7 Total Ozone Mapping Spectrometer (TOMS) Data Products User's Guide.

NASA. 2020. *Ozone Hole Watch* [Online]. Available: http://ozonewatch.gsfc.nasa.gov/ [Accessed 3 September 2020].

NICOLET, M. 1984. On the molecular scattering in the terrestrial atmosphere : An empirical formula for its calculation in the homosphere. *Planetary and Space Science,* 32**,** 1467-1468.

NIST. 1994. *NIST Standard Reference Database 121* [Online]. Available: https://physics.nist.gov/cuu/Constants/index.html [Accessed 18 April 2019].

ORTENBERG, F. 2013. Ozone: Space Vision.

OWEN, B. T. & RICHARD, P. T. 1991. Polar Stratospheric Clouds and Ozone Depletion. *Scientific American,* 264**,** 68.

PENNDORF, R. 1957. Tables of the Refractive Index for Standard Air and the Rayleigh Scattering Coefficient for the Spectral Region between 0.2 and 20.0 μ and Their Application to Atmospheric Optics. *Journal of the Optical Society of America,* 47**,** 176-182.

PERKINELMER INSTRUMENTS 2000. Low level optical detection using lock-in amplifier techniques.

PINTO, D. M., BLANDE, J. D., SOUZA, S. R., NERG, A.-M. & HOLOPAINEN, J. K. 2010. Plant Volatile Organic Compounds (VOCs) in Ozone (O3) Polluted Atmospheres: The Ecological Effects. *Journal of Chemical Ecology,* 36**,** 22-34.

POOLE, L. R., SOLOMON, S., MCCORMICK, M. P. & PITTS, M. C. 1989. The interannual variability of polar stratospheric clouds and related parameters in Antarctica during September and October. *Geophysical Research Letters,* 16**,** 1157-1160.

R. & J. BECK LTD Instructions for use of dr. Dobson's spectrophotometer. London.

RAI, R. & AGRAWAL, M. 2012. Impact of Tropospheric Ozone on Crop Plants. *Proceedings of the National Academy of Sciences, India Section B: Biological Sciences,* 82**,** 241-257.

RAVANAT, J. L., DOUKI, T. & CADET, J. 2001. Direct and indirect effects of UV radiation on DNA and its components. *Journal of Photochemistry and Photobiology B-Biology,* 63**,** 88-102.

REDONDAS, A., NEVAS, S., BERJÓN, A., SILDOJA, M.-M., LEÓN-LUIS, S. F., CARREÑO, V. & SANTANA-DÍAZ, D. 2018. Wavelength calibration of Brewer spectrophotometer using a tunable pulsed laser and implications to the Brewer ozone retrieval. *Atmospheric measurement techniques,* 11**,** 3759-3768.

RUFUS, J., STARK, G., SMITH, P. L., PICKERING, J. C. & THORNE, A. P. 2003. High-resolution photoabsorption cross section measurements of SO2, 2: 220 to 325 nm at 295 K. *Journal of Geophysical Research: Planets,* 108.

SALAWITCH, R. J., WOFSY, S. C. & MCELROY, M. B. 1988. Influence of polar stratospheric clouds on the depletion of Antarctic ozone. *Geophysical Research Letters,* 15**,** 871-874.

SAVASTIOUK, V. & MCELROY, C. T. 2005. Brewer spectrophotometer total ozone measurements made during the 1998 Middle Atmosphere Nitrogen Trend Assessment (MANTRA) campaign. *Atmosphere-Ocean,* 43**,** 315-324.

SCHARMER, K. & GREIF, J. 2000. The European Radiation Atlas. Vol. 1: Fundamentals and maps.

SCHOEBERL, M. R. & HARTMANN, D. L. 1991. The Dynamics of the Stratospheric Polar Vortex and Its Relation to Springtime Ozone Depletions. *Science,* 251**,** 46-52.

SERDYUCHENKO, A., GORSHELEV, V., WEBER, M., CHEHADE, W. & BURROWS, J. P. 2014. High spectral resolution ozone absorption cross-sections - Part 2: Temperature dependence. *Atmospheric Measurement Techniques,* 7**,** 625-636.

SOLOMON, K. R. 2008. Effects of ozone depletion and UV-B radiation on humans and the environment. *Atmosphere-Ocean,* 46**,** 185-202.

STAEHELIN, J., KERR, J., EVANS, R. & VANICEK, K. 2003. Comparison of total ozone measurements of Dobson and Brewer Spectrophotometers and recommended transfer functions. *World Meteorological Organization. Gobal Atmosphere Watch,* 149.

THOMASON, L. W., HERMAN, B. M. & REAGAN, J. A. 1983. The effect of atmospheric attenuators with structured vertical distributions on air-mass determinations and Langley plot analyses. *Journal of the Atmospheric Sciences,* 40**,** 1851-1854.

THORLABS. 2017. *Catalogue of products* [Online]. Available: http://www.thorlabs.de/navigation.cfm [Accessed 06 of March 2020].

TOMASI, C. & PETKOV, B. H. 2014. Calculations of relative optical air masses for various aerosol types and minor gases in Arctic and Antarctic atmospheres. *Journal of Geophysical Research: Atmospheres,* 119**,** 1363-1385.

TOMASI, C., VITAKE, V. & DE SANTIS, L. V. 1998. Relative optical mass functions for air, water vapour, ozone and nitrogen dioxide in atmospheric models presenting different latitudinal and seasonal conditions. *Meteorology and Atmospheric Physics,* 65**,** 11-30.

TOMASI, C., VITALE, V., PETKOV, B., LUPI, A. & CACCIARI, A. 2005. Improved algorithm for calculations of Rayleigh-scattering optical depth in standard atmospheres. *Applied Optics,* 44**,** 3320-3341.

TUMMON, F., HASSLER, B., HARRIS, N. R. P., STAEHELIN, J., STEINBRECHT, W., ANDERSON, J., BODEKER, G. E., BOURASSA, A., DAVIS, S. M., DEGENSTEIN, D., FRITH, S. M., FROIDEVAUX, L., KYRÖLÄ, E., LAINE, M., LONG, C., PENCKWITT, A. A., SIORIS, C. E., ROSENLOF, K. H., ROTH, C., WANG, H. J. & WILD, J. 2015. Intercomparison of vertically resolved merged satellite ozone data sets: interannual variability and long-term trends. *Atmospheric chemistry and physics,* 15**,** 3021-3043.

UNEP 2012. Handbook for the Montreal Protocol on Substances that Deplete the Ozone Layer. *the Montreal Protocol on Substances that Deplete the Ozone Layer*.

VÁZQUEZ, M. & HANSLMEIER, A. 2006. *Ultraviolet Radiation in the Solar System,* Dordrecht, Springer Netherlands.

WMO 2010a. *Scientific assessment of ozone depletion : 2010*, World Meteorological Organization.

WMO 2014. Scientific Assessment of ozone depletion: 2014.

WMO 2015. *Seventh Intercomparison Campaign of the Regional Brewer Calibration Center Europe (RBCC-E) Lichtklimatisches Observatorium, Arosa, Switzerland, 16-27 July 2012*, WORLD METEOROLOGICAL ORGANIZATION / GLOBAL ATMOSPHERE WATCH

WMO 2018. Scientific Assessment of Ozone Depletion: 2018, Global Ozone Research and Monitoring Project

WMO, W. M. O. 2010b. *Guide to meteorological instruments and methods of observation*.

WRIEDT, T. 2012. Mie Theory: A Review. *In:* HERGERT, W. & WRIEDT, T. (eds.) *The Mie Theory: Basics and Applications.* Berlin, Heidelberg: Springer Berlin Heidelberg.

YI, L., WU, J., AN, M., XU, W., FANG, X., YAO, B., LI, Y., GAO, D., ZHAO, X. & HU, J. 2021. The atmospheric concentrations and emissions of major halocarbons in China during 2009–2019. *Environmental pollution (1987),* 284**,** 117190-117190.

YU, H., SHEN, J. & WEI, Y. 2009. Geometrical optics approximation for light scattering by absorbing spherical particles. *Journal of Quantitative Spectroscopy and Radiative Transfer,* 110**,** 1178-1189.

ZHU, Y., TOON, O. B., JENSEN, E. J., BARDEEN, C. G., MILLS, M. J., TOLBERT, M. A., YU, P. & WOODS, S. 2020. Persisting volcanic ash particles impact stratospheric SO2 lifetime and aerosol optical properties. *Nature Communications,* 11**,** 4526.

RIMMER, J. S., REDONDAS, A. & KARPPINEN, T. 2018. EuBrewNet – A European Brewer network (COST Action ES1207), an overview. *Atmos. Chem. Phys.,* 18**,** 10347-10353.

RUFUS, J., STARK, G., SMITH, P. L., PICKERING, J. C. & THORNE, A. P. 2003. High-resolution photoabsorption cross section measurements of SO2, 2: 220 to 325 nm at 295 K. *Journal of Geophysical Research: Planets,* 108.

SALAWITCH, R. J., WOFSY, S. C. & MCELROY, M. B. 1988. Influence of polar stratospheric clouds on the depletion of Antarctic ozone. *Geophysical Research Letters,* 15**,** 871-874.

SAVASTIOUK, V. & MCELROY, C. T. 2005. Brewer spectrophotometer total ozone measurements made during the 1998 Middle Atmosphere Nitrogen Trend Assessment (MANTRA) campaign. *Atmosphere-Ocean,* 43**,** 315-324.

SCHARMER, K. & GREIF, J. 2000. The European Radiation Atlas. Vol. 1: Fundamentals and maps.

SCHOEBERL, M. R. & HARTMANN, D. L. 1991. The Dynamics of the Stratospheric Polar Vortex and Its Relation to Springtime Ozone Depletions. *Science,* 251**,** 46-52.

SERDYUCHENKO, A., GORSHELEV, V., WEBER, M., CHEHADE, W. & BURROWS, J. P. 2014. High spectral resolution ozone absorption cross-sections - Part 2: Temperature dependence. *Atmospheric Measurement Techniques,* 7**,** 625-636.

SOLOMON, K. R. 2008. Effects of ozone depletion and UV-B radiation on humans and the environment. *Atmosphere-Ocean,* 46**,** 185-202.

STAEHELIN, J., KERR, J., EVANS, R. & VANICEK, K. 2003. Comparison of total ozone measurements of Dobson and Brewer Spectrophotometers and recommended transfer functions. *World Meteorological Organization. Gobal Atmosphere Watch,* 149.

THOMASON, L. W., HERMAN, B. M. & REAGAN, J. A. 1983. The effect of atmospheric attenuators with structured vertical distributions on air-mass determinations and Langley plot analyses. *Journal of the Atmospheric Sciences,* 40**,** 1851-1854.

THORLABS. 2017. *Catalogue of products* [Online]. Available: http://www.thorlabs.de/navigation.cfm [Accessed 06 of March 2019].

TOMASI, C. & PETKOV, B. H. 2014. Calculations of relative optical air masses for various aerosol types and minor gases in Arctic and Antarctic atmospheres. *Journal of Geophysical Research: Atmospheres,* 119**,** 1363-1385.

TOMASI, C., VITAKE, V. & DE SANTIS, L. V. 1998. Relative optical mass functions for air, water vapour, ozone and nitrogen dioxide in atmospheric models presenting different latitudinal and seasonal conditions. *Meteorology and Atmospheric Physics,* 65**,** 11-30.

TOMASI, C., VITALE, V., PETKOV, B., LUPI, A. & CACCIARI, A. 2005. Improved algorithm for calculations of Rayleigh-scattering optical depth in standard atmospheres. *Applied Optics,* 44**,** 3320-3341.

TZORTZIOU, M., HERMAN, JR., CEDE, A. & ABUHASSAN, N. 2012. High precision, absolute total ozone column measurements from the Pandora spectrometer system: Comparisons with data from a Brewer double monochromator and Aura OMI. *J. Geophys. Res.-Atmos.,* 117.

UNEP 2012. Handbook for the Montreal Protocol on Substances that Deplete the Ozone Layer. *the Montreal Protocol on Substances that Deplete the Ozone Layer*.

WMO 2010a. *Scientific assessment of ozone depletion : 2010*, World Meteorological Organization.

WMO 2014. Scientific Assessment of ozone depletion: 2014.

WMO 2015. *Seventh Intercomparison Campaign of the Regional Brewer Calibration Center Europe (RBCC-E) Lichtklimatisches Observatorium, Arosa, Switzerland, 16-27 July 2012*, WORLD METEOROLOGICAL ORGANIZATION / GLOBAL ATMOSPHERE WATCH

WMO 2018. Scientific Assessment of Ozone Depletion: 2018, Global Ozone Research and Monitoring Project

WMO, W. M. O. 2010b. *Guide to meteorological instruments and methods of observation*.

WRIEDT, T. 2012. Mie Theory: A Review. *In:* HERGERT, W. & WRIEDT, T. (eds.) *The Mie Theory: Basics and Applications.* Berlin, Heidelberg: Springer Berlin Heidelberg.

YU, H., SHEN, J. & WEI, Y. 2009. Geometrical optics approximation for light scattering by absorbing spherical particles. *Journal of Quantitative Spectroscopy and Radiative Transfer,* 110**,** 1178-1189.